Numerical study on vibration isolation by wave barrier and protection of existing tunnel under explosions

Bo Qiu

Numerical Study on Vibration Isolation by Wave Barrier and Protection of Existing Tunnel under Explosions

Dissertation submitted to Institut National des Sciences Appliquées de Lyon
for the degree of Doctor of Philosophy

by

Bo QIU

Laboratory of Civil & Environmental Engineering (LGCIE)

January 23th, 2014

Members of Jury:

Daniel DIAS	Professor, University of Joseph Fourier, Grenoble	Reporter
Sergey KUZNETSOV	Professor, IPM Russian Academy of Sciences	Reporter
Farimah MASROURI	Professor, Ecole Nationale Supérieure de Géologie	Examiner
Didier SUBRIN	Engineer R&D, CETU, Bron	Examiner
Irini DJERAN-MAIGRE	Professor, INSA Lyon	PhD thesis, Supervisor
Ali LIMAM	Professor, INSA Lyon	PhD thesis, Supervisor

Abstract

Ground vibration induced by human activity such as industrial activities, car or truck traffic, or pilling and blasting in construction or deconstruction operation, generally reaches the troublesome limit for men and occasionally attain the harmful limit. In the densely populated urban regions and buildings housing sensitive equipments, ground vibration has to be strictly controlled. Up to now, many vibration reduction methods have been proposed, one of which is the installation of wave barrier between the dynamic sources and the protected structures. Over the past decades, the vibration isolation effectiveness of wave barrier has been extensively studied. However, to the best of the writer's knowledge, there is little study about the mutual influence of the parameters of soil-barrier system on the barrier screening efficiency, and the optimization design for wave barrier is rare as well. On the other hand, the influence of ground vibration generated by explosions on the nearby existing tunnel has attracted more and more attention due to the recent damage or even failure of tunnels. Up to now, there are few mitigation measures comprehensively proposed by researchers and engineers for the tunnel vibration reduction during explosions. To overcome those drawbacks, this dissertation focuses on the investigation of the influence of various parameters of soil-barrier system on the barrier isolation efficiency. Key parameters are identified. More importantly, a developed optimization design method is developed, aiming to find out the desirable barrier that is able to minimize the ground vibration in protected site. Besides, the dynamic behavior of existing tunnel under nearby explosions is examined. Parameters that significantly affect the response of tunnel are pointed out. Furthermore, two practical mitigation measures: the installation of a protective layer along the tunnel lining and time-delayed explosions (rather than instantaneous explosions), are presented with details. The research in this dissertation is able to provide a good reference for the optimization design of wave barrier in reducing ground vibration in protected site and for the design of practical mitigation measures to protect existing tunnel from nearby explosions.

Keywords: Wave barrier; Vibration isolation; Parametric study; Optimization design; Blast-induced vibration; Existing tunnel; Mitigation measures; Protective layer; Time-delayed explosions; Instantaneous explosions; FEM.

Résumé

Les vibrations du sol induites par les activités humaines telles que, les activités industrielles, la circulation des camions et voitures, les explosions dues aux constructions ou l'exploitation de la déconstruction, atteignent souvent la limite de gêne pour les usagers et parfois la limite de nocivité. Dans les régions urbaines à forte densité et pour les bâtiments abritant des équipements sensibles, les vibrations du sol doivent être strictement contrôlées. Jusqu'à présent, de nombreuses méthodes de réduction de vibration ont été proposées, dont l'une est l'installation d'une barrière d'ondes entre les sources et les structures à protéger. Au cours des dernières décennies, l'efficacité de l'isolation des vibrations à l'aide de barrière d'ondes a été étudiée. Toutefois, il y a peu de travaux consacrés à l'influence mutuelle des paramètres du système sol-barrière sur l'efficacité de l'isolation de la barrière d'ondes, et l'optimisation de la barrière d'onde est également rare. D'autre part, l'influence des vibrations du sol, générées par les explosions durant la construction d'un nouveau tunnel, sur un tunnel avoisinant, interpelle en raison des dommages qui peuvent être produits. Jusqu'à présent, il existe peu de mesures d'atténuation globale proposées par les chercheurs et les ingénieurs concernant la réduction de vibrations dans les tunnels lors des explosions. Pour répondre à ces insuffisances, cette thèse porte sur l'étude de l'influence des différents paramètres du système sol-barrière et qualifie l'efficacité de l'isolation de la barrière d'ondes. Les paramètres clés sont identifiés, leur rôle respectif quantifié. Plus important encore, une méthode de conception d'optimisation est mise au point, dans le but de proposer la barrière qui est capable de réduire au minimum la vibration du sol en site protégé. Enfin, le comportement dynamique du tunnel existant sous les sollicitations des explosions proches est examiné. Les paramètres qui influent considérablement sur la réponse du tunnel sont mis en évidence. Deux mesures d'atténuation pratiques, concernant l'installation d'une couche de protection le long de la paroi du tunnel d'une part et des explosions à retardement (plutôt que des explosions instantanées) d'autre part, sont présentées en détails. Les recherches menées dans le cadre de cette thèse sont en mesure de fournir des éléments pour la conception optimisée de la barrière d'ondes afin de réduire les vibrations du sol en site protégé et pour la conception de mesures d'atténuation concrètes afin de protéger un tunnel existant par des explosions à proximité.

Mots-clés: Barrière d'ondes; Isolation des vibrations; Étude paramétrique; Conception d'optimisation; Vibration induite par explosion; Tunnel existant; Mesures d'atténuation; Couche protectrice; Explosions à retardement; Explosions instantanées; FEM.

Contents

Abstract ..... *i*

Résumé ..... *ii*

Contents ..... *iii*

List of Figures ..... *vii*

List of Tables ..... *xii*

1. Introduction *1*

1.1 Motivation of research **1**

1.2 Scope and objectives **2**

1.3 Structure of dissertation **4**

2. Literature review *6*

2.1 Basics of vibration **6**

2.1.1 Ground vibration sources 6

2.1.2 Wave propagation in soil (or rock) media 9

2.1.3 Impact of vibration 15

2.2 Methods of reducing vibration **17**

2.2.1 Controlling the vibration sources 17

2.2.2 Disrupting the wave propagation through the soil (or rock) media 17

2.2.3 Controlling the vibration of protected structures 18

2.3 Vibration isolation using wave barriers **18**

2.3.1 Analytical method 23

2.3.2 Model test and field experiment 25

2.3.3 Numerical method 27

2.4 Protection of existing tunnels under explosions **30**

2.4.1 Responses of existing tunnels under explosions 32

2.4.2 Measures to protect existing tunnels from explosions 35

2.4.3 Concrete damaged plasticity model (CDP model) 37

2.5 Conclusions 38

3. Investigation on the isolation performance of wave barriers I: under harmonic load 42

3.1 Numerical model 42

3.2 Validation of the numerical solutions 45

3.3 Comparative study of 2D and 3D models 47

3.4 Parametric study 49

3.4.1 Effect of barrier Young's modulus 50

3.4.2 Effect of barrier density 51

3.4.3 Effect of barrier Poisson's ratio 51

3.4.4 Effect of barrier damping ratio 52

3.4.5 Effect of barrier normalized depth 52

3.4.6 Effect of barrier normalized width 54

3.4.7 Effect of barrier inclination angle 55

3.4.8 Effect of normalized distance from the vibratory source to the barrier 55

3.4.9 Effect of external load 56

3.5 Optimization design 57

3.5.1 General study 57

3.5.2 A case study 59

3.6 Conclusions 65

4. Investigation on the isolation performance of wave barriers II: under explosions 66

4.1 Numerical model 66

4.2 Parametric study 70

4.2.1 Effect of barrier Young's modulus 71

4.2.2 Effect of barrier density, Poisson's ratio and damping ratio 71

4.2.3 Effect of barrier depth 73

4.2.4 Effect of distance from the explosive to the barrier 73

4.2.5 Effect of the burial depth of the explosive 74

4.2.6 Effect of barrier width, inclination angle and the blast pressure 74

4.3 Optimization design 76

4.4 Conclusions 79

5. Numerical simulation of the behavior of main tunnel under explosions..80

5.1 Background of the project 80

5.2 Numerical model 83

5.2.1 Blast loading 83

5.2.2 Material model 83

5.3 Finite element model 84

5.4 Parametric study 92

5.4.1 Effect of lining stiffness 92

5.4.2 Effect of lining thickness 93

5.4.3 Effect of the distance of explosions from main tunnel 95

5.4.4 Effect of the position of explosions along the section of cross passage 96

5.4.5 Effect of the blast pressure 99

5.4.6 Effect of the burial depth of main tunnel 100

5.5 Main tunnel damage evaluation 102

5.5.1 Concrete damaged plasticity model (CDP model) 102

5.5.2 Comparisons study between elastic analysis and elastic plastic analysis 105

5.6 Examination on the behavior of slabs inside main tunnel lining 121

5.6.1 The development of numerical model 121

5.6.2 The responses of main tunnel lining (with slabs inside) under explosions 123

5.6.3 The responses of the slabs under explosions 127

5.7 Conclusions 144

6. Mitigation measures for reducing vibration of main tunnel.....145

6.1 Mitigation measure I: installation of a protective layer.....145

6.1.1 Parametric study 152

6.1.2 Optimization design of the EPS protective layer 156

6.2 Mitigation measure II: millisecond-delay explosions 160

6.2.1 Two-hole blast 167

6.2.2 Three-hole blast 169

6.2.3 Four-hole blast 170

6.2.4 Nine-hole blast (in parallelogram shape) 173

6.2.5 Multiple-hole blast in triangle shape 177

6.3 Conclusions 179

7. Conclusions and future work 180

7.1 Conclusions 180

7.2 Recommendations for future work 182

References 184

List of Figures

Figure 1. The destroyed buildings after WenChuan earthquake in 2008, China. 7

Figure 2. The high-speed train (TGV) operated by SNCF Voyages in France. 8

Figure 3. Massive subway explosions rocked in New York in 2012. 9

Figure 4. Perspective view of P-wave propagation through a grid representing a volume of material [14]. 10

Figure 5. Perspective view of S-wave propagation through a grid representing a volume of material [14]. 11

Figure 6. Perspective view of Rayleigh wave propagation through a grid representing a volume of material [14]. 12

Figure 7. The amplitude of Rayleigh wave over depth with different Poisson's ratio [15]. ...13

Figure 8. Perspective view of Love wave propagation through a grid representing a volume of elastic material [14]. 14

Figure 9. Distribution of wave field generated by a circular footing on a homogeneous, isotropic and elastic half-space [17]. 15

Figure 10. Vibration isolation of buildings from traffic-induced vibrations [37]. 20

Figure 11. Vibration isolation of buildings from train-induced vibration [74]. 20

Figure 12. Isolation of sensitive instrument from vibration [76]. 21

Figure 13. Schematic diagram for vibration isolation systems [17]. 22

Figure 14. The distribution of generated waves due to an incident Rayleigh wave on solid wave barrier [58]. 23

Figure 15. Explosion in a Port Huron water intake tunnel in USA in 1971 (Photo from website of The Detroit News). 31

Figure 16. A tunnel explosion happens inside an under-construction expressway tunnel in Hunan province of China in 2012 (Photo from the website of *hugchina*). 31

Figure 17. Schematic diagram of tunnel lining in section. (Picture comes from the website of OSSA) 36

Figure 18. Response of concrete to uniaxial loading in tension (a) and compression (b). 39

Figure 19. Schematic diagram of 2D model of soil-barrier system under surface harmonic load. 42

Figure 20. Finite element mesh model with different element sizes. 44

Figure 21. Mesh convergence study. 44

Figure 22. The motion of point "*a*" in homogeneous isotropic and elastic soil media without damping. 46

Figure 23. Comparative study for vertical vibration isolation by wave barrier. 47

Figure 24. 2D and 3D finite element model meshes in ABAQUS. 48

Figure 25. Comparison of numerical results from 2D and 3D models. 49

Figure 26. Effect of barrier Young's modulus on the vibration isolation effectiveness. 50

Figure 27. Effect of barrier density on the vibration isolation effectiveness. 51
Figure 28. Effect of barrier Poisson's ratio on the vibration isolation effectiveness. 52
Figure 29. Effect of barrier damping ratio on the vibration isolation effectiveness. 52
Figure 30. Effect of barrier depth on the vibration isolation effectiveness (w = 0.1). 53
Figure 31. Effect of barrier depth on the vibration isolation effectiveness (w = 1.0). 54
Figure 32. Effect of barrier width on the vibration isolation effectiveness. 55
Figure 33. Effect of barrier inclination angle on the vibration isolation effectiveness. 56
Figure 34. Effect of normalized distance from the vibratory source to the barrier on the vibration isolation effectiveness. 56
Figure 35. Effect of external load on the vibration isolation effectiveness. 57
Figure 36. Schematic diagram of the 2D model of rock-barrier system under explosions..... 66
Figure 37. The time history of blast pressure. 67
Figure 38. The motion of point "*a*" in homogeneous isotropic and elastic rock media with no damping. 69
Figure 39. Velocity amplitude nephogram at different times in rock with wave barrier. 70
Figure 40. Effect of barrier Young's modulus on the vibration isolation effectiveness. 71
Figure 41. Effect of barrier density on the vibration isolation effectiveness. 72
Figure 42. Effect of barrier Poisson's ratio on the vibration isolation effectiveness. 72
Figure 43. Effect of barrier damping ratio on the vibration isolation effectiveness. 72
Figure 44. Effect of barrier depth on the vibration isolation effectiveness. 73
Figure 45. Effect of distance from explosive to barrier on the vibration isolation effectiveness. 74
Figure 46. Effect of the burial depth of the explosive on the vibration isolation effectiveness. 74
Figure 47. Effect of the barrier width on the vibration isolation effectiveness. 75
Figure 48. Effect of the inclination angle on the vibration isolation effectiveness. 75
Figure 49. Effect of the blast pressure on the vibration isolation effectiveness. 75
Figure 50. The schematic plan view of safety tunnel (read line) and main tunnel (double black lines). 81
Figure 51. The geologic cross section of rock media. 81
Figure 52. The bird's-eye view of the tunnel system (safety tunnel on the left side and main tunnel on the right side). 82
Figure 53. The section of cross passage (units: m). 82
Figure 54. Zones of rock surrounding the explosives. 83
Figure 55. The 2D finite element model in ABAQUS. 85
Figure 56. The 3D finite element model in ABAQUS. 86
Figure 57. The motion of point "a1" in 2D and 3D rock-tunnel models under explosions. 88
Figure 58. The motion of point "b1" in 2D and 3D rock-tunnel models under explosions. 89

Figure 59. The distribution of maximum motion of main tunnel (2D elastic model) under explosions. 90

Figure 60. The distribution of maximum motion of main tunnel (3D elastic model) under explosions. 91

Figure 61. Effect of lining stiffness on the motion of main tunnel. 93

Figure 62. Effect of lining thickness on the motion of main tunnel. 94

Figure 63. Effect of the distance of explosions from the main tunnel on the tunnel motion. . 96

Figure 64. Effect of the horizontal position of explosions along the section of cross passage on the motion of main tunnel. 97

Figure 65. Effect of the vertical position of explosions along the section of cross passage on the motion of main tunnel. 98

Figure 66. Effect of the blast pressure on the motion of main tunnel. 100

Figure 67. Effect of the burial depth of main tunnel on the tunnel motion. 101

Figure 68. Concrete compressive properties: compressive stress and compression damage verse crushing strain. 104

Figure 69. Concrete tensile properties: tensile stress and tension damage verse cracking strain. 104

Figure 70. The motion of main tunnel at point “a1” over time (the tunnel lining with elastic model on the left side, and with CDP model on the right side, the blast pressure is $P_{equivalent}$). 106

Figure 71. The motion of main tunnel at point “b1” over time (the tunnel lining with elastic model on the left side, and with CDP model on the right side, the blast pressure is $P_{equivalent}$). 107

Figure 72. The distribution of the maximum motion of main tunnel (CDP model) under explosions (the blast pressure is $P_{equivalent}$). 108

Figure 73. The distribution of maximum compression damage, tension damage and stiffness degradation of main tunnel (CDP model) under explosions (the blast pressure is $P_{equivalent}$). 109

Figure 74. The motion of main tunnel at point “a1” over time (the tunnel lining with elastic model on the left side, and with CDP model on the right side, the blast pressure is $400P_{equivalent}$). 111

Figure 75. The motion of main tunnel at point “b1” over time (the tunnel lining with elastic model on the left side, and with CDP model on the right side, the blast pressure is $400P_{equivalent}$). 112

Figure 76. The distribution of maximum motion of main tunnel (CDP model) under explosions (the blast pressure is $400P_{equivalent}$). 113

Figure 77. The distribution of maximum compression damage, tension damage and stiffness degradation of main tunnel (CDP model) under explosions (the blast pressure is $400P_{equivalent}$). 114

Figure 78. The evolution of the maximum motion of main tunnel with CDP model and elastic model under blast pressures. 116

Figure 79. The evolution of compression damage, tension damage and stiff degradation of main tunnel under blast pressures. 117

Figure 80. Compression damage nephogram of main tunnel under blast pressures. 118

Figure 81. Tension damage nephogram of main tunnel under blast pressures. 119

Figure 82. Stiffness degradation nephogram of main tunnel under blast pressures. 120

Figure 83. The 3D finite element model (slabs included) in ABAQUS. 122

Figure 84. The distribution of maximum motion of main tunnel lining (CDP model) under explosions (the highlight part in red represents the slabs, the blast pressure is $P_{equivalent}$).....124

Figure 85. The distribution of maximum motion of main tunnel lining (CDP model) under explosions (the highlight part in red represents the slabs, the blast pressure is $400P_{equivalent}$). 125

Figure 86. The distribution of maximum compression damage, tension damage and stiffness degradation of main tunnel lining (CDP model) under explosions (the highlight part in red represents the slabs, the blast pressure is $400P_{equivalent}$).....126

Figure 87. The distribution of maximum motion of the slabs under weak explosions (the blast pressure is $P_{equivalent}$). 128

Figure 88. The distribution of maximum compression damage, tension damage and stiffness degradation of the slabs under weak explosions (the blast pressure is $P_{equivalent}$).....129

Figure 89. The distribution of maximum motion of the slabs under strong explosions (the blast pressure is $400P_{equivalent}$). 131

Figure 90. The distribution of maximum compression damage, tension damage and stiffness degradation of the slabs under strong explosions (the blast pressure is $400P_{equivalent}$). 132

Figure 91. The evolution of maximum motion of nodes on the slabs under strong explosions (the blast pressure is $400P_{equivalent}$). 133

Figure 92. The evolution of maximum motion of the slabs, the lining with slabs inside and the lining without slabs inside under blast pressures. 134

Figure 93. Compression damage nephogram of the slabs and the lining (with slabs inside) under blast pressures. 138

Figure 94. Tension damage nephogram of the slabs and the lining (with slabs inside) under blast pressures. 140

Figure 95. Stiffness degradation nephogram of the slabs and the lining (with slabs inside) under blast pressures. 142

Figure 96. The evolution of compression damage, tension damage and stiff degradation of the slabs, the lining (with slabs inside) and the lining (without slabs inside) under blast pressures. 143

Figure 97. Displacement amplitude nephogram at different times during explosions. 147

Figure 98. The sketch section of main tunnel with a protective layer. 147

Figure 99. The 3D finite element mesh model with a protective layer. 149

Figure 100. The motion of main tunnel at point “a1” with and without the protective layer under explosions. 150

Figure 101. The motion of main tunnel at point “b1” with and without the protective layer under explosions. 151

Figure 102. Effect of the thickness of protective layer on the vibration isolation effectiveness. 153

Figure 103. Effect of the distance of explosions from main tunnel on the vibration isolation effectiveness. 154

Figure 104. Effect of the blast pressure on the vibration isolation effectiveness. 156

Figure 105. The plan of the two-hole blast along the section of cross passage. 161

Figure 106. The 3D finite element mesh model with two-hole blast.....161

Figure 107. The motion of point “a1” during the two-hole blast.....162

Figure 108. The motion of point “b1” during the two-hole blast. 163

Figure 109. Displacement amplitude nephogram over times during two-hole blast (Instantaneous explosions on the left side and millisecond-delay explosions on the right side). 166

Figure 110. The maximum velocity reduction effectiveness of millisecond-delay explosions with two-hole blast (Pattern-H and Pattern-V are shown in Figure 105). 168

Figure 111. The plan of the three-hole blast along the section of cross passage. 168

Figure 112. The maximum velocity reduction effectiveness of millisecond-delay explosions with three-hole blast (Pattern-H1, H2, V1 and V2 are shown in Figure 111).....170

Figure 113. The plan of the four-hole blast along the section of cross passage.....171

Figure 114. The maximum velocity reduction effectiveness of millisecond-delay explosions with four-hole blast (Pattern-H1, H2, H3, V1, V2 and V3 are shown in Figure 113). 172

Figure 115. The plan of the nine-hole blast (in parallelogram shape) along the section of cross passage.....175

Figure 116. The maximum velocity reduction effectiveness of millisecond-delay explosions with nine-hole blast (in parallelogram shape, Pattern-H1, H2, H3, H4, H5, H6, V1, V2, V3, V4, V5 and V6 are shown in Figure 115). 176

Figure 117. The plan of the multiple-hole blast (in triangle shape) along the section of cross passage. 177

Figure 118. The maximum velocity reduction effectiveness of millisecond-delay explosions with multiple-hole blast (in triangle shape, Pattern-1, 2, 3 and 4 are shown in Figure 117).178

List of Tables

Table 1. Estimates of typical human responses to vibration and mechanical shock [29]. 16

Table 2. Safe limits for structural integrity for long-term continuous vibration (DIN4150) [30]. 17

Table 3. Material properties of soil and barrier. 42

Table 4. The distribution of key parameters to be optimized for wave barriers. 59

Table 5. Final results of horizontal response at point "*a*" for parameter optimization of wave barrier. 60

Table 6. Final results of vertical response at point "*a*" for parameter optimization of wave barrier. 61

Table 7. Foam-Control EPS Geofoam Properties. 62

Table 8. The distribution of key parameters to be optimized for EPS barriers. 62

Table 9. Final results of horizontal response at point "*a*" for parameter optimization of EPS barrier. 63

Table 10. Final results of vertical response at point "*a*" for parameter optimization of EPS barrier. 64

Table 11. Material properties of rock and barrier 66

Table 12. The characteristics of EMULSTAR 8000UG. 66

Table 13. The distribution of selected parameters to be optimized for EPS barriers. 76

Table 14. Final results of horizontal response at point "*a*" for parameter optimization of EPS barriers. 77

Table 15. Final results of vertical response at point "*a*" for parameter optimization of EPS barriers. 78

Table 16. Material properties of rock and main tunnel lining 85

Table 17. Concrete damaged plasticity model parameters 103

Table 18. Material properties of the protective layer. 148

Table 19. The distribution of key parameters to be optimized for EPS protective layer 156

Table 20. Final results of the maximum radial velocity reduction of main tunnel for parameter optimization of EPS protective layer 157

Table 21. Final results of the maximum vertical velocity reduction of main tunnel for parameter optimization of EPS protective layer 158

Table 22. Final results of the maximum transverse velocity reduction of main tunnel for parameter optimization of EPS protective layer 159

1. Introduction

This dissertation focuses on two major works: one is the study on the isolation performance of wave barrier in reducing ground vibration generated by external load; the other is the investigation on the dynamic behavior of existing tunnel under nearby explosions and the mitigation measures for reducing the vibration of existing tunnel. In this chapter, the motivation of the research is firstly introduced, then the scope and objectives of the research are pointed out, and finally, a brief description of the dissertation structure is presented.

1.1 Motivation of research

Ground vibration generated by external dynamic sources, such as earthquake, blasting, high speed cars, trains and subways has detrimental influence on the nearby structures and inhabitants. It can possibly damage buildings, annoy people and affect the security and accuracy of sensitive equipments. In the past few decades, researchers tried many ways to prevent or mitigate the adverse effects of ground vibration, of which the installation of wave barriers like open trenches, bentonite trenches, solid or hollow concrete walls, sheet pile walls, expanded polystyrene (EPS) geofoam trenches is assumed to be an effective mitigation measure [15], by preventing waves from transmitting wave energy into the protected areas. Generally, the geometry, the location and the composition of wave barrier are considered to be the most important factors that affect the vibration isolation effectiveness. During the past years, a great number of researches including analytical, experimental and numerical studies have been committed to investigate the barrier isolation performance. Lots of valuable progresses were made and practical applications were already carried out. However, to the best of the author's knowledge, there are some issues that are still unclear. For example, most of the previous researches which involved in parametric study mainly focused on the effect of single parameter on the vibration isolation effectiveness, it is still not clear of the mutual influences of multi-parameters, while such mutual influences widely exist in practice. There are also few investigations on the optimization design of wave barrier in reducing ground vibration, which is very important not only for the isolation performance of barrier but also for the construction cost. The only exception known to the author is Wu [131], who used Taguchi method for the optimization of parameters of underground trench. However, his study was about the underground barrier, rather than surface barrier. Also, the investigation in his work on the optimization of parameters did not include the effect of barrier material, which was believed to play an important role in the screening effect. Another drawback of the previous researches on wave barrier is that wave barrier is

widely assumed to reduce ground vibration generated by surface vibration sources, like the high speed trains, the working heavy machines, but there is little study on mitigating the ground vibration induced by underground dynamic sources, especially by the subsurface explosions. Therefore, there is a need to further understand the isolation performance of wave barrier under different kinds of external loads as well as to conduct the optimization design for wave barrier in practice.

Another important issue in this research is the security of existing tunnel under nearby explosions. It is known that the drilling and blasting method is commonly used in mining and tunneling operation as an economical way of deep excavation, especially in hard rock, where digging method is too expensive or even impossible. However, vibration generated by explosions has adverse influence on the adjacent existing tunnel, ranging from minor structural damage to structural failure and even loss of lives. Therefore, the control of vibration of existing tunnel under explosions is one of the major concerns during the tunnel protection design. It is pointed out that, although a great number of researches on the blast-reduced vibration of existing tunnel (mainly the field tests and numerical simulations) were carried out in the past decades and the dynamic behavior of existing tunnel is now much better understood, there are still few researchers who comprehensively investigate the mitigation measures for the tunnel vibration reduction. Apparently, effective and economic mitigation measures are crucial not only for ensuring the security of existing tunnel (under nearby explosions), but also for reducing the construction cost during the tunnel design. Therefore, it is meaningful to propose cost-effective mitigation measures to reduce the blast-induced vibration of existing tunnel.

1.2 Scope and objectives

As stated above, there is still much work to do to better understand the isolation performance of wave barrier and the optimization design, and lots of efforts are also needed on the mitigation measures for the protection of existing tunnel under nearby explosions. Thus, this dissertation aims to improve the current level of understanding on the usage and optimization design of wave barrier in isolating the surface vibration sources as well as the subsurface explosions. Another important goal of this research is to propose practical mitigation measures for protecting existing tunnel from nearby explosions. It is noted that this research is numerical investigations with the specific objectives presented as follows:

- Investigating the isolation performance of wave barrier under surface harmonic load. Evaluating the significance and sensibility of parameters and proposing an optimization design method for wave barrier.

- Investigating the isolation performance of wave barrier under subsurface explosions. Evaluating the significance and sensibility of parameters and proposing an optimization design method for wave barrier.
- Investigating the dynamic behavior of existing tunnel under nearby explosions. Identifying key parameters that significantly affect the tunnel vibration, and evaluating the motion and damage degree of tunnel (including the lining and the slabs) under explosions.
- Proposing two promising mitigation methods in reducing the vibration of existing tunnel under explosions. Examining the efficiency of each method and providing a reference for the tunnel protection design in practice.

In order to achieve the objectives above, the scope of the research includes:

- Creating a numerical model of soil-barrier system where surface harmonic load is applied, by using the finite element package ABAQUS 6.11. The reliability of the numerical model is validated by previous publications. Then a comprehensive parametric study is carried out to examine the influence of each parameter on the vibration isolation effectiveness. Next, with the combination of Python program language and ABAQUS, an optimization design method is developed to identify wave barriers from performing the best to being the worst. A case study based on the assumption that the wave barriers are made of EPS is presented as well.
- Creating a numerical model of rock-barrier system where subsurface explosions is applied in ABAQUS 6.11. A comprehensive parametric study is performed to examine the influence of each parameter on the vibration isolation effectiveness. Next, an optimization design method is proposed for the wave barrier design.
- Creating a numerical model of rock-tunnel system under explosions in ABAQUS 6.11. Key parameters that significantly affect the tunnel vibration are identified during a parametric analysis. By using the concrete damaged plasticity (CDP) model for the tunnel lining, an extensive comparison study of elastic analysis and elastic-plastic analysis is committed. The maximum motion and the possible damage and stiffness degradation of the tunnel lining and the slabs are evaluated in different conditions.
- Two mitigation measures for protecting existing tunnel under explosions are evaluated by creating and examining the corresponding numerical models in ABAQUS 6.11. The first mitigation measure is to install a protective layer (also known as isolation layer) which lies along the tunnel lining, acting like “wave barrier”. Four kinds of protective layer materials: cement grout, wood, rubber and EPS are examined. An optimization design method for the protective layer made of EPS is presented as well. The second

mitigation measure is to reduce the wave energy by using time-delayed explosions, instead of instantaneous explosions. Comparison study of the motion of existing tunnel under instantaneous explosions and time-delayed explosions is conducted. The influences of the sequence of firing explosives and the patterns of blastholes during time-delayed explosions are examined as well.

1.3 Structure of dissertation

This dissertation can be divided into three major parts: a general literature review of the previous researches which are relevant to the current study; the investigation on the isolation performance of wave barrier under surface harmonic load and under subsurface explosions; and the investigation on the dynamic behavior of existing tunnel under nearby explosions and the mitigation measures for reducing the tunnel vibration. Specifically, the dissertation is organized into seven chapters as follows:

Chapter 1 briefly introduces the motivation of the research, the objectives and scope of the current work and the outline of the dissertation.

Chapter 2 presents a literature review of the previous researches relevant to the current study. Areas of interest include the basic knowledge of vibration, traditional methods for reducing vibration, vibration isolation by using wave barrier, responses of existing tunnel under explosions and mitigation measures for reducing the tunnel vibration.

Chapter 3 investigates the isolation performance of wave barrier under surface harmonic load. Firstly, a 2D model of soil-barrier system is created in ABAQUS, and the reliability of the numerical model is verified by previous publications. Then a comparison study between the 2D analysis and 3D analysis is carried out, the result shows that 2D model is sufficient to produce accurate results. Next, a comprehensive parametric study, including the material properties and the dimensions of wave barrier (Young's modulus, density, Poisson's ratio, damping ratio, the width, the depth, the inclination angle), the distance from the vibration source to the barrier and the magnitude of external load, has been carried out to investigate the influence of each parameter on the barrier isolation performance. Based on the results of parametric study, together with the combination of Python program language and ABAQUS, an optimization design method for wave barrier is developed, aiming to find out the best barrier which is able to minimize the ground vibration in protected site. A case study based on the assumption that the barriers are made of EPS is presented as well.

Chapter 4 presents the investigation of the isolation performance of wave barrier under subsurface explosions. The research method is similar to that presented in Chapter 3: firstly, a numerical model of rock-barrier system is built in ABAQUS; Then, a parametric study is conducted to examine the significance and sensibility of each parameter on the barrier screening

effectiveness; Next, by using the combination of Python scripts and ABAQUS, an optimization design for wave barriers made of EPS is carried out. Wave barriers from performing the best to being the worst are identified.

Chapter 5 investigates the dynamic behavior of existing tunnel under nearby explosions. This study is based on the current project [126], where some cross passages which connect a security tunnel and main tunnel (the two tunnels are parallel to each other) are being constructed by explosions. The dynamic behavior of main tunnel is simulated by creating the corresponding numerical model in ABAQUS. A comprehensive parametric analysis, which includes the lining stiffness, thickness, the distance of explosions from main tunnel, the position of explosions along the section of cross passage, the magnitude of the blast pressure as well as the tunnel burial depth, has been performed to examine the effect of each parameter on the main tunnel vibration. Then, a comparison study between elastic analysis and elastic-plastic analysis is committed, the behaviors of main tunnel under weak and strong explosions are presented. Finally, the maximum motion and the degree of damage and stiffness degradation of the tunnel lining and the slabs are evaluated in different conditions by using the CDP model for the whole tunnel.

Chapter 6 proposes two mitigation measures for reducing the response of main tunnel under explosions. One is the installation of a protective layer which lies along the tunnel lining to reflect and/or absorb the waves. The screening effectiveness of protective layers made of four different materials (cement grout, wood, rubber and EPS) is numerically examined in ABAQUS. The protective layer made of EPS is found to be the most efficient. Once again, with the combination of Python scripts and ABAQUS, the optimization design for EPS protective layer is carried out, the best EPS layer which can minimize the vibration of main tunnel is identified. The second mitigation measure is the usage of time-delayed explosions, rather than instantaneous explosions, to reduce the vibration of main tunnel. A comparison study of the motion of main tunnel under these two kinds of explosions is committed. The influences of the sequence of firing explosives and the patterns of blastholes on the vibration of tunnel are examined as well.

Chapter 7 presents the overall conclusions based on current investigations, the potential future study is also pointed out.

2. Literature review

This chapter briefly introduces the previous works which are relevant to the current investigations. Background information, which includes some basic knowledge of ground vibration, the methods of reducing ground vibration, the usage of wave barrier for vibration isolation, the responses of existing tunnel under nearly explosions and the mitigation measures for tunnel vibration reduction, is presented.

2.1 Basics of vibration

2.1.1 Ground vibration sources

Ground vibration can be generated by many external sources, such as earthquake, explosions and industrial, construction and transportation activities. Broadingly speaking, there are three kinds of vibration sources [1]: the continuous vibration source, which generates uninterrupted vibration for a defined period, like steady road traffic, tunneling boring machinery; the impulsive vibration source, which causes a very strong vibration in a short time and then decays rapidly, like the explosions, the dropping of heavy equipments; and the intermittent vibration source, which is defined as interrupted periods of continuous vibration or repeated periods of impulsive vibration, like pile driving, jack hammers, forging machines. On the other hand, vibration can be caused by the protected structure itself (within the protected structure), such as mechanical vibration source in buildings like the air conditioning. In this dissertation, it is noted that only external vibration sources are considered. The following part introduces three typical and important external vibration sources: earthquake, transport vehicles and construction activities. A short discussion with each type of vibration source is presented as well.

Earthquake An earthquake is generally the result of a sudden release of energy in the earth when the faults slip past each other. Although the ground vibration generated by earthquakes lasts only a few seconds, its impact is traumatic. It can destroy villages, towns and even the whole cities, causing massive loss of life and property and severely damage social essential services like water and electricity supply, sewerage systems, communication and power, public transportation. Figure 1 shows an example of completely destroyed buildings after the Wenchuan earthquake in 2008, China. It is estimated that tens of thousands of people died and millions of buildings were destroyed. Usually, the aftermath of earthquakes results in destabilization of economic and social structure of large affected area. It is one of the most destructive natural disasters in the world.

Due to the tremendous costs and loss of life, investigations on earthquakes have attracted more and more attention from both academics and engineers. Extensive research has already undertaken in earthquake engineering, which aims to protect the society, the natural and the man-made environment from earthquakes by limiting the seismic risk to socio-economically acceptable levels [2]. It focuses on the investigation and the solution of problems caused by earthquakes, as well as the work involved in the practical application of those solutions. The core issue is to plan, design, construct and manage earthquake-resistant structures and facilities [3]. And the particular importance is the nonlinear behavior of soil (or rock), structures and their interaction during strong earthquakes. Recently, effects of nonlinear behavior of soil, including the slippage and separation at the interface of soil and foundation, soil liquefaction problem and hyperbolic stress-strain relationships, have become hot topics in the earthquake protection field [3-5].

Figure 1. The destroyed buildings after WenChuan earthquake in 2008, China.

Transport vehicles Transportation system, which connects together all the social and economic organizations for co-operation between different areas and sections, plays a vital role in the economic growth in every country and contributes a significant improvement in the way of life [7]. On the other hand, however, the activities of transport vehicles may have detrimental impacts on the environment. One of the major problems is the traffic-induced ground vibration. The passing of high-speed vehicles, like cars, trains, subways, can transmit dynamic energy into the surface of the soil (or rock), leading to ground-borne vibration. It has been observed for many years that the passage of vehicles can cause lots of trouble on the nearby buildings and residents, ranging from causing annoyance to structural damage. Figure 2 shows a high-speed train (TGV) operated by SNCF Voyages in France. A recent test showed that the fasted TGV reached to be 574.8

km/h in 2007 [10]. The ground vibration produced by such wheeled train is so strong that proper mitigation measures have to be taken to control its adverse influence on the nearby residences and structures.

The magnitude and the frequency of ground vibration generated by the passage of vehicles are believed to be largely dependent on the type of ground surface and the soil conditions [8, 9]. Theoretically, the vibration problem in an elastic half-space has been studied for many years. However, due to the mathematical complex, the analytical method can only be used in some ideal situations. More often, the experimental and numerical methods are employed to investigate the vehicle-induced ground vibration. Recently, with the appearance of the so-called super-critical speed of trains which can travel even faster than the Rayleigh wave, there is an urgent necessity to understand the ground vibration behaviors of trains, tracks, rails and soils during the train moving in the super-critical range [11].

Figure 2. The high-speed train (TGV) operated by SNCF Voyages in France.

Construction activities According to Kuo [12], there are generally five major sources of ground vibration during the construction activities. They are pile driving, compaction, tunneling, excavation and blasting, of which the blasting is considered the most dangerous, for it releases huge amount of energy in a very short time and may cause severe damage and even loss of life if appropriate precautions are not taken. Figure 3 shows the massive subway explosions in New York in 2012, the blast is so strong that it sends debris out of the subway station and reaches as high as eight stories. In the past decades, a great number of researchers have focused on the creation of reliable prediction models of blast and the development of practical blast control methods [13]. It is suggested that more care should be made on the underground explosions than

surface explosions, for the higher level of ground vibration is generally produced by the underground explosions than the surface explosions.

Figure 3. Massive subway explosions rocked in New York in 2012.

2.1.2 Wave propagation in soil (or rock) media

A basic understanding of the wave propagation in soil (or rock) media is very important during the investigation of developing methods to control ground vibration generated by dynamic sources. Generally, there are two main types of waves: body waves and surface waves. Body waves which include P-wave (also known as primary or compressional or longitudinal wave) and S-wave (also known as secondary or shear or transverse wave) can travel through the interior of the Earth. While surface waves, which include Rayleigh wave, Love wave and Stoneley wave, can only travel along the Earth's surface, and has a slower velocity and a lower frequency than body waves. The following part provides some details about P-wave, S-wave, Rayleigh wave and Love wave.

P-wave is a kind of elastic wave which travels through all types of material, including the gases, liquids and solids. It travels faster than any other waves and is therefore first to be recorded by seismic stations. As it propagates in isotropic and homogeneous solids, the solid particles are pushed and pulled, and move along or parallel to the propagation direction that the wave energy is traveling in. Figure 4 shows the perspective view of P-wave propagation through a grid which represents a volume of material. The X and Y directions are parallel to the Earth's surface and the Z direction is the depth. The successive time T increases from T = 0 to T = 3. It is observed that the disturbance that is propagated is a compression (grid lines are closer together) followed by a dilatation or extension (grid lines are farther apart). The particle motion is in the propaga-

tion direction. And the vibrating material returns to its original shape after the P-wave has passed [14]. The velocity of P-wave in a homogeneous isotropic medium is given as

$$v_P = \sqrt{\frac{E(1-v)}{\rho(1+v)(1-2v)}} = \sqrt{\frac{\lambda+2G}{\rho}} \quad (1)$$

where E, ρ and v are Young's modulus, density and Poisson's ratio of the media, respectively. The constants λ and G are denoted as the first and the second Lamé parameter, which can be expressed as

$$G = \frac{E}{2(1+v)} \quad (2)$$

$$\lambda = \frac{vE}{(1+v)(1-2v)} \quad (3)$$

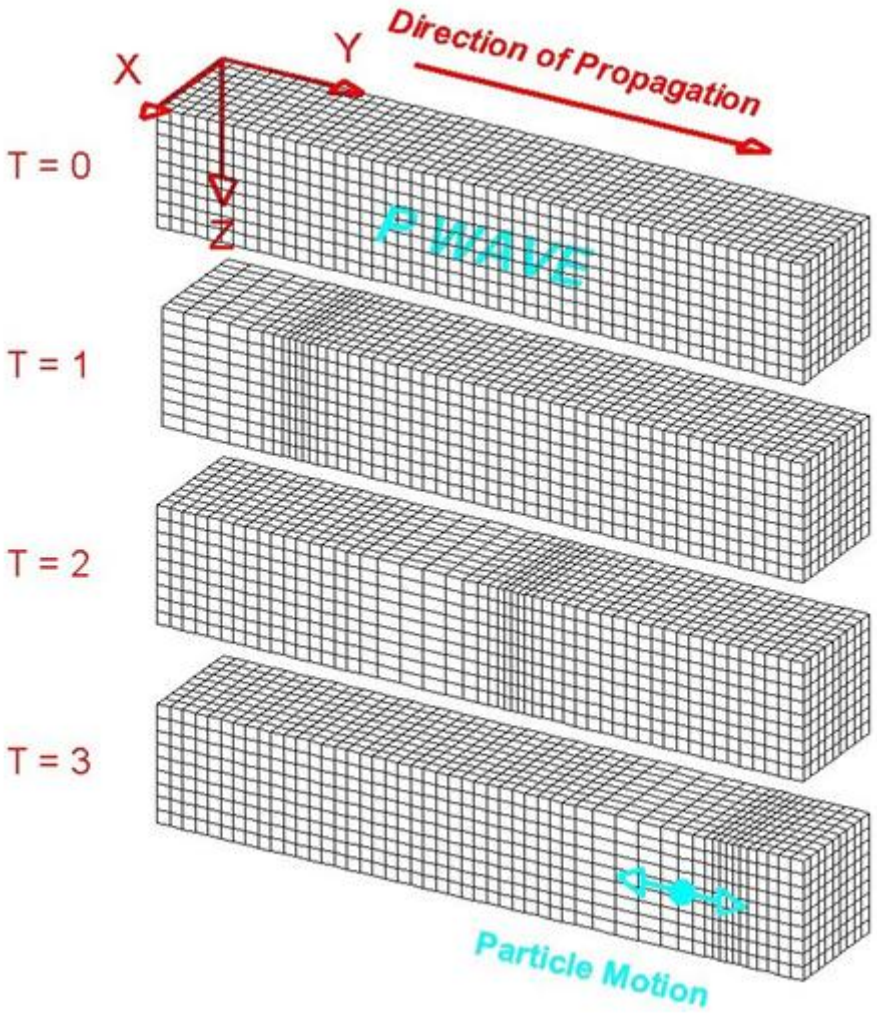

Figure 4. Perspective view of P-wave propagation through a grid representing a volume of material [14].

S-wave The second type of body wave is the S-wave. It travels slower than P-wave, typically 60% of the speed of P-wave in a given solid material, and therefore arrives at the seismic stations after the arrival of P-wave. It is noted that S-wave can only propagate in solids, for there exists no shear stresses in gases or fluids. When it moves in the Earth, the soil or rock particles are

forced to move up and down, or side-to-side, which is perpendicular to the direction of wave propagation (the direction that S-wave is traveling in). And the vibrating material returns to its original shape after the S-wave has passed, as shown in Figure 5, which demonstrates the perspective view of S-wave propagation in the Earth (the grid represents a volume of material) [14]. The velocity of S-wave in a homogeneous isotropic medium is given as

$$v_S = \sqrt{\frac{E}{2\rho(1+v)}} = \sqrt{\frac{G}{\rho}} \tag{4}$$

where E, ρ and v are Young's modulus, density and Poisson's ratio of the media, respectively. The constant G is denoted as the second Lamé parameter, as denoted in Equation (2).

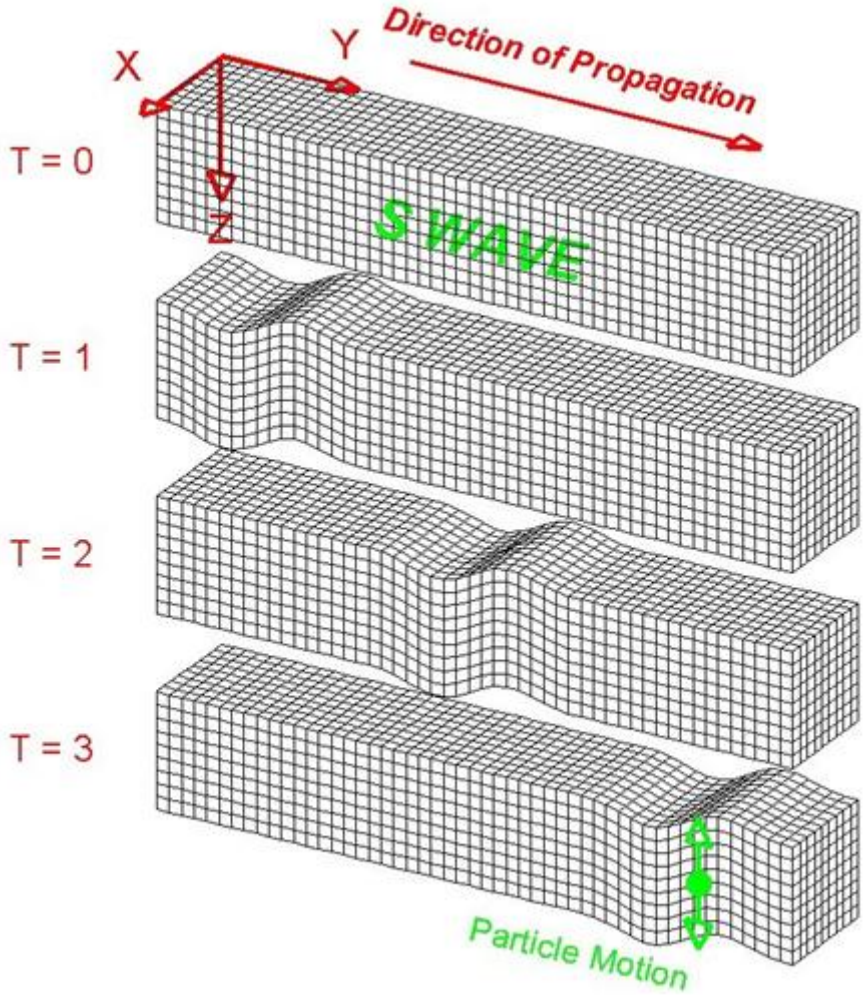

Figure 5. Perspective view of S-wave propagation through a grid representing a volume of material [14].

Rayleigh wave, also known as ground roll, is named for John William Strutt, Lord Rayleigh, who mathematically predicted the existence of this type of wave in 1885. It is one kind of surface wave which travels near the surface of solids, with a speed slightly less than the S-wave in typical homogeneous elastic media. As it travels on the surface of the Earth, it forces the ground to move up and down, and side-to-side in the same direction of wave propagation, like the wave

rolling across a lake or an ocean. Figure 6 shows the perspective view of Rayleigh-wave propagation through a grid representing a volume of elastic material. It can be seen that the Rayleigh wave causes the surface particles to move in an ellipses motion which consists of both vertical (shear; perpendicular to the direction of propagation but in the X-Z plane) and horizontal (compression; in the direction of propagation) particle motion [14]. It should be mentioned that Rayleigh wave could only propagate near the surface of the ground and decay rapidly as it travels deep into the earth. Figure 7 represents the evolution of the amplitude of Rayleigh wave over depth with different Poisson's ratio of soil [15]. The dimensionless amplitude of Rayleigh wave and the depth are adopted. It can be seen that both the horizontal and vertical amplitude of Rayleigh wave decrease dramatically as the Rayleigh wave travels deeper into the earth, and when the depth exceeds to 1.2 wavelength of Rayleigh wave, the amplitude of Rayleigh wave becomes so small that it can almost be ignored. It is noted that the velocity of Rayleigh wave can be computed as

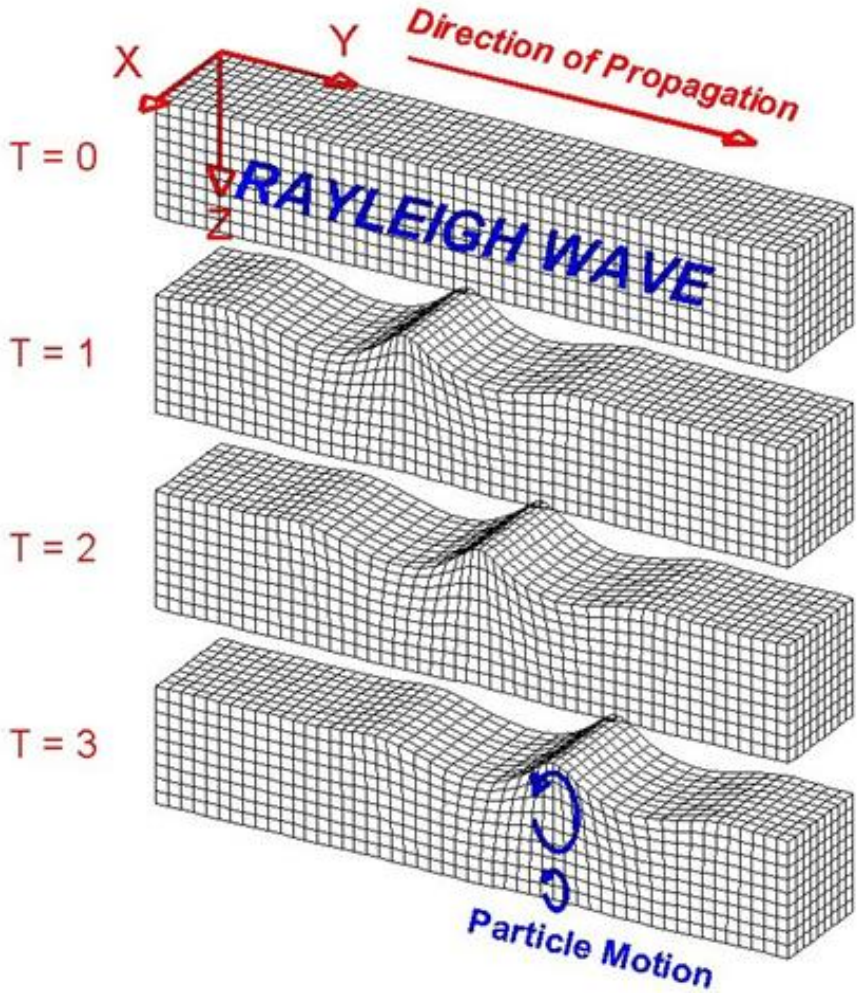

Figure 6. Perspective view of Rayleigh wave propagation through a grid representing a volume of material [14].

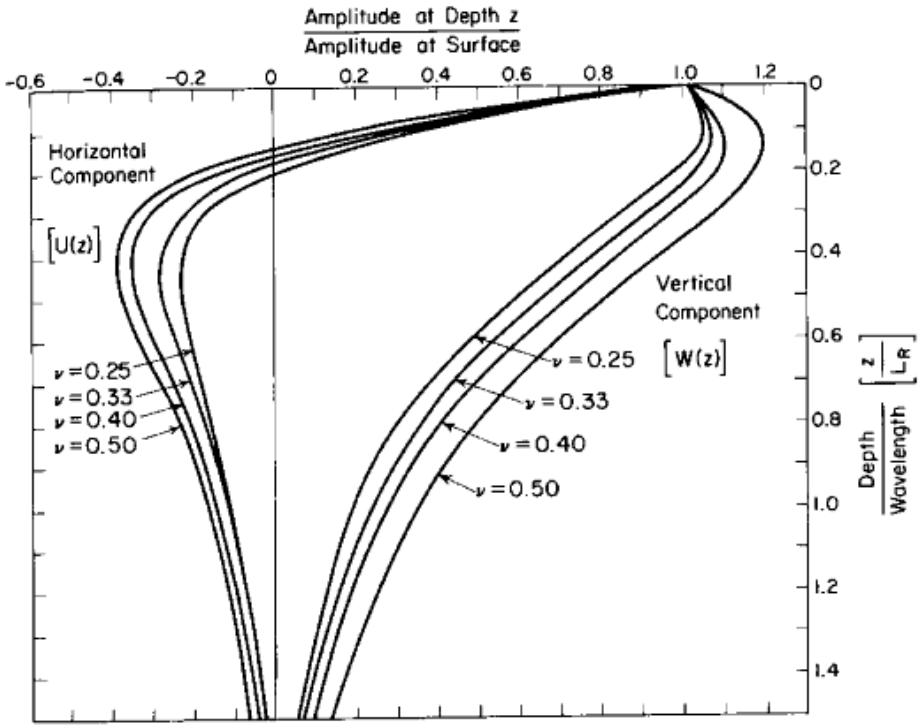

Figure 7. The amplitude of Rayleigh wave over depth with different Poisson's ratio [15].

$$v_R = \frac{0.87+1.12v}{1+v} v_S = \frac{0.87+1.12v}{1+v} \sqrt{\frac{E}{2\rho(1+v)}} = \frac{0.87+1.12v}{1+v} \sqrt{\frac{G}{\rho}} \quad (5)$$

where E, ρ and v are Young's modulus, density and Poisson's ratio of the media, respectively. The constants G is denoted as the second Lamé parameter, as denoted in Equation (2).

Love wave is another kind of surface wave, which exists only in semi-infinite medium overlain by an upper layer of finite thickness [16]. It travels faster than Rayleigh wave, but slightly slower than the S-wave. It has the largest amplitude but its amplitude decreases rapidly with depth. As it propagates on the Earth, the particle motion forms a horizontal line which is perpendicular to the direction of wave propagation, and the material returns to its original shape after the wave has passed, as shown in Figure 8 [14].

Wave field generated by circular footing is presented here for considering that many ground vibration, especially traffic-reduced vibration can be decomposed into the combinations of different ground vibration generated by circular footing undergoing vertical oscillations at the surface of a half-space. Figure 9 demonstrates the distribution of wave field generated by a circular footing on a homogeneous, isotropic and elastic half-space [17]. The wave front of each wave clearly shows that the P-wave propagates the fastest and Rayleigh wave is the slowest. What also can be seen is that the P-wave and S-wave travel radially outward from the vibration source along a hemispherical wave front and Rayleigh wave travels along a cylindrical wave front. The "Horiz Comp" and "Vert Comp" respectively show the distribution of horizontal and

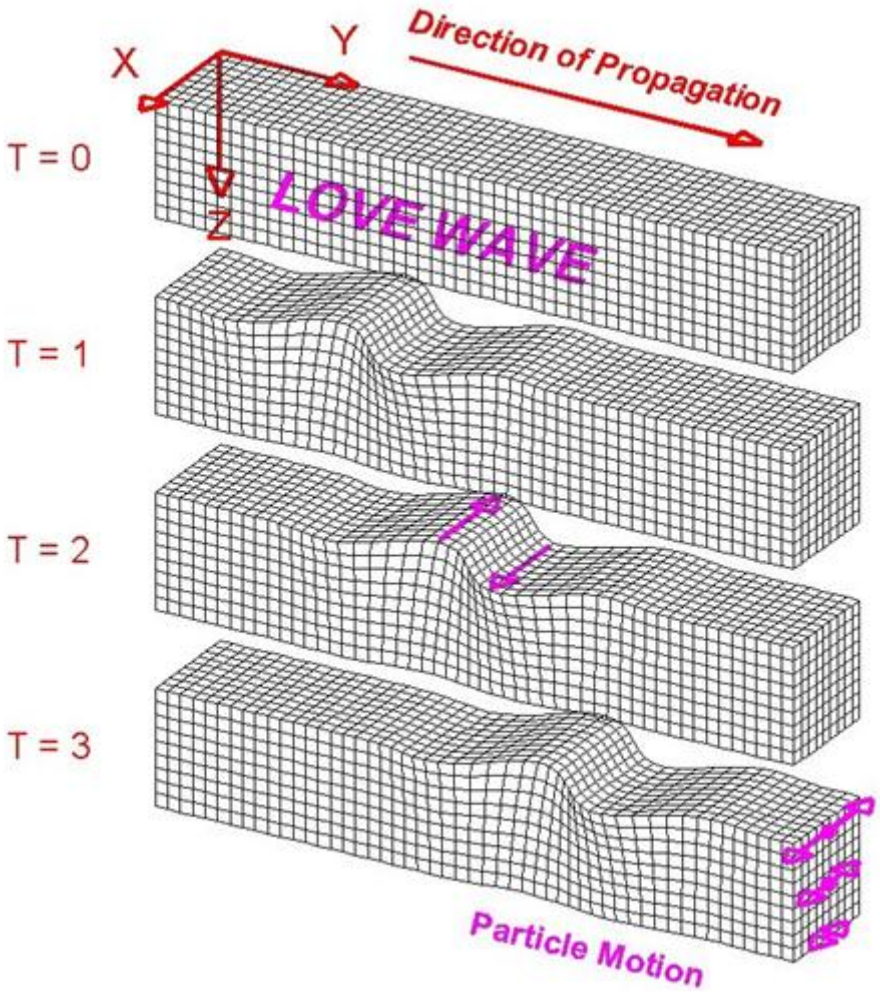

Figure 8. Perspective view of Love wave propagation through a grid representing a volume of elastic material [14].

vertical components of Rayleigh wave along the depth. The shaded areas along the wave fronts of P-wave and S-wave represent the relative amplitude of particle displacement as a function of angle which is measured downward from the surface at the center of the circular footing. It is noted that the energy density and the amplitude of each wave will decrease as the wave propagates outside from the circular footing. This phenomenon is often called geometrical damping. Study [19] shows that the amplitude of Rayleigh wave decreases in proportional to the ratio of $1/r^{0.5}$ (r is the distance from the input source), while the amplitude of P-wave and S-wave decrease as 1/r except along the surface of the half-space, where the value of amplitude decrease is $1/r^2$. Besides, investigations [20] indicate that the distribution of the total input energy among the three waves is that: 67% Rayleigh wave, 26% S-wave and 7% P-wave. It means that Rayleigh wave carries about two thirds of the whole input energy. Moreover, the amplitude of Rayleigh wave decays much more slowly with distance than P-wave and S-wave. Therefore, Rayleigh wave should be the primary concern for the protection of nearby structures and inhabitants from ground vibration.

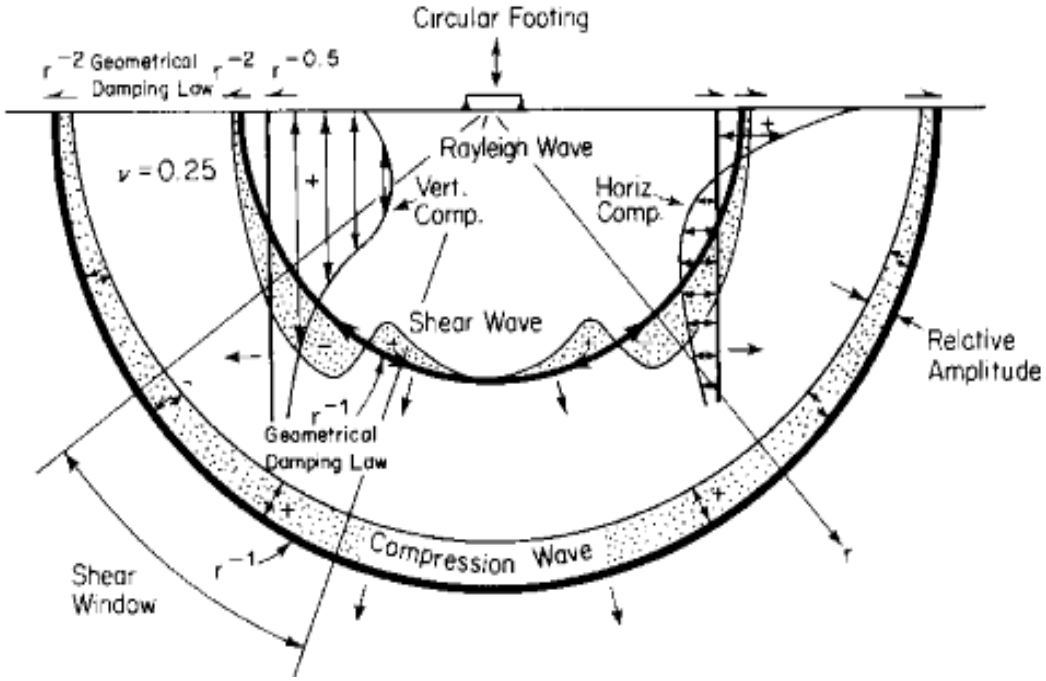

Figure 9. Distribution of wave field generated by a circular footing on a homogeneous, isotropic and elastic half-space [17].

2.1.3 Impact of vibration

The impact of vibration has become an important issue in recent years. In many countries, especially in developed countries, more and more environmental regulations have been introduced to place increasing constraints on the vibration, particularly in the densely populated areas and in the structures which house sensitive machinery. Generally, the adverse impact of vibration induced by dynamic sources can be divided into two parts: the human response and the structural response.

Human response External vibration sources, especially the transportation and construction activities are becoming serious problems which cause disturbance to the human being. A great number of investigations [21-25] in the past few decades show that people living in cities are subjected an increasing air, rail and road traffic vibration, causing high levels of annoyance and sleep problem, which have detrimental effects on the quality of life. Particularly, the sleep problem like being woken through the night, an increase of the time to fall asleep, has serious influences on the people's working performance and mood [26]. Some researchers [27] indicate that excessive exposure to such disturbance could lead to long-term health problems as well.

Another problem is the human exposure to ground vibration and mechanical shock caused by vibration sources, like the passing cars, trains, subways, which are very common in the daily life. Motion can be transformed from the dynamic sources to the soil or rock media, through the buildings, the floor, the seat, and finally reach to a standing or sitting person. Exposures can also happen in occupations involving operation of hand-held power tools, mostly to the hands and

arms. People's response to such vibrations and shocks can range from minor perception to health problems, like motion sickness, back injury, the damage of blood vessels and nerves of hands [28]. Table 1 shows the estimates of typical human responses to vibration and mechanical shock with sources [29].

Table 1. Estimates of typical human responses to vibration and mechanical shock [29].

Human Responses	Source	Typical value
Perception (mean) Whole body Fingertips	ISO 2631, 1997 ISO/FDIS 13091-2, 2002	$0.015 ms^{-2}$ $0.0075\ ms^{-2}$ (4Hz) M-0.25, F-0.32 ms^{-2} (125Hz)
Building vibration	ISO 2631-2, 1989	$0.007\ ms^{-2}$
Discomfort not comfortable Discomfort uncomfortable Discomfort very uncomfortable	ISO 2631, 1997 ISO 2631, 1997 ISO 2631, 1997	$<0.315\ ms^{-2}$ $0.8\text{-}1.6\ ms^{-2}$ $>2.0\ ms^{-2}$
Motion sickness (10%)	ISO 2631, 1997	$30\ ms^{-1.5}$
Health effect hand (HAVA) Health effect whole body Health effect shocks (vertical)	ISO 5349-1. 2001 ISO 2631-1. 1997 ISO/DIS 2631-5, 2002	$1.0\ ms^{-2}$ $8.5\ ms^{-2}$ >0.5MPa

Structural response In recent years, there is an increasing demand for protecting existing structures by mitigating the structural response to the ground vibration generated by external loads. When vibration occurs in the buildings, it may not only disrupt people who are living inside, but also cause possible damage to the building itself, such as cracking, breakage, fatigue damage or even structural failure and collapse. For some special structures which hold sensitive equipments, like nano-technologies, microscopes or lasers, vibration must be strictly controlled in order to ensure the security and accuracy of those sensitive equipments. Table 2 shows the vibration velocity guidelines for use in evaluation the effect of vibration on the structural integrity [30]. It can be seen that the permitted maximum velocity for structures with particular sensitivity to vibration is much lower than the one for other types of structures. On the other hand, severe vibration due to strong earthquakes and explosions can lead to tremendous structural damage, for example, the Wenchuan earthquake, which occurred in the southwest of China in 2008, killed an estimated 68000 people [31], most of them died in the fallen buildings. And about 4.8 million people became homeless [32]. It is said that the whole Wenchuan area as well as the neighboring areas were completely destroyed by this single earthquake.

Table 2. Safe limits for structural integrity for long-term continuous vibration (DIN4150) [30].

Type of Structure		Guideline values for velocity in mm/s, of vibration in horizontal plane of highest floor, at all frequencies
1	Building used for commercial purposes, industrial buildings, and buildings of similar design	10
2	Dwellings and buildings of similar design and/or occupancy	5
3	Structures that, because of their particular sensitivity to vibration, cannot be classified under lines 1 and 2 and are of great intrinsic value (e.g. listed buildings under preservation order)	2.5

2.2 Methods of reducing vibration

Section 2.1 provides some general knowledge of the vibration sources, the wave propagation in media and their impact on the human being and the structures. It is noted that when the vibration effects exceed the permitted level, proper measures have to be taken to reduce the undesirable vibration. And the degree of detrimental vibration impact will determine the extent of vibration control methods. Generally, there are three major mitigation strategies. They are: controlling the vibration sources, disrupting the wave propagation in soil (or rock) media and controlling the vibration of protected structures.

2.2.1 Controlling the vibration sources

Apparently, if the dynamic forces generated by vibration sources are weaken, a decrease of the ground vibration can be expected. There are many ways to control the vibration sources in practice, for example, choosing the low-impact equipments or instruments rather than the heavy-impact ones whenever it is possible, arranging operations appropriately so that the induced-vibration does not occur simultaneously or even becomes weaken by mutual interaction. On the other hand, different vibration sources may require different mitigation measures, for instance, the blast vibration can be controlled by careful design of the blast parameters and the application of right techniques; for the traffic vibration on road, since the most severe vibration is generally due to the passage of heavy vehicles with high speeds on the irregular road surfaces, mitigation measures like limiting the speed, reducing the road surface irregularities, or even restricting the use of heavy vehicles, can be proposed to reduce the road vibration.

2.2.2 Disrupting the wave propagation through the soil (or rock) media

Disrupting the wave propagation inside the soil (or rock) media is also an effective way to reduce vibration. It is known that geological make-up and the media constitution have an

important effect on the wave propagation mechanism. An increase in distance between the vibration sources and the protected structures is considered to be one of the most important measures against vibration, for increasing distance means more wave energy dispersion and mitigation during a longer wave travel path. Study [33] shows that vibration due to the passage of trains is inversely proportional to the distance from the railway tracks, a significant decrease of the magnitude of vibration can be observed as the investigated sites move from 25 m to 150 m. And a slower rate of vibration reduction is achieved as the distance is larger than 200 m. On the other hand, the installation of wave barrier between the vibration sources and the protected zones is also known to be an effective method to reduce the ground vibration. Wave barriers like trenches and sheet-pile walls have been used for many years to mitigate vibration in protected buildings by reflecting and/or absorbing the waves during wave propagation in soil. More details about the wave barrier will be presented in Section 2.3.

2.2.3 Controlling the vibration of protected structures

Since the purpose is to reduce the vibration in protected structures, mitigation methods for strengthening the structures' ability to withstand the power of vibration are also encouraged. As the waves propagate into the structures like buildings, the foundations firstly begin to vibrate, then motion of columns, beams, floors occurs, and finally the whole buildings start to vibrate, causing the buildings to resonate with some vibration modes in some cases [34-36]. Measures like isolating the foundations by using resilient material such as rubber bearing pads or springs can be used to control the vibration of protected structures into a reasonable level.

2.3 Vibration isolation using wave barriers

The installation of wave barrier between the vibration sources and the protected structures is considered to be an effective measure to mitigate ground vibration. Various degrees of success were reported in the past. Figure 10 shows an example of the application of wave barrier in preventing the traffic-induced vibration to a protected nearby building [37]. The building was so close to the street that remarkable vibration inside the building was observed, and wave barriers were installed between the building and the street, attempting to prevent the traffic-induced vibration. Generally speaking, the vibration isolation system can be classified into two categories: one is the active vibration isolation; the other is the passive vibration isolation. Active vibration isolation, as shown schematically in Figure 13(a), is to reduce the vibration by placing the wave barrier close to or surrounding the dynamic sources so that the energy transmitted from the sources can be directly mitigated or cut off. On the other hand, passive vibration isolation, as schematically shown in Figure 13(b), is to prevent the waves from propagating into the protective buildings by placing the wave barrier near the site where vibration must be reduced. In the

past decades, wave barrier has been used in practice. As early as in 1962, Barkan [37] committed a number of field experiments to study the isolation performance of open and sheet-wall barriers, trying to isolate a building from traffic-induced vibration, as shown in Figure 10. The sheet-wall barriers were installed close to the protected building in order to isolate the traffic-induced vibration generated by vehicles on the street. After comparing the vibration of building foundations before and after the installation of sheet-wall barriers, he found that the vibrations from the street continued to affect the building. Based on this, he concluded that the mitigation effect of the installation of wave barriers was so small that wave barriers were useless in reducing the ground vibration. However, he also mentioned later in his study [37] that the failure of vibration reduction by wave barriers could be attributed to the lack of clear understanding of surface wave propagation in the presence of wave barriers in soil media. Therefore, it is inferred that reasonable design for wave barriers which are able to effectively reduce ground vibration may be expected if a thorough understanding of surface waves around the areas of wave barriers becomes available. Later, Dolling [74] and Neumeuer [75] used a bentonite-slurry-filled trench to protect a printing plant from the subway train induced vibrations, as shown in Figure 11. This application of trench seemed to be effective, since the magnitude of vibration of the printing plant after the installation of trench was only half of the one before the appearance of trench. Another successful application of wave barriers was presented by Meneill et al. [76] in 1965, who used a trench and a sheet-wall barrier to isolate a sensitive dimensional-standards laboratory (see Figure 12). It was reported that the measured acceleration of the slab met the owner's specification (maximum acceleration smaller than 0.1 g). Since the 1960s, a great number of researches have been carried out to investigate the isolation effectiveness of wave barrier, aiming to determine the barrier screening efficiency and to develop the guidelines for the barrier design. Here, a short description of the wave phenomena in the areas surrounding wave barrier is firstly presented. Then, a general introduction of previous investigations on wave barrier is summarized. Three basic research methods: analytical method, model and field experiment, and numerical method are described with details.

As mentioned above, in the early application of wave barrier for isolating the protected buildings, one of the major problems is that people did not have a clear understanding of the wave phenomena in the vicinity of wave barrier in soil media, which was yet crucial for the practical design of wave barrier. After years of research on the wave propagation in soil with the appearance of an obstacle, remarkable progresses have been made. Since Rayleigh waves carry most of the wave energy and are the most destructive waves, a brief qualitative description on the complex wave process when a Rayleigh wave impinges on a rectangular obstacle is presented [15, 58, 62, 97-99].

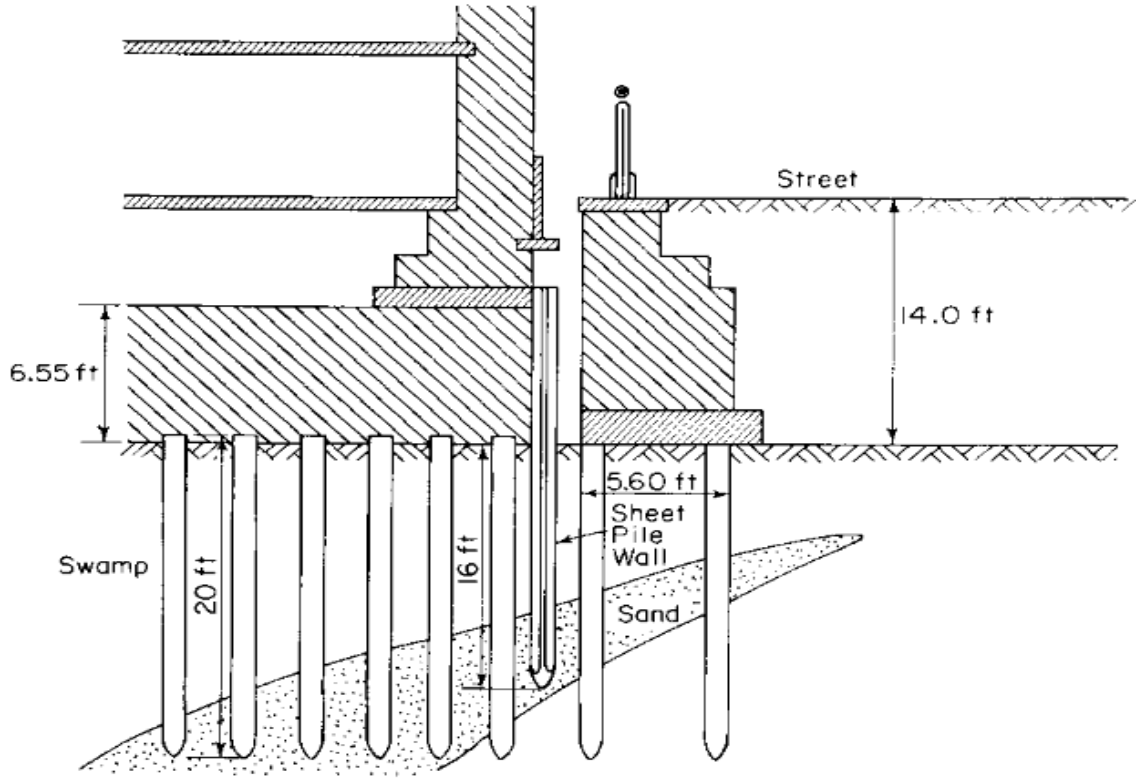

Figure 10. Vibration isolation of buildings from traffic-induced vibrations [37].

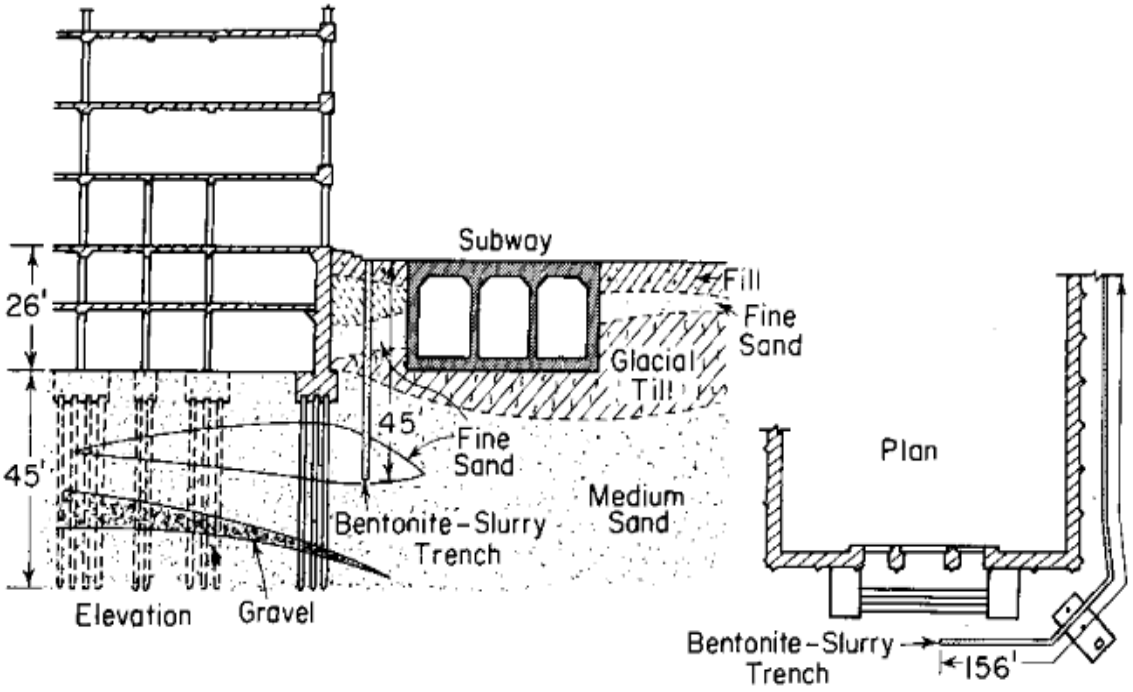

Figure 11. Vibration isolation of buildings from train-induced vibration [74].

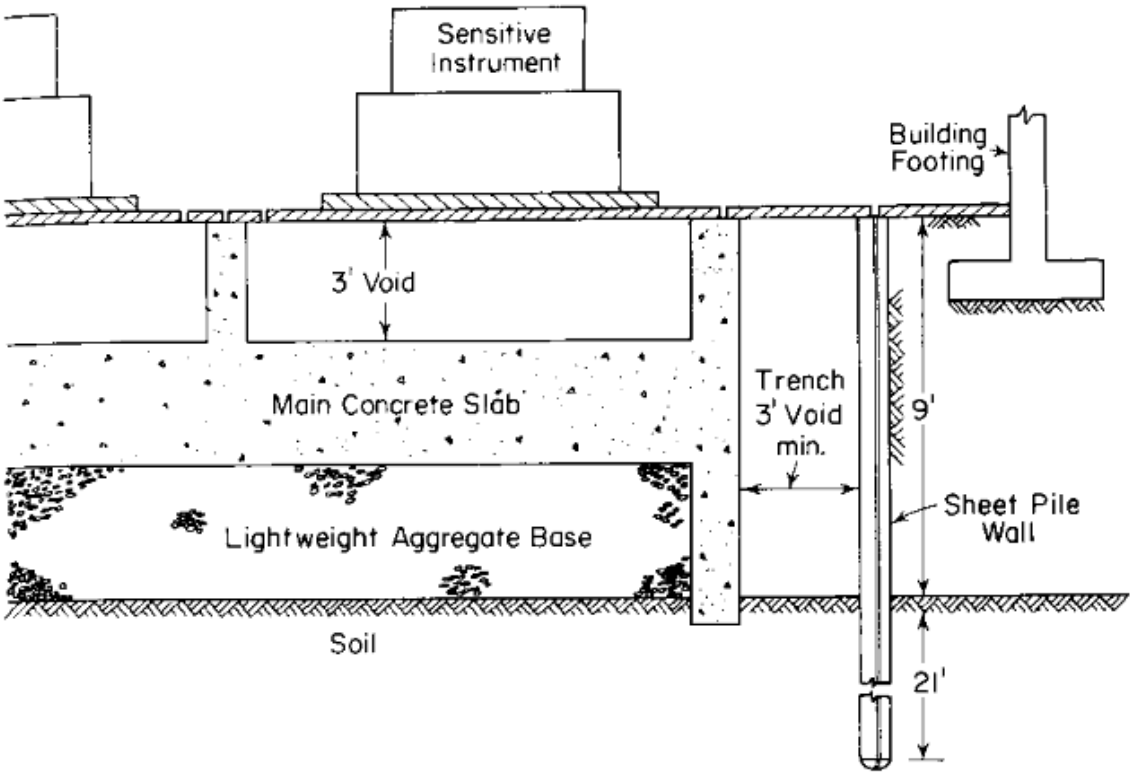

Figure 12. Isolation of sensitive instrument from vibration [76].

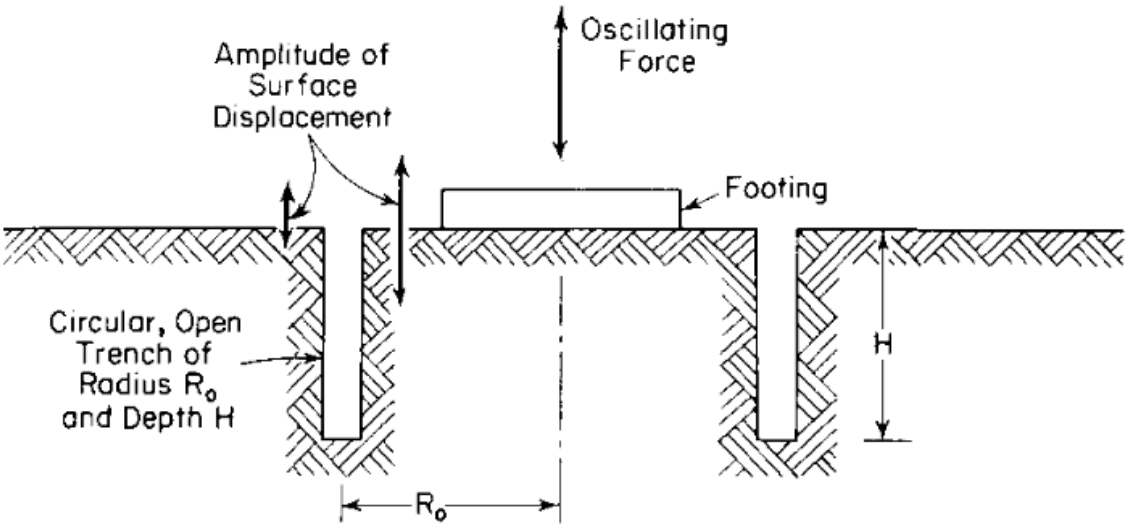

(a) Active isolation vibration: circular open trench surrounding vibration footing

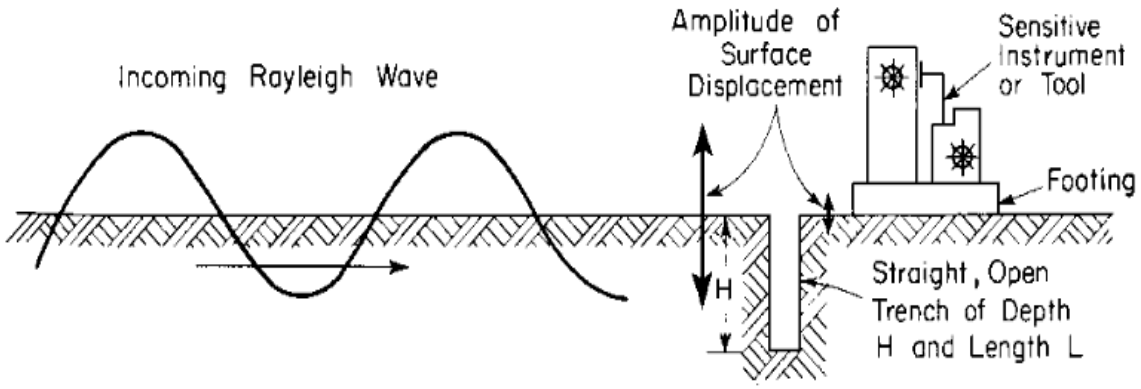

(b) Passive open trench to protect buildings with sensitive installations

Figure 13. Schematic diagram for vibration isolation systems [17].

The installation of wave barrier into the soil means the creation of a finite material discontinuity for the wave field in soil. Figure 14 shows the different wave distribution after a Rayleigh wave incident on a rectangular solid barrier [58]. After the incoming Rayleigh wave travels to the interface between the soil and the barrier, the wave generation and distribution is as follows: part of the incident Rayleigh wave is reflected by the barrier, and part of the incident Rayleigh wave transmits through the barrier. At the same time, body waves including P wave and S wave are generated. They propagate outwards from the barrier. Specifically, the generated body waves can be divided into two different types: one is the reflected body waves which propagate downward and to the left of the barrier; the other is the transmitted body waves which radiate to the right of the barrier. It is noted that it is the transmitted Rayleigh wave and body wave (double-headed arrows in Figure 14) that enforce the soil on the right side of the barrier to vibrate. The phenomenon of the conversion of Rayleigh wave to other forms of waves due to the appearance of a solid obstacle is called as mode conversion. It is known that mode conversion can occur when a wave encounter an interface between materials with different acoustic impedances and the incident angle is not normal to the interface. After traveling through the barrier, part of the transmitted body waves transform into Rayleigh waves with an increasing distance. Based on the statement above, it can be seen that the wave reflection and mode conversion play the key role in the isolation phenomena.

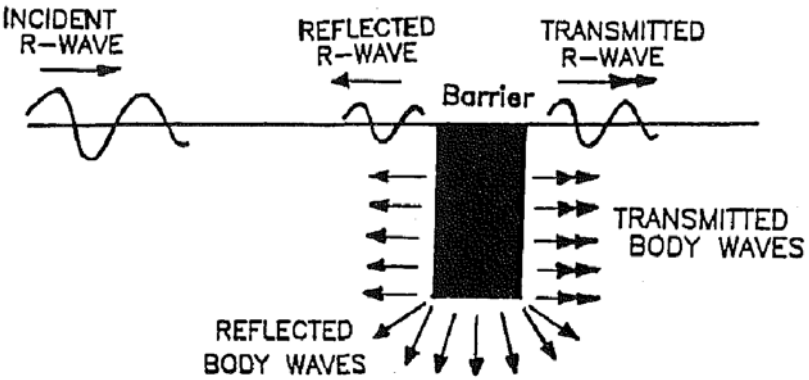

Figure 14. The distribution of generated waves due to an incident Rayleigh wave on solid wave barrier [58].

2.3.1 Analytical method

It is revealed from the published literatures that one of the major efforts in early studies on wave barriers is directed towards analytical method. It is well known that wave equations in homogeneous, isotropic, elastic semi-infinite medium are [38]:

$$\mu\nabla^2 u + (\lambda+\mu)\frac{\partial\Delta}{\partial x} - \rho\frac{\partial^2 u}{\partial t^2} = 0 \tag{6}$$

$$\mu\nabla^2 v + (\lambda+\mu)\frac{\partial\Delta}{\partial y} - \rho\frac{\partial^2 v}{\partial t^2} = 0 \tag{7}$$

$$\mu\nabla^2 w + (\lambda+\mu)\frac{\partial\Delta}{\partial z} - \rho\frac{\partial^2 w}{\partial t^2} = 0 \tag{8}$$

where λ is the Lamé's constant, μ is the material shear modulus, ρ is the material density. And u, v, w represent the displacements in X, Y and Z directions, respectively. Δ is the sum of strain components in X, Y and Z directions. The definition of ∇^2 can be expressed as

$$\nabla^2 = \frac{\partial^2}{\partial x^2} + \frac{\partial^2}{\partial y^2} + \frac{\partial^2}{\partial z^2} \tag{9}$$

It is worth mentioning that there are two important works which have great contributions to the elastic wave theory. One work, which was done by Lord Rayleigh [39] in 1885, who mathematically predicted the existence of what later called Rayleigh wave, investigated the behavior of waves upon the plane free surface of an infinite homogeneous isotropic elastic solid. It was found that the disturbance generated by such plane wave was confined to a superficial region, which had the thickness comparable with the wavelength. This work was so important that it created the basic theory of surface wave propagation. Another valuable work was done by Horace Lamb [40] in 1903. He investigated the propagation of vibration over the surface of the isotropic elastic half space solid, with the assumption that the vibration was generated by an arbitrary force at a point, rather than simple-harmonious vibration. The influence of internal source of disturbance was also examined. It was found that the surface disturbance produced by a single impulse of short duration might be analyzed roughly into two parts, which were called "minor tremor" and "main shock", respectively. The characters of these two different compo-

nents of surface disturbance were presented as well. Lamb's work was considered the cornerstone of theoretical solutions on the assumption that the vibration source was on the surface of a homogeneous, isotropic, elastic semi-infinite solid.

It is noted that the analytical solutions of the wave Equations (6)-(8) are available in homogeneous, isotropic elastic media; however, if there is an obstacle like wave barrier which is installed in the soil media, it will become much more difficult or even impossible to solve the wave motion equations. To overcome the wave propagation problems with the appearance of obstacles in media, many efforts had been made but most of the analytical treatments were limited in the field of linear elastodynamics using the theory of wave diffraction. White [41] studied the scattering of plane compressional and shear elastic waves incident obliquely on a cylindrical discontinuity in a solid. Knopoff [42] formulated the scattering of plane P wave by a spherical obstacle, and a computation was provided in the special case of scattering by a perfectly rigid sphere where the medium outside had a Poisson's ratio of 0.25. In the same year, Knopoff [43] studied the problem of the scattering of plane S wave by a perfectly rigid, and infinitely dense sphere was formulated. By using the expansion of solutions to the wave equation in terms of Weber's functions, Thau and Pao [44] examined the diffractions of horizontally polarized shear waves by a parabolic cylinder. Thiruvenkatachar and Viswanathan [45] developed a rigorous solution to the 2D problem of wave propagation in an elastic half-space, which was induced by harmonically time-dependent surface tractions applied over the boundary of an embedded circular cylindrical cavity. Based on this work, they [46] further analyzed a uniform compressional force of excitation acting over the surface of the cavity. Trifunac [47] investigated the 2D scattering and diffraction of plane SH waves by a semi-cylindrical canyon for a general angle of wave incidence, the closed-form solution showed that the surface topography could have prominent effect on the incident waves only when the wavelengths of incident motion were short compared with the radius of a canyon. Mei and Foda [48] analytically studied the scattering of SH waves in a half-space with simple overground structures, the matched asymptotics method was used for sinusoidal waves long compared to the thickness of the 2D structures. Höllinger and Ziegler [49] investigated the problem of a pulsed Rayleigh surface wave of given shape which was incident on a cylindrical cavity, multiple reflections at the cylindrical and plane free surface were considered, and the resulting displacements and stress components were calculated. Boström and Kristensson [50] examined the scattering of elastic waves in a half space which was considered to be an isotropic, linear and homogeneous medium except for a finite inhomogeneity. The T-matrix method (also known as extended boundary condition method or null field approach) was used to obtain the expressions for the elastic field inside the half space and the surface field on the interface. Four years later, they [51] further considered the time-dependent scattering by a spherical cavity in an elastic half space, when the

incoming wave was a pulsed Rayleigh wave; the displacement components at some selected points on the surface of the half space were computed. Lee [52] studied the scattering and diffraction of plane waves when a hemispherical canyon appeared in the homogeneous elastic 3D half space, by using the series solution for a general angle of wave incidence, the exact solution of the ground motion near the canyon had been drawn. Avilés and Sánchez-Sesma [81] theoretically analyzed the problem of foundation isolation from vibrations generated in the neighborhood using piles as barriers. The investigated problem was formulated in two and three dimensions as one of multiple diffractions of elastic waves. The exact solution was obtained for the 2D model where the diffracted field by each pile was constructed as expansions of cylindrical wave functions, and approximate solution was obtained for the 3D model where the diffracted filed by each pile was constructed only with Rayleigh waves.

It is pointed out that the analytical research presented above aims at solving the vibration problem on the surface as well as inside the media with the presence of obstacles, like the cylindrical cavity, the hemispherical canyon. However, since it is quite difficult to obtain close-formed solutions due to the mathematical complexity except for obstacles with very simple shapes and media with idealized boundary conditions, the analytical approach is limited. Therefore, more and more researchers and engineers turn to use the experimental and numerical approaches to investigate the vibration problem in soil (or rock) media with the presence of wave barrier.

2.3.2 Model test and field experiment

It is stated above that the analytical method is not encouraging due to the fact that the close-formed solutions are difficult to be obtained for complicated geometries and realistic conditions. Model test and field experiment, which are the closest to the reality and thus produce the most reliable results, have been receiving increasing interest during the investigation on the isolation performance of wave barrier.

During the 1960s, a number of practical cases of screening effectiveness of wave barriers had been reported [17, 74-76]. Above all, perhaps the most comprehensive research was done by Woods [17], who conducted a series of field tests to evaluate the isolation effectiveness of trenches in reducing the amplitude of vertical ground motion. Both the active isolation and passive isolation were examined. Based on the experimental results, he provided some recommendations for the rational design of open trenches.

Massarsch [53] presented the gas cushion method for vibration isolation and described its applications in full-scale projects. The efficiency of the gas cushion method was assessed in different soil conditions and design recommendations were given. The recent improvement of the gas cushion method was described as well.

Murillo [54] conducted a centrifuge parametric study to investigate the influences of various parameters (barrier depth, width, location and input frequency) in reduced scale models made of EPS isolation barriers within Fontainebleau sand. The EPS geofoam isolation efficiency was examined and some useful suggestions about the practical design of wave barriers were provided.

Alzawi and EI-Naggar [55] carried out a full-scale field experiment to study the protective performance of both open and in-filled trenches with geofoam material. The effects of the geometry and location of trenches on the screening efficiency were examined. An innovation approach of the construction of the GeoFoam trench as wave barriers was proposed as well.

Al-Hunaidi and Rainer [56] investigated the factors influencing the level of the vibration generated by the passage of vehicles on a road surface, and the effects of vehicle type, vehicle speed, vehicle weight and road surface condition were examined. Based on the findings of their study, effective remedial actions for traffic-induced vibration at a residential site were suggested.

Itoh et al. [70] described the development of a multiple ball-dropping system to simulate the wave generation and propagation from surface ground vibration sources in a centrifuge. The effectiveness of a range of wave barriers was investigated using a variety of geometry and materials. It was found that soft barrier was more effective in reducing vibration than stiff barrier, and the geometry of the barrier significantly affected the motion of the barrier itself. Three years later, Itoh et al. [71] developed a centrifuge vibration testing system to generate vertical vibration which was similar to that generated by high-speed trains. The characteristics of wave propagation in a shallow circular foundation on sand were investigated. The effects of two types of wave barriers on vibration reduction were studied as well. In addition, the authors evaluated the impact of the usage of vibration attenuating materials to build trackbeds.

Liao and Sangrey [72] evaluated the use of rows of piles as passive isolation barriers for the ground vibration reduction. The experimental measurements indicated that the effectiveness of the barriers was highly dependent on the mismatch between pile and soil material properties, and greater mismatch resulted in greater effectiveness. They indicated that the pile-to-pile aperture spacing of 0.4 times the wavelength was the upper bound for a barrier having some effectiveness, and a minor dependence of effectiveness on the pile diameter was observed as well.

Davies [79] committed a number of 20-g centrifuge tests to investigate the vibration isolation performance of the concrete wall, the expanded polystyrene (EPS) wall and their composites on the nearby underground structures. The data from centrifuge tests showed that barriers with low acoustic materials were very efficient in mitigating the stress wave propagation.

It is worth mentioning that although the model test and field experiment are able to simulate the real conditions in practice, there are still some problems. One major disadvantage is that

field experiments, especially the full-scale experiments, are often too expensive to be carried out comprehensively; while small-scale model tests seem to be unreliable, for it is difficult to reveal the true mechanism and to extrapolate to prototype situations based on the test results. Thus, numerical technique has become an affordable and effective alternative for investigating the vibration isolation performance of wave barrier.

2.3.3 Numerical method

Due to the fact that the investigations on wave barrier in soil media are theoretically difficult and experimentally expensive, numerical methods like finite element method (FEM), boundary element method (BEM), and coupled boundary element-finite element (BE-FE) method, have emerged as a powerful and economical tool for conducting a thorough investigation on the vibration isolation phenomena by solving the wave propagation problem approximately. The following part shows some details of the previous publications on wave barrier using numerical method.

2.3.3.1 Finite element method (FEM)

Finite element method (FEM), which is an efficient numerical method, is widely used in civil, mechanical and aeronautical engineering. It discretizes a continuum into a series of small elements with limited sizes in order to produce approximate but stable solutions. It is generally considered better than other numerical methods, one of the major advantages is that it can easily deals with the complicated geometry, the heterogeneity of soil and structure media as well as the nonlinear phenomena. Up to now, many commercial FEM software packages like ANASYS, ADINA, ABAQUS and DYNAFLOW, have widely used in both engineering field and academic research, and notable progresses have been achieved.

As early as in 1972, Wass [73] presented the vibration isolation effectiveness of the trenches on elastic surface waves in the frequency domain by the finite element method. The case of SH waves was particularly examined by using special finite elements taking into account the radiation condition. Some useful conclusions were summarized in his thesis.

Lysmer and Waas [84] developed a numerical procedure for the dynamic analysis of plane, linearly elastic systems consisting of an irregular zone which was joined to semi-infinite layered zones. They employed a finite element analysis of the irregular zone of the structure, and the effect of the semi-infinite layered zones was accounted for by boundary conditions. Their proposed method could be used to evaluate the screening effect of a trench.

Motamed et al. [60] studied the train-induced ground vibration using numerical modeling by ABAQUS, the influences of important parameters of barriers on the vibration reduction were analyzed and the simulation results were verified by the geotechnical centrifuge tests.

Segol et al. [61] investigated the effect of wave barriers in reducing the disturbances generated by a time-harmonic line load, which was acting on the surface of a linearly elastic, layered slab. The results showed that when the value of h/λ (h = the barrier depth, λ = the wavelength of the propagating disturbances) greater than 0.6, the vibration could be significantly reduced. It was also found that the barrier location and the shape of barrier's cross section had little influence on the vibration isolation effectiveness.

Based on the experimental investigation [56], Al-Hunaidi and Rainer [67] used finite element simulations to commit a comparison study about the remedial measures for traffic-induced vibrations at a residential site. The role of pavement/sub-base characteristics, the effectiveness of vibration screening by concrete walls and soil improvement were discussed.

Wang et al. [80] studied the effects of soft porous layer barriers on the reduction of buried blast-induced ground shock. Based on the prototype dimensions of a centrifuge test, a numerical model was set up in LS-DYNA. The numerical simulations indicated that both open trenches and geofoam barriers could reduce the blast-induced stress waves remarkably, but the inundated water trench and concrete wall seemed to be useless.

EI-Naggar and Chehab [82] examined the efficiency of both soft and stiff barriers in isolating pulse-induced waves for foundations which were resting on an elastic half-space or a layer of limited thickness underlain by rigid bedrock. The effectiveness of concrete, gas-cushion and bentonite trenches was discussed for different cases of soil layer depth, trench location and embedment of the foundation. The screening performance of different types of wave barriers was evaluated and some guidelines for their design were given.

2.3.3.2 Boundary element method (BEM)

In the past thirty years, the boundary element method (BEM) becomes a very efficient tool for solving the wave propagation problem. It has several inherent advantages, for example, there is no requirement about special treatment of the far field, for the Green's function automatically satisfies the radiation condition in the far field. And it is particularly suitable to investigate the wave propagation in soil media involving semi-infinite domain, for the radiation into the ground (e.g. into a half-space) is directly included in the formulation and the main interest is the soil motion on the surface [64, 68]. Therefore, many researchers employed it to investigate the vibration isolation performance of wave barrier.

Beskos et al. [77], and Emad and Manolis [78] seem to be the first researchers to adopt BEM to investigate the vibration isolation performance of open trenches. Later on, Beskos [64, 65] studied the problem of structural isolation from ground-transmitted vibration by open or infilled trenches under condition of plane strain. The formulation and solution of the problem was accomplished by the boundary element method. Some parametric study was carried out to as-

sess the importance of various geometrical, material and dynamic input parameters during the numerical study of the open or in-filled trenches, and several useful guidelines were provided for the design engineers.

Al-Hussaini and Ahmad [58, 59] performed a rigorous boundary element algorithm incorporating higher-order elements to examine the influence of geometrical and material parameters on the screening efficiency of a rectangular barrier, and a simple model was developed for the design of vibration screening systems.

Emad and Manolis [63] used a 2D direct BEM approach to study the placement of shallow trenched of semi-circular or rectangular shape in the path of propagation of surface waves. The results indicated that the actual shape of the trench was of minor importance.

Kattis et al. [85] solved the vibration isolation problem by a row of piles in a 3D context by an advanced frequency domain BEM. The piles and the soil were modeled by boundary elements and coupled together through equilibrium and compatibility at their interfaces. The results were validated by analytical and other numerical solutions in the published literatures. Numerical examples that dealt with passive vibration isolation by a row of piles were presented and the screening performance of these wave barriers was then assessed.

Tsai et al. [86] employed the 3D BEM in frequency domain to investigate the screening effectiveness of circular piles in a row for a massless square foundation subjected to harmonic vertical loading. Four types of piles: steel pipe piles, concrete hollow piles, concrete solid piles and timber piles, were examined. The results from the parametric study showed that steel pipe piles performed better than the solid piles, and the concrete hollow pile barrier seemed to be useless due to its stiffness. In addition, the authors pointed out that the pile length was a much more important parameter than the pile spacing and the distance between the vibration foundation and the pile barrier in vibration isolation.

2.3.3.3 Coupled boundary element-finite element (BE-FE) method

As mentioned earlier, the FEM is quite useful in dealing with the nonlinear and non-homogeneous phenomena. It should be mentioned, however, that it is difficult for the FE models to simulate the infinite or semi-infinite regions, for example, in the dynamic soil-barrier interaction problem, it is certain that elastic waves are reflected by the boundaries of FE models. Remedies to this may require either a very large model and thus an uneconomical calculation time, or the creation of complicated quiet boundary (also known as non-reflection boundary). As a contrast, such problem can be conveniently analyzed with BEM, where the quiet boundary is perfectly and easily accounted for. On the other hand, however, it is not efficient to use the BEM for simulating the models with irregular geometries or models with non-linear material behavior.

Therefore, the couple boundary element-finite element (BE-FE) method, which can make use of the advantages and avoid the disadvantages of the FEM and BEM, have been proposed.

Estorff and Prabucki [69] developed a finite element-boundary element coupling procedure for the analysis of arbitrary shaped elastic bodies which were subjected to dynamic loads. The coupling was accomplished through equilibrium and compatibility considerations along the boundary element-finite element interface. Several numerical cases including the trench problems were presented for dynamic soil-structure interaction.

Aboudi [57] used a combined perturbation-numerical approach to solve the problem of wave propagation across a thin barrier which was embedded in an elastic half-space, two various barrier sheets were given and analyzed.

Yang [66] employed a finite/infinite element scheme to investigate the isolation effectiveness of three different wave barriers: the open trench, the in-filled trench and the elastic foundation, in reducing the ground vibration caused by the passage of high-speed trains. Conclusions were made regarding the selection of optimal parameter values for the three barriers in isolating the train-induced ground vibration.

Pflanz et al. [83] studied the ground vibration generated by a moving load on the soil surface, and their reduction due to the installation of a trench and a wave-impeding barrier (WIB). The numerical investigation was performed by using the couple BE-FE method. It was found that the response of the protected structure increased with the moving speed of the load, which was independent of the reduction approach. Their study also revealed that both trench and wave barrier were effective measures for reducing ground vibration.

2.4 Protection of existing tunnels under explosions

Another important investigation in this thesis is the protection of existing tunnels or subways under explosions. As stated before, the explosion is one of the most destructive dynamic sources, often causing severe damage of structures and massive loss of live. Throughout the history, a number of explosions occurred inside or outside tunnels, leading to the failure of tunnel structures and loss of life, for example, in 1971, a blast happened through a tunnel under construction 220 feet beneath the shoreline of Lake Huron in USA, killing 21 people and leaving 9 people injured. Figure 15 shows the inside tunnel after explosions, it can be seen that the entire facilities in the tunnel were completely destroyed. It was reported that the force of the explosions was so strong that not only the tunnel structure was severely damaged, but also the bodies of the dead were mangled beyond recognition [108]. Another example was that explosions happened

Figure 15. Explosion in a Port Huron water intake tunnel in USA in 1971 (Photo from website of The Detroit News).

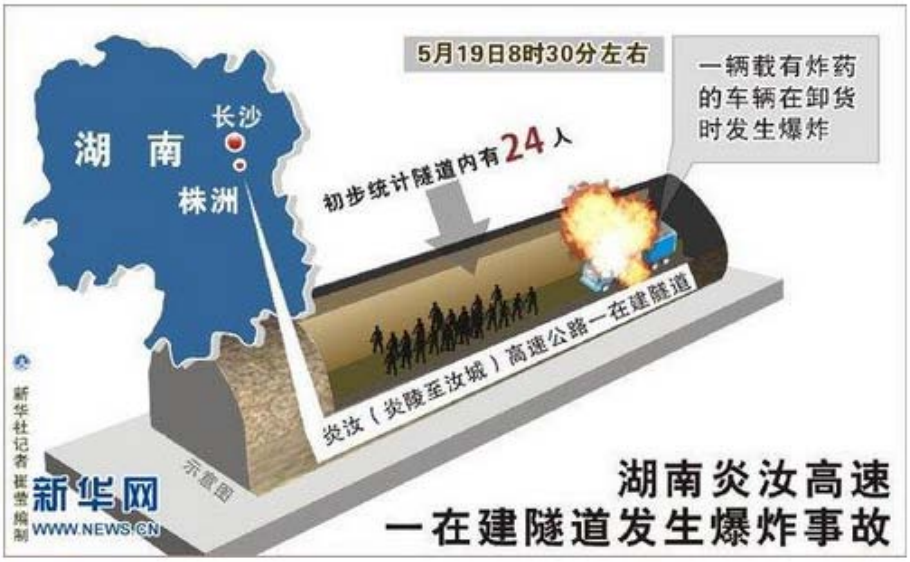

Figure 16. A tunnel explosion happens inside an under-construction expressway tunnel in Hunan province of China in 2012 (Photo from the website of *hugchina*).

inside an under-construction expressway tunnel in central China's Hunan province in 2012, as schematically shown in Figure 16. It was said that 288 kg of explosives were suddenly fired when a vehicle carrying the explosives was unloading in the tunnel, and 20 out of the 24 workers inside the tunnel were killed, only four people survived [109]. Therefore, the impact of explosions on the safety of tunnels should be a major concern during the tunnel or subway protection design. The following part provides a general introduction about the responses of existing tunnels subjected to explosions and the mitigation measures for reducing the adverse effects on existing tunnels.

2.4.1 Responses of existing tunnels under explosions

Nowadays, there are more and more second-line tunnel and subway systems that are being built to meet the increasing transportation demands in countries, especially in emerging countries where a lot of construction activities are being carried out. Due to various reasons, like saving the land resources, reducing the construction costs and protecting the environment, the distance between the existing tunnel and the new built tunnel is preferred to be as short as possible. Since the non-vibration excavation methods are often too expensive, the drilling and blasting method is widely used in mining and tunneling engineering as an economical way of deep excavation, especially in hard rock, where digging is impossible. For building the second-line tunnel that is parallel to the existing tunnel, the blasting method is commonly used as well. However, it is noted that blast accompanying ground vibration problem has detrimental influence on the nearby tunnels, ranging from causing minor damage to structural failure and loss of life. For example, the Jiu Guaidao Railway Tunnel in China was severely damaged by the blasting load generated from a nearby slope excavation. It was measured that about 123 m length of tunnel was damaged and 49.5 m length of tunnel collapsed with total landslide of about 3000 m^2, leading to the closure of the entire railway for 42 days and other related loss of several million dollars [94]. On the other hand, a number of explosions generated by terrorists occurred in the urban subways in recent years. For instance, the Islamic extremists planned to set off truck bombs in New York's subways and bridges in 1993 and in 1997; the Algerian extremists set off bombs on the subways of Paris in 1995 and the 2004 attack on the Moscow subway [87, 88]. Based on the observations on the explosions inside or outside the tunnels in history, it is known that explosions can not only damage the structures themselves, but also severely threaten the people's life. Thus, preventive measures which are against the blasting load are required to protect the existing tunnels during the tunnel and subway design in many countries, for example, the Blue Ribbon Panel on Bridge and Tunnel Security in the United States addressed the importance of this issue with details in their report [89]. In the past decades, a great number of theoretical, numerical and experimental investigations as well as the in-field tests were carried

out to investigate the responses of underground structures under explosions. Valuable progresses have been achieved. The following paragraphs summarize some important researches on it.

Berta [95] discussed the methods of modifying round blasting to reduce the initial vibration level. The parameters that influenced the blast-induced vibration in rock were identified. The author also described some cases of tunnels excavated by explosives that were close to structures under particular types of hazards.

Wang et al. [89] evaluated the impact of the explosions on the underground tunnel through 3D finite element method analysis. The effects of key factors including charge weights, size and shape of the tunnel, standoff distance (a distance from the detonation point to the tunnel wall) and the types of surrounding ground were examined. They also developed the explosion wave parameters and tunnel damage assessment charts and provided a methodology for simple and practical application to vulnerability assessment of tunnels.

Lu et al. [91] simulated the response of a buried concrete structure under subsurface blast through a comparative study of 2D and 3D modeling schemes. The SPH (smooth particle hydrodynamics) technique was used to model the explosive charge and the close-in zones where large deformation appeared, and the normal FEM was employed to model the remaining soil region and the buried structure. Results showed that the 2D model was able to provide reasonably accurate results. However, there were noticeable differences between the 2D and 3D models in the response of the remaining part of the structure. The authors also discussed the characteristics of the in-structure shock environment in terms of the shock response spectra.

Shahnazari et al. [105] studied the explosion effects of a projectile impacting on a railway tunnel located in a jointed rock medium by using 2D discrete element method. A GP2000 projectile and its penetration depth plus its crater diameter were firstly calculated in rock mass. The blast pressure from empirical formula then applied on the boundary of crater as input load. The wave pressure propagation through the jointed rock medium was finally investigated. Through a sensitivity analysis, the effects of jointed rock parameters on the tunnel lining axial force as well as the bending moment were discussed.

Liu [93] used ABAQUS to analyze the dynamic response and damage of subway structures that were supposed to be bombed by terrorists. The elasto-plasticity of ground media, possible damage of lining material and the nonlinear interaction between the lining and the ground were examined in his numerical models. It was found that the maximum lining stress occurred right after explosions, before the blast air pressure reduced to the atmospheric pressure. He pointed out that small tunnels embedded in soft soil, with small burial depth, were more likely permanently damaged by modest internal explosions that might be perpetuated by terrorists.

Liang et al. [96] comprehensively examined the impacts of blast-induced vibrations from a new tunnel on an existing railway tunnel in Xinjiang province in China, by using laboratory

tests, in situ monitoring and numerical simulations. The measured data from laboratory tests and in-situ monitoring were used to determine the input parameters required for numerical simulation, and the results were compared with the calculated ones. Based on the obtained results, the original blasting design and corresponding parameters were adjusted to reduce the maximum blasting vibration velocity. Finally, the effects of both the static stress before blasting vibrations and the dynamic stress induced by blasting on the total stresses in the existing tunnel lining were discussed.

Li et al. [100] presented a theoretical method to predict the behavior of underground tunnel subjected to explosions, by using the peak particle velocity (PPV). The influence of explosion-induced wave from an underground charge tunnel on a nearby tunnel was explicitly examined to evaluate the tunnel stability. A case study was demonstrated using the proposed analytical method and the results were calibrated by comparing the PPV of the adjacent tunnel wall with empirical formulae results. Parametric study was also carried out to investigate the effects of the separation distance and the loading density on the potential brittle failure tunnel wall.

Hatzigeorgiou and Beskos [103] examined the seismic response of the soil-tunnel system by the finite element method in the time domain. It was assumed that the seismic waves could have any arbitrary time variation and direction of propagation. The soil-tunnel system was analyzed with and without soil-tunnel interaction in order to assess its importance on the response of the system. And a comprehensive parametric study revealed the influence of key parameters that affect the tunnel response.

Jiang [101] used finite element software LS-DYNA to analyze the vibration velocities and the effective stresses of tunnel lining and surrounding rock during blast vibrations. The relationship between the dynamic stresses and PPVs of tunnel structure under different blasting condition was examined. The numerical results, which were confirmed by field blasting tests, were able to provide a reference for specifying the blasting vibration criteria in other similar projects.

Yang et al. [102] investigated the dynamic responses of the operating metro in soft soil to evaluate the effects of possible ground explosion on a shallow-buried metro tunnel. The numerical results indicated that the upper part of the tunnel lining cross-section with directions ranging from 0 to 22.5 and horizontal distances from 0 m to 7 m away from the explosive center were the most vulnerable areas. The authors suggested that the metro tunnel should be safe on the condition that the tunnel depth was more than 7 m and TNT charge on the ground was no more than 500 kg.

2.4.2 Measures to protect existing tunnels from explosions

As stated previously, the safety and stability of existing tunnels are likely to be threatened by blast-induced vibration, which can be generated by explosions, a drill/blast excavation of a nearby tunnel or other dynamic sources. It is noted that when the waves propagate through the rock masses and arrive at the interface between the rock and the existing tunnel, complicated wave conversion occurs. The complex interactions among the reflected waves, transmitted waves and new generated waves cause the vibration of tunnels and the possible appearance of stress-induced damage of tunnel structures. Therefore, a reliable estimation of the motion and the potential damage of existing tunnels subjected to nearby explosion is crucial to the tunnel protection design and stability assessment. It is mentioned that the mitigation measures, which are important work during the tunnel design, are strongly encouraged to reduce the adverse impact of explosions on existing tunnels. Generally, there are three mitigation measures: one is to change the shape, the constituent as well as the material property of tunnel structures so as to strengthen the structural ability to resist the vibration or to reduce the inner force and the motion of tunnel generated by external seismic load. For example, fiber concrete can be used to increase the strength of lining, while light concrete for reducing the weight of lining. The second mitigation measure is to install protective layer along the tunnel lining as being "wave barrier" to reflect and/or absorb the waves which propagate into the tunnel. Figure 17 shows an example of the schematic diagram of tunnel lining in section. It is seen that a protective geotextile lies along the supporting lays of tunnel. Such protective layer can be used to weaken the soil-tunnel interaction. As a result, the adverse vibration of tunnel due to the external explosion is expected to be attenuated. The third method is to control the explosion sources by reducing the wave energy before it even propagates outwards. For instance, during the construction of a new parallel tunnel, if the blasting method is used, time-delayed explosions are considered to be able to reduce the vibration of nearby existing tunnel compared with the instantaneous explosions. In recent years, many researchers focus on finding the practical delay times which can result in the minimum peak particle velocity. The following paragraphs give a general description of mitigation measures proposed in the previous publications.

Leet [113] discussed the systems of delay blasting on the effectiveness in reducing vibrations in the vicinity. Due to the reason that the mechanism by which short-delay blasting reduced vibration appreciably and increased rock breakage was not well understood, the author proposed a theory of the operation of short-delay blasting as a working hypothesis to provide reference on the blasting design in engineering.

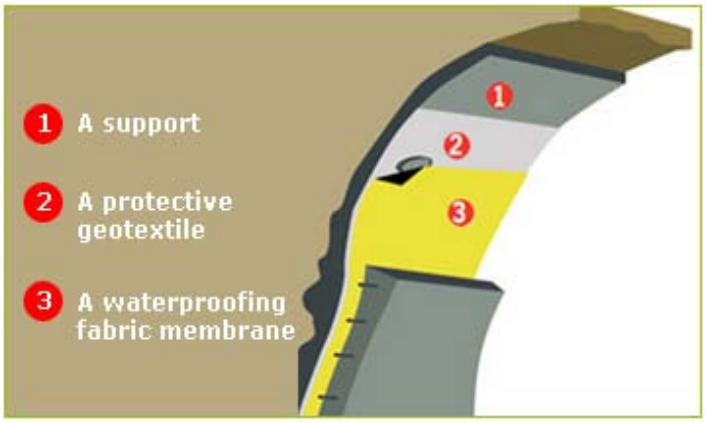

Figure 17. Schematic diagram of tunnel lining in section. (Picture comes from the website of OSSA)

Wang [104] used ABAQUS to investigate the performance of Expanded Polystrene (EPS) geofoam as seismic buffer to mitigate the vibration of tunnel generated by earthquake. Four different types of protective EPS layers with different elastic modulus and thickness were examined. The numerical results revealed that the axial strain and section force of tunnel lining were greatly reduced with the installation of a protective EPS layer. And a decrease of the layer's elastic modulus and an increase of the layer's thickness can both reduce the tunnel motion. However, the former can achieve more noticeable mitigation effect.

Gui and Chien [92] committed the blast-resistant analysis for a tunnel passing beneath Taipei Shongsan airport. The overall analysis process was presented to obtain the maximum lining thrust generated by a bomb explosion. A comprehensive parametric study had been carried out to evaluate the significance and sensitivity of key parameters on the lining thrust. Based on the numerical study, they concluded that the dynamic soil parameters obtained from ground investigation and soil testing should be adopted for more accurate and economical analysis and design for underground tunnels. They also mentioned that the installation of an additional protective layer over the tunnel structure might be able to minimize the impact of the explosion, which was considered much less costly than designing rigid structure.

Shimamura et al. [107] investigated the seismic isolation effects of soft seismic isolation layers for a rectangular shape tunnel during an earthquake. Two different isolation layers were examined: one was an isolation layer installed around the tunnel for a newly build tunnel; the other was the vertical isolation walls installed at both sides of an existing tunnel. It was found that the isolation layer with shear modulus of 1/100-1/1000 of the ground could effectively restrain the propagation of shear strain during an earthquake. Specifically, additional section forces could be reduced to a half of those without isolation for the newly built tunnel, and the section forces could be reduced up to 40-70% of those without isolation for the existing tunnel.

Huang et al. [106] studied the earthquake-induced responses of Galogla Tunnel along Zhamo Highway in China by using infinite element dynamic artificial boundary technique, and analyzed the shock absorption effects of two kinds of seismic isolation layers made of rubber and foam concrete respectively. The results showed that remarkable shock absorption effects could be achieved due to the installation of isolation layers, and there was little difference in the mitigation effects for the two different isolation materials, but the foam concrete was proposed because of its low cost and durability.

Kopp and Siskind [110] investigated the effects of millisecond-delay intervals on the vibration and airblast from surface coal mine blasting. A total of 52 production blasts were instrumented and monitored. Various delay intervals were used within and between rows of blastholes. The gathered data were analyzed for peak values of vibration and airblast and for frequency content. It was found that large delay intervals between rows reduced the amplitude of ground vibrations, and subsonic delay intervals within rows reduced airblast by 6 decibels.

Shi and Chen [111] conducted a series of field experiments in XinQiao Mining Co. Ltd to optimize the blasting parameters for mitigating the blast-induced vibration on final pit walls' stability. They used the predictor equation proposed by the United States Bureau of Mines to establish a relationship between the peak particle velocity and the scale distance factor. Based on the field experiments, they determined the maximum charge amount per delay and proposed 15 ms delay to be used in practice, which could reduce the vibration by 24.5%.

Ester et al. [112] examined the influence of blasting on a nearby existing road tunnel Sv. Rok during the construction of a new tunnel. The total number of 30 measurements was executed and 720 values, including all the three component oscillation velocities, were recorded. And the maximum ground oscillation velocity was recorded as 232.061 mm/s. The authors drew their conclusions based on the collected data, the damage level criteria for the rock mass and support system, and discussed how these results could assist further development in the control of blasting technique.

2.4.3 Concrete damaged plasticity model (CDP model)

The concrete damaged plasticity model (CDP model) [123] provides a general capability for modeling concrete and other quasi-brittle materials in all types of structures, such as beams, trusses, shells and solids. It uses concepts of isotropic damaged elasticity in combination with isotropic tensile and compressive plasticity to represent the plastic behavior of concrete. It can simulate both plain concrete and concrete reinforcement under monotonic, cyclic, and/or dynamic loading with low confining pressures. This model consists of the combination of nonassociated multi-hardening plasticity and scalar (isotropic) damaged elasticity to describe the irreversible damage that occurs during the fracturing process, and allows user control of

stiffness recovery effects during cyclic load reversals. In addition, it can include strain rate dependency and can be used in conjunction with a viscoplastic regularization of the constitutive equations in ABAQUS/Standard to improve the convergence rate in the softening regime. It is noted that elastic behavior of the material (isotropic and linear) is required before the introduction of CDP model. The following part discusses some major assumptions about the mechanical behavior of concrete [123].

Generally, it is assumed that there are two main failure mechanisms of the concrete material in the CDP model, one is the tensile crack; the other is the compressive crush. And the development of the failure surface is controlled by two hardening variables, the tensile equivalent plastic strains ξ_t^{pl} and the compressive equivalent plastic strains ξ_c^{pl}, which are linked to the failure mechanisms under tension and compression loading, respectively. To illustrate the evolution of the mechanical behavior of concrete in a comprehensive way, the responses of concrete subjected to uniaxial loading in tension and compression are presented, shown in Figure 18. As it can be seen, in the case of concrete under uniaxial tension, the linear elastic relationship between the stress and strain is firstly observed until the failure stress σ_{t0} is reached. After that, the micro-cracking begins to appear in the concrete material, and the formation of micro-cracks is represented macroscopically by a softening stress-strain response. On the other hand, when the concrete is subjected to the uniaxial compression, the stress-strain response firstly follows a linear elastic relationship until the value of the initial yield σ_{c0}. As the stress continuously increases, plastic deformation occurs, and the response of concrete is typically characterized by stress hardening followed by strain softening beyond the ultimate stress σ_{tu}. It is noted that such description is somehow simplified; however, it is able to capture the main features of the response of concrete material under uniaxial compression.

2.5 Conclusions

Ground vibration induced by dynamic sources has attracted more and more attentions in recent years. Traditionally, dynamic sources, like strong earthquakes, not only cause a huge number of civil structures damages, but also take many lives away. Nowadays, many new forms of dynamic sources, like the working heavy machines, the construction activities, the high-speed trains and subways, have generated increasing structural integrity problems and environmental disturbances. Although those adverse influences are relatively less severe and destructive compared with strong earthquakes, they still cause troublesome problems in many areas, especially in the densely populated urban regions and buildings housing sensitive equipments. For example, the traffic-induced ground vibration can result in moderate or minor damage of structures, affect the accuracy of sensitive equipments, and generate sleep disturbance, work

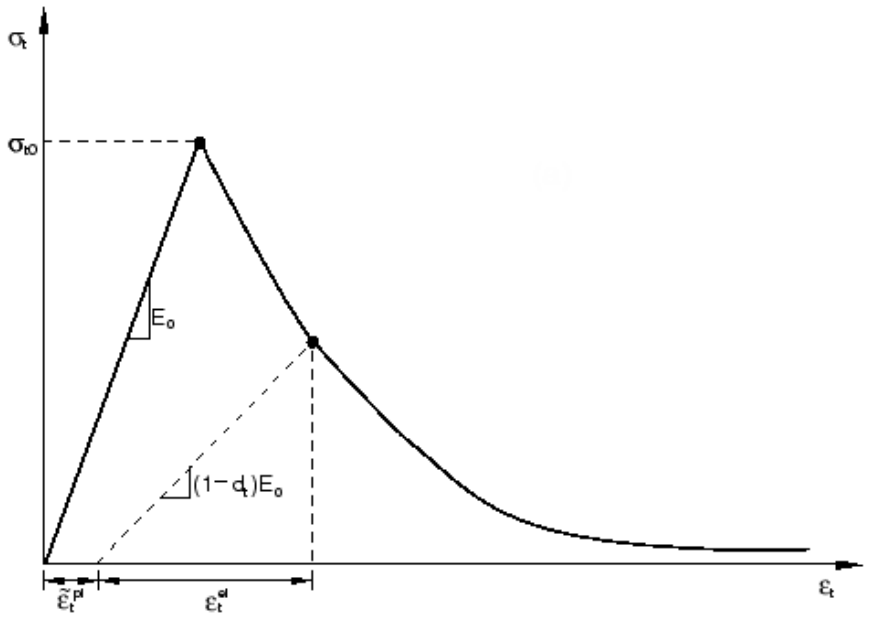

(a) Response of concrete to uniaxial loading in tension.

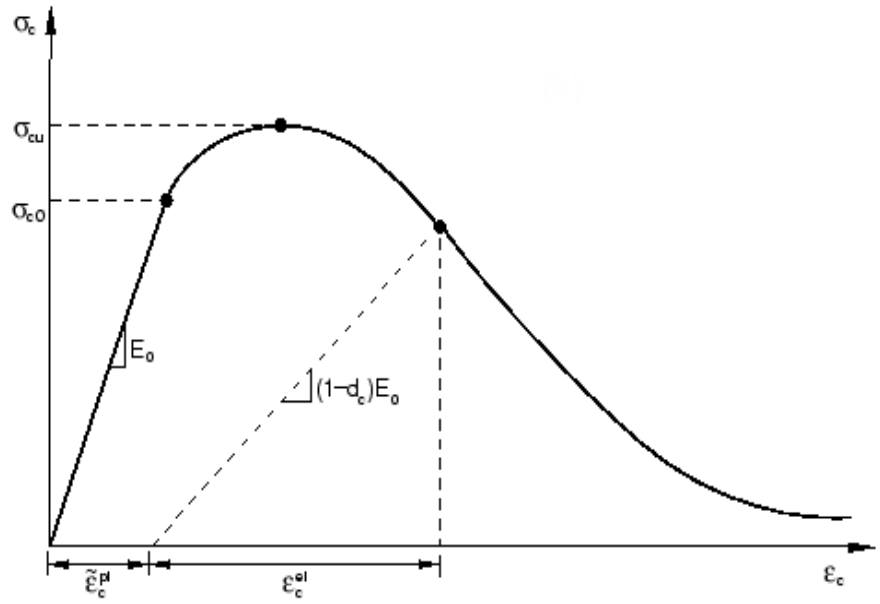

(b) Response of concrete to uniaxial loading in compression.

Figure 18. Response of concrete to uniaxial loading in tension (a) and compression (b).

degradation and possible health risks of the nearby occupants. To deal with the ground vibration problems, many efforts have been made in order to minimize its detrimental impact. One common effort is to take the mitigation measures. From the view of wave propagation path in media, mitigation measures could be divided into three types: controlling the vibration sources, disrupting the wave propagation through soil or rock media and controlling the vibration of protective structures. It is pointed out that which type of mitigation measure should be adopted in practice depends on many factors, such as the vibration reduction effectiveness, the costs, and other construction requirements. In the past decades, the installation of wave barrier, which is considered to be an effective mitigation measure to reduce ground vibration by scattering and/or absorbing waves that propagate in soil and rock media, has received increasing interest among engineers and researchers. A great number of researches have been committed to examine the vibration isolation effectiveness of barriers. It is known that the research methods could be generally divided into three kinds: analytical method, model test and field experiment, and numerical method. The analytical method is rarely used because it is quite difficult to obtain close-formed solutions due to the mathematical complexity except for barriers with very simple shapes and media with idealized boundary conditions. While the model test and field experiment, especially the full-scale field experiment, which can simulate the real problems in reality, are often too expensive to be carried out comprehensively, and small-scale model tests seem to be difficult to reveal the true mechanism and to extrapolate to prototype situations based on the test results. Therefore, numerical method has become an affordable and effective alternative for investigating the screening efficiency of wave barrier. It is noted that in this dissertation, the FEM has be adopted to investigate the isolation performance of wave barrier.

On the other hand, with the increasing constructions of a second parallel tunnel by drilling and blasting method and a series of terrorist attack to the public subway systems by explosives in recent years, the security of existing tunnel under explosions has become a major concern. Lots of researches have been committed to investigate the dynamic behavior of tunnel under nearby explosions. It is known that the responses of tunnel, especially the inner stress and strain, the maximum motion (displacement, velocity and acceleration), are often used as controlling index for in situ monitoring and safety assessment of tunnel lining structures. In order to reduce the vibration of protected tunnel, mitigation measures could be proposed in practice. Generally, there are three typical mitigation methods. The first method is to change the shape, the constituent as well as the material property of tunnel structures so as to strengthen the structural ability to resist the vibration or to reduce the inner force and the motion of tunnel generated by explosions. The second method is the installation of a protective layer which lies along the tunnel lining to reflect and/or absorb the waves before they propagate into the lining, which acts like being ”wave barrier”. And the third method is time-delayed explosions (to fire the explosives

with delay times), rather than instantaneous explosions (to fire the explosives simultaneously). Tunnel vibration is expected to be attenuated by choosing appropriate delay times which can generate destructive wave interference during wave propagation in soil or rock media. In addition, concrete damaged plasticity (CDP model), which can provide a general capability for modeling plain or reinforced concrete under the monotonic, cyclic, and/or dynamic loading, and can simulate the irreversible damage involved in the fracturing process and the recovery of stiffness as loads change from tension to compression or vice versa [123], has to be introduced to reflect the real behavior of tunnel lining made of concrete under explosions.

3. Investigation on the isolation performance of wave barriers I: under harmonic load

3.1 Numerical model

Figure 19 shows a 2D plane-strain model constructed in ABAQUS. It has a length of 120 m and a depth of 24 m. A rectangle barrier is installed in a half space soil, its depth *D*, width *W* and inclination angle *U* are given as 5 m, 0.5 m and 90°, respectively. A dynamic load *P*, which is represented by a function $P = P_0\, e^{i\omega t}$, is applied on the top surface of the soil and has a width of *r*. The quantities P_0, ω and *r* are specified as 1 kN, 100π rad/s and 1.25 m, respectively. The distance L_1 between the dynamic load and the wave barrier is 25 m, and L_2, which denotes the distance from the wave barrier to the point of interest (point "*a*") on the ground surface, is assumed 25 m. There is no horizontal displacement along the left side of the soil and non-reflection boundary is applied on the right side and at the bottom of the soil. It is noted that Rayleigh velocity v_r in soil is given as 250 m/s, so Rayleigh wavelength λ_r can be calculated as:

$$\lambda_r = \frac{2\pi v_r}{\omega} = 5\ m \tag{10}$$

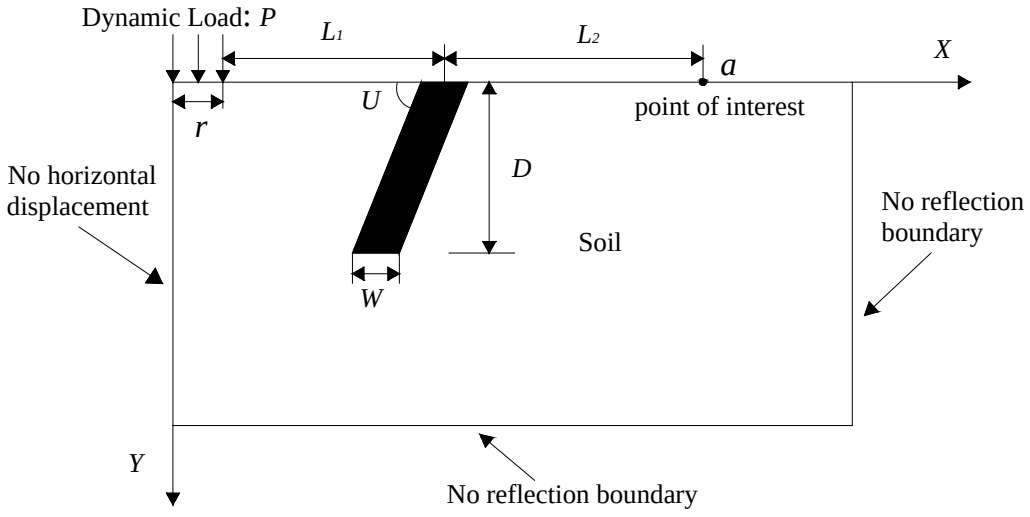

Figure 19. Schematic diagram of 2D model of soil-barrier system under surface harmonic load.

Table 3. Material properties of soil and barrier.

Material*	Density ρ(kg/m^3)	Poisson's ratio v	Young's modulus E(GPa)	Damping ratio β
Soil	1750	0.25	0.33	6
Barrier	2397.5	0.25	11.30	30

*The density, Poisson's ratio, Young's modulus and damping ratio of soil and barrier are denoted as ρ_s, v_s, E_s, β_s and ρ_b, v_b, E_b, β_b, respectively.

To perform the numerical modeling, explicit dynamic analysis procedure is adopted in ABAQUS. The soil and the barrier are modeled as homogeneous, isotropic and elastic media, using 4-node bilinear plane strain quadrilateral, reduced integration elements. The interface between them is assumed perfectly bonded. And the material properties are provided in Table 3. It is noted that Rayleigh damping is adopted. To avoid reflected waves generated by soil boundaries, 4-node linear, one-way infinite element is used to simulate the non-reflection boundary conditions. In order to validate the convergence of numerical analyses, mesh convergence study is committed. The investigated element sizes are 1.0 × 1.2 m, 0.75 × 0.9 m, 0.5 × 0.6 m, 0.4 × 0.45 m and 0.25 × 0.3 m, respectively, as shown in Figure 20. Figure 21 presents the amplitude of vertical displacement of ground surface beyond wave barrier with different element sizes. It is clear to see that models with crude meshes (element size: 1.0 × 1.2 m and 0.75 × 0.9 m) produce bad results. As the mesh becomes finer and finer, the results appear to gradually achieve convergence. The differences among the three curves (corresponding element sizes: 0.5 × 0.6 m, 0.4 × 0.45 m and 0.25 × 0.3 m) are very small. Considering that the finer the mesh is, the longer time ABAQUS takes to finish calculations, element size in this study is taken as 0.5 × 0.6 m. This agrees well with Kramer's suggestion [114] that the maximum element size should be less than one eighth of the shortest possible Rayleigh wavelength.

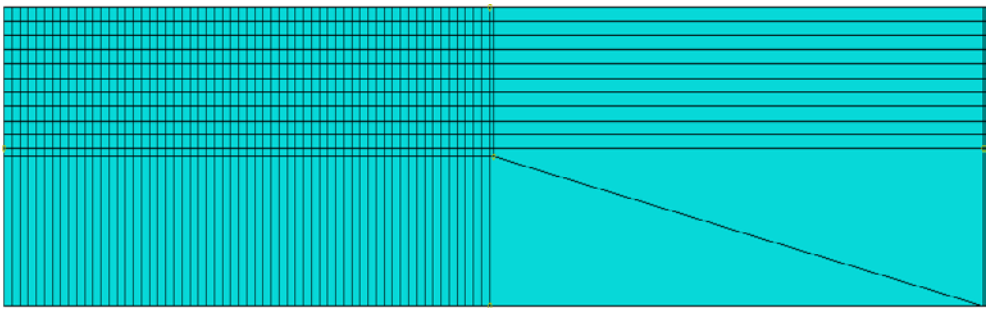

(a) Element size: 1.0 × 1.2 m

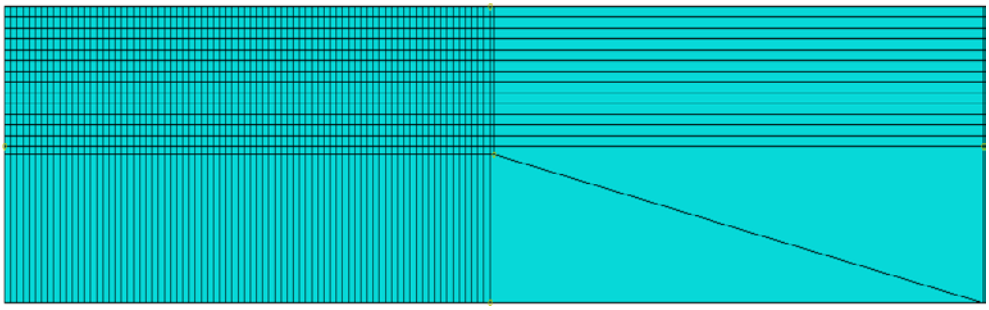

(b) Element size: 0.75 × 0.9 m

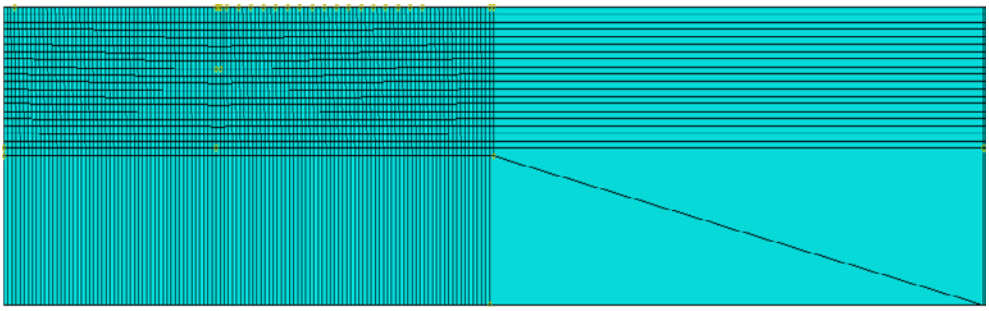

(c) Element size: 0.5 × 0.6 m

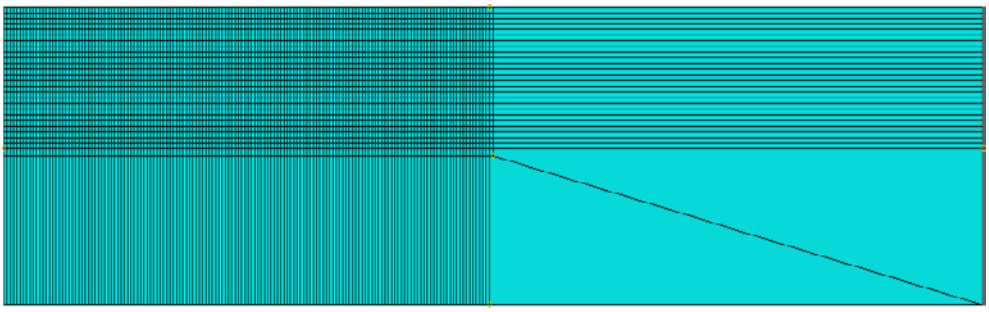

(d) Element size: 0.4 × 0.45 m

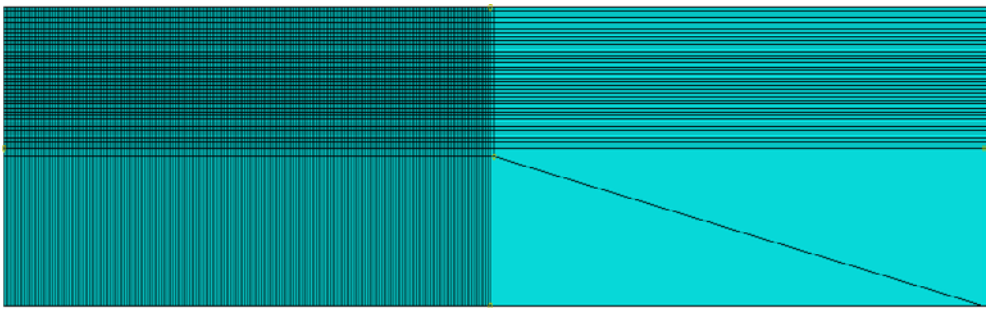

(e) Element size: 0.25 × 0.3 m

Figure 20. Finite element mesh model with different element sizes.

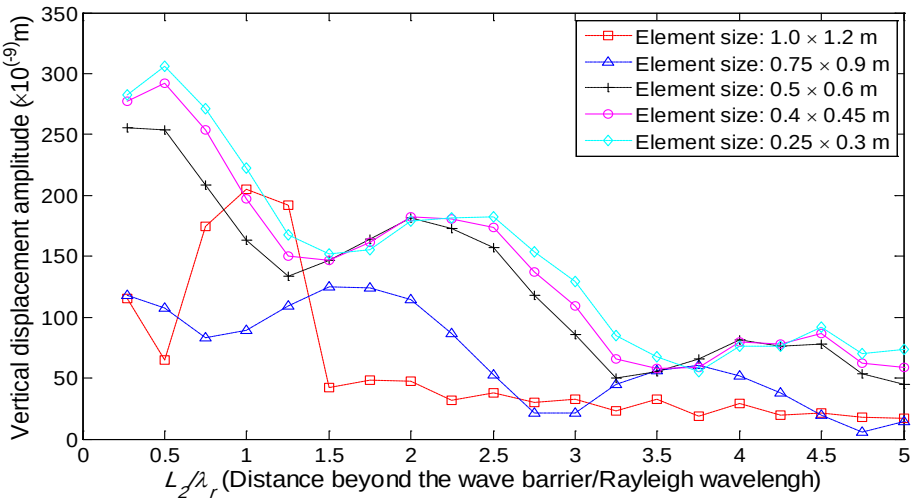

Figure 21. Mesh convergence study.

3.2 Validation of the numerical solutions

Before committing the investigation of the screening effect of wave barrier, the ability that numerical model in ABAQUS can produce accurate results has to be verified. Since it is known that in the elastic wave theory, the velocity of waves can be computed as:

$$v_P = \sqrt{\frac{E(1-v)}{\rho(1+v)(1-2v)}} \tag{11}$$

$$v_S = \sqrt{\frac{E}{2\rho(1+v)}} \tag{12}$$

$$v_R = \frac{0.87+1.12v}{1+v} v_S \tag{13}$$

where E = Young's modulus; ρ = density; v = Poisson's ratio. And v_P, v_S and v_R are the velocity of compressional waves (P waves), shear waves (S waves) and Rayleigh waves (R waves), respectively. It is noted that those equations above can only be used in homogeneous isotropic and elastic medium without damping. Figure 22 shows the motion of point "*a*" over time with the assumption that wave barrier is replaced by soil in Figure 19 and the soil media has no damping. Based on the Equations (11)-(13), the wave velocities can be calculated as:

$$v_P = \sqrt{\frac{E(1-v)}{\rho(1+v)(1-2v)}} = \sqrt{\frac{3.3\times10^8\times(1-0.25)}{1750\times(1+0.25)(1-2\times0.25)}} = 475.70m/s \tag{14}$$

$$v_S = \sqrt{\frac{E}{2\rho(1+v)}} = \sqrt{\frac{3.3\times10^8}{2\times1750\times(1+0.25)}} = 274.64m/s \tag{15}$$

$$v_R = \frac{0.87+1.12v}{1+v} v_S = \frac{0.87+1.12\times0.25}{1+0.25} \times 274.64 = 252.67m/s \tag{16}$$

Therefore, the first arrival times of P waves, S waves and R waves at point "*a*" are:

$$t_P = \frac{L_1+L_2}{v_P} = \frac{50m}{475.70m/s} = 0.1051s \tag{17}$$

$$t_S = \frac{L_1+L_2}{v_S} = \frac{50m}{274.64m/s} = 0.1821s \tag{18}$$

$$t_R = \frac{L_1+L_2}{v_R} = \frac{50m}{252.67m/s} = 0.1979s \tag{19}$$

It is noted that the three vertical lines from left to right in Figure 22 exactly represent t_P , t_S and t_R, respectively. It can be seen from the Figure 22(a) that the time point when the point "*a*" begins to vibrate (caused by the first arrival of P waves) agrees well with the theoretical solution (i.e. t_P). The initial displacements are quite small, because P waves carry relatively small wave energy. A sharp increase of displacement can be observed at about 0.2 s, when Rayleigh waves, which carry most of wave energy, finally arrive, causing tremendous vibration at point "*a*". This agrees well with the theoretical solution (i.e. t_R) as well. Similar phenomena can be observed from the evolution of velocity and acceleration of point "*a*", as shown in Figure 22(b) and (c), respectively. Based on the analysis above, it is found that the numerical results produced by ABAQUS agree well with the solutions in classic elastic wave theory.

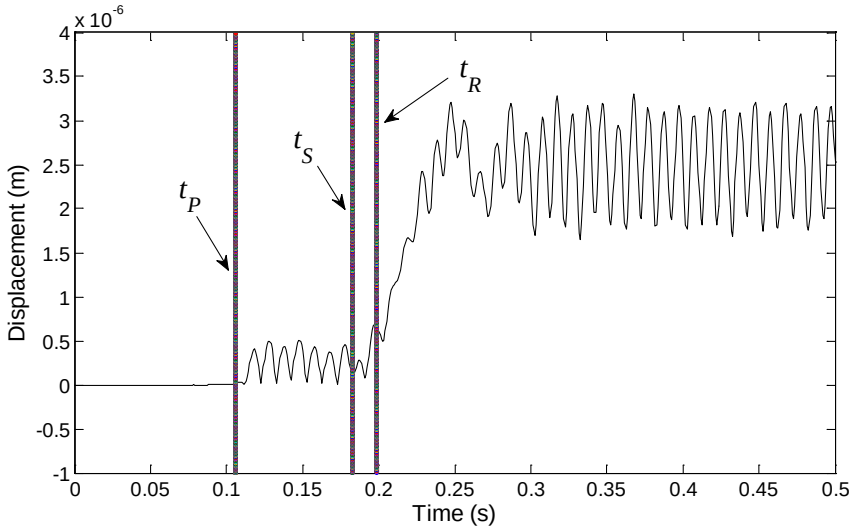

(a) Displacement of point "*a*"

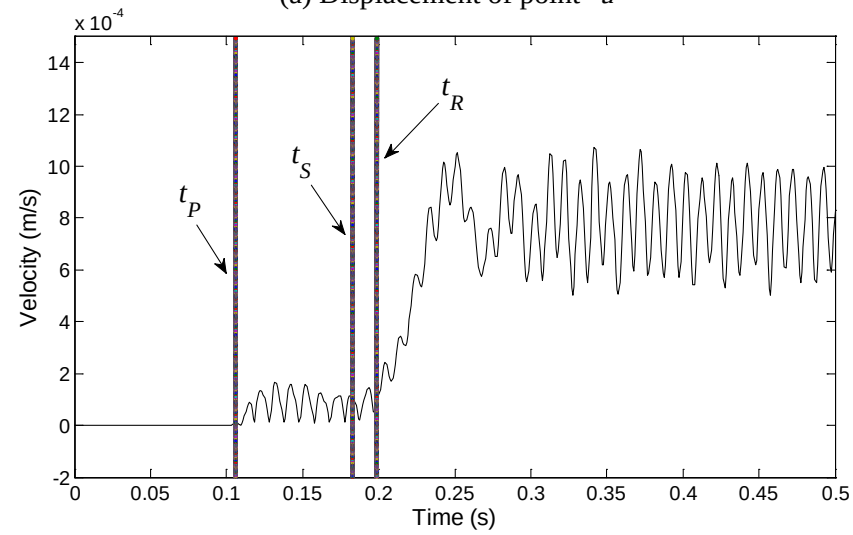

(b) Velocity of point "*a*"

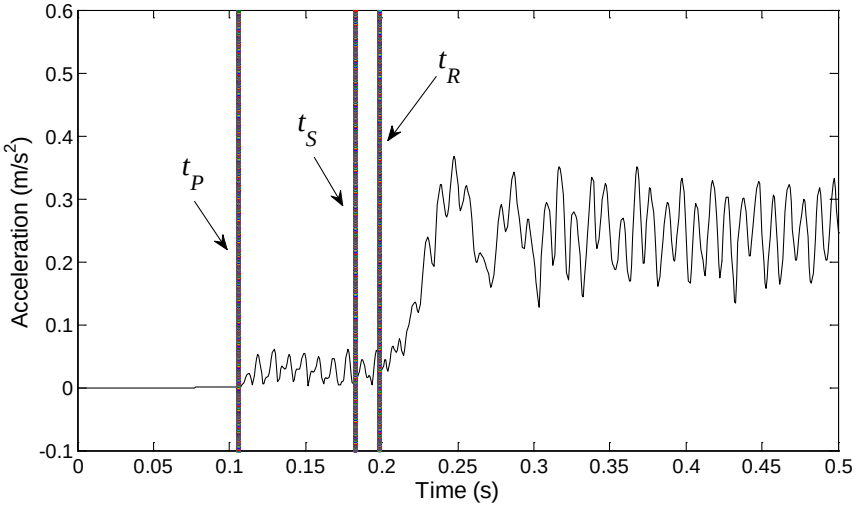

(c) Acceleration of point "*a*"

Figure 22. The motion of point "*a*" in homogeneous isotropic and elastic soil media without damping.

A second comparative study is carried out for the case of soil-barrier system (see Figure 19). Observed from Figure 23, which presents the amplitude of vertical displacement reduction ratio of soil (=(the amplitude of vertical displacement of soil with the barrier)/(the amplitude of vertical displacement of soil without the barrier)) on the surface due to the installation of wave barrier, it can be seen that the numerical results have a satisfactory agreement with those reported by Al-Hussaini and Ahmad [58] and Beskos [64], using boundary element methods.

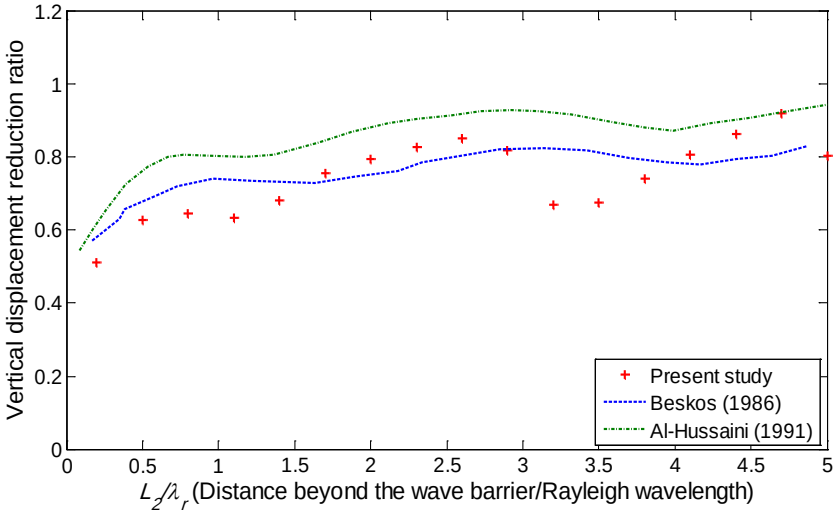

Figure 23. Comparative study for vertical vibration isolation by wave barrier.

Generally, the vibration isolation effectiveness of wave barrier can be evaluated by comparison of maximum displacement, velocity or acceleration with and without barriers. Investigation shows that velocity of vibration is a better measure of residential structure damage than either the displacement or acceleration [116]. Therefore, in this study, the velocity amplitude reduction ratio A_r at point "*a*" (see Figure 19) is chosen to assess the vibration isolation effectiveness of wave barrier:

$$A_r = \frac{A_b}{A_s} \tag{20}$$

where A_b and A_s are the velocity amplitude at point "*a*" with and without wave barrier, respectively. Since the velocity has horizontal and vertical components, A_{rh} and A_{rv} are respectively used to express the horizontal and vertical velocity amplitude reduction ratios. These two ratios give a quantitative evaluation of screening effect of barrier, for example, A_{rh} = 0.6, A_{rv} = 0.7, it means that 40% reduction in the horizontal velocity amplitude and 30% reduction in the vertical velocity amplitude at point "*a*" are achieved due to the installation of wave barrier.

3.3 Comparative study of 2D and 3D models

Due to the nature three-dimensional problem in reality, it should be more suitable to simulate the soil-barrier system in 3D model than in 2D model. However, the major problem is that 3D

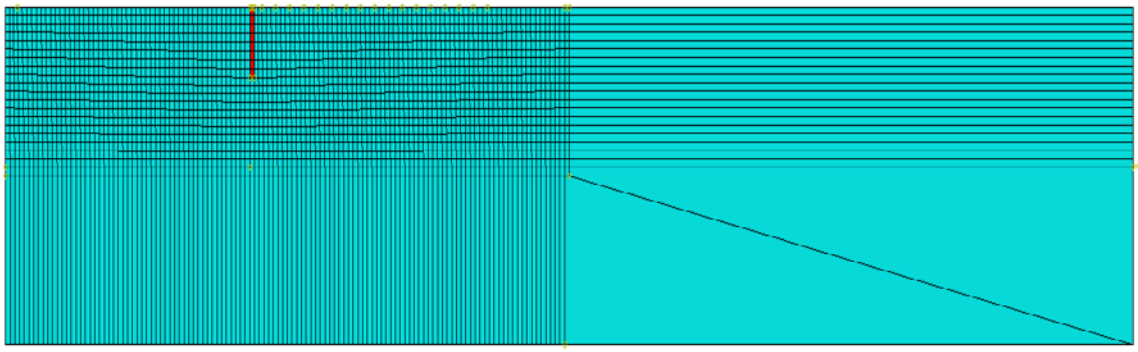

(a) 2D finite element model mesh.

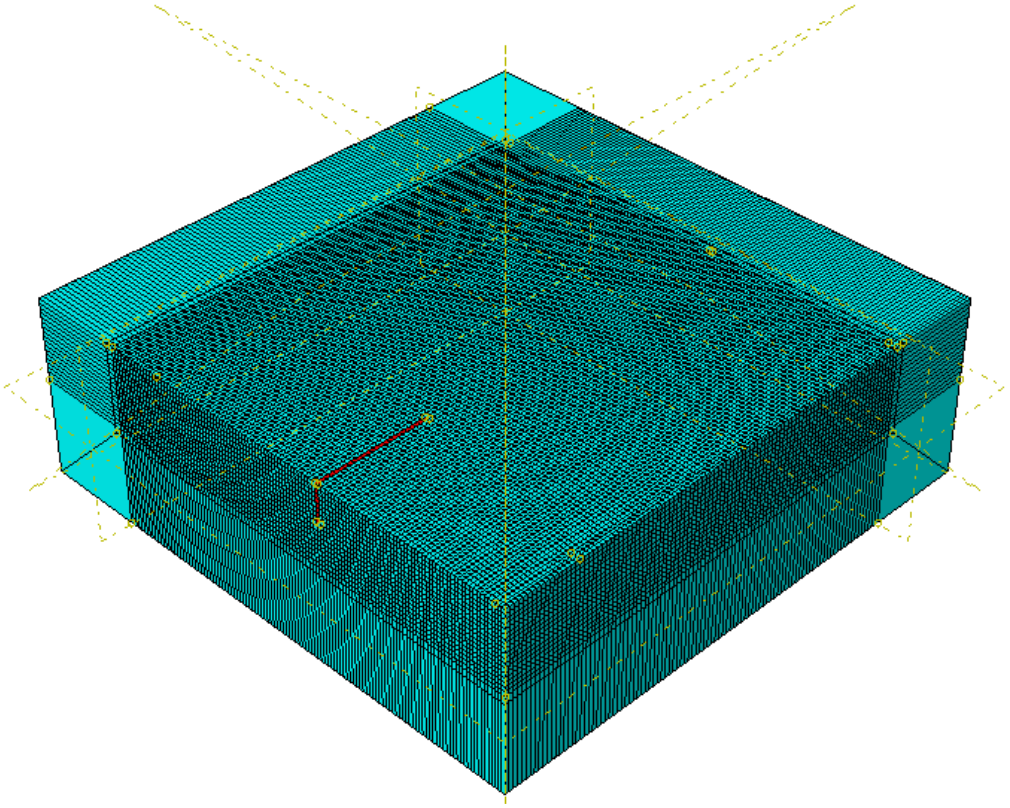

(b) 3D finite element model mesh.

Figure 24. 2D and 3D finite element model meshes in ABAQUS.

analysis usually requires much more time for calculation. If the 2D model can produce similar results as 3D model does, then 3D analysis can be avoided. This section focuses on the investigation on the feasibility of replacing 3D model by 2D model through the comparison of numerical results from 2D and 3D analysis. Figure 24(a) and (b) show the 2D and 3D finite element model meshes built in ABAQUS, respectively, with the part in red color representing wave barrier and the part in blue color representing soil media. For the 3D model, only one fourth of the model is created due to the symmetry, and the 3D infinite elements are used to simulate the non-reflection boundaries. The lengths of the dynamic load and the wave barrier are assumed to be 10 m and 15 m, respectively. Other parameters are the same as those used in 2D model. Figure 25 presents the evolution of the amplitude of vertical displacement reduction ratio due to the installation of wave barrier in 2D and 3D models. It can be seen the numerical results from 2D analysis agree well with the ones from 3D analysis. It is mentioned that the 3D models with other typical lengths of the dynamic load and the wave barrier produce similar results (not shown here). Thus, it is inferred that the 2D model is sufficient to predict the vibration isolation performance of wave barrier. The following parametric study and optimization design are based on the 2D model.

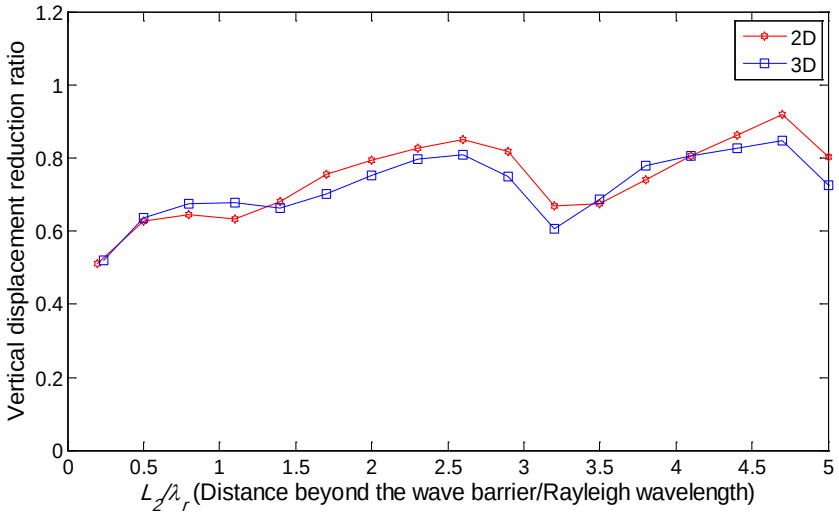

Figure 25. Comparison of numerical results from 2D and 3D models.

3.4 Parametric study

In this section, an extensive parametric study, including the material properties of wave barrier, the barrier dimensions, its positions, its damping ratio as well as the dynamic load, has been conducted to investigate their influences on the vibration isolation effectiveness. All the investigations are based on the model shown in Figure 19, except the dynamic load, which is replaced by a sinusoidal load $P = P_0 sin\ (\omega t)$, for it is easier and clearer to study the influence of dynamic load in such form. In addition, the damping ratios of the barrier and soil are given as 5%.

Note that when the effect of one parameter is examined, all the other parameters are kept constant. Besides, to keep independency of the analysis on the exciting frequency, the geometric parameters of barriers and the distances discussed in this section are normalized by Rayleigh wavelength. The following dimensionless parameters are adopted:

$$d = \frac{D}{\lambda_r} \quad w = \frac{W}{\lambda_r} \quad l_1 = \frac{L_1}{\lambda_r} \quad l_2 = \frac{L_2}{\lambda_r} \tag{21}$$

where *d, w, l_1 and l_2* are dimensionless parameters of barrier depth, width, distance from vibratory source to the barrier and distance from the barrier to the point of interest (point "*a*"), respectively. The numerical results and analyses are presented as follows.

3.4.1 Effect of barrier Young's modulus

Figure 26 shows the effect of the ratio of Young's modulus (E_b/E_s) on the vibration isolation effectiveness, where E_b and E_s are the Young's modulus of wave barrier and soil, respectively. And E_b/E_s is varied from 0.03 to 25. It can be seen that when the barrier Young's modulus is small (E_b/E_s < 0.2), both the horizontal and vertical velocity reduced significantly. Particularly, when E_b/E_s is close to zero, the best isolation effect is achieved. This agrees with the general conclusion that open trenches are considered to be the best barriers [17, 64], while the Young's modulus of open trenches is zero. As the barrier becomes stiffer, both the horizontal and vertical velocity amplitude reduction ratios A_{rh} and A_{rv} firstly increase dramatically, and then gradually reach to be stable values. It seems that large Young's modulus (E_b/E_s > 2.5) has little contribution in reducing vibration, but small Young's modulus (E_b/E_s < 0.2) is very effective. Moreover, the smaller the barrier Young's modulus is, the much greater vibration reduction is expected to be achieved.

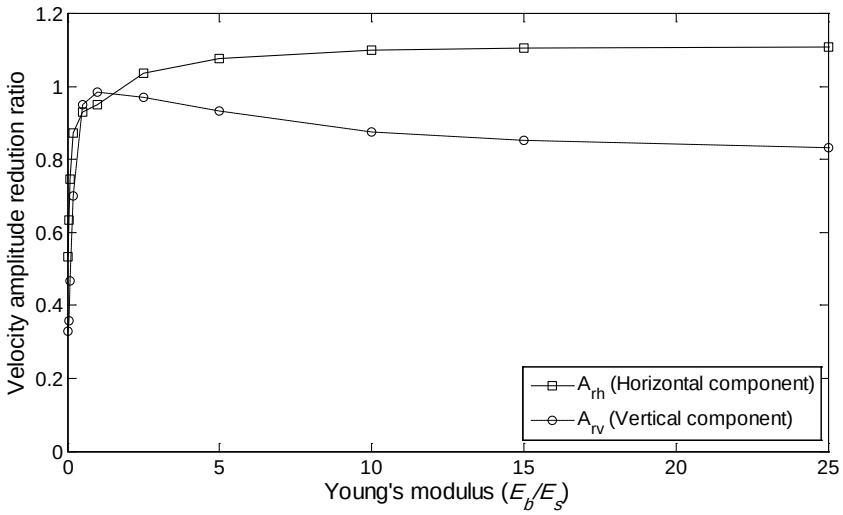

Figure 26. Effect of barrier Young's modulus on the vibration isolation effectiveness.

3.4.2 Effect of barrier density

Figure 27 shows the effect of the ratio of density (ρ_b/ρ_s) on the vibration isolation effectiveness. The density of barrier and soil are defined as ρ_b and ρ_s, respectively, and ρ_b/ρ_s ranges from 0.005 to 5. It can be seen, in general, that the larger the density is, the better isolation effect the barrier produces. On the other hand, barriers with large density tend to be more efficient in reducing vertical vibration than reducing horizontal vibration, for example, when ρ_b is equal to $5\rho_s$, the vertical velocity amplitude reduction ratio A_{rv} reduces to 0.450, while for the horizontal response, A_{rh} decreases only to 0.946. The possible reason for this difference is that the vertical motion of barrier tends to send wave energy deep into the soil. While for the barrier horizontal motion, it is more likely to transfer the energy into the protected areas [58]. Thus, more energy that results in vertical vibration is consumed, leading to a better vertical vibration isolation effect. Besides, the phenomenon that part of body waves are transformed into Rayleigh waves after they propagate the barrier may also amplifies the horizontal vibration in the protected site. It should be mentioned, however, that material with too large density are probably unavailable in practice, for instance, when $\rho_b = 5\rho_s$, which means the barrier density is about 8750 kg/m^3, material with such large density is rare in civil engineering.

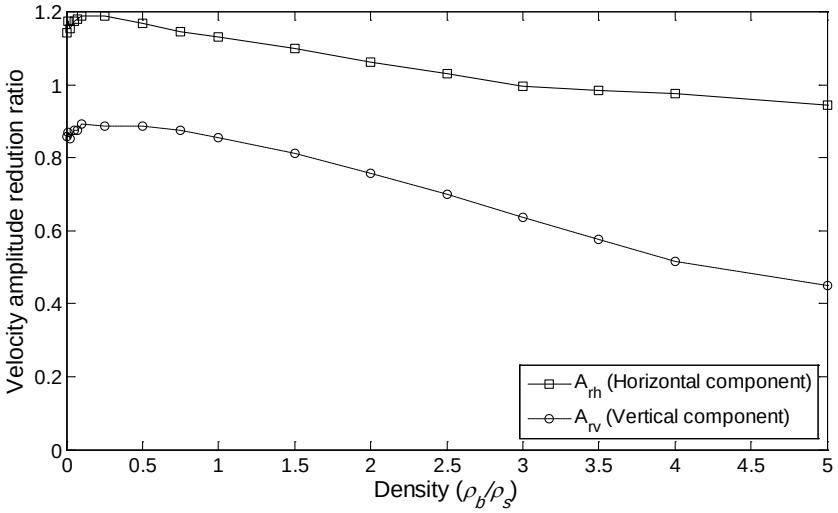

Figure 27. Effect of barrier density on the vibration isolation effectiveness.

3.4.3 Effect of barrier Poisson's ratio

Figure 28 represents the influence of barrier Poisson's ratio (v_b) on the vibration isolation effectiveness. It is clear to see that both the horizontal and vertical velocity amplitude reduction ratios almost keep constant with an increasing v_b. It seems that the response of soil at point "*a*" is not affected by the variation of barrier Poisson's ratio. Therefore, it is inferred that the barrier Poisson's ratio has negligible influence on its vibration isolation performance.

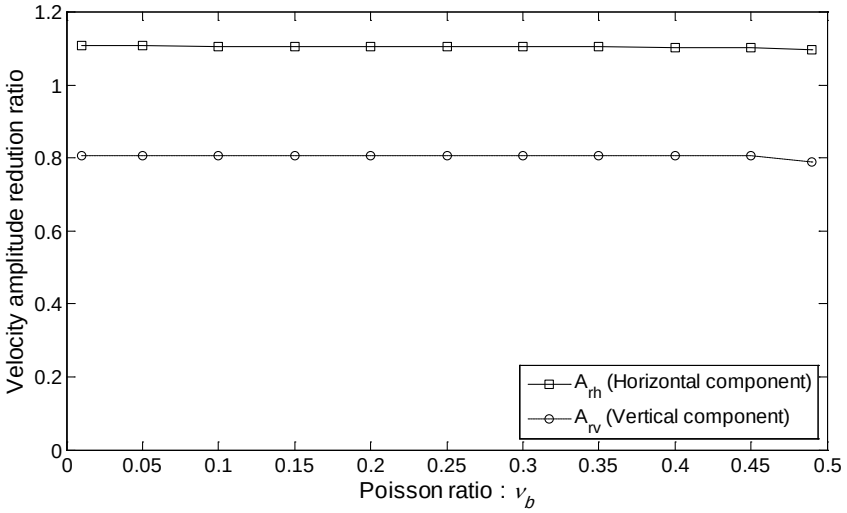

Figure 28. Effect of barrier Poisson's ratio on the vibration isolation effectiveness.

3.4.4 Effect of barrier damping ratio

Figure 29 shows the effect of barrier damping ratio (β_b) on the vibration isolation effectiveness. Similar to the phenomenon observed in Figure 28, the horizontal and vertical responses change little as β_b increases from 0 to 0.1. Thus, the influence of barrier damping ratio can also be ignored.

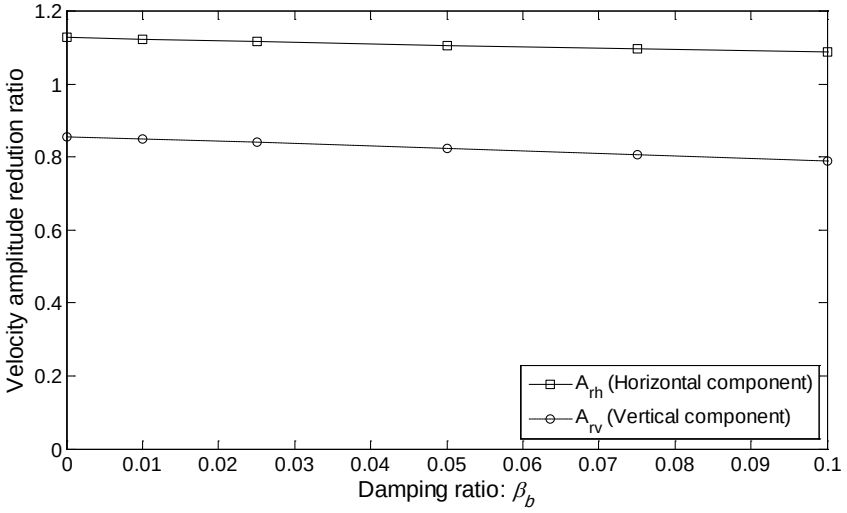

Figure 29. Effect of barrier damping ratio on the vibration isolation effectiveness.

3.4.5 Effect of barrier normalized depth

Figure 30 shows the effect of barrier normalized depth (*d*) on the vibration isolation effectiveness. It is seen that with an increasing *d*, the vertical velocity amplitude reduction ratio A_{rv} gradually decreases until it basically reaches to be stable values. On the other hand, barrier depth seems to have little impact on the horizontal response, the value of A_{rh} changes little with

the variation of *d*. This appears to contradict with the general conclusion made by most researchers that deep barrier has a significant contribution in mitigating ground vibration. However, it should be noted that, as mentioned before, when one parameter is discussed, all the other parameters are kept constant. In this case, the width of barrier is 0.1, while the longest investigated depth is 2.0. This means that it is a rather thin barrier. In fact, if a larger width of barrier is given, e.g. w = 1.0, a different phenomenon can be observed. Figure 31 presents the influence of barrier depth on the vibration isolation effectiveness in the case of the barrier with a width of 1.0. It can be observed that as *d* increases, both of the horizontal and vertical responses firstly amplify, and then attenuate dramatically until A_{rh} and A_{rv} reach to become stable values. Based on the phenomenon observed above, it may be stated that the thin barrier allows a significant part of waves to transmit through it directly, leading to poor isolation effect. But for the wide barrier, it enforces much more waves to travel along its borders and propagate deeply into the soil, causing substantial energy attenuation and dispersion. However, when the barrier exceeds a certain depth, since the deeper part of the barrier hardly contributes to block Rayleigh waves, which carry most of wave energy and decay rapidly as they propagate deeply into the soil, there will be little further improvement in the isolation effect. From the two figures, it can be generally concluded that barriers with a large depth contribute to reduce the ground vibration, but too slender barriers (i.e. barriers with very large depth but very small width) should be avoided. In addition, a limiting depth of barriers exists; a further increase in depth has little improvement in the screening effect.

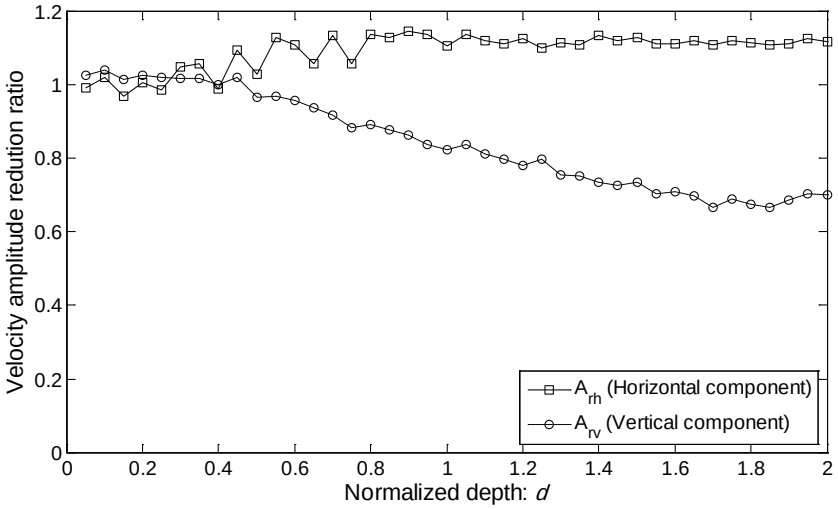

Figure 30. Effect of barrier depth on the vibration isolation effectiveness (w = 0.1).

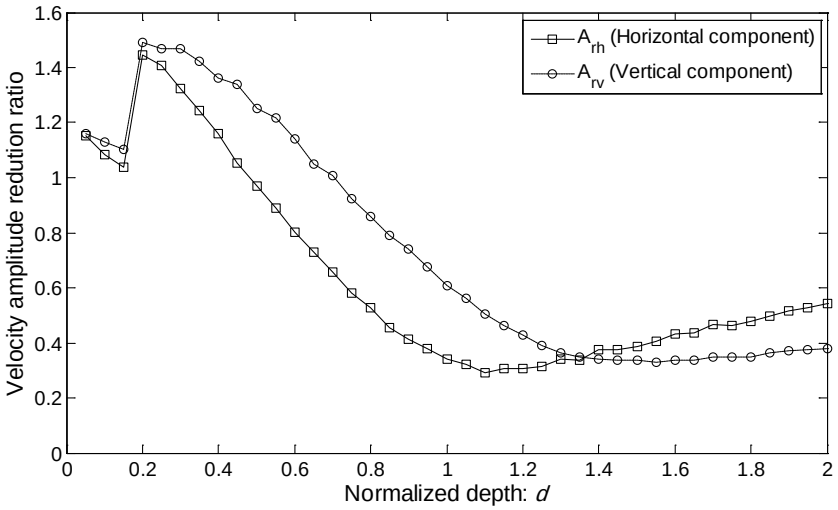

Figure 31. Effect of barrier depth on the vibration isolation effectiveness (w= 1.0).

3.4.6 Effect of barrier normalized width

Figure 32 shows the effect of barrier normalized width (w) on the vibration isolation effectiveness. As it can be seen, with an increasing w, the horizontal and vertical velocity amplitude reduction ratios A_{rh} and A_{rv} firstly decrease and then increase, the major difference between the evolution of the two ratios is that there is a delay of the appearance of minimum value of A_{rv} compared with that of A_{rh}. It is worth mentioning that many researchers concluded that the barrier width has minor or ignorable influence on the vibration isolation effectiveness [15, 17, 18, 61], but many of them made such conclusion based on a narrow range of barrier width during their experimental or numerical investigations. In fact, wave barrier whose width is larger than its depth is a different barrier, which is called wave impeding block (also known as wave impeding barrier). The performance of such type of barrier is not fully investigated to date. From Figure 32, it can be observed that an appropriate increase in width is beneficial. Particularly, when the barrier width becomes slightly larger than its depth (w = 1.1 for A_{rh}, and w = 1.4 for A_{rv}), the isolation effect basically becomes the best. However, a further increase in width turns to become detrimental, the vibration reversely amplified. One possible explanation for this phenomenon is as follows: an increase in width imparts greater rigidity to the barrier, which means that the barrier has higher shear modulus. This strengths its ability to resist the impinging waves and results in more mode conversion [58]. As a result, the isolation effect is improved. However, as the width continuously increases, there are more chances for the occurrence of wave interference between waves that transmitted directly through the barrier and those that propagate under the barrier due to different wave velocity. The complicated wave interference may cause a re-amplification of vibration. Since shear waves that cause the vertical vibration propagate faster than Rayleigh waves which generate the main horizontal vibration (compressional waves also

generate the horizontal vibration, but relatively small), larger barrier width is required for the appearance of minimum vertical vibration than for that of minimum horizontal vibration, this may explain the delay observed as mentioned above.

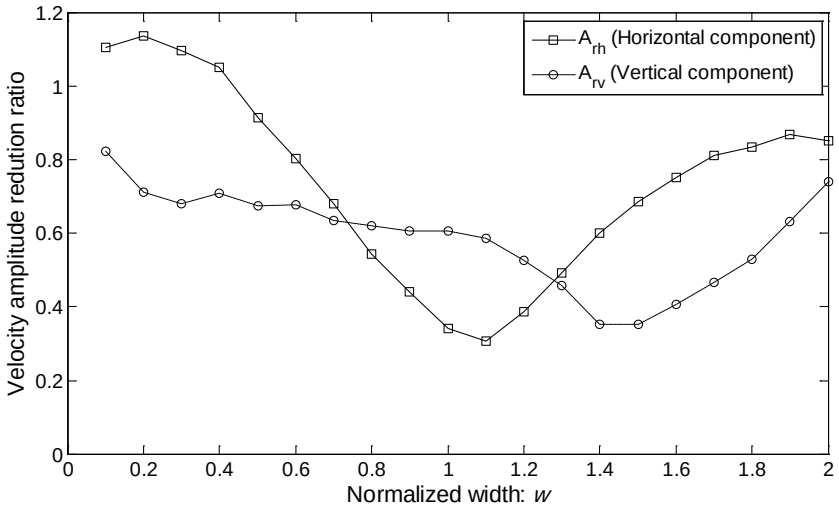

Figure 32. Effect of barrier width on the vibration isolation effectiveness.

3.4.7 Effect of barrier inclination angle

Most of the previous research on wave barrier focused on vertical barriers, which are inserted into the soil media totally vertically. However, in some cases, inclined barriers are feasible in practice. For instant, it is possible to install wave barrier obliquely in soft clay soil. Thus, it is necessary to examine the isolation effect of inclined barrier, which has rarely been investigated. Figure 33 shows the effect of the barrier inclination angle (U) on the vibration isolation effectiveness. As it can be seen, the best isolation effect does not occur when U = 90°, but when U is slightly larger or smaller than 90°, for example, U = 65°, U = 115°. Therefore, if it is practical to build inclined barrier in reality, wave barrier with a slight inclination angle away from the vertical direction is expected to have a better vibration isolation performance than the vertical one.

3.4.8 Effect of normalized distance from the vibratory source to the barrier

Figure 34 shows the effect of the normalized distance (l_1) from the vibratory source to the barrier on the vibration isolation effectiveness. In this study, it is assumed that the distance between the vibratory source and the point "*a*" keeps constant, namely, $l_1 + l_2$ = 50m/5m = 10. So when l_1 increases, l_2 will correspondingly decreases, and vice versa. The purpose of this setting is to investigate the effectiveness of active isolation and passive vibration at the same time and to find out the best barrier location when the vibratory source and the protected site are fixed. From Figure 34, it is seen that there is not monotonic variation for both the horizontal and vertical responses, a series of relative maxima and minima of A_{rh} and A_{rv} appear alternately when l_1 in-

creases. This confirmed with the conclusion made by Segol [61] that the location of wave barriers is not an important parameter for the vibration isolation effectiveness. What also can be seen is that larger velocity reduction is achieved in the vertical direction than in the horizontal direction. In addition, better isolation effect is observed in a rough sense when the barrier is close to the vibratory source or near the protected site (point "*a*").

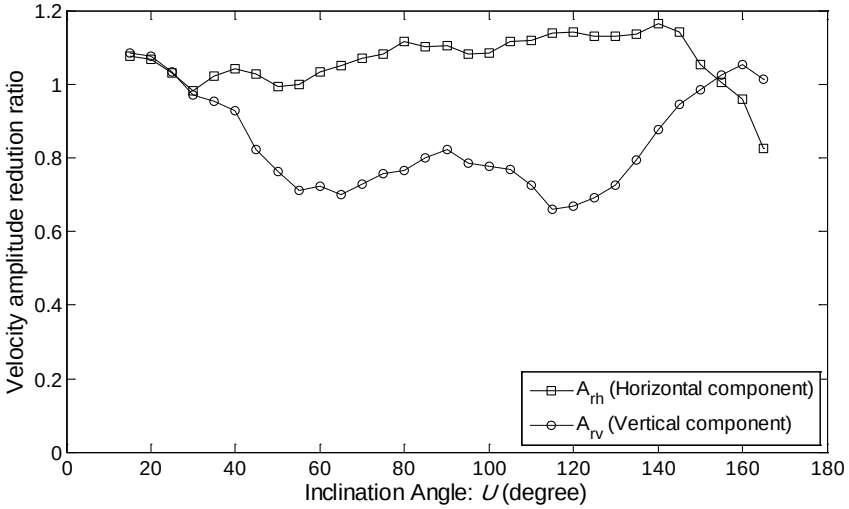

Figure 33. Effect of barrier inclination angle on the vibration isolation effectiveness.

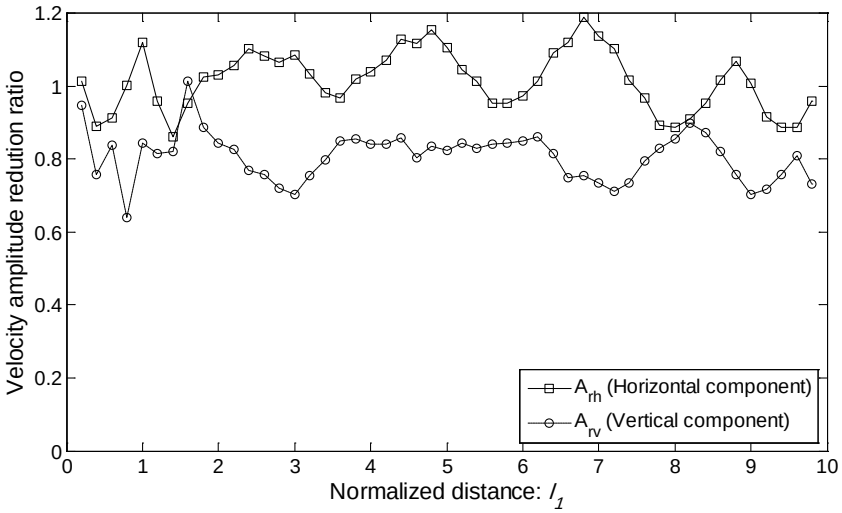

Figure 34. Effect of normalized distance from the vibratory source to the barrier on the vibration isolation effectiveness.

3.4.9 Effect of external load

Figure 35 shows the effect of the amplitude of external load on the vibration isolation effectiveness. Obviously, it is seen that the horizontal and vertical velocity amplitude reduction ratios A_{rh} and A_{rv} remain constant with an increasing load. It appears that the amplitude of load has no influence on the screening effect of barrier. This is reasonable, because both the soil and the

barrier are assumed elastic and the interface between them is considered perfectly bonded. For the influence of exciting frequency, as mentioned before, all the barrier geometric dimensions and distances are normalized by the wavelength of Rayleigh wave, so the results of the parametric study keep independent with the exciting frequency of external load. It should be pointed out, however, that the exciting frequency cannot be too high, otherwise, the element size will be very small, and the amount of the elements in the whole numerical model will become too large to be calculated. Fortunately, for the most common surface vibrations, like the traffic-induced vibrations, their frequencies are generally below 40 Hz [117].

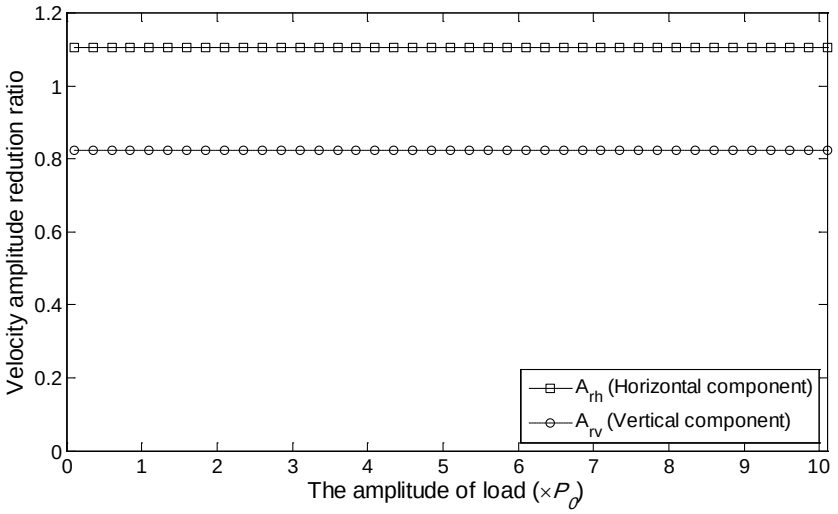

Figure 35. Effect of external load on the vibration isolation effectiveness.

3.5 Optimization design

3.5.1 General study

Based on the parametric study performed in the Section 3.4, it is clear to see the effect of each single parameter on the vibration isolation effectiveness of barrier. However, it is still unclear what will happen if mutual influences exist, for example, Figure 30 shows that the depth of thin barrier (w = 0.1) has little impact on the horizontal velocity reduction, but for the wide barrier (w = 1.0), as shown in Figure 31, large depth has a great contribution in improving horizontal isolation effect. Therefore, it is imperative to investigate the mutual influences of all the parameters so as to find out the optimal combination of parameters, in other words, to commit the optimization design for wave barrier.

Before committing the optimization design, one programming language called Python has to be introduced. Python script is a very powerful tool, it can easily accomplish tasks in ABAQUS like automating repetitive jobs, performing parametric study, accessing and extracting data from output databases, and even creating user interfaces according to the customer own habit. Actual-

ly, the parametric study above including creating models, changing values of investigated parameters and extracting the amplitude of velocity from output databases, all is done by writing and running Python scripts in ABAQUS. Compared with manual operation in the GUI mode (ABAQUS/CAE), Python script is fast, labor-saving and highly efficient.

Concerning the optimization design for wave barrier, there are 9 investigated parameters during the parametric study, if all the parameters are included, suppose each parameter has 8 levels, based on traditional optimum method, the total number of combination to be calculated will be $(8)^9$ = 134217728. By using the current facility we have (ABAQUS version 11, Intel Core i5, Inner memory 12 G), although Python script is efficient, each calculation takes only about 19.4 s, due to the so large combination number, it is estimated that (134217728×19.4)/(24×60×60×365) = 82.5 years are required to finish the calculations of optimization combination of parameters. Undoubtedly, this is unacceptable.

Therefore, proper simplifications have to be made to reduce the calculation time. The developed method is suggested as follows:

1. Identify parameters that have major influences on the vibration isolation effectiveness of barriers, select key parameters and ignore trivial ones. According to the results from parametric study, it is clear to see that the barrier Poisson's ratio, damping ratio and the amplitude of external load have little or no contribution to the soil vibration reduction. So these three parameters can be excluded during optimization design, causing the number of combination from $(8)^9$ = 134217728 to $(8)^6$ = 262144, that is a huge decrease.
2. Choose typical values of key parameters to reduce levels of parameters. Since the purpose of optimization design is to minimize the soil vibration in protected site, only values of parameters that can dramatically reduce the soil motion are expected to be chosen. In this case, based on the 2D model presented in Figure 19 and the evolution of velocity observed during the parametric study, the typical values of key parameters are selected, which are shown in Table 4. Thus, the estimated number of combination is further reduced to 5×4×4×4×6×6 = 11520.
3. Write a Python script and run it in ABAQUS. In this study, it takes about 20.03 hours to finish the whole calculations. This time period is generally acceptable. Tables 5 and 6 show the final calculating results for horizontal and vertical velocity amplitude reduction ratios at point "*a*", respectively. Due to space constraint, only the best and the worst vibration isolation effect are presented.

Table 4. The distribution of key parameters to be optimized for wave barriers.

Parameters	Typical values
Barrier Young's modulus (E_b)	$0.03E_s$, $0.06E_s$, $0.10E_s$, $0.20E_s$, $0.50E_s$*
Barrier density (ρ_b)	$1\rho_s$, $2\rho_s$, $3\rho_s$, $4\rho_s$*
Barrier normalized depth (d)	1.0, 1.3, 1.6, 1.9
Barrier normalized width (w)	0.8, 1.0, 1.2, 1.4
Normalized distance (l_1)	0.6, 0.8, 1.0, 9.4, 9.6, 9.8
Inclination angle (U)	55°, 65°, 75°, 105°, 115°, 125°

* E_s and ρ_s respectively represent the Young's modulus and density of soil shown in Table 3.

From Tables 5 and 6, it can be seen that different combination of parameters results in very different vibration isolation effectiveness. If the values of parameters are specified according to the Sequence 1 in these two tables, the minimum A_{rh} and A_{rv} can be achieved, which are 0.06551 and 0.04002, respectively. This is a huge vibration reduction. It should be mentioned, however, that due to variety of constraints, like it is too expensive to build deep barriers, or it is difficult to insert inclined barriers in hard soil media, some values of parameters are unavailable in practice, but the suggested method can still be used to optimize the barrier design, considering all the limitations in reality. For example, if the barrier with a depth of 1.9 is too long, reduce its depth as 1.6, it is seen from Table 5 that the horizontal velocity reduction ratio is 0.09218. It is still a good vibration isolation result; or if the barrier has to be inserted vertically, just specify the value of inclination angle as 90° in Python script.

3.5.2 A case study

In the Section above, the optimization design is based on the best combination of parameters in order to minimize the soil vibration, for example, the Young's modulus of barrier in Table 4 is assumed to be very small, while the density is very large. It is noted that materials with small Young's modulus and large density are likely to be unavailable in practice. Common wave barriers like concrete walls, sheet pile walls, EPS barriers, gas-filled cushions do not have the properties provided by Table 4. Therefore, in a practical view, it is better to commit optimization design for wave barrier made of real material. Since EPS geofoam, which is a lightweight yet strong plastic material, is widely used in constructions, especially in ground fill applications, in this study, we choose EPS barrier as an example for the optimization design.

According to the American Society for Testing and Materials (ASTM D6817), there are seven types of EPS geofoam, they are EPS12, EPS15, EPS19, EPS22, EPS29, EPS39, EPS46. Its material properties are presented in Table 7 [118]. For the Poisson's ratio ν of EPS geofoam, the empirical equation proposed by Horvath [119] is adopted:

$$\nu = 0.0056\rho + 0.0024 \tag{22}$$

where ρ is the material density (kg/m^3).

Table 5. Final results of horizontal response at point "*a*" for parameter optimization of wave barrier.

Sequence	E_b/E_s	ρ_b/ρ_s	d	w	l_1	U	A_{rh}
1	0.03	4	1.9	0.8	9.4	105°	0.06551
2	0.03	4	1.9	0.8	9.4	75°	0.07407
3	0.03	3	1.9	0.8	9.4	75°	0.07639
4	0.03	4	1.9	1.0	1.0	75°	0.07909
5	0.06	4	1.9	0.8	9.4	75°	0.08049
6	0.06	4	1.9	1.0	1.0	75°	0.08115
7	0.03	4	1.9	0.8	9.4	65°	0.08173
8	0.03	2	1.9	1.0	9.4	105°	0.08553
9	0.03	3	1.9	1.0	1.0	75°	0.08771
10	0.06	4	1.9	0.8	9.4	65°	0.08919
11	0.10	4	1.9	1.0	1.0	75°	0.09000
12	0.03	2	1.9	1.0	9.4	125°	0.09192
13	0.06	4	1.9	0.8	9.4	105°	0.09212
14	0.03	4	1.6	0.8	9.4	75°	0.09218
15	0.03	4	1.9	1	9.4	105°	0.09314
16	0.03	3	1.9	0.8	9.4	105°	0.09319
17	0.03	2	1.9	1.0	9.4	115°	0.09749
18	0.06	3	1.9	0.8	9.4	75°	0.09966
19	0.03	2	1.9	1.0	1.0	75°	0.10219
20	0.10	4	1.9	0.8	9.4	65°	0.10436
21	0.03	2	1.3	0.8	9.4	125°	0.10622
22	0.03	2	1.9	0.8	9.4	75°	0.10634
...	...	...	...	...	...	...	...
3700	0.50	2	1.6	0.8	0.6	125°	1.63611
3701	0.2	1	1.3	0.8	0.8	105°	1.63669
3702	0.50	2	1.3	1.0	0.6	115°	1.63814
3703	0.50	2	1.3	1.0	0.6	125°	1.63930
3704	0.20	1	1.0	0.8	0.8	115°	1.64046
3705	0.20	1	1.0	0.8	1.0	75°	1.64597
3706	0.50	2	1.3	1.4	0.8	105°	1.64771
3707	0.50	2	1.3	0.8	0.8	125°	1.65583
3708	0.50	2	1.3	1.2	0.8	105°	1.66599
3709	0.50	2	1.3	1.0	0.8	105°	1.67411
3710	0.50	2	1.0	1.0	0.6	105°	1.70458
3711	0.20	1	1.3	0.8	0.6	125°	1.71212
3712	0.50	2	1.0	1.0	0.6	115°	1.72141
3713	0.50	2	1.3	1.0	0.6	105°	1.72228
3714	0.50	2	1.0	0.8	0.6	125°	1.75912
3715	0.50	2	1.0	0.8	0.8	105°	1.79394
3716	0.50	2	1.0	0.8	0.6	105°	1.79684
3717	0.50	2	1.0	0.8	0.8	115°	1.80729
3718	0.20	1	1.0	0.8	0.8	105°	1.83079
3719	0.50	2	1.0	0.8	0.6	115°	1.85545
3720	0.50	2	1.3	0.8	0.6	125°	1.87199

Table 6. Final results of vertical response at point "*a*" for parameter optimization of wave barrier.

Sequence	E_b/E_s	ρ_b/ρ_s	d	w	l_1	U	A_{rv}
1	0.10	4	1.9	1.0	1.0	75°	0.04002
2	0.03	2	1.9	1.0	1.0	75°	0.04056
3	0.03	4	1.9	1.0	1.0	105°	0.04204
4	0.03	3	1.9	1.0	1.0	75°	0.04349
5	0.03	4	1.9	1.2	1.0	105°	0.04490
6	0.06	4	1.9	1.0	1.0	75°	0.04497
7	0.06	4	1.9	0.8	1.0	105°	0.04576
8	0.03	4	1.9	0.8	1.0	105°	0.04759
9	0.03	4	1.9	1.0	1.0	75°	0.04970
10	0.06	3	1.9	1.0	1.0	75°	0.04984
11	0.03	4	1.9	1.0	9.4	105°	0.04997
12	0.06	4	1.9	1.0	1.0	105°	0.05100
13	0.03	3	1.9	0.8	1.0	105°	0.05146
14	0.03	1	1.9	1.0	1.0	75°	0.05279
15	0.03	4	1.9	0.8	0.8	105°	0.05306
16	0.03	4	1.9	1.0	1.0	115°	0.05507
17	0.10	4	1.9	1.0	9.4	105°	0.05873
18	0.10	4	1.3	1.2	1.0	75°	0.05913
19	0.06	4	1.9	1.0	9.4	105°	0.05913
20	0.03	4	1.9	1.2	1.0	115°	0.05954
21	0.03	3	1.9	1.0	1.0	105°	0.06188
22	0.03	4	1.9	0.8	1.0	115°	0.06188
...	...	...	...	...	...	...	...
3700	0.50	1	1.0	1.0	0.8	115°	1.34021
3701	0.50	1	1.6	1.0	0.8	125°	1.34283
3702	0.50	1	1.6	1.0	1.0	125°	1.34467
3703	0.50	1	1.0	1.0	9.4	65°	1.34493
3704	0.50	1	1.0	1.0	9.4	75°	1.34807
3705	0.50	1	1.6	1.4	1.0	125°	1.34912
3706	0.50	1	1.6	1.2	0.8	125°	1.35043
3707	0.50	1	1.3	1.0	9.4	125°	1.35279
3708	0.50	1	1.0	1.0	9.4	105°	1.35331
3709	0.50	1	1.0	1.0	0.6	125°	1.36012
3710	0.50	1	1.3	1.2	0.8	125°	1.37270
3711	0.50	1	1.3	1.0	0.8	125°	1.38239
3712	0.50	1	1.3	1.2	1.0	115°	1.38553
3713	0.50	1	1.9	1.0	9.4	105°	1.39104
3714	0.50	1	1.3	1.2	1.0	125°	1.39575
3715	0.50	1	1.6	1.0	9.4	125°	1.41723
3716	0.50	1	1.6	1.2	1.0	125°	1.41880
3717	0.50	1	1.9	1.0	9.4	125°	1.42561
3718	0.50	1	1.9	1.0	9.4	115°	1.42745
3719	0.50	1	1.0	1.0	9.4	115°	1.42771
3720	0.50	1	1.0	1.0	9.4	125°	1.52595

Similarly, a Python script is written for the optimization design for EPS barrier. Since each type of EPS has intrinsic material property, there is no discussion about the combination of different material parameters. Other values of normalized parameters are listed in Table 8. It should be mentioned that the inclination angle $U = 90°$ is included, for considering that vertical barriers are very common in practice. In addition, due to the fact that the barrier width is generally smaller than its depth in reality, the values of w are given to be relatively small. Tables 9 and 10 respectively show the final results for horizontal and vertical velocity amplitude reduction ratios at point "*a*" due to the installation of EPS barriers. Only the best and the worst isolation effect are shown. It is clear to see that EPS barrier with different types, dimensions and positions have quite different vibration isolation performance. Deep barriers which are close to the protected site and have an inclination angle slightly larger than 90° are more likely to produce good isolation effect, especially for the horizontal vibration isolation. These two tables can provide a reference for civil engineers to design EPS barrier in practice.

Table 7. Foam-Control EPS Geofoam Properties.

Properties		ASTM D6817						
		EPS12	EPS15	EPS19	EPS22	EPS29	EPS39	EPS46
Density. min.	lb/ft^3	0.70	0.90	1.15	1.35	1.80	2.40	2.85
	(kg/m^3)	11.2	14.4	18.4	21.6	28.8	38.4	45.7
Compressive resistance @ 1% deformation.min.	psi	2.2	3.6	5.8	7.3	10.9	15	18.6
	psf	320	520	840	1050	1570	2160	2680
	(kPa)	15	25	40	50	75	103	128
Elastic modulus. min.	psi	220	360	580	730	1090	1500	1860
	(kPa)	1500	2500	4000	5000	7500	10300	12800
Flexural strength .min.	psi	10	25	30	40	50	60	75
	(kPa)	69	172	207	276	345	414	517
Water absorption by total immersion.max.	volume%	4.0	4.0	3.0	3.0	2.0	2.0	2.0
Oxygen index. min.	volume%	24	24	24	24	24	24	24
Buoyancy force.	lb/ft^3	61.7	61.5	61.3	61.1	60.6	60	59.5
	(kg/m^3)	990	980	980	980	970	960	950

Table 8. The distribution of key parameters to be optimized for EPS barriers.

Parameters	Typical values
Barrier normalized depth (d)	1.0, 1.3, 1.6, 1.9
Barrier normalized width (w)	0.1, 0.2, 0.3, 0.4
Normalized distance (l_1)	0.6, 0.8, 1.0, 9.4, 9.6, 9.8
Inclination angle (U)	55°, 65°, 75°, 90°, 105°, 115°, 125°
Types of EPS geofoam	EPS12, EPS15, EPS19, EPS22, EPS29, EPS39, EPS46

Table 9. Final results of horizontal response at point "*a*" for parameter optimization of EPS barrier.

Sequence	Types of EPS	d	w	l_1	U	A_{rh}
1	EPS12	1.9	0.4	9.4	105°	0.03043
2	EPS12	1.6	0.2	9.4	125°	0.03058
3	EPS15	1.9	0.3	9.4	105°	0.03442
4	EPS15	1.9	0.4	9.4	105°	0.03476
5	EPS12	1.9	0.3	9.4	105°	0.03624
6	EPS12	1.3	0.2	9.6	115°	0.03999
7	EPS15	1.3	0.2	9.6	115°	0.04233
8	EPS19	1.9	0.3	9.4	105°	0.04280
9	EPS15	1.3	0.3	9.6	115°	0.04367
10	EPS12	1.3	0.3	9.6	115°	0.04377
11	EPS15	1.9	0.3	9.4	90°	0.04379
12	EPS19	1.9	0.4	9.4	105°	0.04454
13	EPS19	1.9	0.3	9.4	90°	0.04459
14	EPS22	1.9	0.3	9.4	90°	0.04550
15	EPS15	1.6	0.2	9.4	125°	0.04607
16	EPS12	1.9	0.4	9.4	90°	0.04813
17	EPS19	1.3	0.3	9.6	115°	0.04813
18	EPS12	1.9	0.3	9.4	90°	0.04822
19	EPS19	1.9	0.4	9.4	115°	0.04927
20	EPS15	1.9	0.4	9.4	90°	0.04989
21	EPS15	1.9	0.4	9.4	115°	0.05056
22	EPS22	1.9	0.3	9.4	105°	0.05065
…	…	…	…	…	…	…
4096	EPS39	1.0	0.2	0.6	90°	1.29220
4097	EPS19	1.0	0.2	0.8	75°	1.29750
4098	EPS22	1.0	0.2	0.8	75°	1.30150
4099	EPS19	1.0	0.1	0.6	90°	1.30940
4100	EPS29	1.0	0.2	0.8	75°	1.31110
4101	EPS12	1.0	0.3	0.8	75°	1.31140
4102	EPS15	1.0	0.3	0.8	75°	1.31260
4103	EPS19	1.0	0.3	0.8	75°	1.31430
4104	EPS39	1.0	0.1	0.8	75°	1.31460
4105	EPS22	1.0	0.3	0.8	75°	1.31920
4106	EPS39	1.0	0.2	0.8	75°	1.32070
4107	EPS46	1.0	0.2	0.8	75°	1.32500
4108	EPS46	1.0	0.2	0.6	90°	1.32650
4109	EPS46	1.0	0.1	0.8	75°	1.32850
4110	EPS29	1.0	0.3	0.8	75°	1.33050
4111	EPS22	1.0	0.1	0.6	90°	1.33690
4112	EPS39	1.0	0.3	0.8	75°	1.34100
4113	EPS46	1.0	0.3	0.8	75°	1.34590
4114	EPS29	1.0	0.1	0.6	90°	1.40080
4115	EPS39	1.0	0.1	0.6	90°	1.46280
4116	EPS46	1.0	0.1	0.6	90°	1.50380

Table 10. Final results of vertical response at point "*a*" for parameter optimization of EPS barrier.

Sequence	Types of EPS	d	w	l_1	U	A_{rv}
1	EPS12	1.9	0.3	1.0	65°	0.02978
2	EPS15	1.9	0.3	1.0	65°	0.03457
3	EPS12	1.9	0.2	0.8	105°	0.03906
4	EPS12	1.9	0.4	1.0	105°	0.04296
5	EPS15	1.9	0.2	0.8	105°	0.04398
6	EPS19	1.9	0.3	1.0	65°	0.04426
7	EPS15	1.9	0.4	1.0	105°	0.04470
8	EPS12	1.9	0.4	9.6	105°	0.04504
9	EPS19	1.9	0.4	1.0	105°	0.04747
10	EPS15	1.9	0.4	9.6	105°	0.04754
11	EPS12	1.9	0.3	0.8	105°	0.04797
12	EPS22	1.9	0.4	1.0	105°	0.04976
13	EPS12	1.9	0.2	9.6	125°	0.04991
14	EPS19	1.9	0.4	9.6	105°	0.05150
15	EPS22	1.9	0.3	1.0	65°	0.05156
16	EPS15	1.9	0.3	0.8	105°	0.05180
17	EPS12	1.9	0.1	0.8	105°	0.05212
18	EPS19	1.9	0.2	0.8	105°	0.05258
19	EPS12	1.9	0.3	9.6	115°	0.05262
20	EPS15	1.9	0.2	9.6	125°	0.05356
21	EPS12	1.9	0.3	1.0	105°	0.05387
22	EPS12	1.9	0.3	9.6	125°	0.05397
…	…	…	…	…	…	…
4096	EPS12	1.0	0.4	0.6	125°	0.54515
4097	EPS15	1.0	0.3	9.8	115°	0.54670
4098	EPS19	1.0	0.4	9.4	55°	0.54725
4099	EPS39	1.0	0.2	0.8	75°	0.55034
4100	EPS46	1.0	0.2	0.8	75°	0.55442
4101	EPS19	1.0	0.3	9.8	115°	0.55825
4102	EPS22	1.0	0.3	9.8	115°	0.56532
4103	EPS15	1.0	0.4	9.4	55°	0.56977
4104	EPS39	1.0	0.2	9.8	125°	0.57004
4105	EPS46	1.0	0.3	9.8	115°	0.57135
4106	EPS29	1.0	0.3	9.8	115°	0.57868
4107	EPS39	1.0	0.3	9.8	115°	0.58130
4108	EPS12	1.0	0.4	9.4	55°	0.58392
4109	EPS46	1.0	0.2	9.8	125°	0.58811
4110	EPS12	1.0	0.3	9.8	125°	0.72905
4111	EPS15	1.0	0.3	9.8	125°	0.74843
4112	EPS19	1.0	0.3	9.8	125°	0.76992
4113	EPS22	1.0	0.3	9.8	125°	0.78092
4114	EPS46	1.0	0.3	9.8	125°	0.79690
4115	EPS29	1.0	0.3	9.8	125°	0.80083
4116	EPS39	1.0	0.3	9.8	125°	0.80816

3.6 Conclusions

A 2D numerical model is established in ABAQUS to investigate the performance of wave barrier in isolating ground motion generated by surface harmonic loads. The vibration isolation effectiveness is evaluated and analyzed through an intensive parametric study. The comparative study of 2D and 3D analyses shows that 2D model is sufficient to produce accurate results. By using Python programming language, an optimization design method for wave barrier is developed, and an example of optimization design for barrier made of EPS is finally presented. Based on the obtained results, the following understandings and conclusions are made:

- The installation of wave barrier is effective in reducing ground vibration generated by surface harmonic loads. Significant vibration reduction can be achieved if wave barriers with proper parameters are installed, as Tables 5, 6, 9 and 10 show.
- Decreasing the barrier Young's modulus or increasing the barrier density results in an increase in vibration reduction, but decreasing Young's modulus is more effective. On the other hand, the barrier Poisson's ratio and damping ratio have ignorable influence on the vibration isolation effectiveness.
- Large depth of barrier contributes to reduce soil motion, but a limiting value exists, beyond which an increase of barrier depth produces little further vibration reduction. Increasing barrier width is also helpful, wave barrier whose width is slightly larger than its depth performs better than those with other widths. In addition, it is noted that too slender barrier (i.e. barrier with very large depth but very small width) should be avoided in practice due to its poor isolation performance.
- Barriers with a small inclination angle away from vertical direction have a better screening effect than vertical ones. If it is feasible to install inclined barriers, slightly oblique barriers are encouraged. Besides, the location of barriers generally does not have remarkable influence on the vibration isolation effectiveness. But basically, barriers perform better when they are installed near the vibratory source or close to the protected site than in the intermediate areas.
- The developed method of the combination of Python scripts and ABAQUS can be used for the optimization design for wave barrier in practice. Once all the possible parameters are given, barriers ranging from performing the best to being the worst can be identified. With the suggested method, plus the experiences of engineers and the limitations in reality, the best choice of barriers is expected to become available.

4. Investigation on the isolation performance of wave barriers Ⅱ: under explosions

4.1 Numerical model

Figure 36 shows a 2D plane-strain model constructed in ABAQUS. It has a length of 216 m and a height of 100 m. A rectangle barrier is installed in the rock media; its depth *D*, width *W* and inclination angle *U* are given as 10 m, 1.0 m and 90°, respectively. The explosive charge is placed near the barrier, as shown in Figure 36. The horizontal distance L_1 between the explosive and the barrier is 6 m, and L_2, which denotes the distance from the barrier to the protected point "*a*", is specified as 10 m. The model is fixed at the bottom, roller boundaries are applied to its sides and free boundary on the top surface. The material properties are listed in Table 11. It is noted that Rayleigh damping is adopted in ABAQUS.

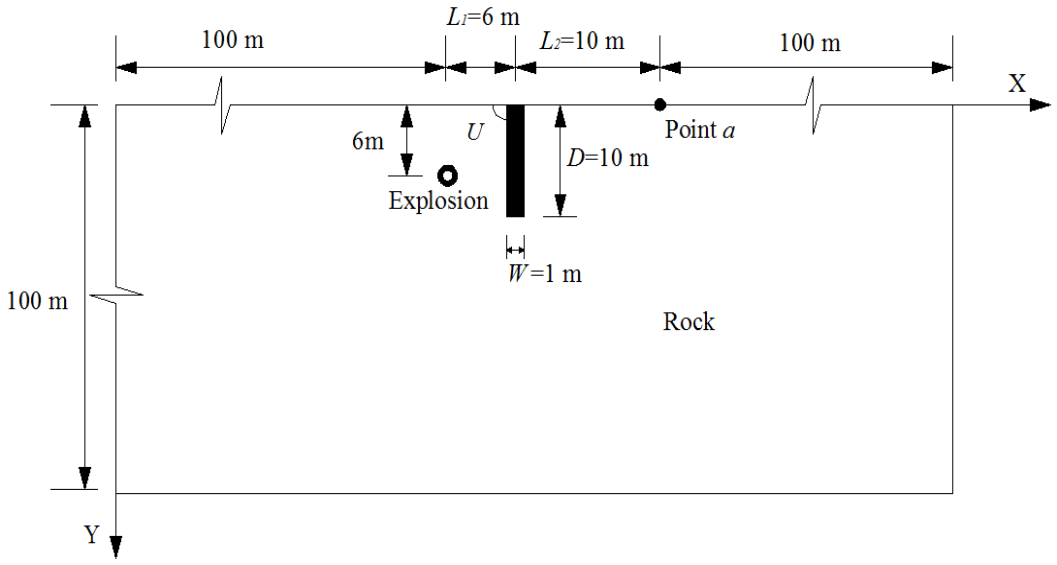

Figure 36. Schematic diagram of the 2D model of rock-barrier system under explosions.

Table 11. Material properties of rock and barrier.

Material	Density (kg/m^3)	Poisson's ratio	Young's modulus (GPa)	Damping ratio
Rock	2500	0.15	15	5%
Barrier	45.7	0.258	0.0128	5%

Table 12. The characteristics of EMULSTAR 8000UG.

ρ_0 (kg/m^3)	MVD (m/s)	CDP(GPa)	d_c (mm)	d_h (mm)
1.25	5300	8.78	35	45

ρ_0 = measured average density; MVD = measured velocity of detonation; CDP = calculated detonation pressure; d_c = diameter of explosive; d_h = diameter of blasthole.

The explosive charge used in this study is EMULSTAR 8000UG. It is an emulsion explosive cartridge. Some of its characteristics are shown in Table 12. In order to apply the blast pressure in the numerical model, the time history of pressure has to be obtained. Exponential functions are often used to describe the explosive pressure as a function of time [120-122]. Here, the evolution of pressure P in time which was given by Park [122] is adopted:

$$P = P_d \left(\frac{d_c}{d_h}\right)^3 \left(\frac{t}{t_r}\right) e^{\left(t-\frac{t}{t_r}\right)} \tag{23}$$

where P_d is the calculated detonation pressure, d_c and d_h are the diameters of the explosive and the blasthole, respectively. And t_r is the time to reach peak pressure (=0.0003361s). Combined with Table 12, the time history of pressure can be obtained, which is shown in Figure 37. It should be pointed out, however, that the diameter of the blasthole, which is 45 mm, is too small compared with the model size, causing meshing problem in the finite element model. To solve this problem, equivalent pressure $P_{equivalent}$ is adopted on the assumption that the equivalent pressure is inversely proportional to the square of the blasthole diameter. Thus,

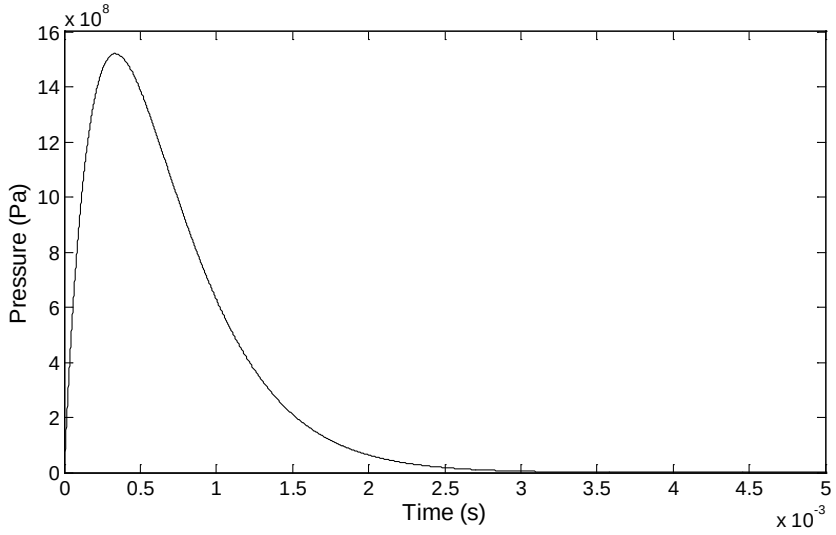

Figure 37. The time history of blast pressure.

$$P_{equivalent} d_{equivalent}^2 = P d_h^2 \tag{24}$$

where $d_{equivalent}$ is the equivalent diameter of the blasthole. In this study, $d_{equivalent}$ is specified as 0.5 m, large enough for meshing the model. Therefore, $P_{equivalent}$ can be obtained

$$P_{equivalent} = P \frac{d_h^2}{d_{equivalent}^2} = P\left(\frac{45}{500}\right)^2 = 0.0081P \tag{25}$$

To perform the numerical simulation effectively, explicit dynamic analysis procedure is adopted in ABAQUS. The rock and the barrier are modeled as homogeneous, isotropic and elastic media, using 4-node bilinear plane strain quadrilateral, reduced integration elements. The interface between the rock and the barrier is assumed perfectly bonded. Since the model has a finite domain, quiet boundary conditions are often used to absorb the outward propagating

waves. However, as the duration of blast is very short and the initial response of structures is a major concern [66], fictitious boundaries can be set at a sufficient distance away, resulting in no reflected waves within the duration of interest or the amount of reflected waves is so small that it can be ignored. In the present study, the finite element model is large enough to avoid the influence of wave reflection.

Before investigation of vibration isolation effectiveness of wave barrier, the ability that numerical model in ABAQUS can produce accurate results has to be verified. As mentioned before, the velocity of compressional waves (P waves) v_P can be computed as:

$$v_P = \sqrt{\frac{E(1-\nu)}{\rho(1+\nu)(1-2\nu)}} \tag{26}$$

where E, ρ and ν are the Young's modulus, density and Poisson's ratio of media, respectively. It is noted that this equation can only be used in homogeneous isotropic and elastic media without damping. Figure 38 shows the velocity of point "*a*" over time with the assumption that wave barrier is replaced by rock in Figure 36 and the rock media has no damping. It is observed that point "*a*" begins to vibrate at about 0.0063 s, while according to the Equation (26), the calculated velocity of P waves in the rock media is:

$$v_P = \sqrt{\frac{E(1-\nu)}{\rho(1+\nu)(1-2\nu)}} = \sqrt{\frac{1.5(10)^{10}(1-0.15)}{2500(1+0.15)(1-0.3)}} = 2517\ m/s \tag{27}$$

Therefore, the first arrival time of P waves at point "*a*" is:

$$t = \frac{L}{v_P} = \frac{\sqrt{6^2+16^2}}{2517} = 0.0068\ s \tag{28}$$

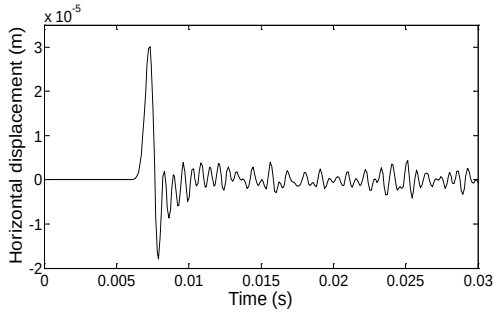

(a) Horizontal displacement

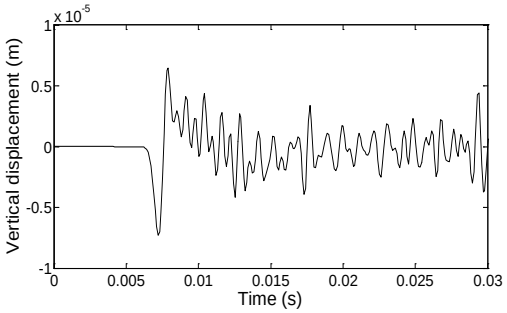

(b) Vertical displacement

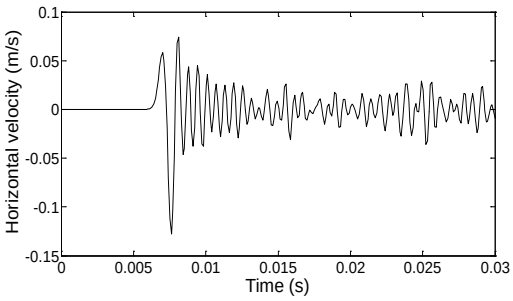

(c) Horizontal velocity

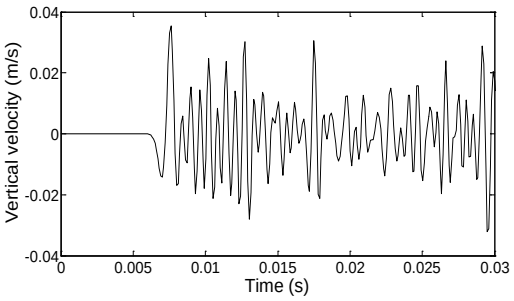

(d) Vertical velocity

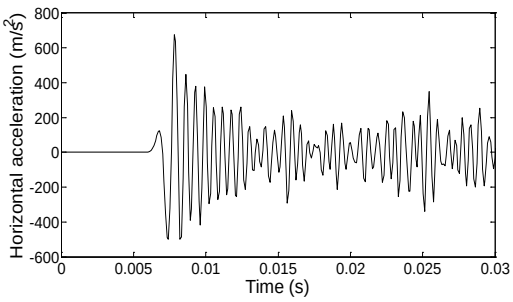

(e) Horizontal acceleration

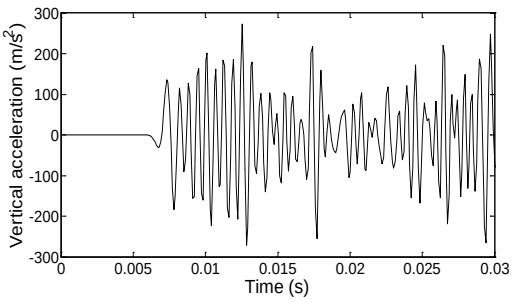

(f) Vertical acceleration

Figure 38. The motion of point "*a*" in homogeneous isotropic and elastic rock media with no damping.

where L is the distance from the explosive to the point "*a*". It is found that the numerical results have a good agreement with the theoretical solution. Figure 39 shows the dynamic scenarios of blasting vibration propagation in rock within 0.0303 s. It can be clearly seen that wave propagation is blocked by the barrier, and waves are forced to propagate under the barrier (see Figure 39(b)-(e)), as a result, the velocity amplitudes behind the barrier are smaller than the ones before the barrier, as Figure 39(f)-(h) show. Therefore, it is inferred that the installation of wave barrier is able to reduce the ground vibration effectively.

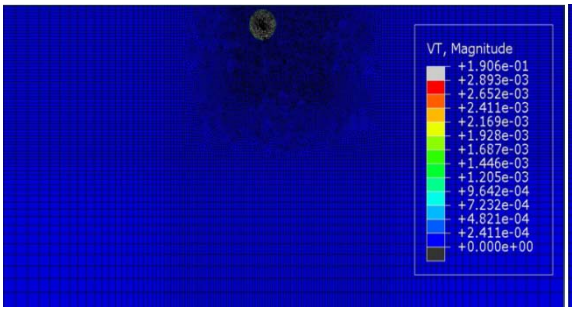

(a) Time = 1.17 ms

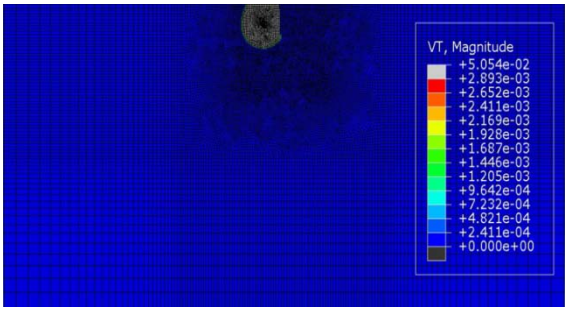

(b) Time = 2.35 ms

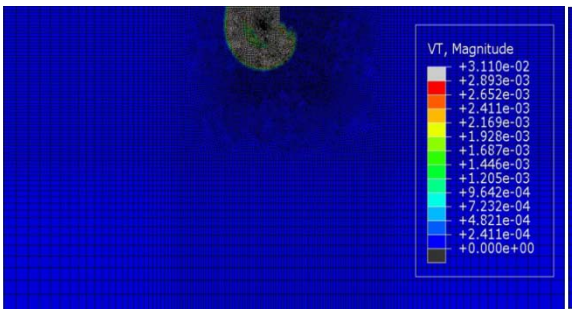

(c) Time = 4.68 ms

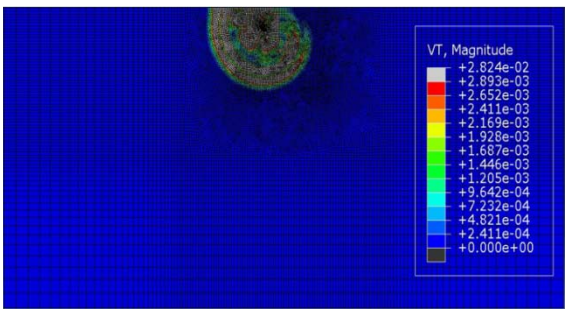

(d) Time = 7.01 ms

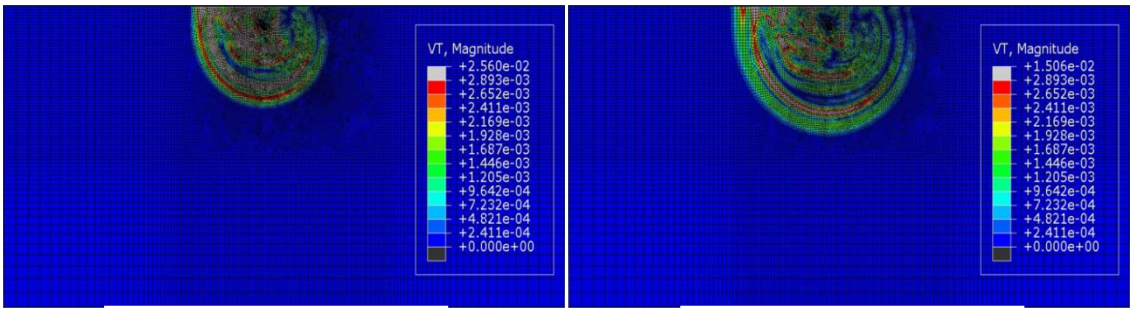

(e) Time = 9.34 ms (f) Time = 12.8 ms

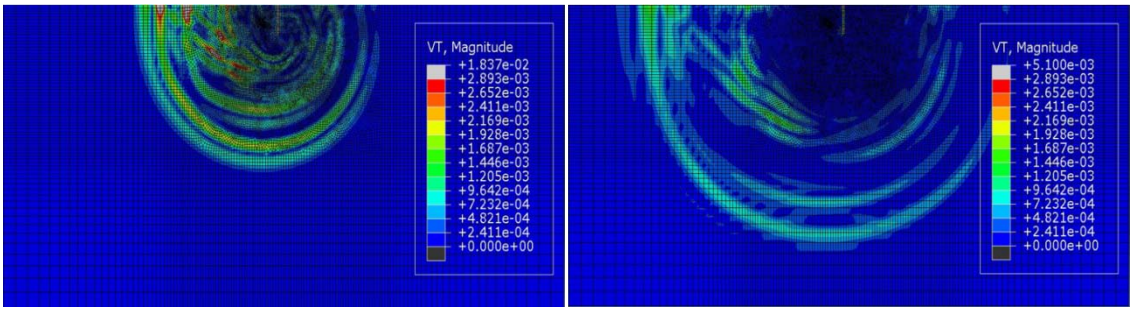

(g) Time = 17.5 ms (h) Time = 30.3 ms

Figure 39. Velocity amplitude nephogram at different times in rock with wave barrier.

To evaluate the performance of wave barrier quantitatively, the velocity amplitude reduction ratio A_r at point "*a*" (shown in Figure 36) is used to assess the vibration isolation effectiveness of wave barrier:

$$A_r = \frac{A_B}{A_R} \tag{29}$$

where A_B and A_R are the velocity amplitude at point "*a*" with and without wave barrier, respectively. Since the velocity has vertical and horizontal components, A_{rv} and A_{rh} are respectively used to represent vertical and horizontal velocity amplitude reduction ratios. These two ratios give a quantitative evaluation of vibration isolation effectiveness, for example, A_{rv} = 0.6, A_{rh} = 0.7, it means that 40% reduction in the vertical amplitude and 30% reduction in the horizontal amplitude at point "*a*" are achieved due to the installation of wave barrier.

4.2 Parametric study

In this section, an extensive parametric study, including the material properties of barrier, the barrier dimensions, its positions, its damping ratio, the burial depth of the explosive and the blast pressure, has been conducted to examine their influence on the vibration isolation effectiveness of barrier. All the investigations are based on Figure 36. Note that when the effect of one parameter is investigated, all the other parameters are kept constant. The following results and analyses are presented.

4.2.1 Effect of barrier Young's modulus

Figure 40 shows the effect of the ratio of Young's modulus (E_B/E_R) on the vibration isolation effectiveness, where E_B and E_R are the Young's modulus of barrier and rock, respectively, and E_B/E_R is varied from 10^{-4} to 5. It can be seen that when the barrier Young's modulus is small ($E_B/E_R < 0.1$), both the horizontal and vertical velocity are reduced significantly. As the barrier becomes stiffer ($E_B/E_R > 0.1$), the velocity increases rapidly. It is worth mentioning that when $E_B/E_R = 1$, which means that the barrier and the rock have the same Young's modulus, there is little velocity amplitude reduction, while in this case, the density and the Poisson's ratio of barrier are very different with the ones of the rock. Therefore, it is inferred that Young's modulus should be a more important parameter in affecting the barrier's vibration isolation effectiveness than the density and the Poisson's ratio. The following discussion on the effect of density and Poisson's ratio will confirm it.

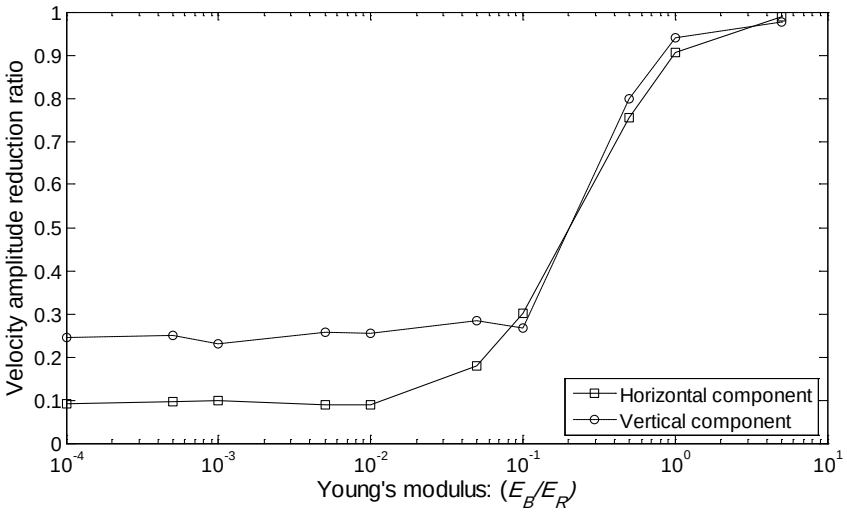

Figure 40. Effect of barrier Young's modulus on the vibration isolation effectiveness.

4.2.2 Effect of barrier density, Poisson's ratio and damping ratio

Figures 41-43 show the effect of barrier density, Poisson's ratio and damping ratio on the vibration isolation effectiveness, respectively, where ρ_B and ρ_R respectively denote the density of barrier and rock. From the three figures, it can be seen that the influences of all these parameters are so little that they can be ignored.

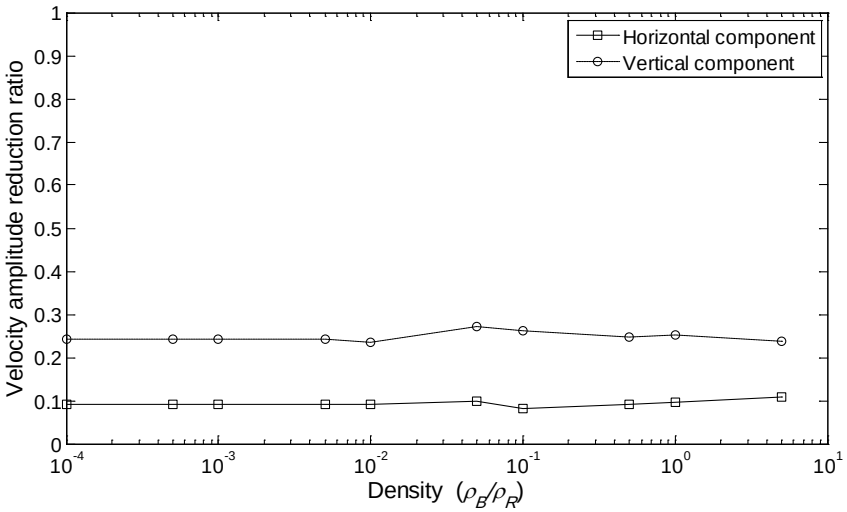

Figure 41. Effect of barrier density on the vibration isolation effectiveness.

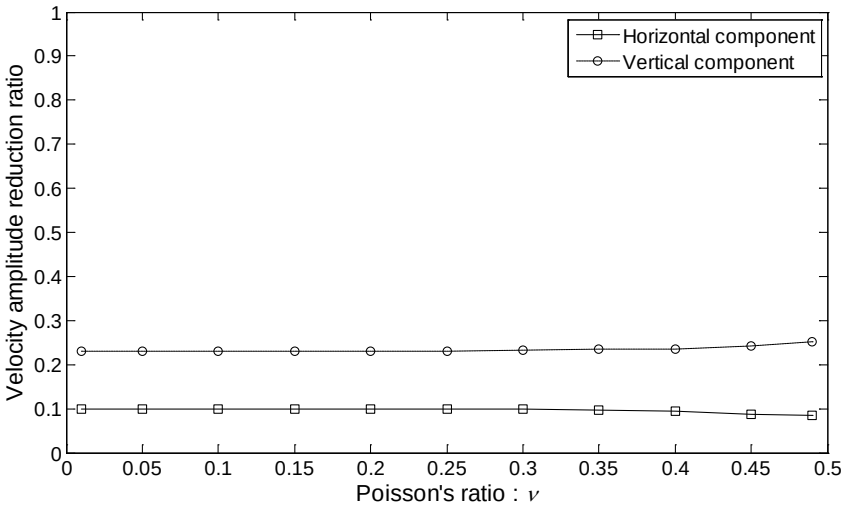

Figure 42. Effect of barrier Poisson's ratio on the vibration isolation effectiveness.

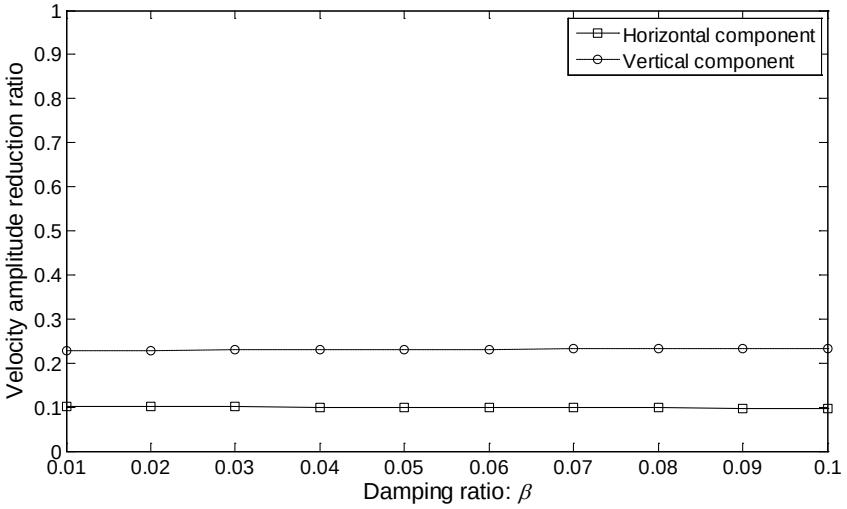

Figure 43. Effect of barrier damping ratio on the vibration isolation effectiveness.

4.2.3 Effect of barrier depth

Figure 44 shows the effect of the barrier depth on the vibration isolation effectiveness. It is clear to see that as the barrier becomes deeper, the horizontal velocity reduces continuously. While the vertical vibration firstly increases, and then decreases dramatically. When the barrier depth exceeds 10 m, further reduction in both horizontal and vertical velocity becomes very small. This is reasonable: as the barrier becomes deeper, more waves are blocked by the barrier, especially the Rayleigh wave, which only propagates in the area near the surface. But when the barrier depth becomes too large, the deeper part hardly contributes to attenuate the ground motion, causing little further contribution in vibration isolation. The phenomenon that a short increase in the vertical velocity occurs with an increasing depth of shallow barrier may attribute to the complex wave interference between waves that transmitted directly through the barrier and those that propagate under the barrier.

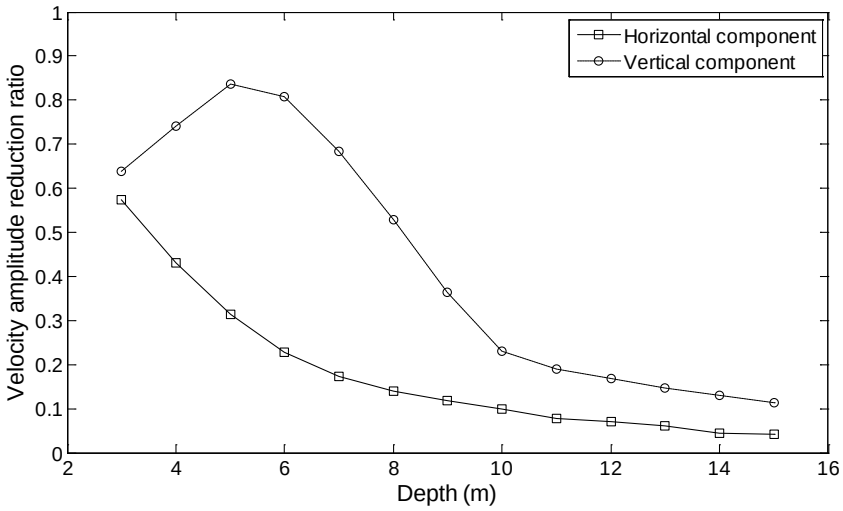

Figure 44. Effect of barrier depth on the vibration isolation effectiveness.

4.2.4 Effect of distance from the explosive to the barrier

Figure 45 shows the effect of the distance (L_1) from the explosive to the barrier on the vibration isolation effectiveness. In this study, it is assumed that the distance between the explosive and the point "*a*" keeps constant, namely, $L_1 + L_2 = 16$ m. So when L_1 increases, L_2 will correspondingly decreases, and vice versa. The purpose of this setting is to investigate the effectiveness of active isolation and passive vibration at the same time and to find out the best location of barriers when the underground explosion and the protected site are fixed. From Figure 45, it can be found that as the barrier moves from the explosive to the protected point "*a*", both the horizontal and vertical responses do not change much, especially for the horizontal velocity. It is inferred that the position of barrier has a minor influence on the vibration isolation effectiveness.

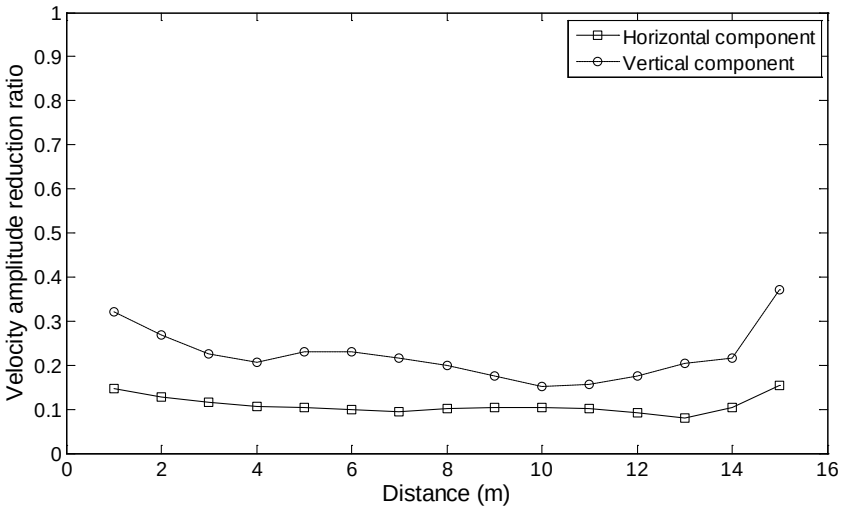

Figure 45. Effect of distance from explosive to barrier on the vibration isolation effectiveness.

4.2.5 Effect of the burial depth of the explosive

Figure 46 shows the effect of the explosive burial depth on the vibration isolation effectiveness. It is seen, in general, the deeper the explosion occurs, the stronger the horizontal and vertical velocities are. This is reasonable, for fewer waves are blocked by the barrier due to the larger depth of the explosive. A decrease of vertical velocity is observed when the burial depth is less than 5 m, this may attribute to the complex wave interference and mode conversion [58] when waves propagate on the surface of the rock and on the interface of the barrier and the rock.

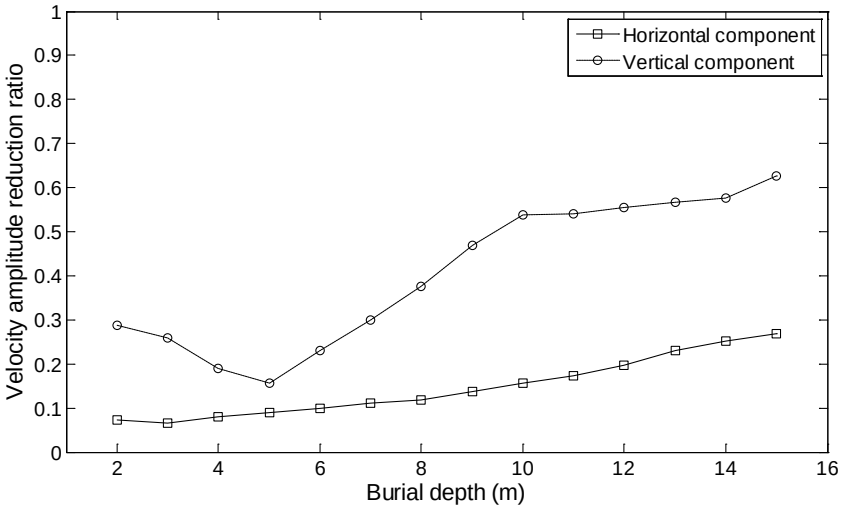

Figure 46. Effect of the burial depth of the explosive on the vibration isolation effectiveness.

4.2.6 Effect of barrier width, inclination angle and the blast pressure

Figures 47-49 show the effect of barrier width, inclination angle and the blast pressure on the vibration isolation effectiveness, respectively. Like the phenomenon observed in Section 4.2.2., those three parameters have little or no influence on the vibration isolation effectiveness.

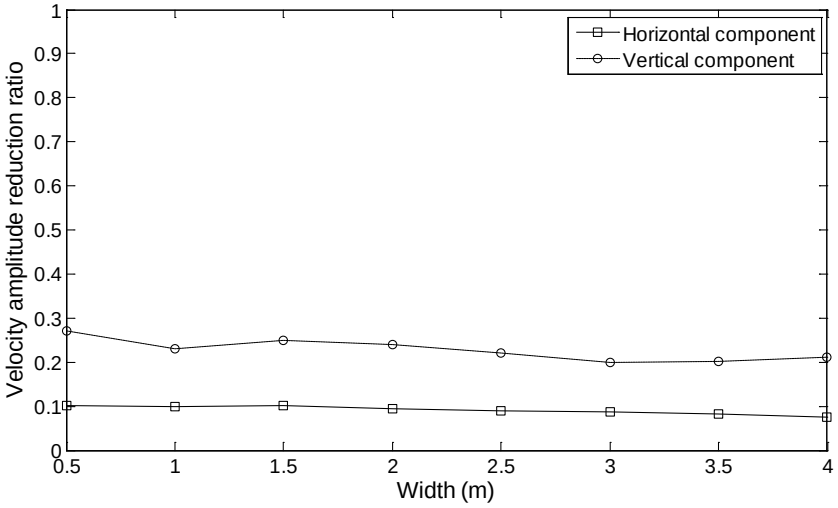

Figure 47. Effect of the barrier width on the vibration isolation effectiveness.

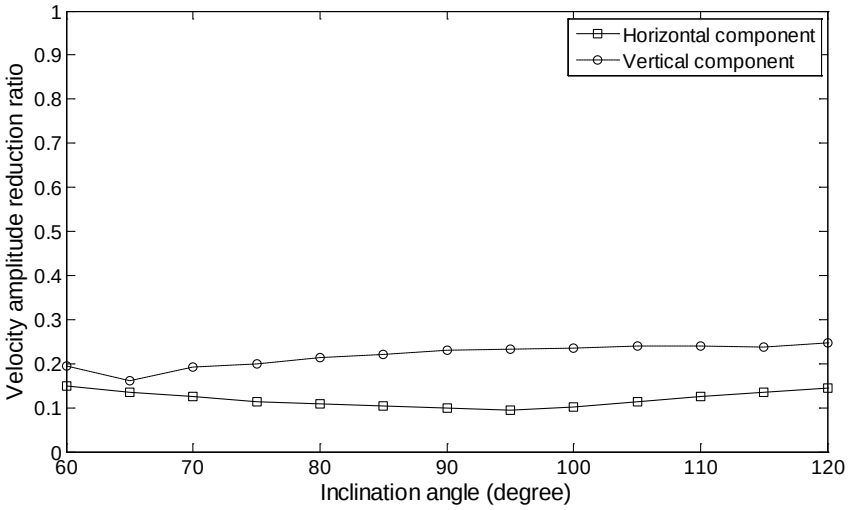

Figure 48. Effect of the inclination angle on the vibration isolation effectiveness.

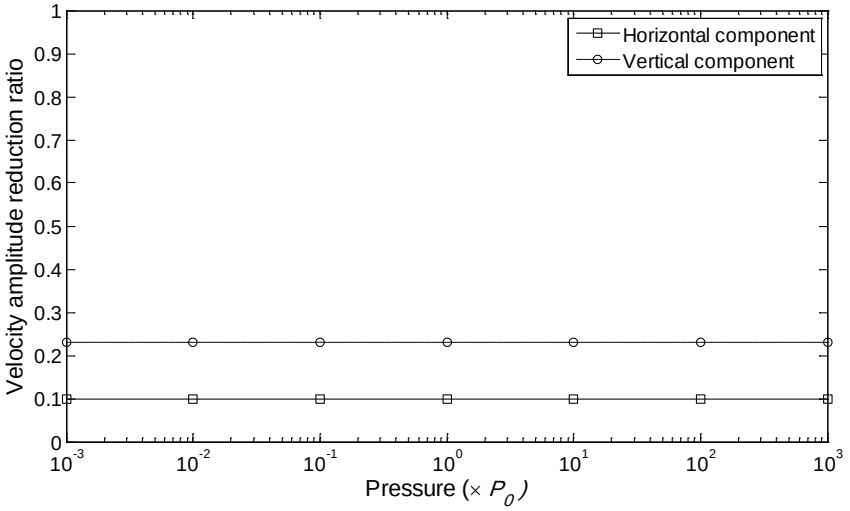

Figure 49. Effect of the blast pressure on the vibration isolation effectiveness.

4.3 Optimization design

In order to study the mutual influences of various investigated parameters, an optimization design for wave barrier is carried out. Again, EPS is selected as the material for wave barrier. The material properties of EPS can be found in Table 7. To study the performance of EPS barrier in a practical way, only key parameters are selected for the optimization design. Based on the parametric study in the Section 4.2, it is found that the most important parameters that affecting the isolation effect are the barrier Young's modulus, the barrier depth and the burial depth of the explosive. Since each type of EPS has its own intrinsic material property, the selected material parameter (i.e. the barrier Young's modulus) is replaced by the EPS type. The typical values of the three investigated parameters are shown in Table 13. It is mentioned that shallow barriers are included, for considering that in reality it may be too difficult or too expensive to install long wave barriers deeply into the rock media. And explosions ranging from shallow explosions (e.g. 2 m) to deep explosions (e.g. 15 m) are examined as well. Here, a Python script is written and run in ABAQUS for the optimization design for EPS barrier. Tables 14 and 15 respectively show the final results for horizontal and vertical velocity amplitude reduction at point "*a*" due to the installation of EPS barriers. Because of the space constraint, only the best and the worst vibration isolation effectiveness are presented. It can be seen that different combination of parameters results in very different vibration isolation effectiveness. If the values of parameters are specified according to the Sequence 1 in these two tables, the minimum A_{rh} and A_{rv} can be achieved, which are 0.02737 and 0.08454, respectively. Generally, a shallow burial depth of the explosive and a large depth of barrier are more efficient in reducing vibration. It should be pointed out that many limitations which exist in reality can be reflected in Python script. For example, if the burial depth of explosive is fixed, specify the only corresponding value of burial depth in Python script; or if it is too expensive to insert deep barriers in hard rock, just examine the shallow barriers which are available in construction. Those two tables are able to provide a useful reference for the wave barrier design in practice.

Table 13. The distribution of selected parameters to be optimized for EPS barriers.

Parameters	Typical values
Barrier depth (m)	3, 4, 5, 6, 7, 8, 9, 10, 11, 12, 13, 14, 15
Burial depth of explosive (m)	2, 3, 4, 5, 6, 7, 8, 9, 10, 11, 12, 13, 14, 15
Types of EPS geofoam	EPS12, EPS15, EPS19, EPS22, EPS29, EPS39,EPS46

Table 14. Final results of horizontal response at point "*a*" for parameter optimization of EPS barriers.

Sequence	Types of EPS	Burial depth(m)	Barrier depth(m)	A_{rh}
1	EPS15	3	15	0.02737
2	EPS46	2	15	0.02873
3	EPS15	2	15	0.02889
4	EPS12	3	15	0.02936
5	EPS15	4	15	0.02941
6	EPS12	2	15	0.02948
7	EPS19	3	15	0.02960
8	EPS12	4	15	0.02960
9	EPS22	3	15	0.03040
10	EPS39	2	15	0.03049
11	EPS19	4	15	0.03071
12	EPS19	2	15	0.03082
13	EPS29	2	15	0.03150
14	EPS22	2	15	0.03152
15	EPS22	4	15	0.03194
16	EPS46	8	15	0.03195
17	EPS46	3	15	0.03205
18	EPS12	5	15	0.03213
19	EPS29	3	15	0.03226
20	EPS19	3	14	0.03251
21	EPS15	3	14	0.03298
22	EPS39	7	15	0.03306
...	...	...	...	...
1254	EPS46	8	3	0.67600
1255	EPS39	8	3	0.67632
1256	EPS29	8	3	0.67659
1257	EPS22	8	3	0.67682
1258	EPS19	8	3	0.67690
1259	EPS15	8	3	0.67701
1260	EPS12	8	3	0.67707
1261	EPS46	10	3	0.69110
1262	EPS39	10	3	0.69125
1263	EPS29	10	3	0.69136
1264	EPS22	10	3	0.69145
1265	EPS19	10	3	0.69149
1266	EPS15	10	3	0.69153
1267	EPS12	10	3	0.69154
1268	EPS46	9	3	0.69450
1269	EPS39	9	3	0.69472
1270	EPS29	9	3	0.69489
1271	EPS22	9	3	0.69503
1272	EPS19	9	3	0.69507
1273	EPS15	9	3	0.69514
1274	EPS12	9	3	0.69517

Table 15. Final results of vertical response at point "*a*" for parameter optimization of EPS barriers.

Sequence	Types of EPS	Burial depth(m)	Barrier depth(m)	A_{rv}
1	EPS15	2	13	0.08454
2	EPS12	2	13	0.08457
3	EPS15	2	14	0.08500
4	EPS12	2	14	0.08504
5	EPS12	3	15	0.08515
6	EPS19	2	13	0.08587
7	EPS46	4	13	0.08592
8	EPS15	3	15	0.08623
9	EPS22	2	13	0.08677
10	EPS12	2	15	0.08717
11	EPS39	4	13	0.08858
12	EPS19	2	14	0.08919
13	EPS15	3	14	0.08930
14	EPS15	2	15	0.08970
15	EPS39	3	13	0.08973
16	EPS12	3	14	0.08984
17	EPS19	3	15	0.09000
18	EPS39	4	14	0.09000
19	EPS29	3	13	0.09009
20	EPS29	4	14	0.09013
21	EPS19	3	14	0.09015
22	EPS29	2	13	0.09051
...	...	...	...	...
1254	EPS46	13	3	1.16713
1255	EPS39	13	3	1.16717
1256	EPS29	13	3	1.16722
1257	EPS19	13	3	1.16726
1258	EPS22	13	3	1.16726
1259	EPS15	13	3	1.16729
1260	EPS12	13	3	1.16731
1261	EPS46	15	3	1.18980
1262	EPS39	15	3	1.18982
1263	EPS29	15	3	1.18984
1264	EPS19	15	3	1.18989
1265	EPS22	15	3	1.18989
1266	EPS12	15	3	1.18991
1267	EPS15	15	3	1.18991
1268	EPS46	14	3	1.20170
1269	EPS39	14	3	1.20175
1270	EPS29	14	3	1.20179
1271	EPS22	14	3	1.20182
1272	EPS15	14	3	1.20184
1273	EPS19	14	3	1.20184
1274	EPS12	14	3	1.20186

4.4 Conclusions

This chapter investigates the isolation performance of wave barrier under subsurface explosions. Like the investigation presented in Chapter 3, a 2D numerical model is firstly established in ABAQUS. Then an extensive parametric study is carried out to examine the influence of each parameter on the screening effectiveness of wave barrier. By using Python language, an optimization design method is developed for the design of barriers made of EPS, and the best EPS barrier that is able to minimize the ground vibration is identified. Based on the obtained results, the following understandings and conclusions are made:

- The installation of wave barrier is effective in reducing ground motion generated by subsurface explosions. Significant vibration reduction can be achieved if wave barrier with proper parameters are installed, as Tables 14 and 15 show.
- The burial depth of explosive, the barrier Young's modulus and the barrier depth are key parameters that affect the vibration isolation effectiveness. Specifically, the shallower the explosive is buried, the smaller the barrier Young's modulus, the larger the barrier depth, the better screening effectiveness can be achieved. Other parameters (the barrier density, Poisson's ratio, damping ratio, the width, the inclination angle, the distance of barrier from the explosive, the magnitude of the blast pressure) have negligible or no influence in reducing the ground vibration.
- Python scripts can be used for the optimization design of wave barrier in practice. After all the possible values of key parameters are given, barriers ranging from performing the best to being the worst can be identified. With the suggested method, plus the engineer's experiences, the best choice of wave barrier is expected to become available.

5. Numerical simulation of the behavior of main tunnel under explosions

5.1 Background of the project

The main road tunnel, which runs under Col du Fréjus in the Cottian Alps between Modane in France and Bardonecchia in Italy, is the fifth longest road tunnel in the world (by 2005). It is constructed and managed by the French company SFTRF (Société française du tunnel routier du Fréjus) on the French side and the Italian company SITAF (Società Italiana per il Traforo Autostradale del Fréjus SpA) on the Italian side. Since it came to service in 1980, during the first 20 years, more than 20 million vehicles had passed through this tunnel. It plays a vital role in connecting France and Italy. In May 2009, a safety tunnel, which is parallel to the main tunnel, began to be built, as the red line shown in Figure 50 (the double black lines represent the main tunnel). Based on the rock survey (see Figure 51), the rock media in some areas is so hard that blasting method has to be used. Some cross passages that connect the main tunnel and the safety tunnel are also excavated by means of explosives. Figure 52 shows the bird's-eye view of the tunnel system. The main tunnel (on the right side) has a horseshoe shape cross section with an inner height of 7.49 m, an inner width of 10.52 m and 0.6 m thick plain concrete as the tunnel lining, the inner radius of the arch in the top heading of tunnels was 5.26 m. The safety tunnel (on the left side) with a circular cross section has an inner diameter of 4.1 m. The distance between the two parallel tunnels is 50 m. Figure 53 presents the section of cross passage, its height and width are 5.09 m and 5.8 m, respectively, and the excavation of cross passages from the safety tunnel to the location which is 6 m away from the main tunnel is carried out by blasting method [126-129]. This study on main tunnel will be divided into two parts. The chapter 5 focuses on the investigation of the dynamic behavior of main tunnel under explosions through the numerical simulation in ABAQUS, examining the maximum motion and the possible damage and stiffness degradation of the main tunnel under different conditions. In the next chapter, two mitigation measures are proposed and examined in reducing the vibration of main tunnel, aiming to protect main tunnel from explosions in an effective and practical way. The results from these two chapters are able to provide a reference for the tunnel protection design under explosions in practice. It is noted that in the present study, the main tunnel is considered as a reference configuration on which some theoretical studies will be carried out in the following investigations varying a huge number of parameters.

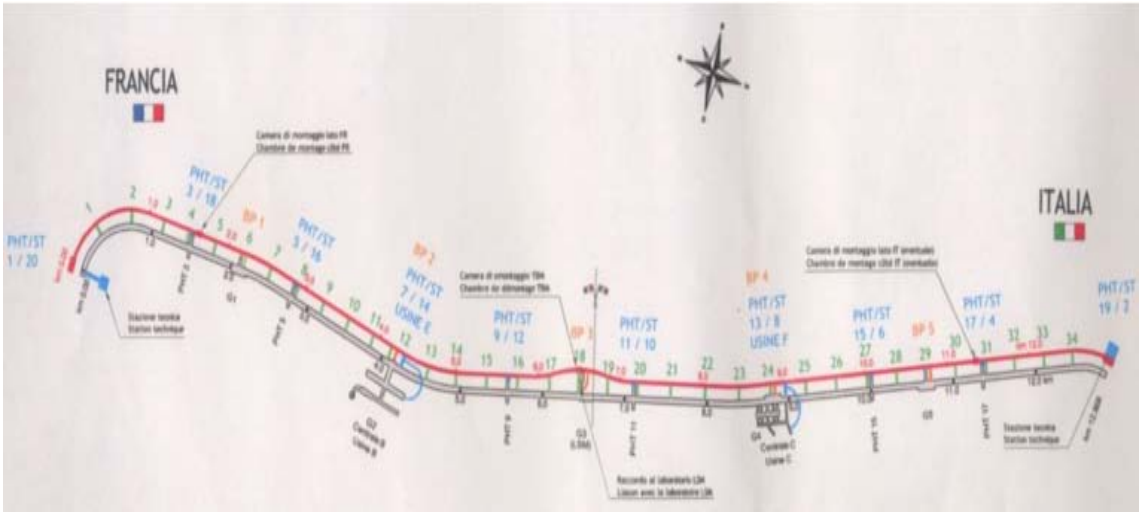

Figure 50. The schematic plan view of safety tunnel (read line) and main tunnel (double black lines).

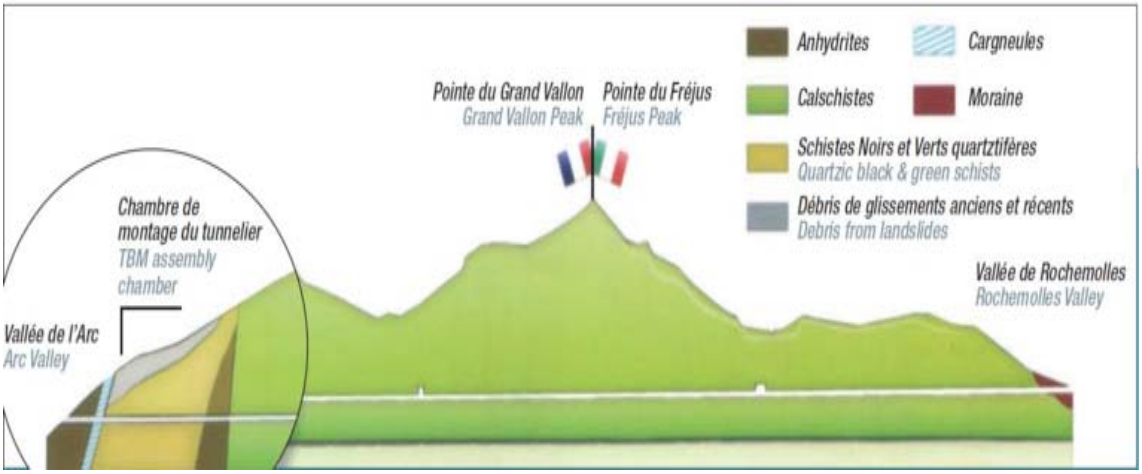

Figure 51. The geologic cross section of rock media.

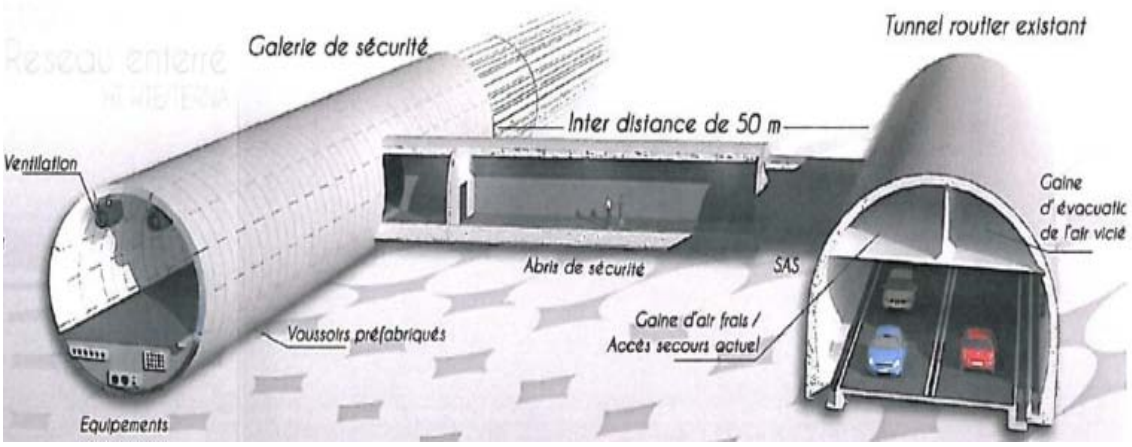

Figure 52. The bird's-eye view of the tunnel system (safety tunnel on the left side and main tunnel on the right side).

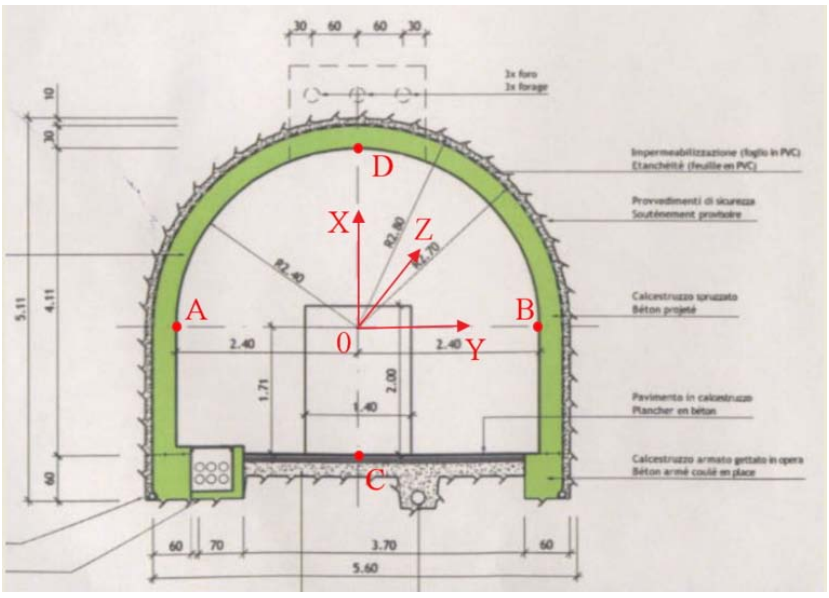

Figure 53. The section of cross passage (units: m).

5.2 Numerical model

Physical process of explosions in rock media and the blast-induced vibration on the existing tunnel are very complicated. They involve many complex processes: dynamic interactions among the explosives, the formation of craters or camouflets, the propagation of shear and compressional waves in rock, rock-tunnel interaction and the responses of the tunnel. To deal with these complicated problems, some simplifications have to be made. The following considerations and assumptions are made during the development of numerical model in ABAQUS.

5.2.1 Blast loading

Figure 54 shows the interaction with rock surrounding the explosives. From the center to the outside, there are original hole, crushed zone, plastic zone and elastic zone, respectively. Much of the energy is dissipated in crushed and plastic zones. To apply the blast pressure in numerical model, the time history of pressure has to be obtained. It is noted that the explosive charge EMULSTAR 8000UG which is used in Chapter 4 is also adopted in this project. Thus, the same evolution of pressure P (see Equation (23) and Figure 37) is used in this chapter. Still, to avoid the meshing problem due to the too small diameter of explosives compared with the whole model size, equivalent pressure $P_{equivalent}$ (see Equation (25)) is adopted.

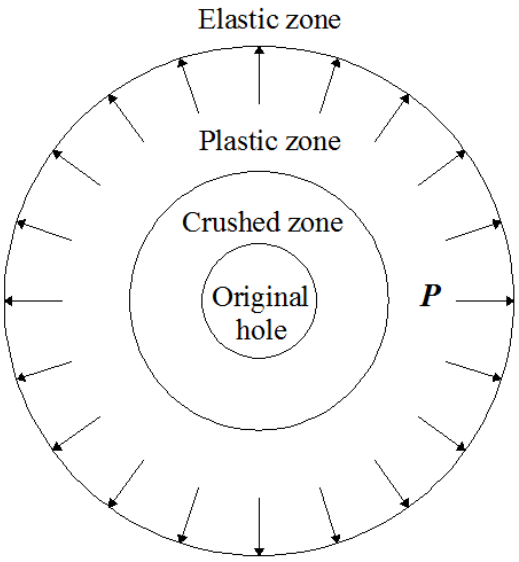

Figure 54. Zones of rock surrounding the explosives.

5.2.2 Material model

5.2.2.1 Rock model

Rock, which ranges from intact to highly fractured, can exhibit very different behavior under explosions. Until now, there is no constitutive relation that is able to describe the behavior of rock accurately and simply. Traditional constitutive models, like elastic, elastoplastic and visco-

elastic are widely used. The choice of one type of model mainly depends on the purpose of the analysis. During the blast loading, there are certainly fracture zone and plastic deformation of the rock in the vicinity of the explosives. But beyond some distance from the detonation, the response of rock can be basically assumed to be elastic. From the Figure 54, it can be seen that the pressure *P* is applied on the interface between the plastic zone and the elastic zone, and the examined rock area in this study is within the elastic zone. Therefore, it is reasonable to assume that the dynamic behavior of rock is linear elastic.

For the damping in rock, Rayleigh damping is adopted. Although rock ranging from soft to hard exhibits very different damping, the time period of explosions is so short that the effect of energy absorption by damping is generally insignificant. Here, 5% of damping ratio is given for the possible energy loss.

5.2.2.2 Tunnel model

Typically, elastic or elastoplastic model is used to describe the behavior of tunnel, more complicated constitutive relations may be needed if strong nonlinear behavior exists. In the present study, elastic model is firstly adopted. Then, to investigate the behavior of tunnel in a more accurate way, concrete damage plasticity (CDP) model is employed to investigate the possible damage and stiffness degradation of main tunnel subjected to strong explosions under different conditions. (For more details about CDP model, please refer to Section 2.4.3)

5.3 Finite element model

Based on the preceding discussion, a finite element model which includes the main tunnel, the safety tunnel and their cross passage are created in ABAQUS. To perform the numerical simulation effectively, explicit dynamic analysis procedure is adopted. The rock and tunnels are modeled as homogeneous, isotropic and elastic media, using 4-node bilinear plane strain quadrilateral, reduced integration elements (for 2D model) and 8-node linear brick, reduced integration elements (for 3D model), respectively. The interfaces between them are assumed perfectly bonded. The material properties are given in Table 16. It should be mentioned that the main tunnel and the safety tunnel are built deeply into the mountains (see Figure 51); it is very difficult to create a model with the whole mountains included. Instead, a limited area, which contains only the explosives, the most possible vulnerable region of rock and tunnels, is investigated. Figures 55 and 56 show the 2D and 3D finite element models developed in ABAQUS, respectively. The 2D model with safety tunnel on the left side and main tunnel on the right side has a length of 150 m and a height of 140 m. Enlarged views about the sites surrounding the explosives and the main tunnel are presented as well. The 3D model in the plane perpendicular to the direction of tunnels has the same size as the 2D model does and extends 140 m along the direc-

tion of tunnels. A perspective view and a cut view of the 3D model (see Figure 56(a) and (c)) are also presented in order to provide a clear image of the whole numerical model. It is pointed out that the density of the mesh around the main tunnel is much denser than the one around the safety tunnel in both 2D and 3D models (see Figures 55, 56(b) and (c)). The reason is that the major purpose of this investigation is the responses of main tunnel under explosions. Therefore, the element size around the main tunnel should be small enough to generate accurate result from the numerical simulation. While for the safety tunnel, some security measures are expected to be carried out to protect it from explosions, so the mesh around it is relatively coarse. This can reduce the whole calculation time effectively in ABAQUS.

Table 16. Material properties of rock and main tunnel lining.

Material	Density (kg/m^3)	Poisson's ratio	Young's modulus (GPa)	Damping ratio
Concrete	2500	0.15	20	5%
Rock	2700	0.20	15	5%

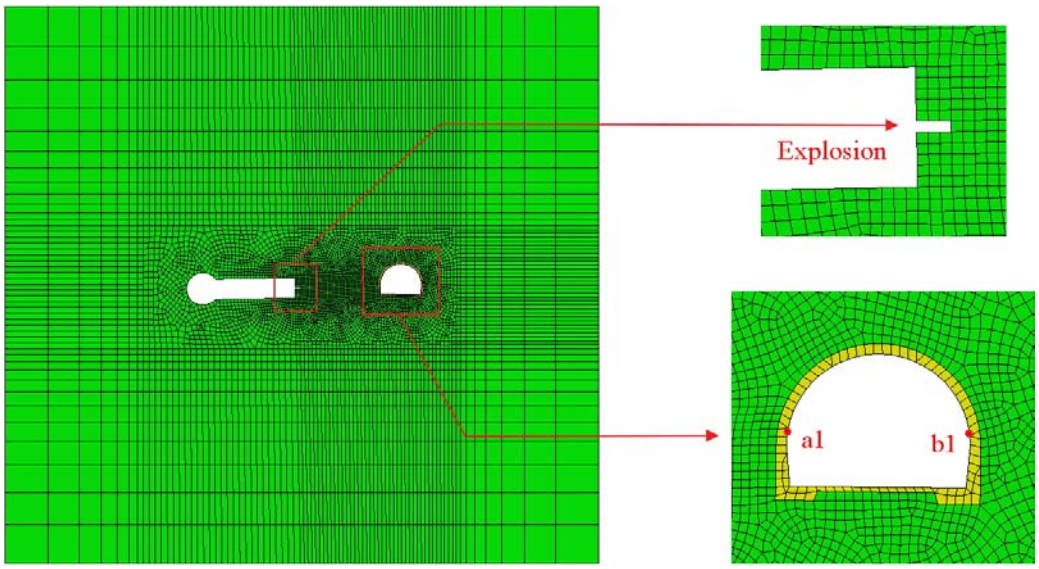

Figure 55. The 2D finite element model in ABAQUS.

For the boundary conditions, roller boundaries are applied on the four sides of 2D model and on the six faces of 3D model. It should be mentioned that fictitious boundaries like roller boundary or fixed boundary could reflect outward propagating waves, bringing considerable energy back into the model. To solve this problem, quiet boundary conditions can be used to avoid the reflected waves. Nevertheless, according to Yang [66], the duration of blast loading is very short and the initial response of structures is a major concern, so fictitious boundaries can be set at a sufficient distance away, resulting in no waves are reflected within the duration of interest or the reflection of waves is so small that it can be ignored. In the present study, the finite element models are large enough to avoid the influence of reflected waves within the investigated time.

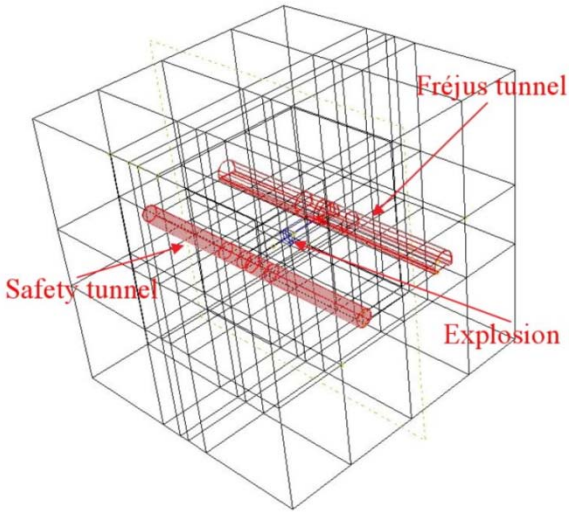

(a) The 3D perspective view

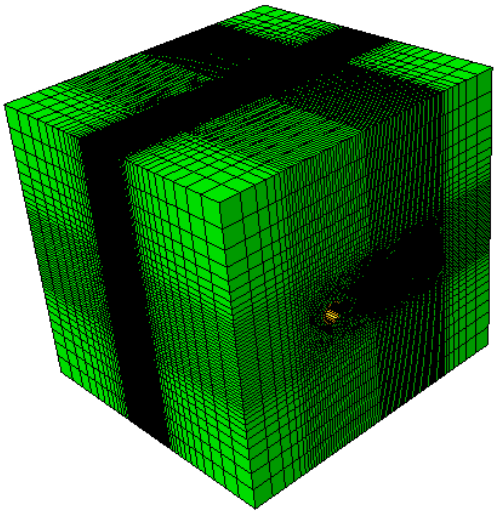

(b) The 3D finite element mesh

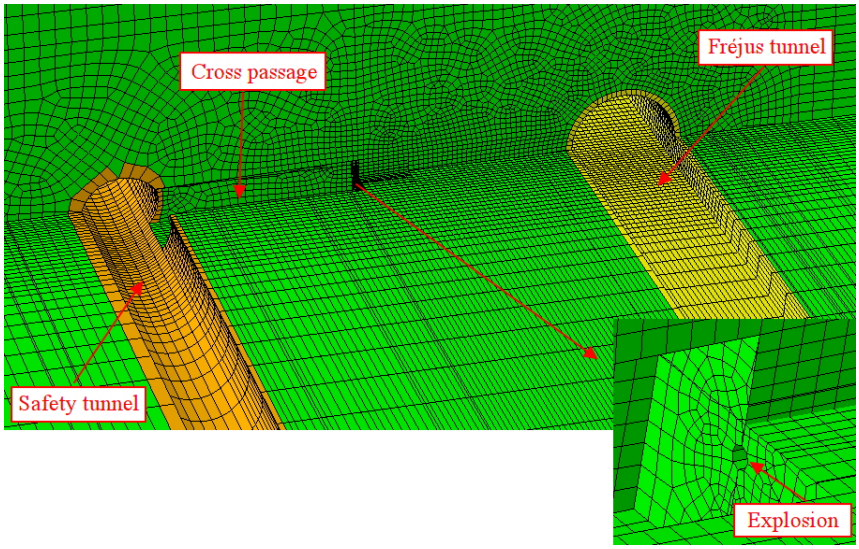

(c) Cut view of the mesh of rock-tunnel system

Figure 56. The 3D finite element model in ABAQUS.

Here, two typical points (denoted as *"*a1*"* and *"*b1*"*, see Figure 55), which are the junctions of the arch crown and the sidewall of the cross passage are chosen. The motion of these two points is considered able to representatively reflect the vibration of main tunnel under explosions. Figures 57 and 58 show the displacement, velocity and acceleration of main tunnel at these two points. It is clear to see that the motion of both point *"*a1*"* and *"*b1*"* firstly increases dramatically in a very short time, and then decreases sharply after the initial response. It is inferred that the most dangerous damage to main tunnel is the arrival of the initial shock waves. This agrees with the conclusion made by Yang [66], who pointed out that the initial shock waves were the major concern during the investigation of tunnels under explosions. In addition, it can be seen that the motion of point "a1" and "b1" in 2D model is much larger than the one in 3D model. This may be attributed to the fact that the blast pressure in 2D model can be equally treated as being applied in 3D model all along the tunnel direction, while the blast pressure in 3D model, which represents the real blast pressure, apparently has a very limited width along the tunnel direction. Therefore, the blast pressure in 2D model is actually much larger than the one in 3D model, causing much stronger vibration in the 2D analysis. Besides, it is obvious to see that the peak motion of point "a1" is much bigger than that of point "b1". This is reasonable, the point "a1", which is near to the explosives, suffers the high level of explosions to the initial shock wave from the explosions. In fact, the left half part of main tunnel (e.g. the half part near the explosions) generally has a much stronger vibration than the tunnel's right half part (e.g. the half part far away from the explosions). This inference can be confirmed by Figures 59 and 60, which show the distribution of maximum displacement, velocity and acceleration of main tunnel in 2D and 3D models under explosions, respectively. The positions where the largest motion occurs and their corresponding values are also pointed out. It is clear to see from Figure 59 that the strongest vibrations occur in the arch, or around the junction of the arch and the sidewall on the left half part of main tunnel. It is noted that the maximum motion of different parts of main tunnel appears in different times, rather than in the same time due to the wave propagation through the tunnel. Similar phenomenon can be observed in the 3D simulation (see Figure 60). In addition, it is seen that, due to the symmetry of the 3D model, the distribution of the maximum motion of main tunnel is symmetric along its central section, as expected. However, the maximum motion of main tunnel in 3D model does not occur in the central section, but some distances away from it, as shown in Figure 60. This phenomenon may be attributed to the complicated wave propagation and wave interference generated by the blast pressure, which is assumed to be applied on a blasthole with a shape of cylinder (see Figure 56). Once again, it is observed that the maximum motion of main tunnel in 3D model is much smaller than the one in 2D model. Therefore, in order to study the dynamic behavior of main tunnel in a more accurate way, the following investigations are carried out through 3D analysis.

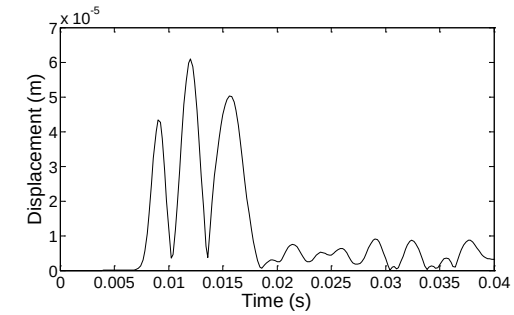

(a) Displacement at point *"*a1*"* in 2D

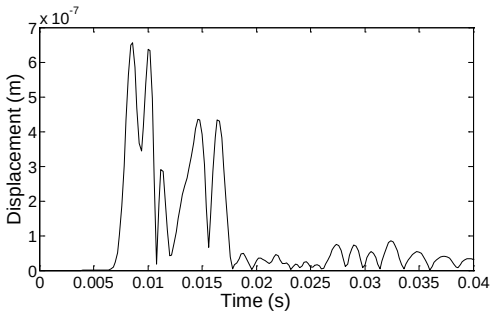

(b) Displacement at point *"*a1*"* in 3D

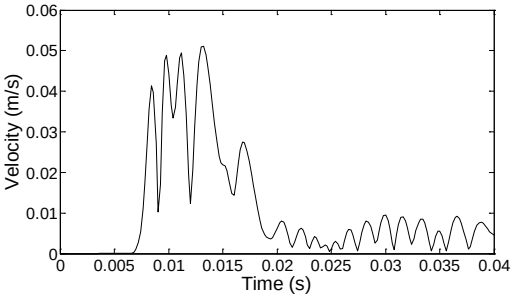

(c) Velocity at point *"*a1*"* in 2D

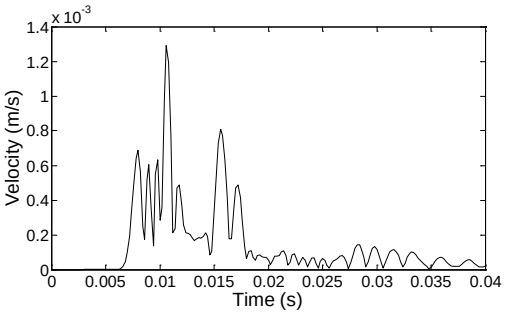

(d) Velocity at point *"*a1*"* in 3D

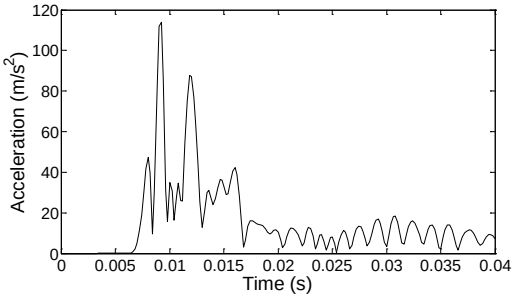

(e) Acceleration at point *"*a1*"* in 2D

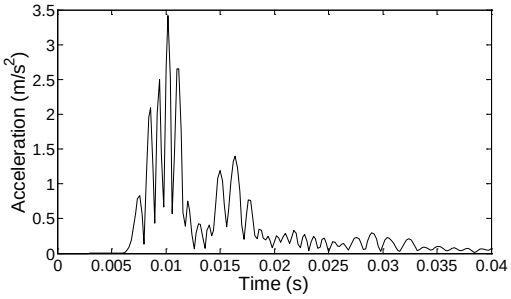

(f) Acceleration at point *"*a1*"* in 3D

Figure 57. The motion of point "a1" in 2D and 3D rock-tunnel models under explosions.

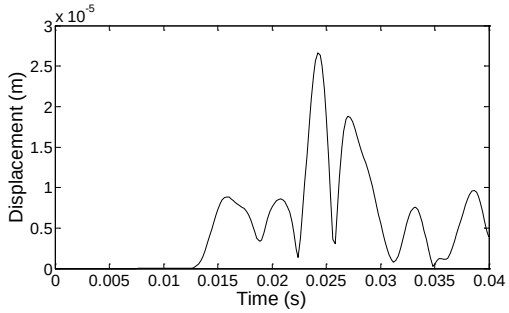

(a) Displacement at point "b1" in 2D

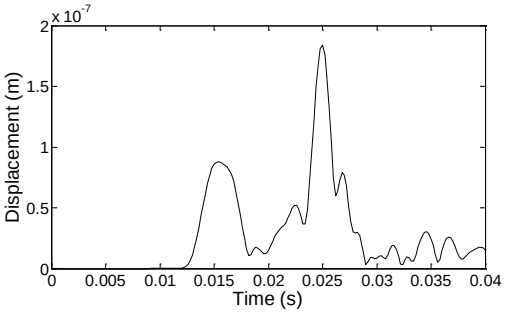

(b) Displacement at point "b1" in 3D

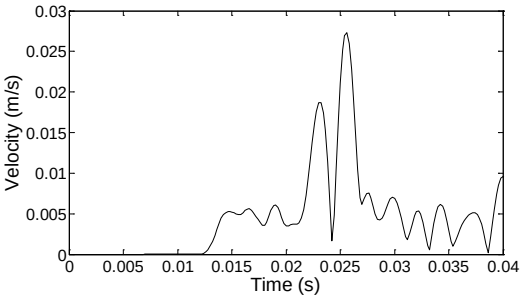

(c) Velocity at point "b1" in 2D

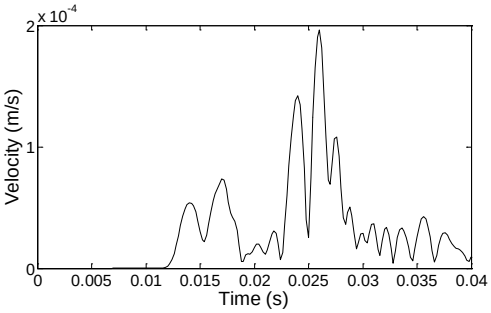

(d) Velocity at point "b1" in 3D

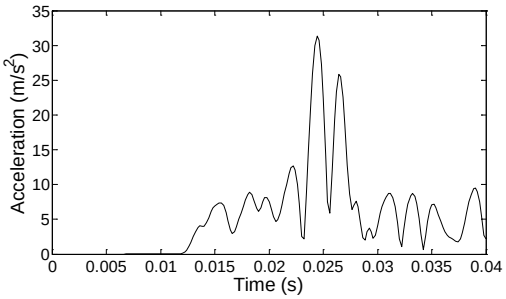

(e) Acceleration at point "b1" in 2D

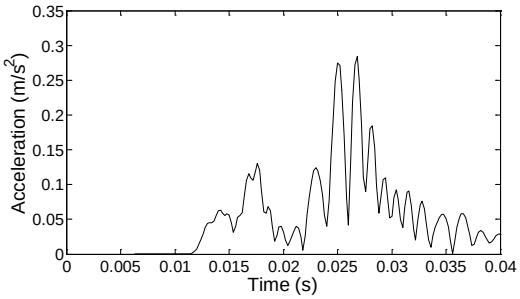

(f) Acceleration at point "b1" in 3D

Figure 58. The motion of point "b1" in 2D and 3D rock-tunnel models under explosions.

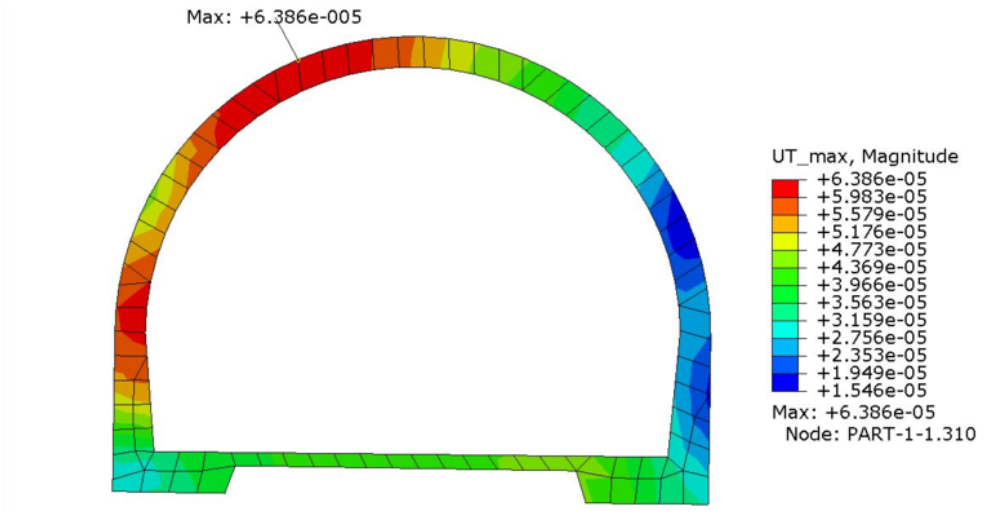

(a) The distribution of maximum displacement

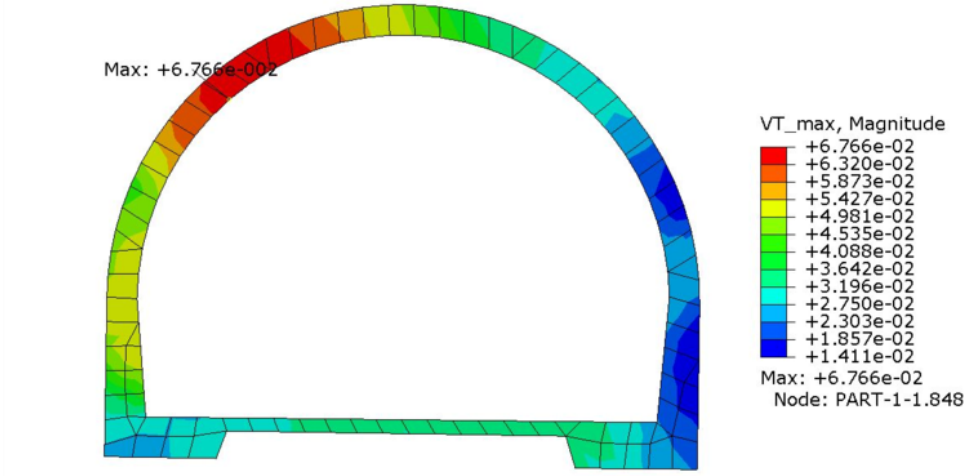

(b) The distribution of maximum velocity

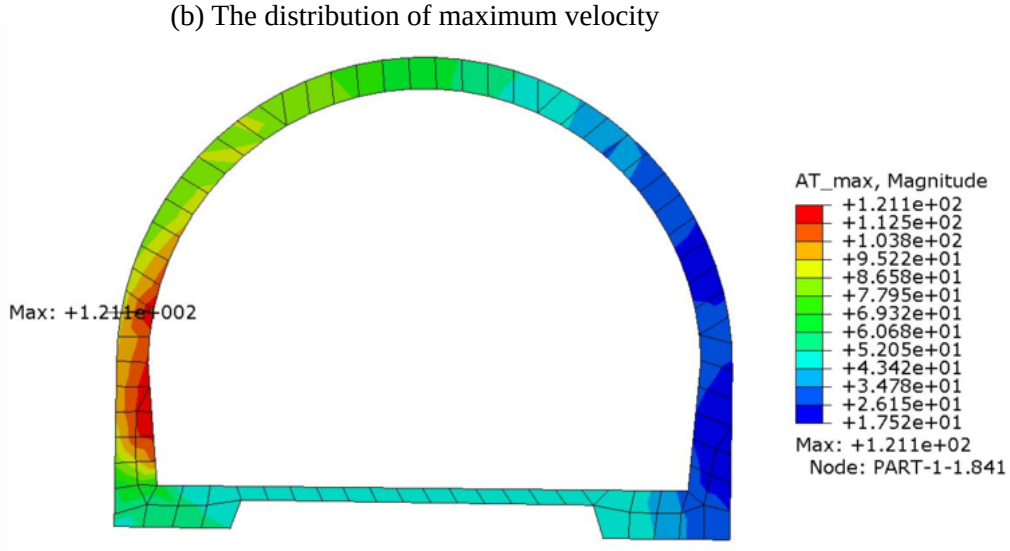

(c) The distribution of maximum acceleration

Figure 59. The distribution of maximum motion of main tunnel (2D elastic model) under explosions.

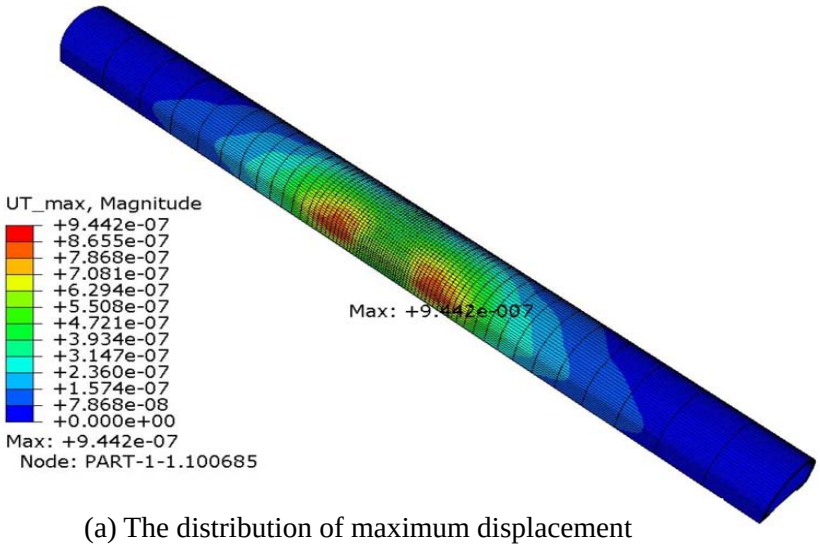

(a) The distribution of maximum displacement

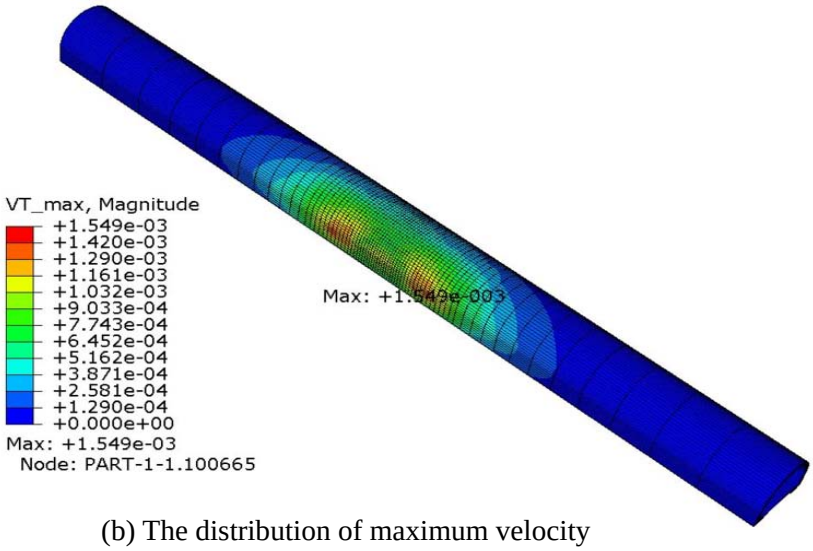

(b) The distribution of maximum velocity

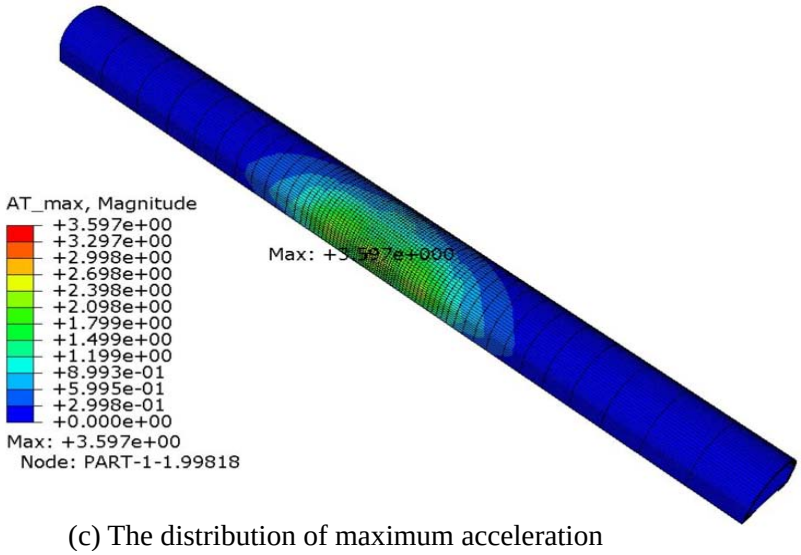

(c) The distribution of maximum acceleration

Figure 60. The distribution of maximum motion of main tunnel (3D elastic model) under explosions.

5.4 Parametric study

In this section, an extensive parametric study, which includes the lining stiffness, the lining thickness, the distance of explosions from main tunnel, the position of explosions along the section of cross passage, the blast pressure and the tunnel burial depth, has been conducted to examine their influences on the responses of main tunnel under explosions. All the investigations are based on the 3D model shown in Figure 56. Note that when the effect of one parameter is investigated, all the other parameters are kept constant. Since the maximum motion of tunnel is one of the most important evaluations on the tunnel safety, the magnitudes of maximum displacement, velocity and acceleration are used to assess the security of main tunnel during explosions. The numerical results and analyses are presented as follows.

5.4.1 Effect of lining stiffness

Figure 61 shows the effect of the lining stiffness E on the motion of main tunnel. Considering that the construction material for tunnel lining is concrete or reinforced concrete, the value of E is assumed to be ranged from 10 GPa to 200 GPa. Generally, the Young's modulus of concrete is larger than 10 GPa, but the decay of concrete over time may reduce its stiffness, and 200 GPa, which is almost the Young's modulus of steel, is used to examine the vibration of lining which is mainly constructed by steel. It can be seen that with an increasing E, the maximum motion of main tunnel firstly reduces and then remains to be stable. Specifically, when the value of E is smaller than a certain value (100 GPa, 40 GPa and 40 GPa for maximum displacement, velocity and acceleration, respectively), increasing the lining stiffness is effective in reducing the vibration of tunnel, but when E is larger than the values mentioned above, an increase of lining stiffness seems to be useless. Therefore, it is inferred that “hard” lining generally performs better than “soft” lining in resisting the vibration generated by nearby explosions.

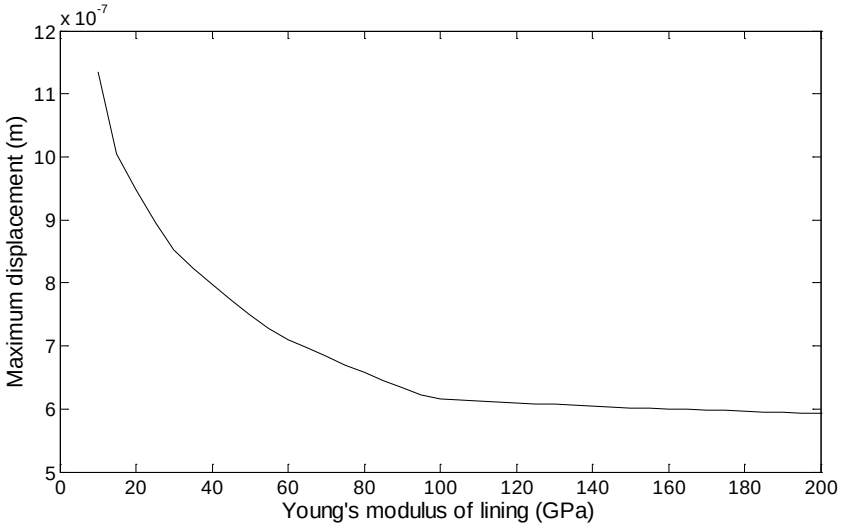

(a) The maximum displacement

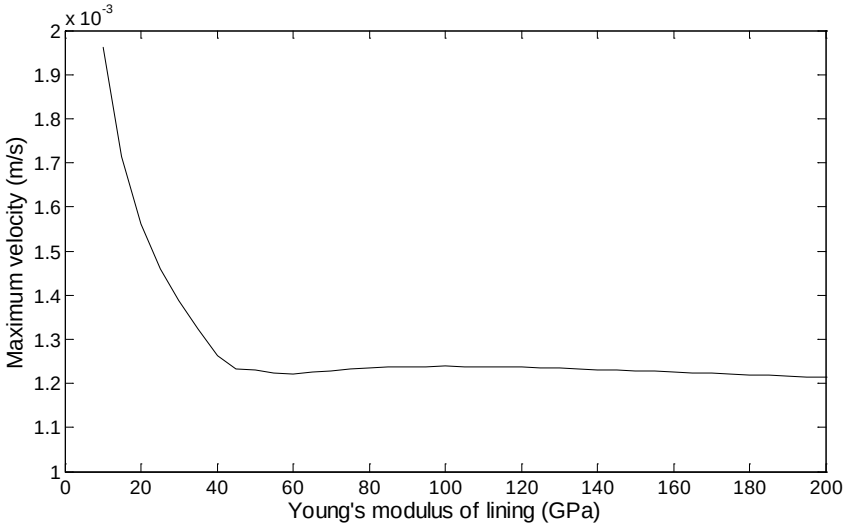

(b) The maximum velocity

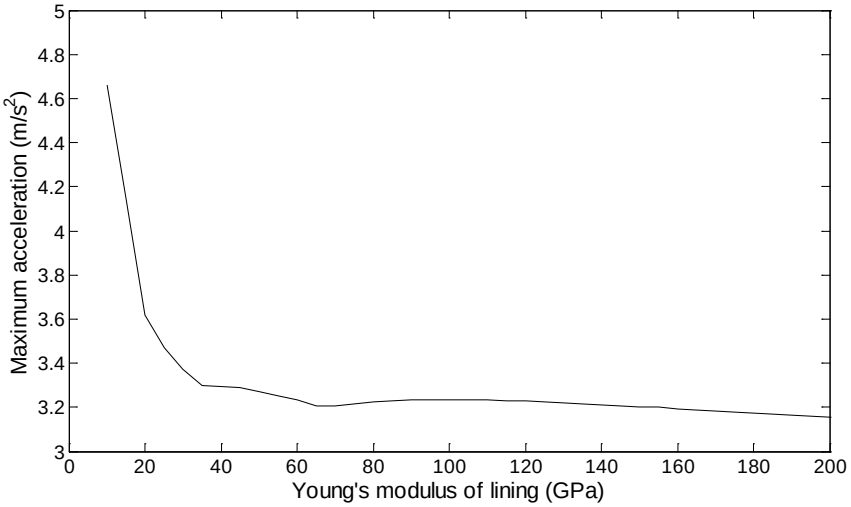

(c) The maximum acceleration

Figure 61. Effect of lining stiffness on the motion of main tunnel.

5.4.2 Effect of lining thickness

Figure 62 shows the effect of the lining thickness *l* on the motion of main tunnel. The investigated *l* ranges from 0.3 m to 1.5 m, which generally reflects the widths of the practical lining thickness. It is observed that there is little change of the maximum displacement, velocity and acceleration with an increasing *l*. In other words, the variations of the tunnel maximum motion are so small that they can almost be ignored. Thus, it is concluded that the effect of the lining thickness on the tunnel motion is negligible.

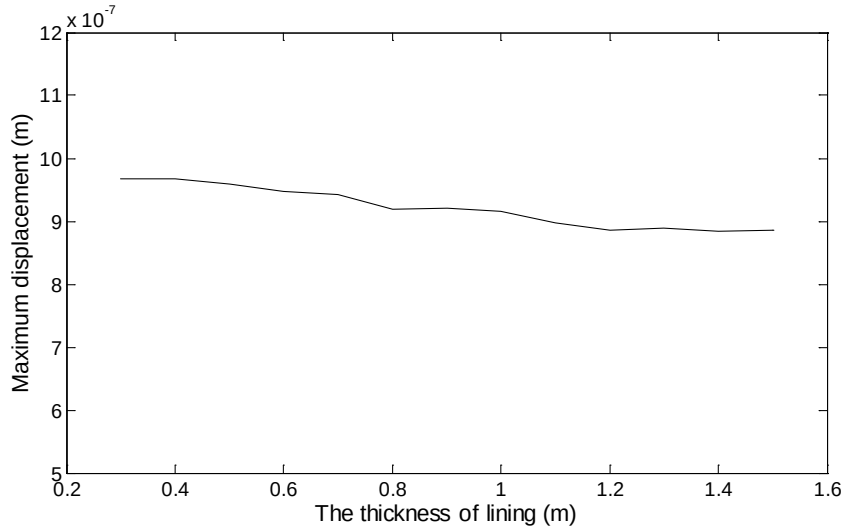

(a) The maximum displacement

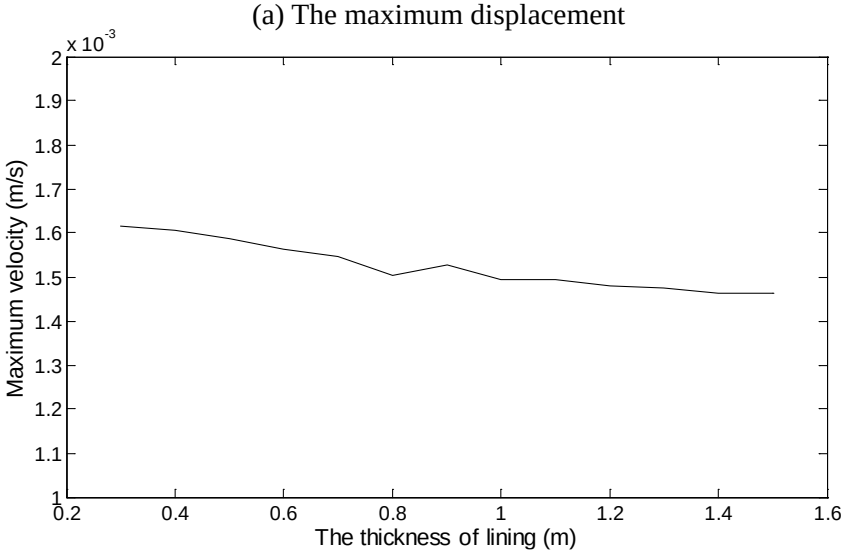

(b) The maximum velocity

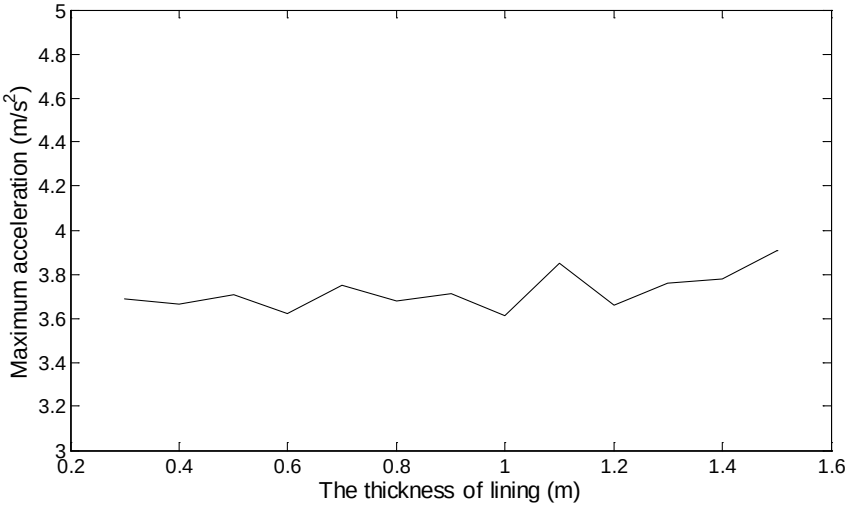

(c) The maximum acceleration

Figure 62. Effect of lining thickness on the motion of main tunnel.

5.4.3 Effect of the distance of explosions from main tunnel

Figure 63 shows the effect of the distance of explosions *s* from main tunnel on the tunnel motion. It is mentioned that the excavation of cross passage between the safety tunnel and the main tunnel is carried out by blasting method except the sections which are within 6 m away from main tunnel (excavated by mechanics for security consideration). Therefore, the examined distance *s* is larger than 6 m. From Figure 63, it is clear to see that the maximum displacement, velocity and acceleration of main tunnel increases as the explosions move closer to the main tunnel. Particularly, when the explosions are very close to the main tunnel ($s < 15$ m), a small decrease of *s* can result in a significant increase of the tunnel vibration. Thus, great care has to be made to make sure that the vibration of main tunnel is under the permissible level when explosions occur near the protected tunnel.

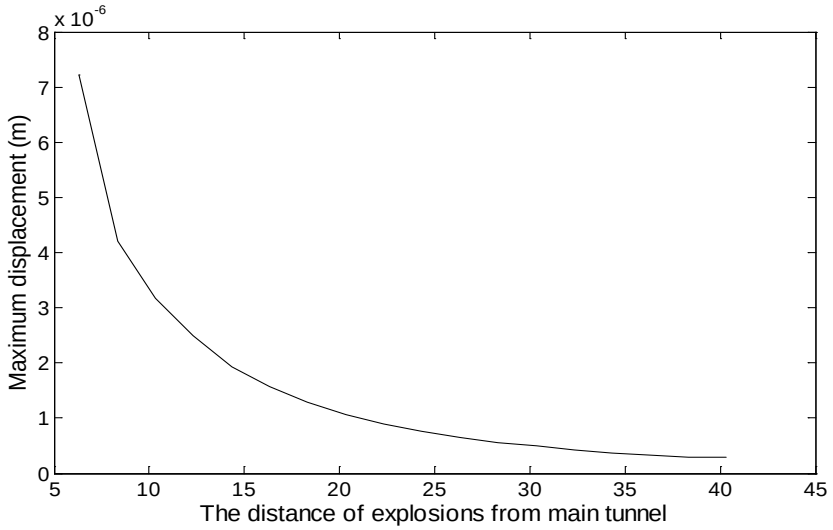

(a) The maximum displacement

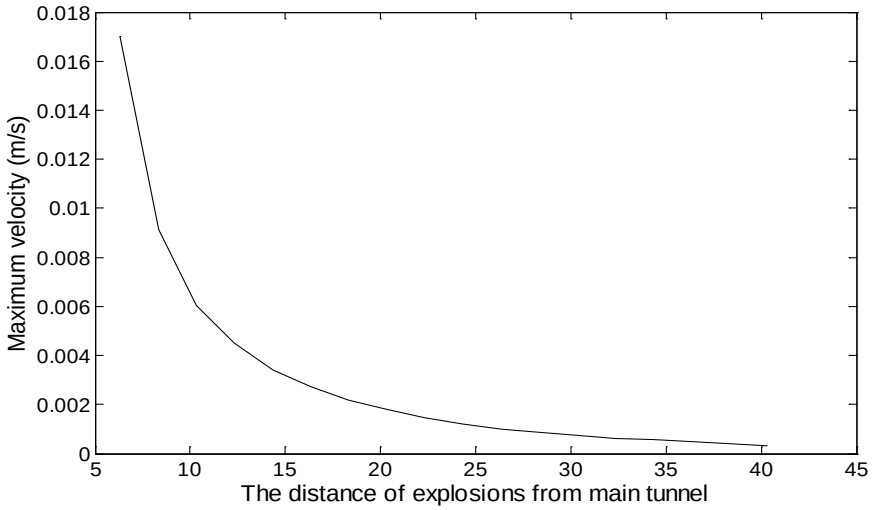

(b) The maximum velocity

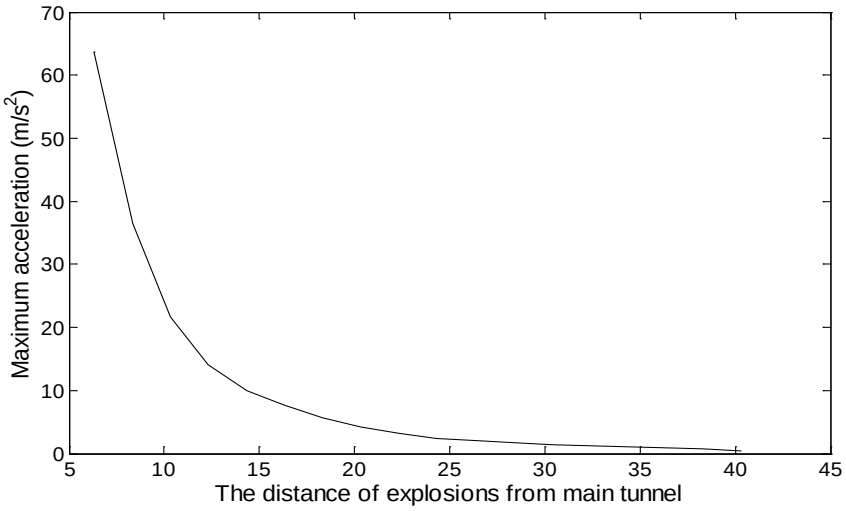

(c) The maximum acceleration

Figure 63. Effect of the distance of explosions from the main tunnel on the tunnel motion.

5.4.4 Effect of the position of explosions along the section of cross passage

Since multiple blastholes are drilled along the section of cross passage during the excavation of cross passage in practice, it is necessary to investigate the influence of different positions of explosions on the main tunnel motion. Figures 64 and 65 respectively show the effect of the horizontal position of explosions (from A to B shown in Figure 53) and vertical position of explosions (from C to D shown in Figure 53) on the motion of main tunnel. It is seen from Figure 64 that the maximum motion of main tunnel seems to be symmetric along the vertical line which passes the zero point (see Figure 53). This is reasonable, because the 3D model is symmetric along the X-Z plane. However, because that the 3D model is asymmetric along the Y-Z plane, the motion of main tunnel is not strictly symmetric when the explosions move from C to D, as shown in Figure 65. In addition, it is observed from the two figures that the vibration of main tunnel seems not to change much when explosions move along both the horizontal and vertical positions, particularly for the tunnel maximum displacement and velocity. Therefore, it is inferred that the position of blastholes along the section of cross passage generally has minor influence on the main tunnel motion. It should be mentioned, however, that the section of cross passage where blastholes are drilled has a very limited area, if explosions happen in other areas, it is uncertain that there are still few variations of the maximum motion of main tunnel. Since only explosions along the section of cross passage are of interest in this study, the investigation on the influence of explosions in other areas is beyond the scope of this study.

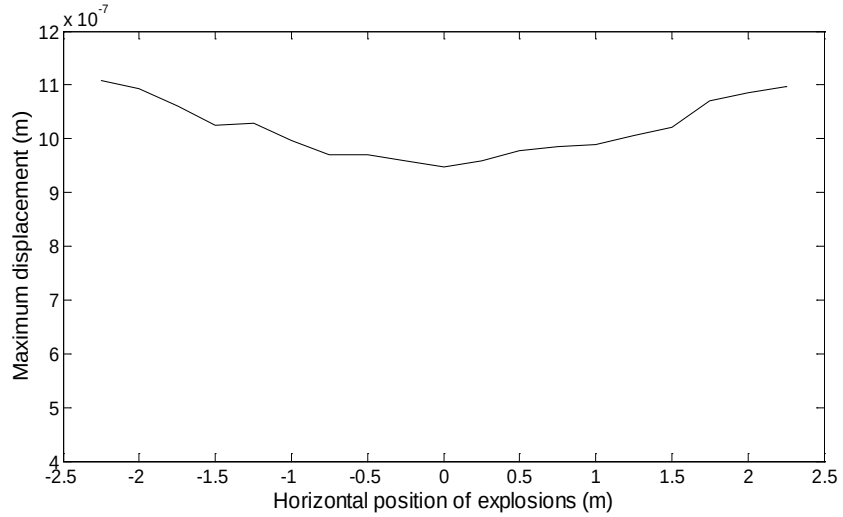

(a) The maximum displacement

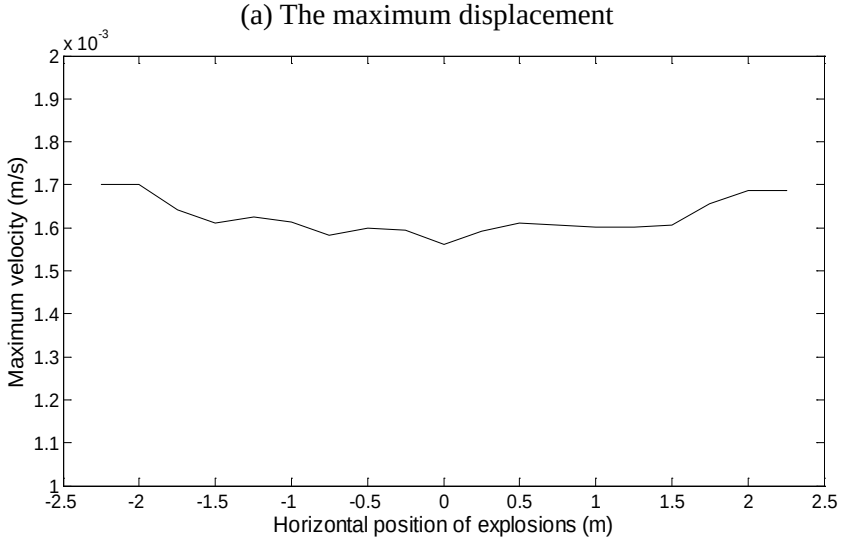

(b) The maximum velocity

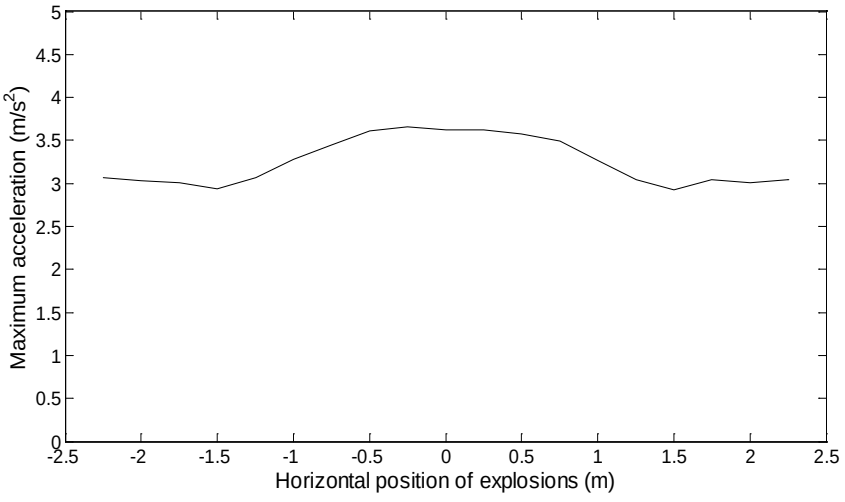

(c) The maximum acceleration

Figure 64. Effect of the horizontal position of explosions along the section of cross passage on the motion of main tunnel.

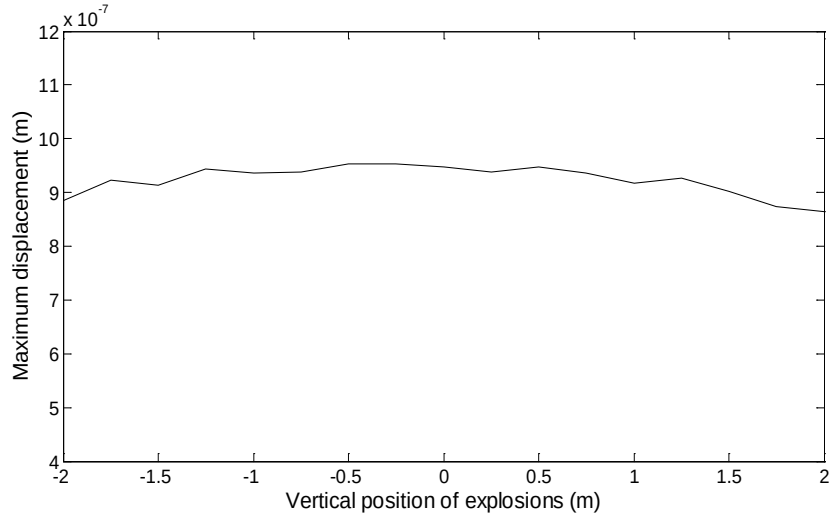

(a) The maximum displacement

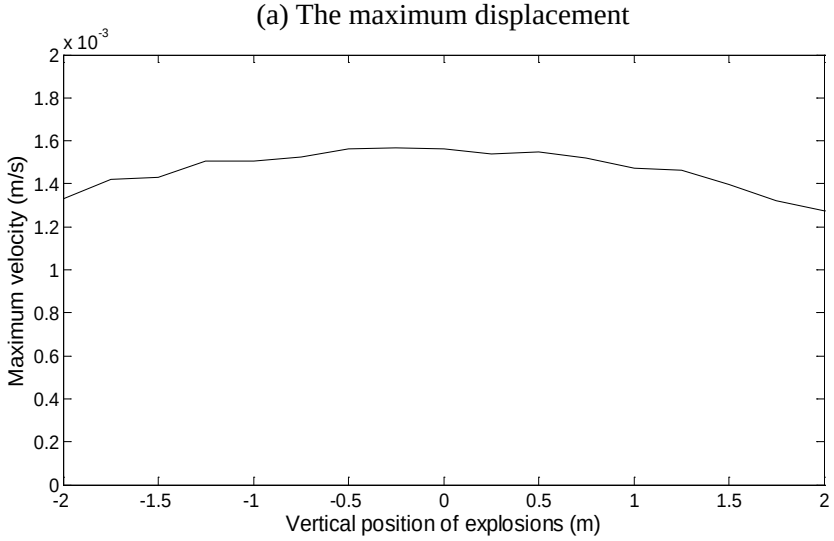

(b) The maximum velocity

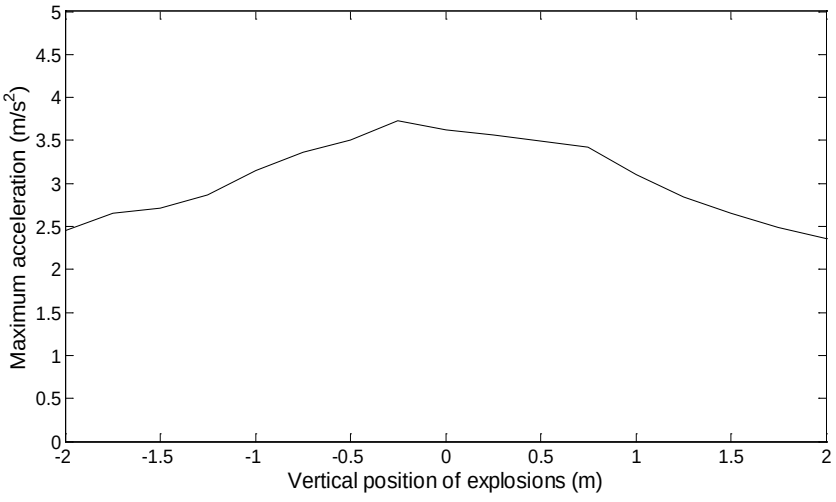

(c) The maximum acceleration

Figure 65. Effect of the vertical position of explosions along the section of cross passage on the motion of main tunnel.

5.4.5 Effect of the blast pressure

Figure 66 shows the effect of the blast pressure on the motion of main tunnel. It is clear to see that the maximum displacement, velocity and acceleration of main tunnel increase linearly with an increasing blast pressure, as expected. This can be attributed to the assumptions that the rock and tunnels are elastic and their interfaces are perfected bonded. Apparently, it is impossible for main tunnel to keep elastic constantly with an increasing blast pressure. Plastic analysis has to be introduced when the blast pressure is strong enough to generate the plastic deformation of tunnel. As mentioned earlier, the CDP model for the tunnel will be adopted later on to investigate the evolution of the motion, the possible damage and stiffness degradation of main tunnel.

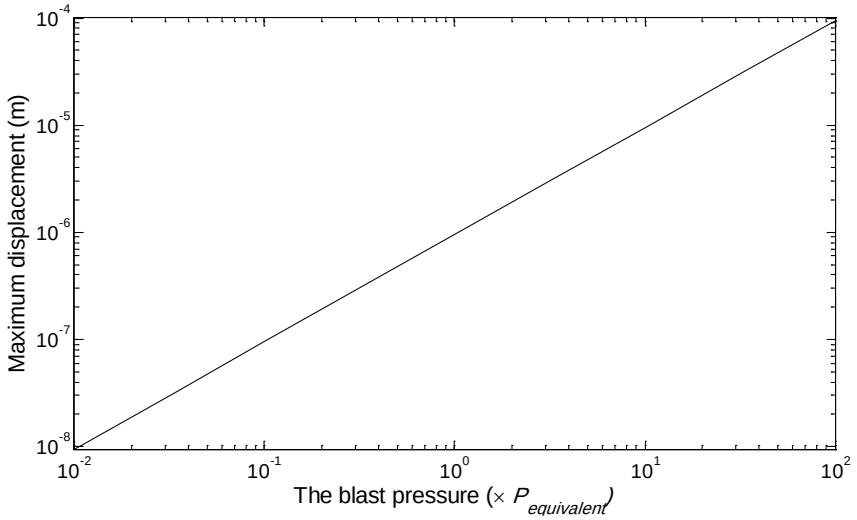

(a) The maximum displacement

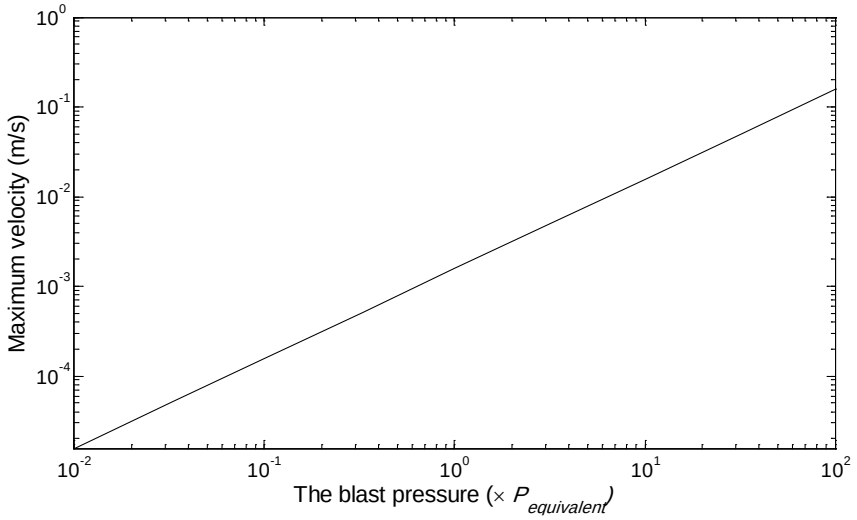

(b) The maximum velocity

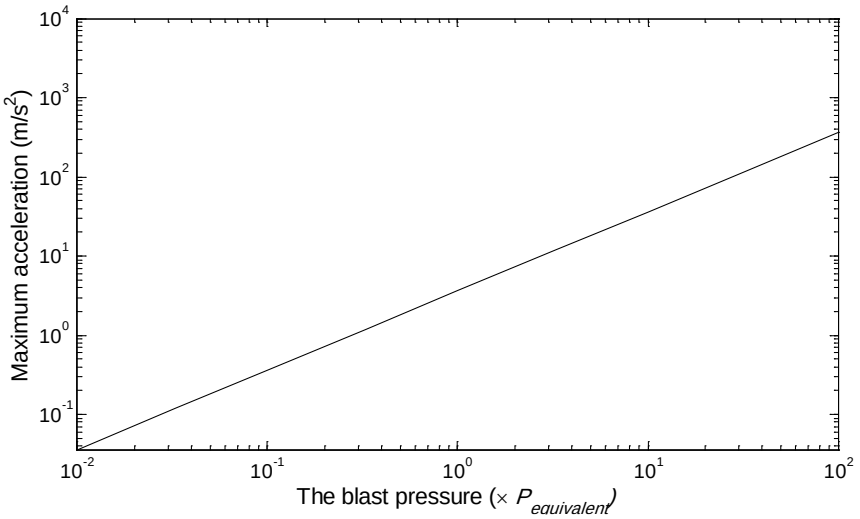

(c) The maximum acceleration

Figure 66. Effect of the blast pressure on the motion of main tunnel.

5.4.6 Effect of the burial depth of main tunnel

In this study, both the main tunnel and the safety tunnel are built deeply into the mountains, so there is no consideration of the influence of waves reflected by the boundaries of the rock media (the rock is assumed homogeneous, isotropic and elastic media). However, some tunnels, like the subways, are built near the surface of rock or soil media, where waves generated by explosions may be reflected when they propagate on the top surface, and the motion of tunnels may be affected. Thus, it is necessary to investigate the effect of explosions on the tunnel which has shallow burial depths. Figure 67 shows the evolution of the main tunnel motion over the burial depth. The investigated burial depth of main tunnel ranges from 5.5 m to 30 m. It can be seen that the maximum velocity and acceleration of main tunnel changes little with an increasing *h*. For the maximum displacement, it almost remains constant except that there is a slight increase when the burial depth *h* decreases from 10 m to 5.5 m. Based on the observations above, it is inferred that the burial depth of tunnel basically has a minor influence on the tunnel motion. This may be due to the phenomenon that the waves reflected by the top surface propagate in all directions, and the amount of reflected waves which are able to reach the existing tunnel is so small that its influence on the vibration of main tunnel can be almost ignored.

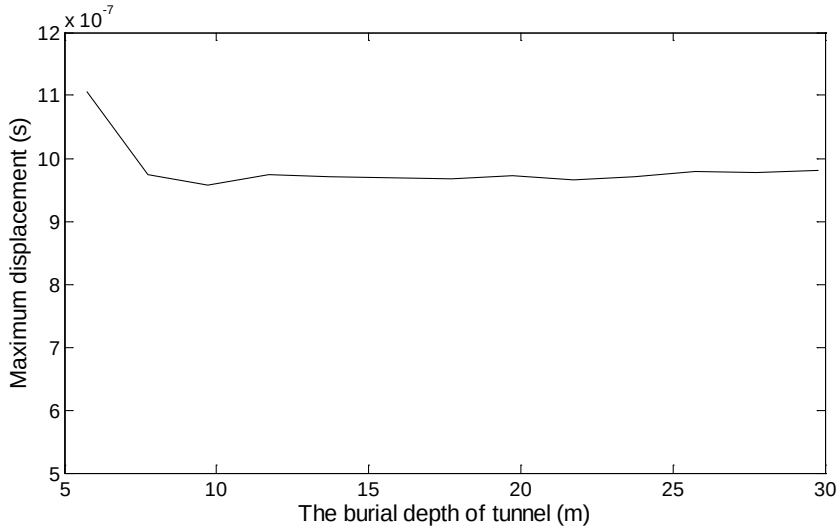

(a) The maximum displacement

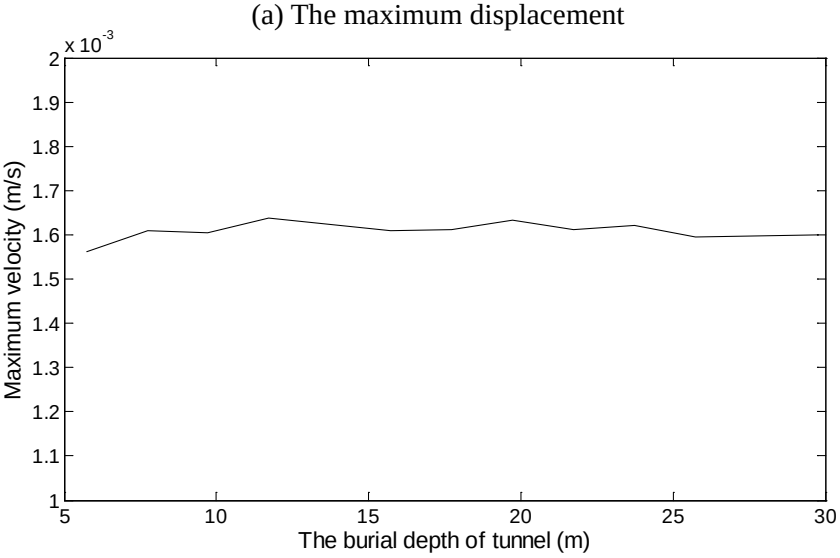

(b) The maximum velocity

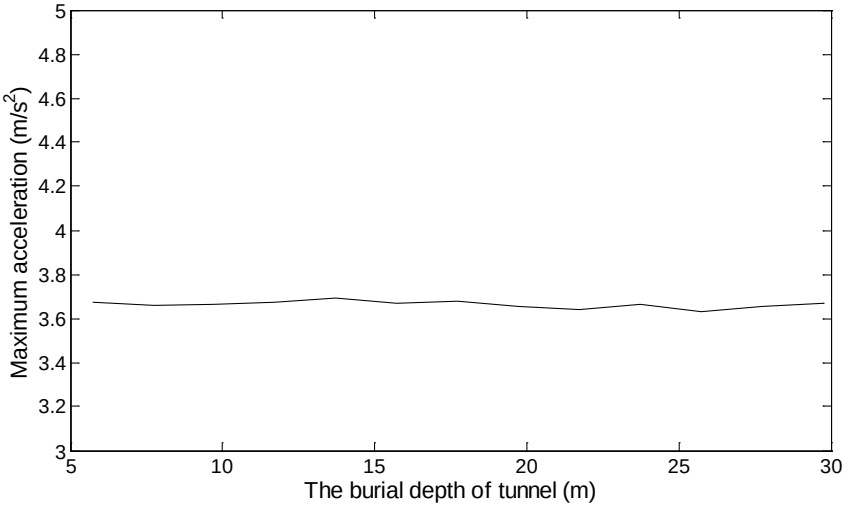

(c) The maximum acceleration

Figure 67. Effect of the burial depth of main tunnel on the tunnel motion.

5.5 Main tunnel damage evaluation

5.5.1 Concrete damaged plasticity model (CDP model)

During the parametric study in Section 5.4, it is found that the variation of the maximum motion of main tunnel is linear to that of the magnitude of the blast pressure (see Figure 66). However, as previously stated, such conclusion is based on the assumptions that the lining structure is elastic. With an increasing blast pressure, there is no doubt that the main tunnel lining structure no longer keeps elastic. When the blast pressure exceeds a certain value, plastic deformation or even damage will certainly appear on the lining. Therefore, from a practical view, it is better to adopt a constitutive model which is able to reflect the nonlinear behavior of main tunnel. While the CDP model, which is a continuum, plasticity-based, damage model, can exactly provide a general capability for modeling concrete and other quasi-brittle materials subjected to monotonic, cyclic, and/or dynamic loading [123]. Thus, in the present study, the CDP model is adopted to simulate the plastic deformation of main tunnel and to find out the locations of the lining damage and stiffness degradation during strong explosions. Besides, it is noted that only the tunnel lining structure is examined in this Section, there is no slabs inside. In the next Section (Section 5.6), the influence of the slabs and the dynamic behavior of both the lining and the slabs will be discussed.

Here the developed finite element model of the rock-tunnel system is still based on the model presented in Figure 56. The only difference is that the CDP model, rather than elastic model is used for the lining structure, and the setting of Nlgeom should be ON in ABAQUS, for possible large-displacement consideration. The input parameters of CDP model in ABAQUS is listed in Table 17. And Rayleigh damping of 5% is adopted for the whole model. Based on the Table 17, the concrete compressive and tensile properties can be plotted, as shown in Figures 68 and 69, respectively. It can be seen that the concrete compressive stress is almost linear to the crushing strain until the value of initial yield stress, which is about 40.30 MPa. As the compressive stress keep increasing, plastic deformation is observed, such plastic response is generally characterized by stress hardening until the value of ultimate stress, which is about 50.01 MPa. Then followed by the concrete strain softening state, where the crushing strain increases dramatically with a decreasing compressive stress. For the tensile response, a linear elastic relationship is observed until the value of failure stress, which is about 2.84 MPa. Beyond the failure stress, a similar softening stress-strain response can be observed. Besides, it is seen that there is no compression (tension) damage when the crushing (cracking) strain is very small, but the compression (tension) damage tends to increase rapidly with an increasing crushing (cracking) strain. It is noted that the values of damage variables should be smaller than 0.99, for excessive

damages have a critical effect on the rate of convergence [123], which may cause convergence difficulty. In this study, all the compression damage and tension damage are below 0.99.

Table 17. Concrete damaged plasticity model parameters

Parameter	Description	Value
ρ	Density	2500 kg/m^3
E	Young's modulus	20 GPa
ν	Poisson's ratio	0.15
ψ	Dilation angle	38°
ε	Flow potential eccentricity	0.1
f_{bo}/f_{co}	The ratio of initial equi-biaxial compressive yield stress to Initial uniaxial compressive yield stress	1.16
K	The ratio of the second stress invariant on the tensile meridian	0.667
V_c	Viscosity coefficient	0

Concrete compression hardening*		Concrete compression damage*	
Stress [Pa]	Crushing strain	Damage	Crushing strain
15000000	0	0	0
20197804	0.0000747307	0	0.0000747307
30000609	0.0000988479	0	0.0000988479
40303781	0.0001541230	0	0.0001541230
50007692	0.0007615380	0	0.0007615380
40236090	0.0025575590	0.195402	0.0025575590
20236090	0.0056754310	0.596382	0.0056754310
5257557	0.0117331190	0.894865	0.0117331190
Concrete tension stiffening*		Concrete tension damage*	
Stress [Pa]	Cracking strain	Damage	Cracking strain
1998930	0	0	0
2842000	0.000033330	0	0.000033330
1869810	0.000160427	0.406411	0.000160427
862723	0.000279763	0.696380	0.000279763
226254	0.000684593	0.920389	0.000684593
56576	0.001086730	0.980093	0.001086730

* The representative values provided by Jankowiak [124] are adopted.

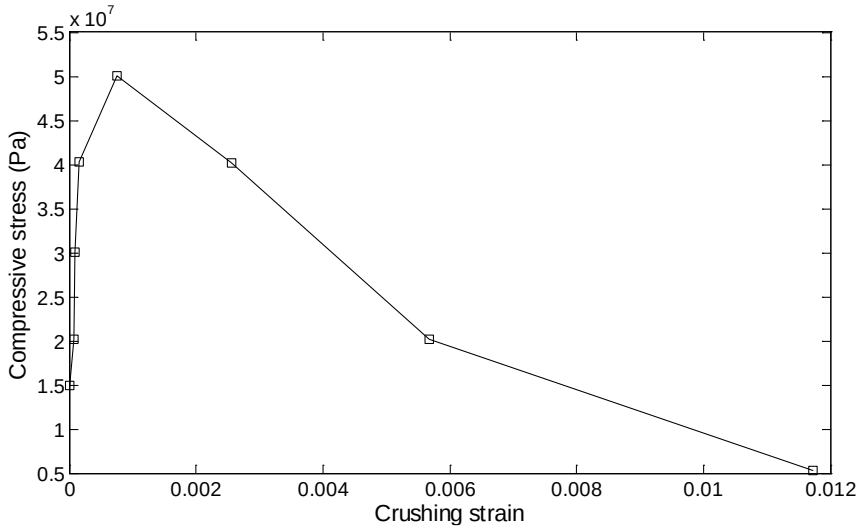

(a) Concrete compression hardening

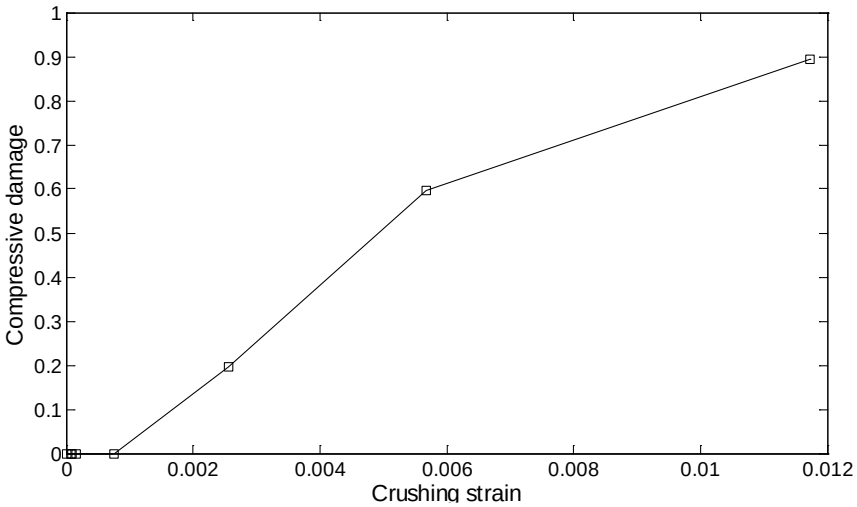

(b) Concrete compression damage

Figure 68. Concrete compressive properties: compressive stress and compression damage verse crushing strain.

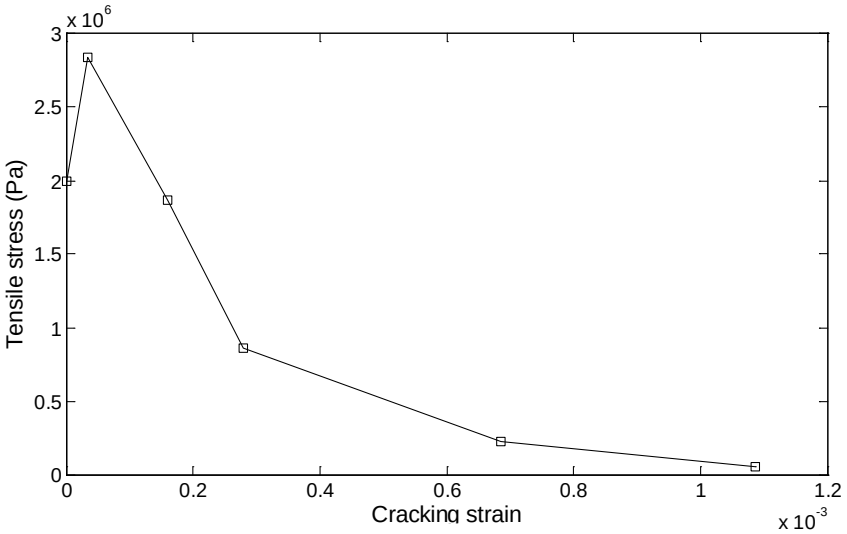

(a) Concrete tension stiffening

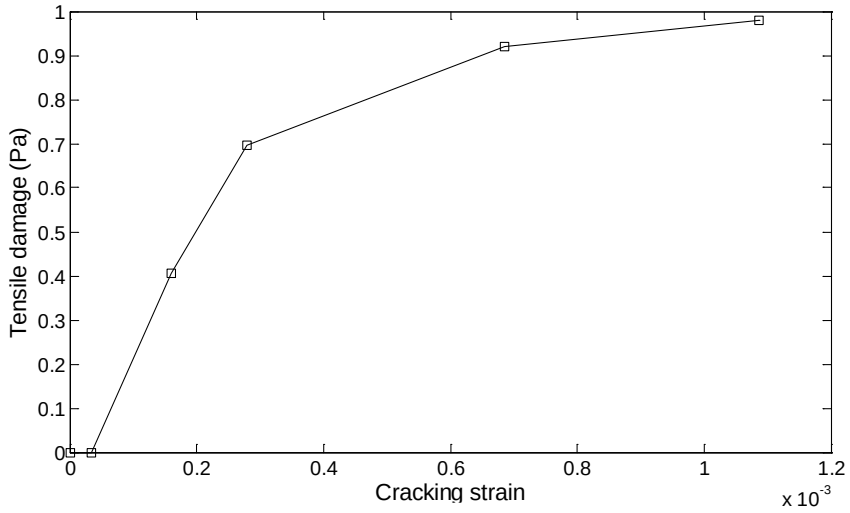

(b) Concrete tension damage

Figure 69. Concrete tensile properties: tensile stress and tension damage verse cracking strain.

5.5.2 Comparisons study between elastic analysis and elastic plastic analysis

5.5.2.1 Main tunnel under weak explosions

It is known that when the blast pressure is small, it is reasonable to assume that the tunnel lining keeps elastic under explosions. However, as the explosions become stronger and stronger, it is certain that the plastic deformation of the tunnel will appear. In such case, elastic plastic analysis must be introduced. Here, based on the 3D finite element model created in Figure 56, a comparison study on the behavior of main tunnel with elastic model and CDP model is presented, aiming to find out when and where the plastic deformation, compression damage, tension damage and stiffness degradation of main tunnel occur and develop with an increasing blast pressure. Figures 70 and 71 show the evolution of the motion at point "a1" and "b1" (see Figure 55) over time, respectively, using elastic model (on the left side) and CDP model (on the right side) for the main tunnel lining. It is observed that there is no visualized difference of the displacement, velocity and acceleration for both the point "a1" and "b1" between elastic model and CDP model. From Figure 72, which shows the distribution of maximum displacement, velocity and acceleration of main tunnel (CDP model) under explosions, it is found that the tunnel maximum motion occurs in the following positions: the maximum displacement in the Node: PART-1-1.100685, the maximum velocity in the Node: PART-1-1.100665 and the maximum acceleration in the Node: PART-1-1.99818. It is noted that these points are exactly the same positions of the maximum motion of main tunnel when elastic model for the lining is adopted (see Figure 60). And the values of the maximum displacement, velocity and acceleration, which are respectively 9.456×10^{-7} m, 1.551×10^{-3} m/s and 3.604 m/s^2, are very close to the corresponding ones of main tunnel in the case that elastic model is used, which are 9.442×10^{-7} m, 1.549×10^{-3} m/s and 3.579 m/s^2, respectively (see Figure 60). The very likely explanation for the phenomenon above is the small blast pressure generated by the weak explosions (the blast pressure is $P_{equivalent}$). In fact, the magnitude of the investigated blast pressure is so small that no plastic deformation of main tunnel appears. This can be verified by Figure 73, which shows the distribution of the maximum compression damage, tension damage and stiffness degradation of main tunnel under explosions. It is found that there are no compression damage, no tension damage and no stiffness degradation. This means that main tunnel keeps being elastic during the explosions. Therefore, the numerical results produced by elastic model and CDP model are almost the same.

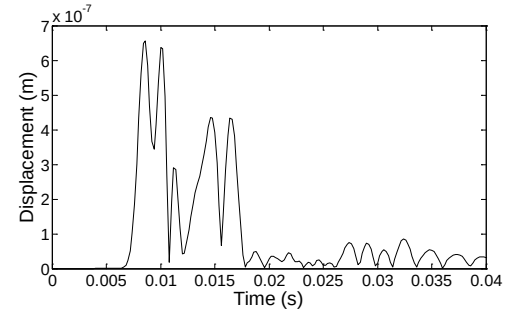

(a) Displacement at point *"*a1*"* in 3D (for elastic model)

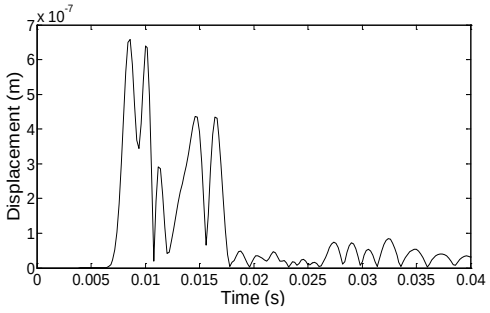

(b) Displacement at point *"*a1*"* in 3D (for CDP model)

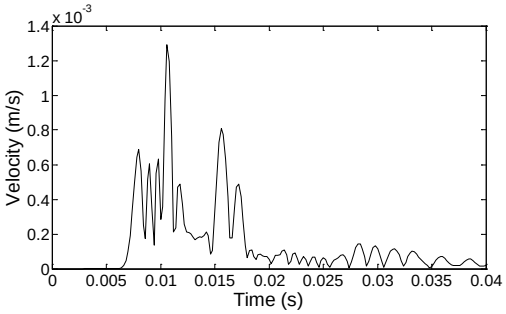

(c) Velocity at point *"*a1*"* in 3D (for elastic model)

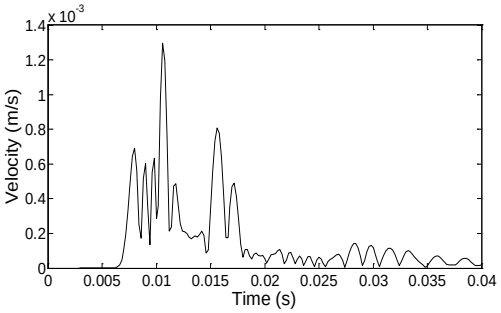

(d) Velocity at point *"*a1*"* in 3D (for CDP model)

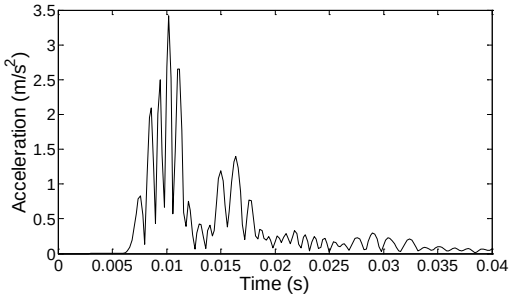

(e) Acceleration at point *"*a1*"* in 3D (for elastic model)

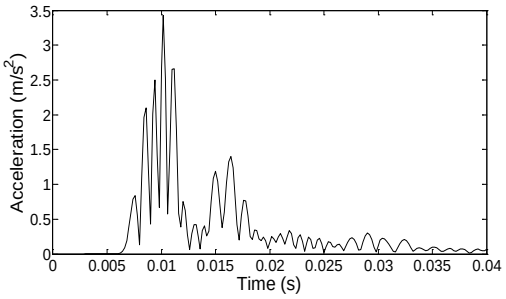

(f) Acceleration at point *"*a1*"* in 3D (for CDP model)

Figure 70. The motion of main tunnel at point "a1" over time (the tunnel lining with elastic model on the left side, and with CDP model on the right side, the blast pressure is $P_{equivalent}$).

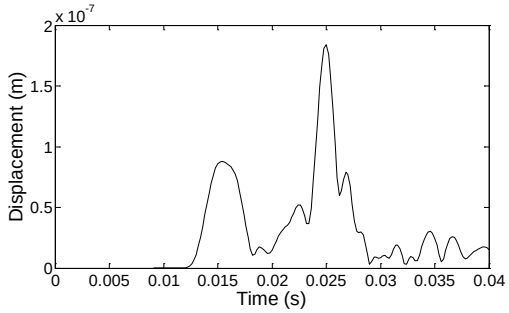

(a) Displacement at point "b1" in 3D (for elastic model)

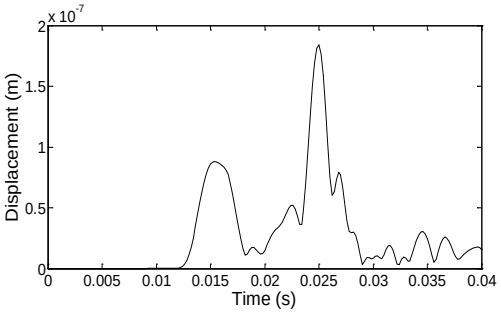

(b) Displacement at point "b1" in 3D (for CDP model)

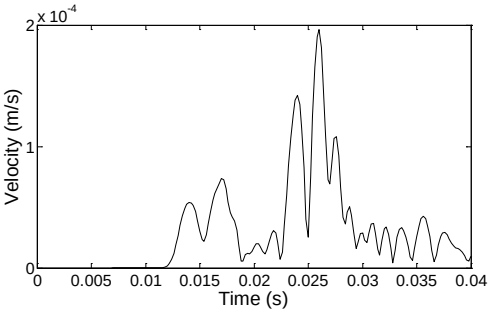

(c) Velocity at point "b1" in 3D (for elastic model)

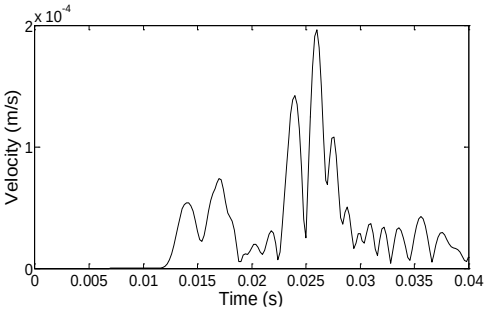

(d) Velocity at point "b1" in 3D (for CDP model)

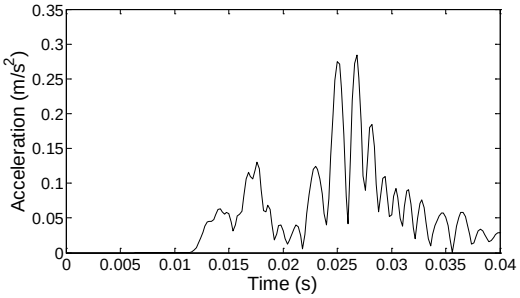

(e) Acceleration at point "b1" in 3D (for elastic model)

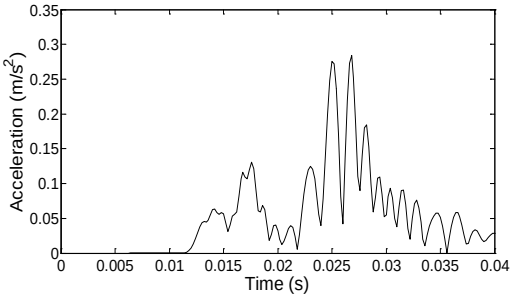

(f) Acceleration at point "b1" in 3D (for CDP model)

Figure 71. The motion of main tunnel at point "b1" over time (the tunnel lining with elastic model on the left side, and with CDP model on the right side, the blast pressure is $P_{equivalent}$).

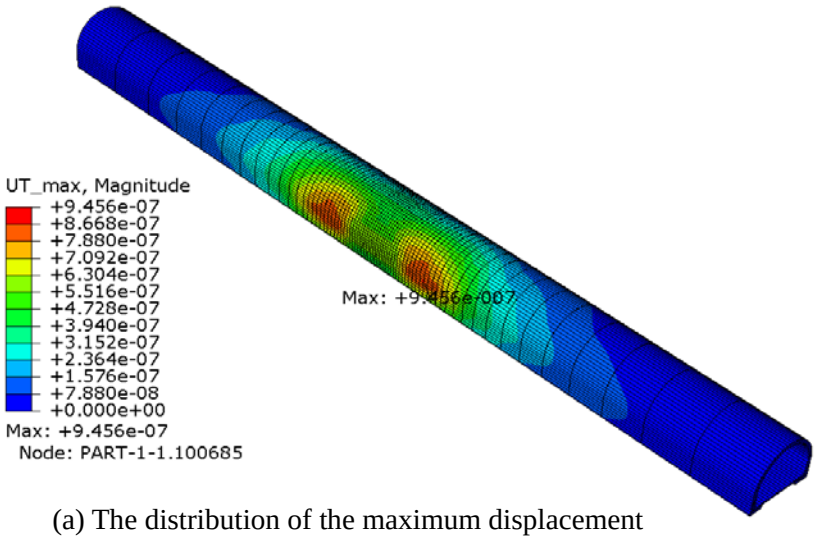

(a) The distribution of the maximum displacement

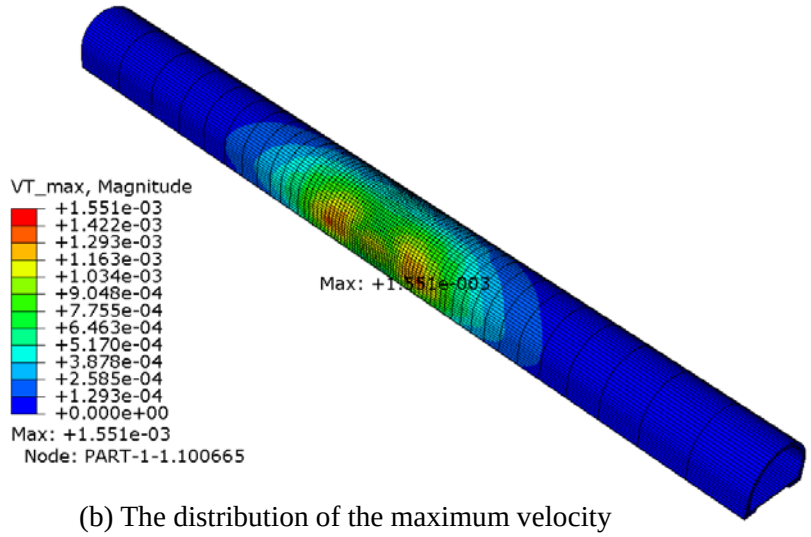

(b) The distribution of the maximum velocity

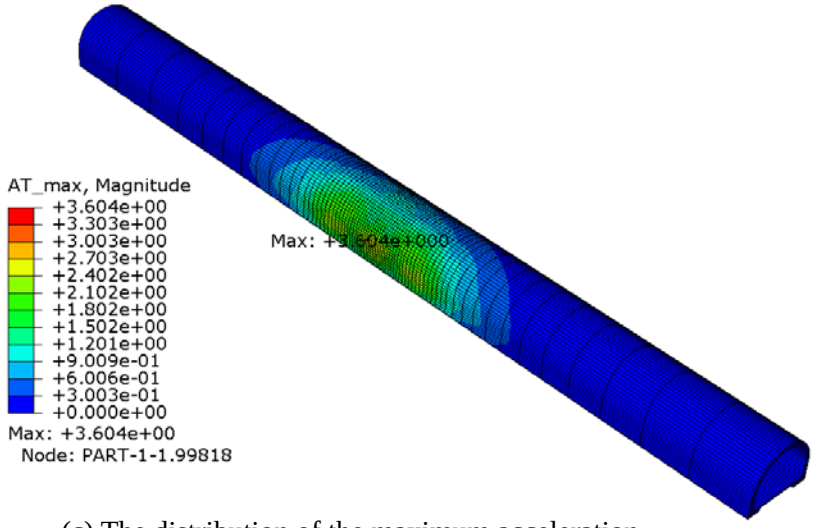

(c) The distribution of the maximum acceleration

Figure 72. The distribution of the maximum motion of main tunnel (CDP model) under explosions (the blast pressure is $P_{equivalent}$).

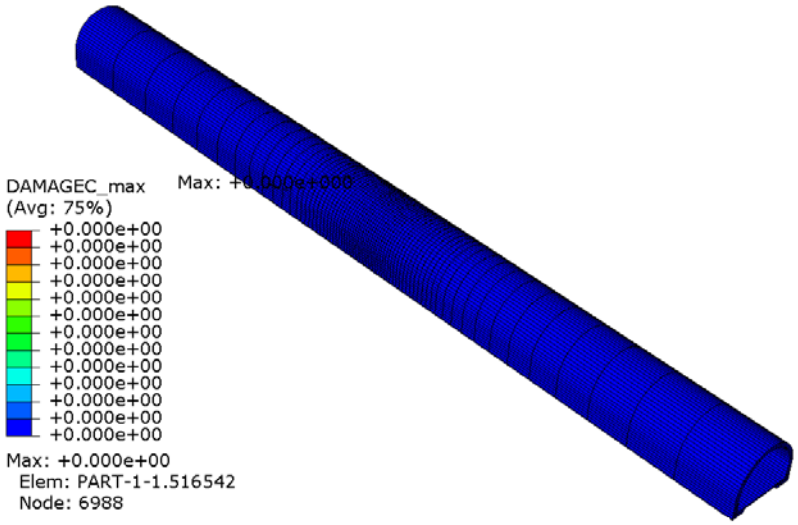

(a) The distribution of the maximum compression damage

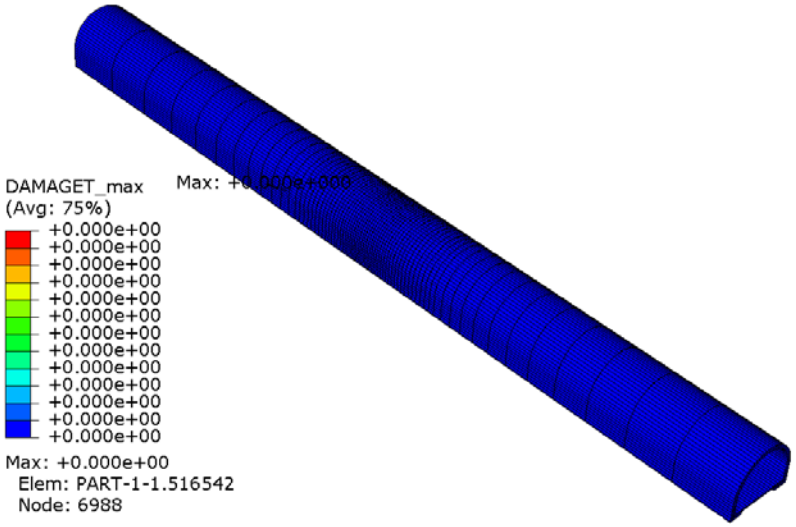

(b) The distribution of the maximum tension damage

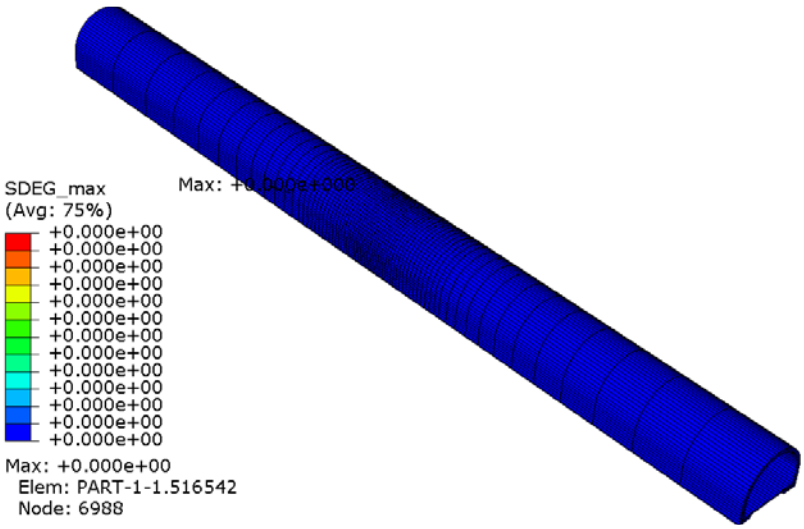

(c) The distribution of the maximum stiffness degradation

Figure 73. The distribution of maximum compression damage, tension damage and stiffness degradation of main tunnel (CDP model) under explosions (the blast pressure is $P_{equivalent}$).

5.5.2.2 Main tunnel under strong explosions

From the Section 5.5.2.1, it is found that the main tunnel with CDP model has almost the same motion as the one with elastic model under weak explosions. However, will the tunnel motion keep the same if the explosions become stronger? Here, a much larger blast pressure, which is assumed 400 times as large as the one used previously, is adopted. It is noted that only the blast pressure is changed from $P_{equivalent}$ to $400P_{equivalent}$, all the other parameters in the model (see Figure 56) keep constant. Figures 74 and 75 respectively show the motion of point "a1" and "b1" over time, using elastic model (on the left side) and CDP model (on the right side) for the main tunnel lining. Compared with the Figure 70(a), (c), (e) and Figure 74(a), (c), (e), it can be seen that in the case of elastic model, the displacement, velocity and acceleration of point "a1" become about 400 times large as the blast pressure increases from $P_{equivalent}$ to $400P_{equivalent}$, as expected. However, an increase of about 800 times large is found for the motion of point "a1" in the case of CDP model during the same increase of the blast pressure (see Figure 70(b), (d), (f) and Figure 74(b), (d), (f)). Similar phenomenon can be observed for the motion of point "b1" when elastic model and CDP models are adopted as the blast pressure increases from $P_{equivalent}$ to $400P_{equivalent}$ (see Figure 71 and 75). Figure 76 shows the distribution of maximum motion of the main tunnel with CDP model under explosions, where the blast pressure is 400 $P_{equivalent}$. It is seen that the maximum displacement, velocity and acceleration of main tunnel, which are 7.601×10^{-4} m, 1.272 m/s and 2.883×10^{3} m/s^2, respectively, are 805.020, 821.175 and 805.532 times as large as the corresponding ones of main tunnel in the case of elastic model is adopted under the blast pressure $P_{equivalent}$ (see Figure 60). Based on the observation above, it is inferred that the motion of main tunnel predicted by CDP model is about two times as large as the one predicted by elastic model. This indicates that large plastic deformation appears when the main tunnel suffers the strong explosions, where a slight increase in the blast pressure can result in a significant increase in the tunnel deformation. This inference can be confirmed by Figure 77, which shows the distribution of the maximum compression damage, tension damage and stiffness degradation of main tunnel under the blast pressure of $400P_{equivalent}$. Enlarged views about the central area of main tunnel are presented as well. It is obvious to see that the compression damage, tension damage and stiffness degradation, all appear on the tunnel lining. It is noted that the compression damage is so small (the maximum value is 3.992×10^{-4}) that it is hard to be noticed; however, the tension damage and stiffness degradation develop very quickly and are quite remarkable. The maximum tension damage and stiffness degradation are 0.9026 and 0.8626, respectively. This means that 90.26% reduction of the tension resistance capability and 86.26% loss of the tunnel lining stiffness occur under the blast pressure of $400P_{equivalent}$. Finally, it is worth pointing out that the most vulnerable areas for the tunnel lining are the top heading of the lining arch and the foot of the sidewall on the side near the explosions.

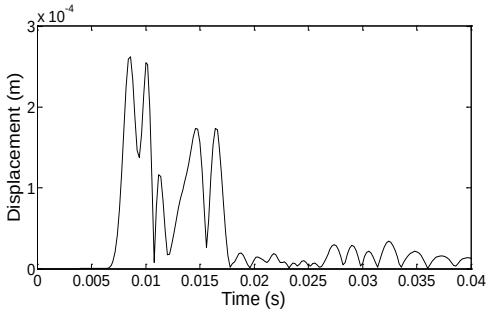

(a) Displacement at point "a1" in 3D (for elastic model)

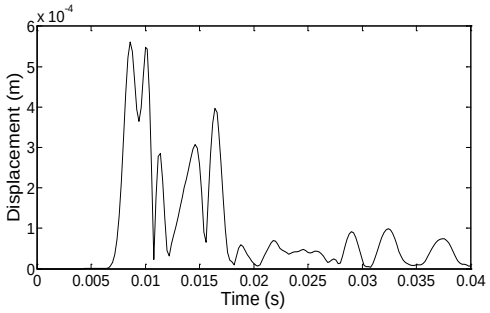

(b) Displacement at point "a1" in 3D (for CDP model)

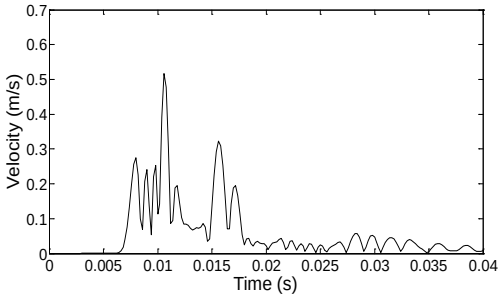

(c) Velocity at point "a1" in 3D (for elastic model)

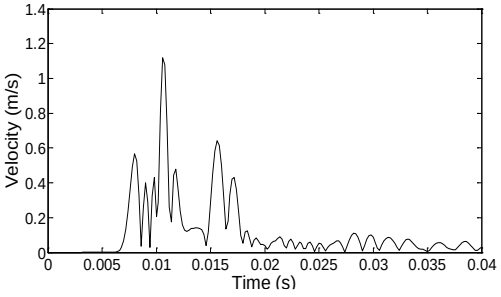

(d) Velocity at point "a1" in 3D (for CDP model)

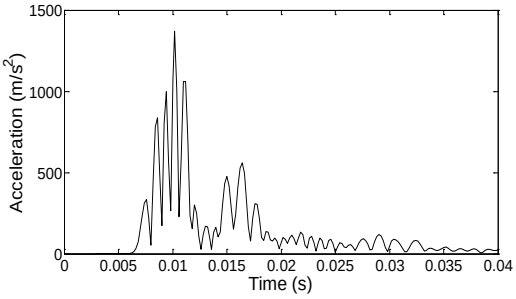

(e) Acceleration at point "a1" in 3D (for elastic model)

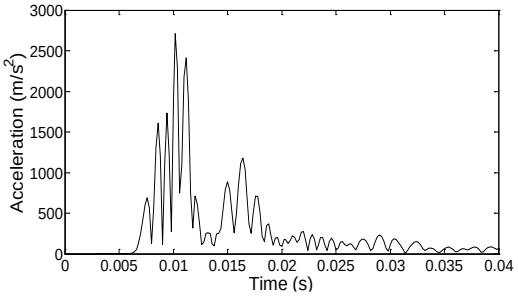

(f) Acceleration at point "a1" in 3D (for CDP model)

Figure 74. The motion of main tunnel at point "a1" over time (the tunnel lining with elastic model on the left side, and with CDP model on the right side, the blast pressure is $400P_{equivalent}$).

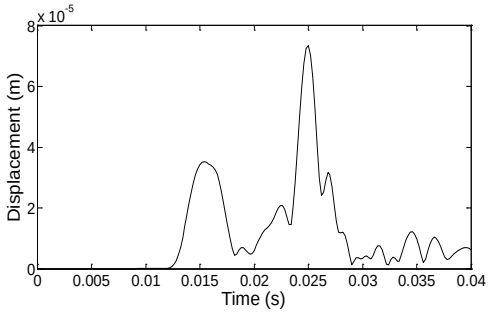

(a) Displacement at point *"*b1*"* in 3D (for elastic model)

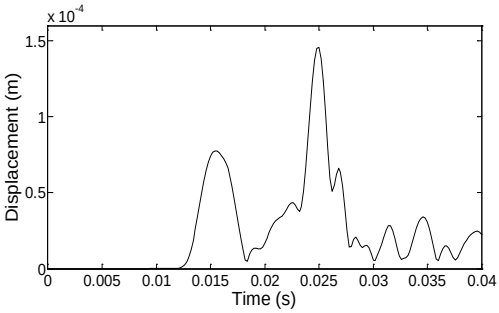

(b) Displacement at point *"*b1*"* in 3D (for CDP model)

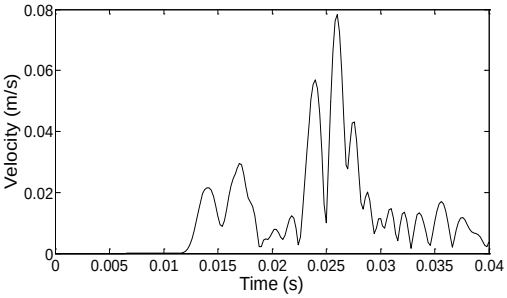

(c) Velocity at point *"*b1*"* in 3D (for elastic model)

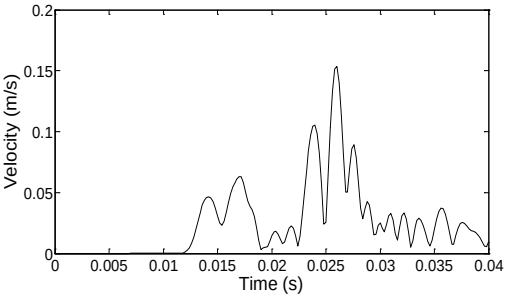

(d) Velocity at point *"*b1*"* in 3D (for CDP model)

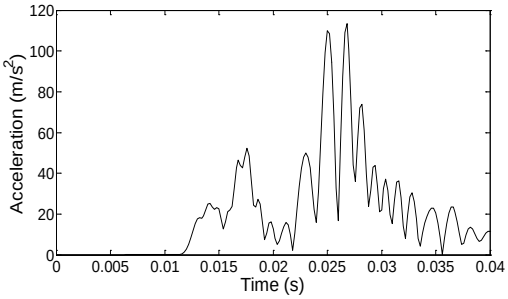

(e) Acceleration at point *"*b1*"* in 3D (for elastic model)

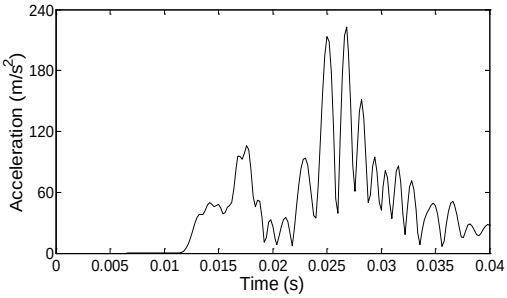

(f) Acceleration at point *"*b1*"* in 3D (for CDP model)

Figure 75. The motion of main tunnel at point "b1" over time (the tunnel lining with elastic model on the left side, and with CDP model on the right side, the blast pressure is $400P_{equivalent}$).

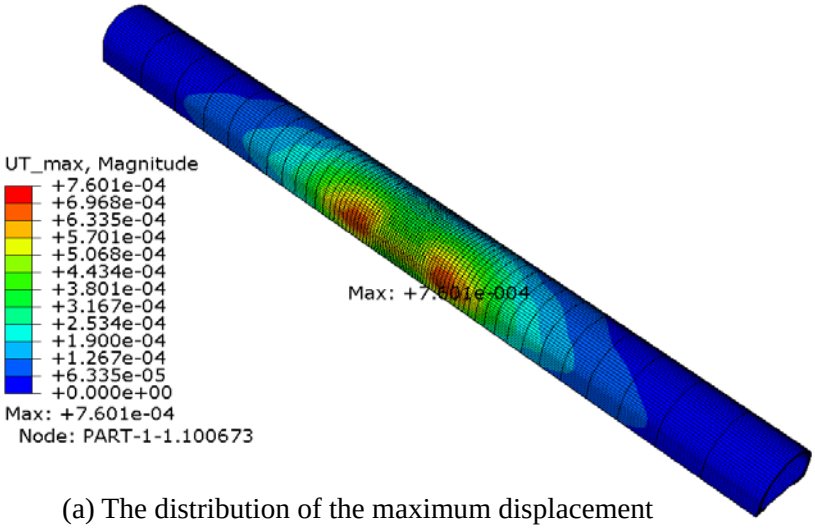

(a) The distribution of the maximum displacement

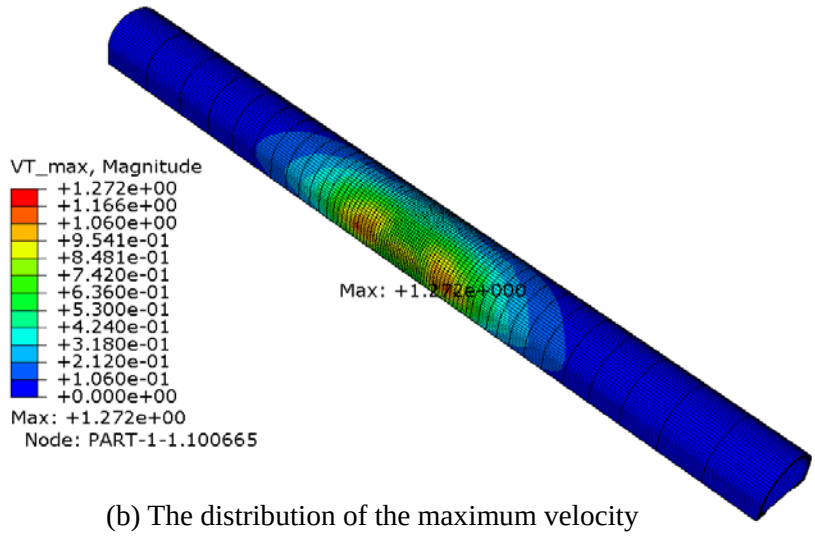

(b) The distribution of the maximum velocity

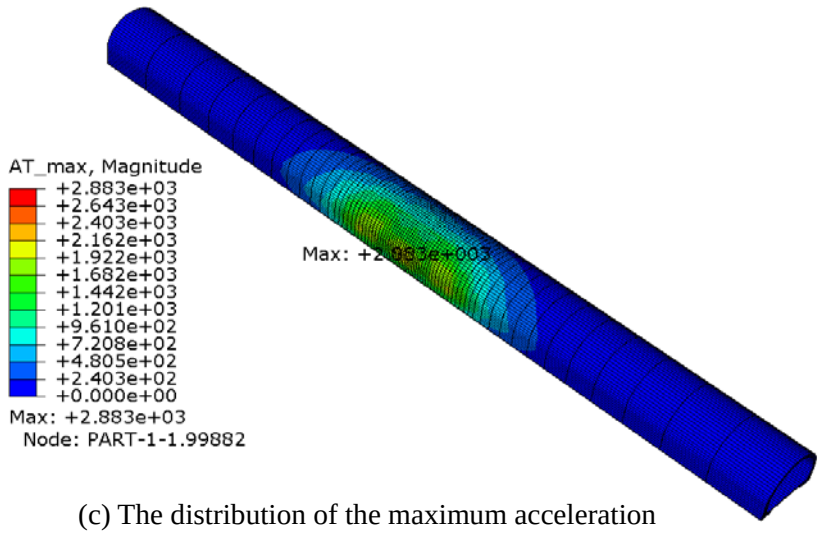

(c) The distribution of the maximum acceleration

Figure 76. The distribution of maximum motion of main tunnel (CDP model) under explosions (the blast pressure is $400P_{equivalent}$).

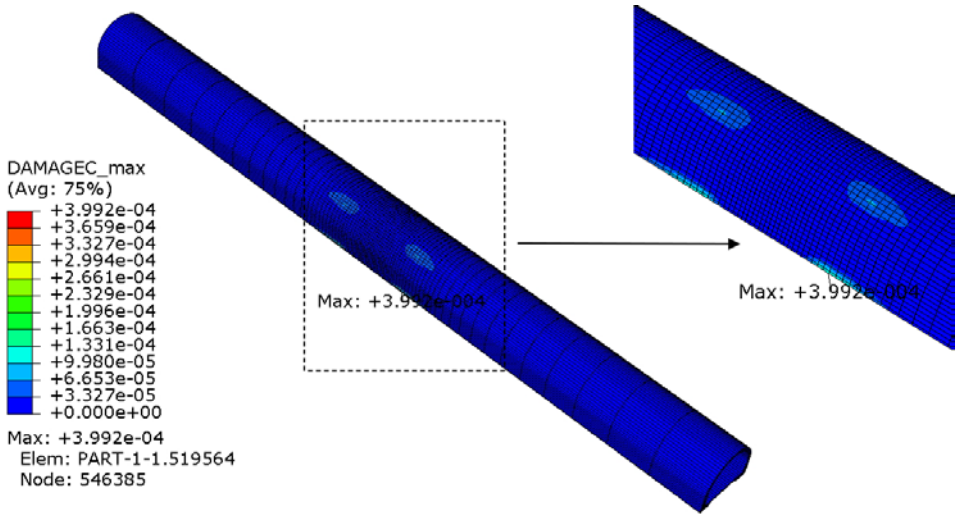

(a) The distribution of the maximum compression damage

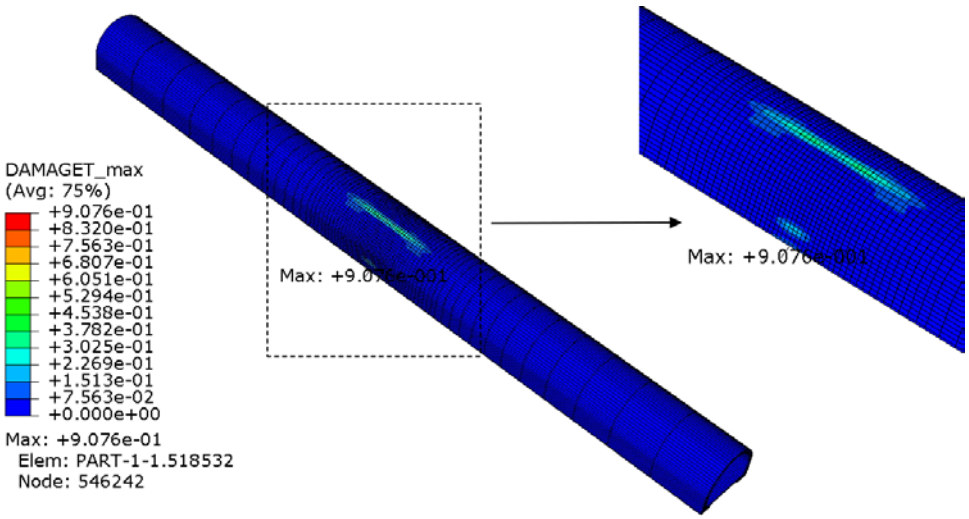

(b) The distribution of the maximum tension damage

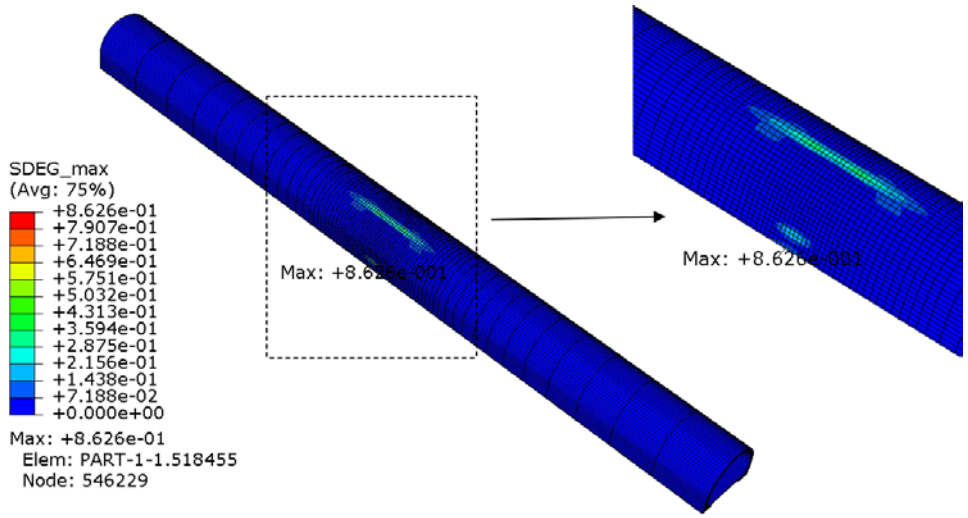

(c) The distribution of the maximum stiffness degradation

Figure 77. The distribution of maximum compression damage, tension damage and stiffness degradation of main tunnel (CDP model) under explosions (the blast pressure is $400P_{equivalent}$).

Here, to investigate the behavior of main tunnel in a comprehensive way, the evolution of the maximum motion of main tunnel with both elastic model and CDP model under explosions with an increasing blast pressure is presented, as shown in Figure 78. It is clear to see that when the blast pressure is small ($< 60P_{equivalent}$), there is no difference of the tunnel motion between the CDP model and the elastic model. However, as the blast pressure increases ($> 60P_{equivalent}$), the tunnel motion predicted by the CDP model gradually becomes larger than the one predicted by the elastic model. Furthermore, the larger the blast pressure is, the much larger tunnel motion that CDP model produces. These phenomena can be explained as follows: explosions with small blast pressure can only result in the tunnel's elastic deformation. But as the explosions become stronger, there is no doubt that plastic deformation will appear, moreover, a small increase of the blast pressure will generate a significant increase in the tunnel plastic deformation. Based on the analysis above, it is recommended that CDP model have to be adopted to better reflect the real behavior of main tunnel under strong explosions. In this study, the blast pressure of $60P_{equivalent}$ can be considered as the minimum value for adopting CDP model during the numerical simulation. Figure 79 shows the evolution of compression damage, tension damage and stiffness degradation of main tunnel with an increasing blast pressure. It can be observed that the compression damage begins to appear when the blast pressure reaches to be $225P_{equivalent}$, while the tension damage occurs as the blast pressure increases to be as large as $325P_{equivalent}$. It should be mentioned that although the appearance of the compression damage is much earlier than that of tension damage during the increasing blast pressure from $P_{equivalent}$ to $500P_{equivalent}$, the maximum compression damage, which is 0.0002 when the blast pressure is $500P_{equivalent}$, is almost negligible compared with the maximum tension damage, which is close to 1 when the blast pressure is larger than $450P_{equivalent}$. Therefore, it is inferred that the main tunnel is very likely to suffer tension failure, rather than compression failure under strong explosions. Besides, it is seen that the variation of stiffness degradation seems to be firstly coincident with that of compression damage, and then become coincident with that of tension damage. Specifically, when the blast pressure is larger than $225P_{equivalent}$ but smaller than $325P_{equivalent}$ (i.e. there is compression damage but no tension damage), the variation of stiffness degradation keeps coincident with that of compression damage. Examination of the values of stiffness degradation shows that they are very close to the values of compression damage. However, it should be pointed out that the compression damage is so small that the stiffness degradation also seems to be unnoticeable. As the blast pressure becomes larger ($> 325P_{equivalent}$), remarkable tension damage, which is much larger than the compression damage, begins to appear. In such case, the variation of stiffness degradation turns to become coincident with that of tension damage. And when the tunnel lining is close to tension failure, almost all its stiffness is expected to be lost as well. In a word, it is found that the tunnel plastic deformation appears when the blast pressure increases to be

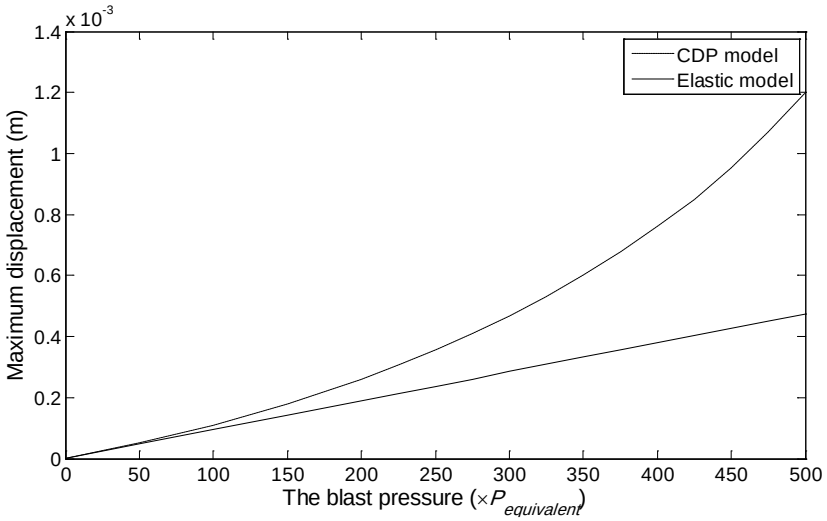

(a) The evolution of the maximum displacement

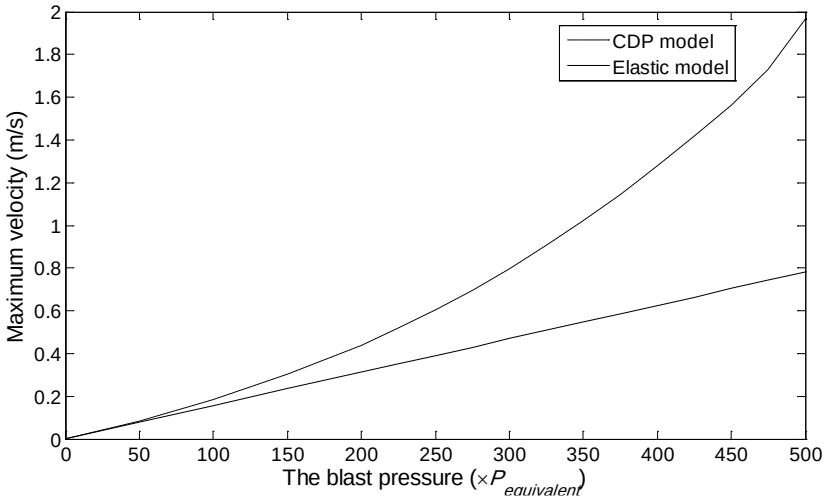

(b) The evolution of the maximum velocity

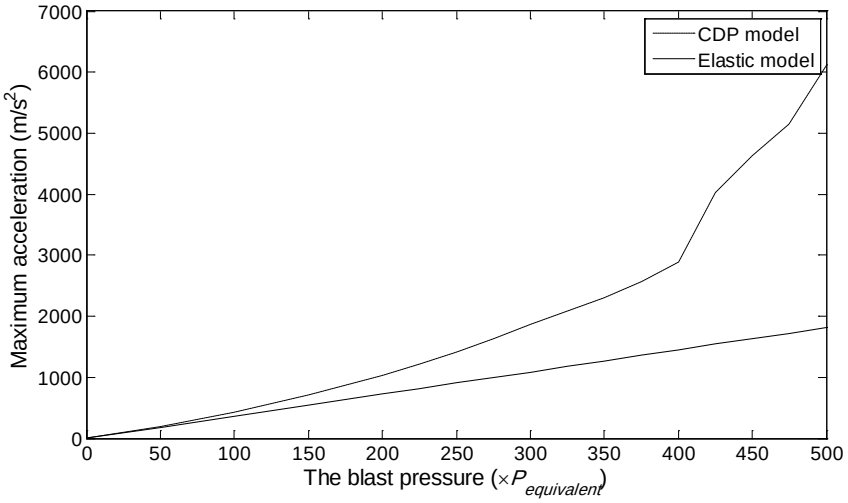

(c) The evolution of the maximum acceleration

Figure 78. The evolution of the maximum motion of main tunnel with CDP model and elastic model under blast pressures.

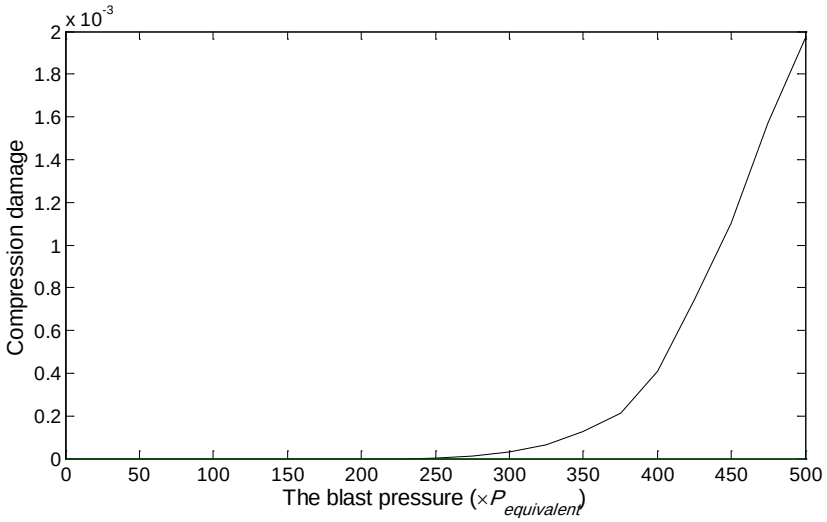

(a) The evolution of compression damage

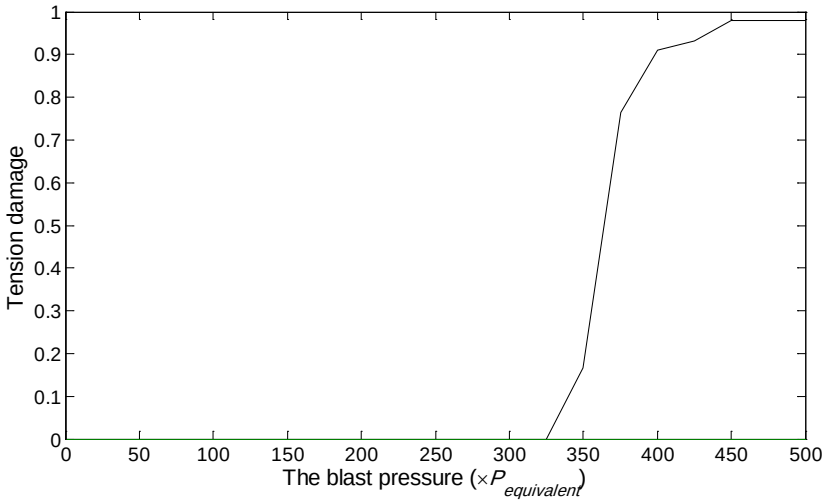

(b) The evolution of tension damage

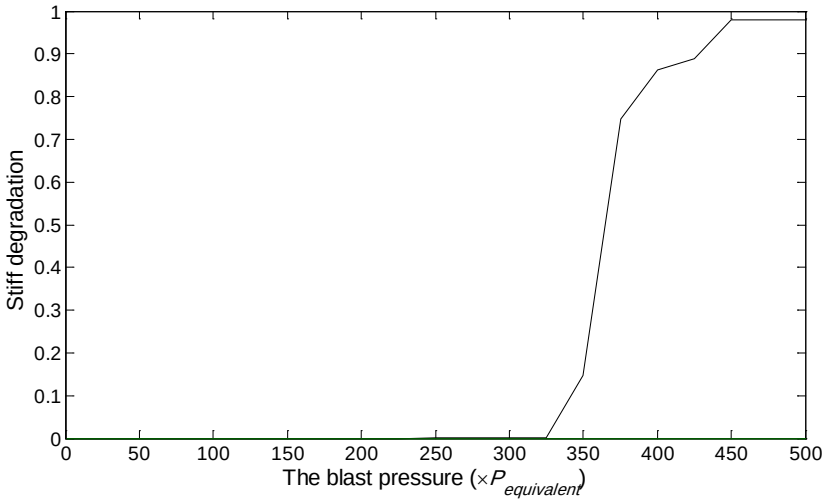

(c) The evolution of stiff degradation

Figure 79. The evolution of compression damage, tension damage and stiff degradation of main tunnel under blast pressures.

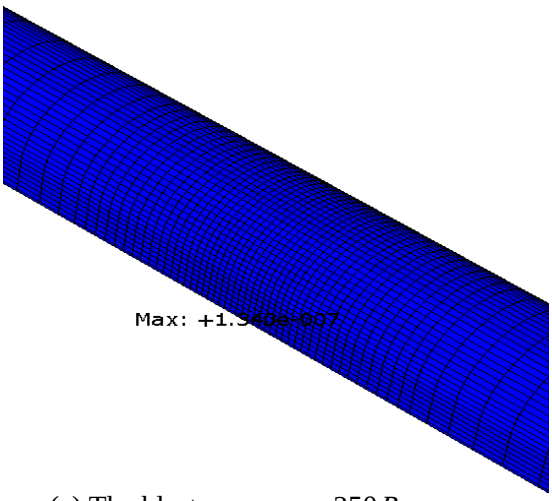

(a) The blast pressure = $250P_{equivalent}$

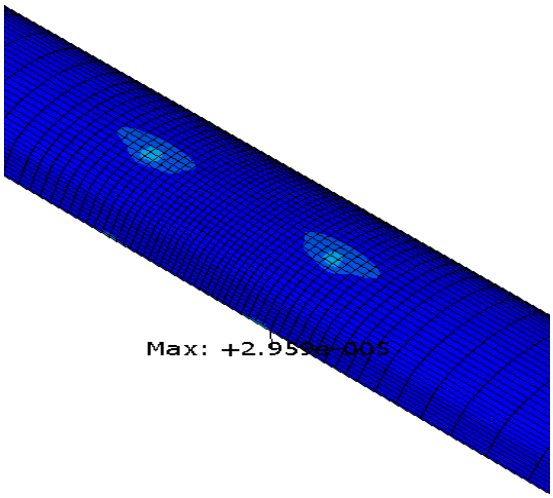

(b) The blast pressure = $300P_{equivalent}$

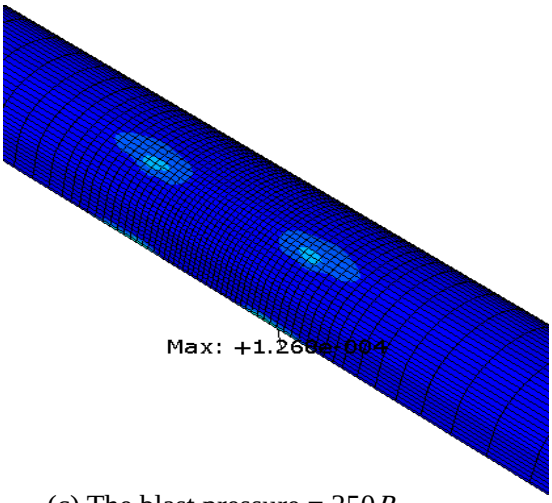

(c) The blast pressure = $350P_{equivalent}$

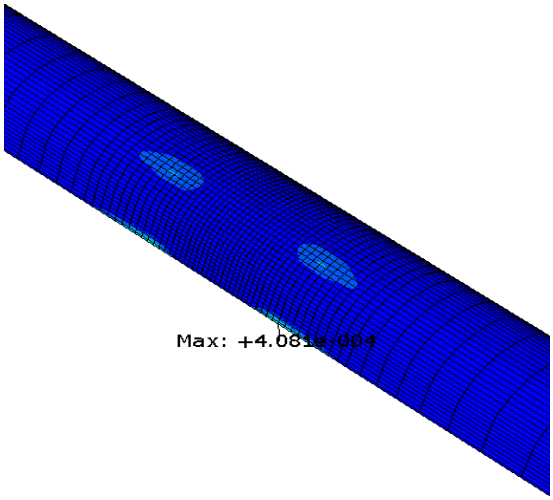

(d) The blast pressure = $400P_{equivalent}$

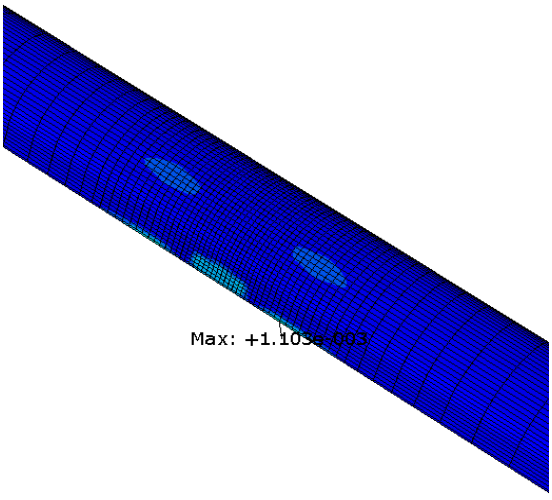

(e) The blast pressure = $450P_{equivalent}$

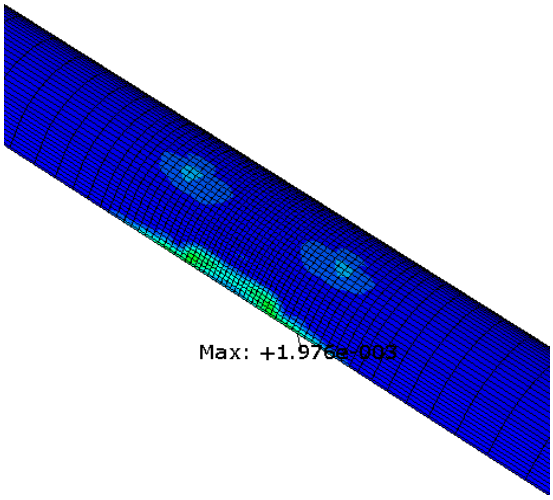

(f) The blast pressure = $500P_{equivalent}$

Figure 80. Compression damage nephogram of main tunnel under blast pressures.

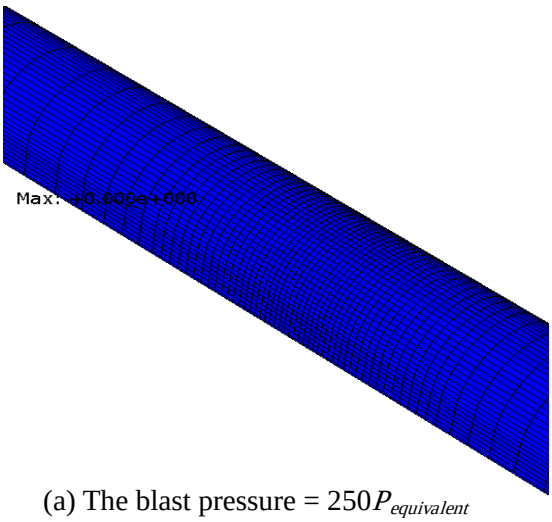

(a) The blast pressure = $250P_{equivalent}$

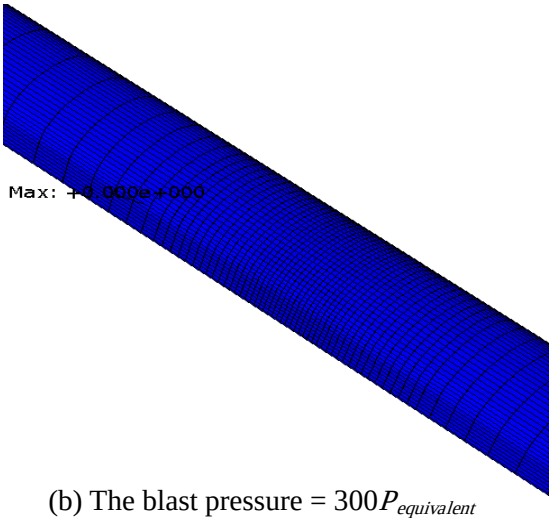

(b) The blast pressure = $300P_{equivalent}$

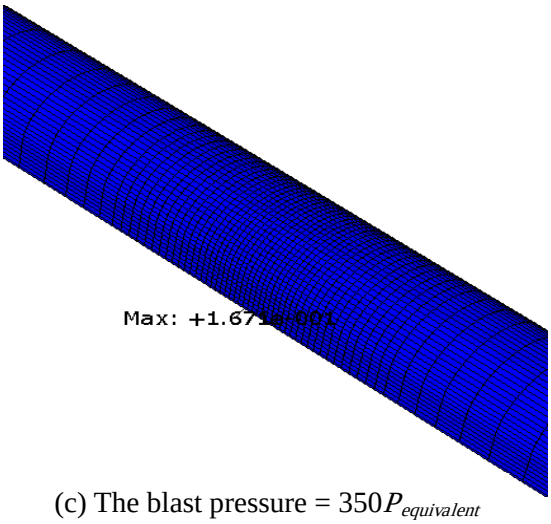

(c) The blast pressure = $350P_{equivalent}$

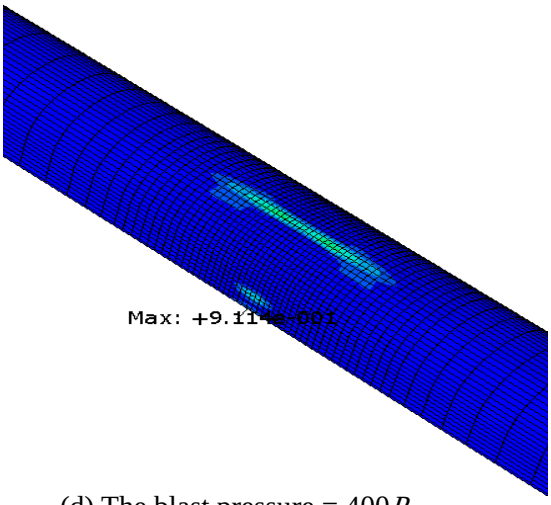

(d) The blast pressure = $400P_{equivalent}$

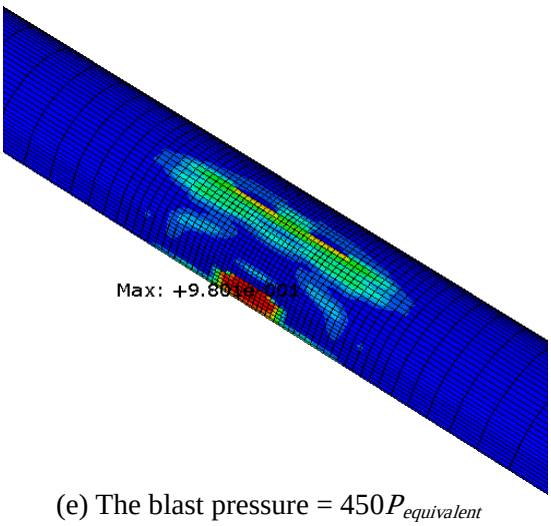

(e) The blast pressure = $450P_{equivalent}$

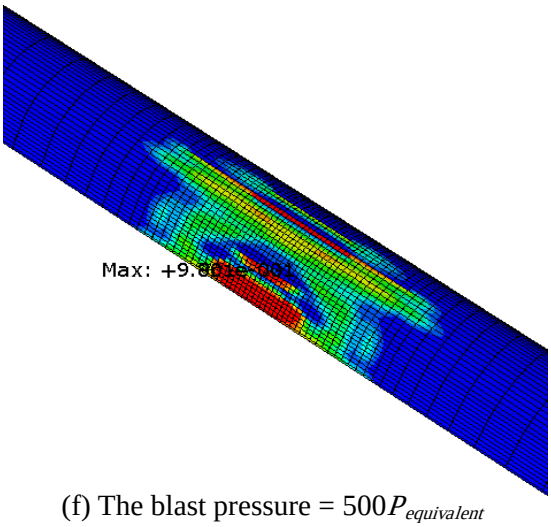

(f) The blast pressure = $500P_{equivalent}$

Figure 81. Tension damage nephogram of main tunnel under blast pressures.

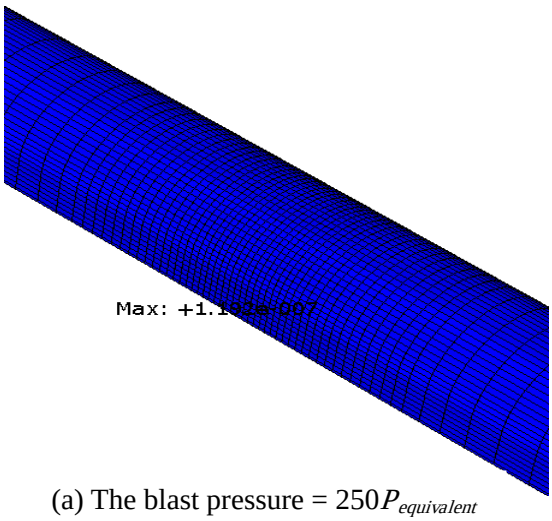

(a) The blast pressure = 250$P_{equivalent}$

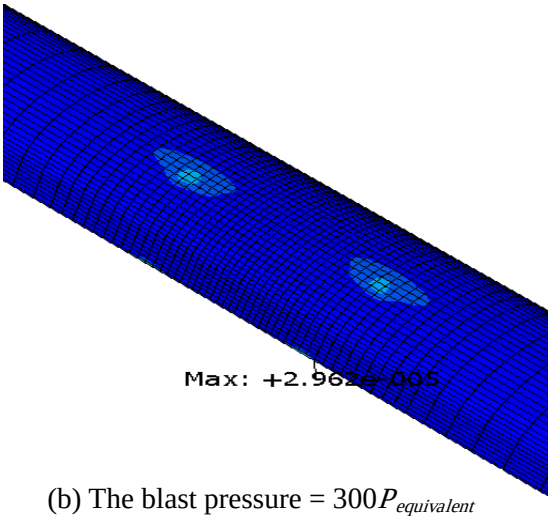

(b) The blast pressure = 300$P_{equivalent}$

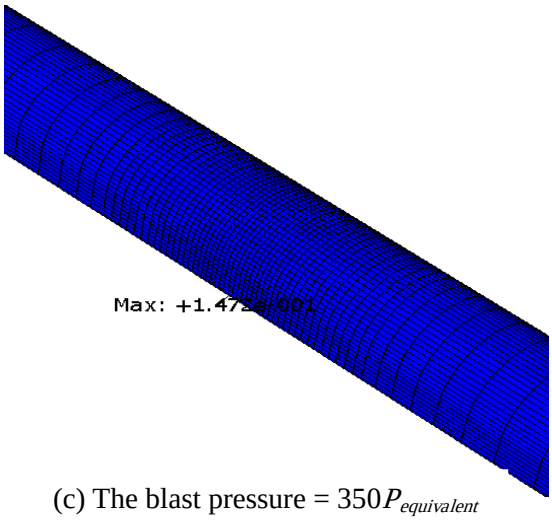

(c) The blast pressure = 350$P_{equivalent}$

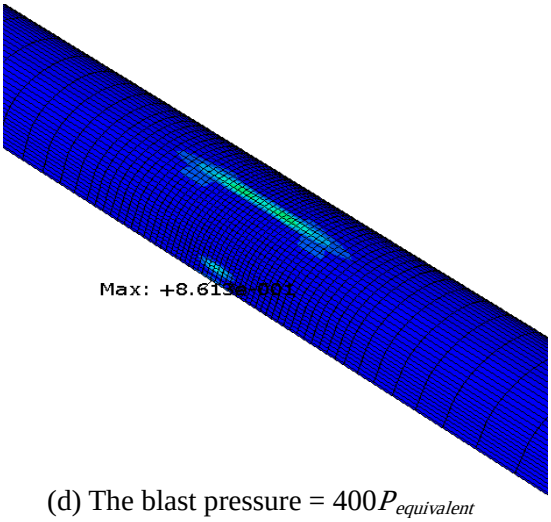

(d) The blast pressure = 400$P_{equivalent}$

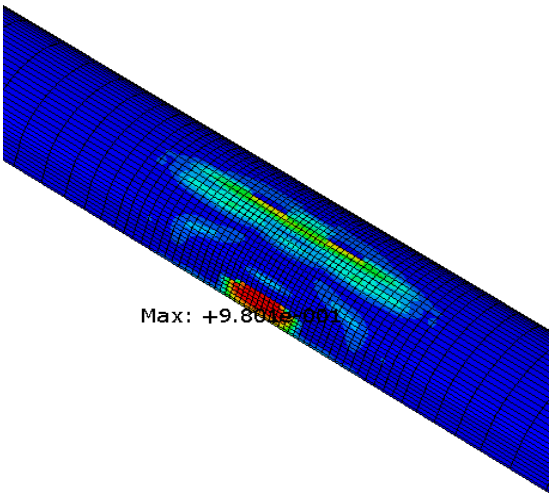

(e) The blast pressure = 450$P_{equivalent}$

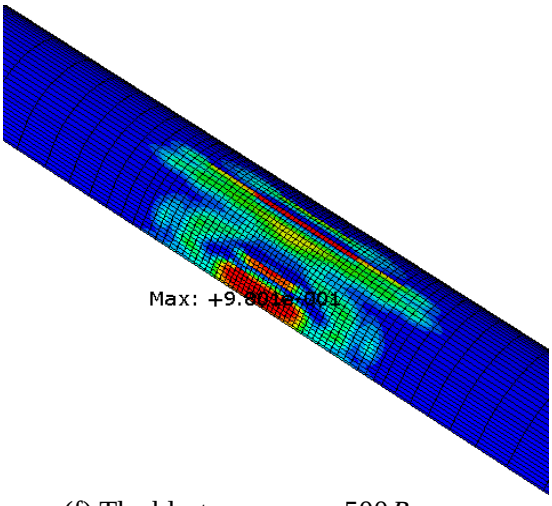

(f) The blast pressure = 500$P_{equivalent}$

Figure 82. Stiffness degradation nephogram of main tunnel under blast pressures.

$60P_{equivalent}$, but the appearances of compression damage and tension damage require much stronger blast pressure ($225P_{equivalent}$ for compression damage and $325P_{equivalent}$ for tension damage). Besides, the tunnel lining is very likely to experience failure under strong explosions due to the too large and serious tension damage rather than the compression damage.

Figures 80-82 demonstrate the compression damage, tension damage and stiffness degradation nephogram of main tunnel under blast pressures. Only the central regions of main tunnel are presented in order to clearly show the most affected areas of tunnel lining under explosions, and the maximum values of investigated parameters are pointed out as well. It is clear to see the evolution of damage areas and stiffness degradation areas with an increasing blast pressure. Both the compression damage and the tension damage firstly appear on the top heading of the lining arch (on the side near the explosions), and then damage can be observed at the bottom of the sidewall (on the side near the explosions as well). Obviously, the tension damage areas are much larger than the compression damage areas when the explosions are strong, and the corresponding values of the maximum tension damage are also much larger than the values of the maximum compression damage. For the stiffness degradation, since there is compression damage and no tension damage when the blast pressure is relatively small, the distribution of the tunnel stiffness degradation areas is similar to that of the tunnel compression damage areas. However, as the blast pressure increases, tension damage areas significantly develop and become the dominant damage mechanism for main tunnel, the distribution of stiffness degradation areas then becomes similar to that of tension damage areas.

5.6 Examination on the behavior of slabs inside main tunnel lining

5.6.1 The development of numerical model

It is obvious to see from Figure 52 that there are slabs inside the main tunnel lining, however, there is no consideration of the influence of slabs during the investigations presented above. Undoubtedly, it is better to develop a numerical model of rock-tunnel system with slabs included. This Section will focus on the examination of the behavior of the slabs inside main tunnel under explosions, the behavior of the main tunnel lining with and without slabs is examined as well. Figure 83 shows the corresponding 3D finite element model created in ABAQUS, a perspective view, a finite element mesh and an enlarged view of the rock-tunnel system are presented. Compared with the numerical model shown in Figure 56, the only differences are that there are slabs inside the main tunnel lining, and the CDP model is adopted for both the slabs and the tunnel lining. The material property of slabs are assumed to be the same as the main tunnel lining, which is given in Table 16. It is noted that the slabs are so thin (about 15 cm) that shell elements are used for the slabs. This can reduce the whole calculation time significantly

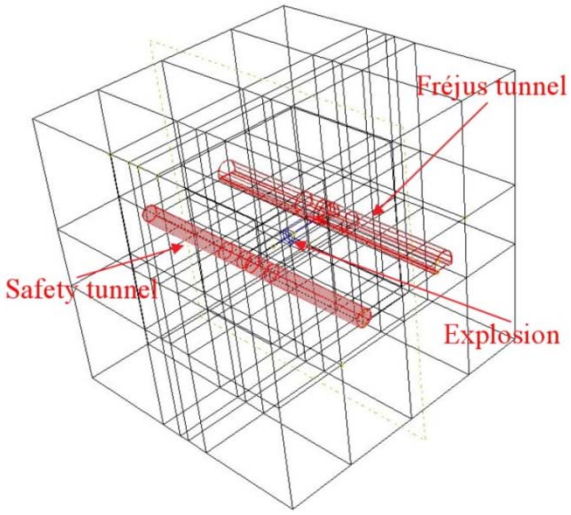

(a) The 3D perspective view

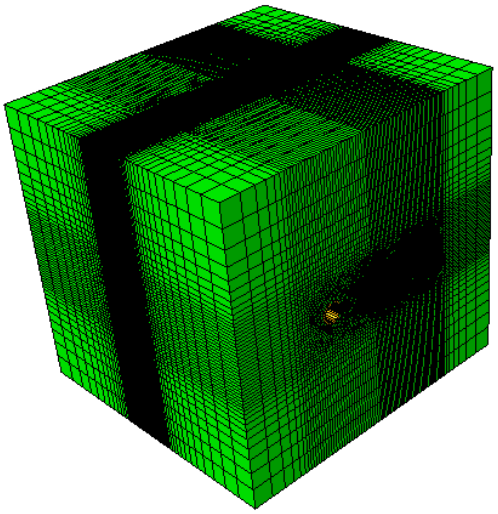

(b) The 3D finite element mesh

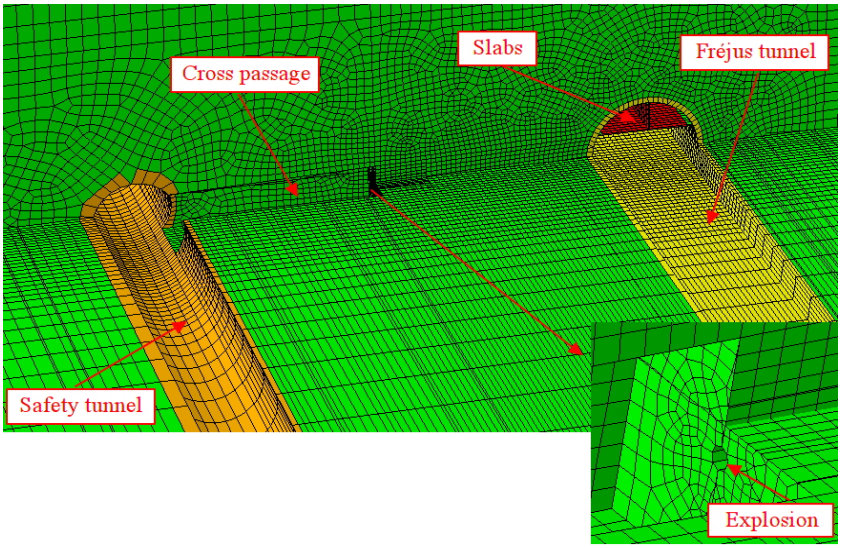

(c) Cut view of the mesh of rock-tunnel system

Figure 83. The 3D finite element model (slabs included) in ABAQUS.

compared with the usage of solid elements for slabs. In addition, the "tie" constraints are used to connect the solid part (main tunnel lining) and the shell part (the slabs) during the creation of Assembly in ABAQUS. The following paragraphs will investigate the responses of the main tunnel lining and the slabs under explosions. A comparison study on the behavior of the slabs and the tunnel lining (with and without the slabs) is presented as well.

5.6.2 The responses of main tunnel lining (with slabs inside) under explosions

Figures 84 and 85 show the distribution of maximum motion of main tunnel lining with slabs inside under explosions, where the blast pressure is assumed $P_{equivalent}$ and $400P_{equivalent}$, respectively. The highlight part in red color represents the slabs. The purpose of choosing two different blast pressures is to examine the responses of tunnel lining under weak explosions ($P_{equivalent}$) and strong explosions ($400P_{equivalent}$) with the presence of the slabs. It is seen from Figure 84 that the lining's maximum displacement, velocity and acceleration, which are 9.451×10^{-7} m, 1.566×10^{-3} m/s and 3.612 m/s^2, respectively, are very close to the corresponding ones of tunnel lining without the slabs, which are 9.456×10^{-7} m, 1.551×10^{-3} m/s and 3.604×10^{3} m/s^2, respectively (see Figure 72). Moreover, it is observed that the maximum motion of the tunnel lining with and without the slabs occurs exactly in the same positions: NODE PART-1-1.100685 (maximum displacement), NODE PART-1-1.100665 (maximum velocity) and NODE PART-1-1.99818 (maximum acceleration). Similar phenomenon can be observed for the motion of the tunnel lining under strong explosions (see Figures 76 and 85). It should be mentioned, however, that the possible damages and stiffness degradation of main tunnel with and without the slabs under strong explosions are different. From Figure 86, which shows the distribution of maximum compression damage, tension damage and stiffness degradation of main tunnel lining with slabs inside under the blast pressure of $400P_{equivalent}$, it is found that the lining's maximum compression damage, tension damage and stiffness degradation, which are 4.146×10^{-4}, 9.187×10^{-1}, 8.770×10^{-1}, respectively, are relatively larger than the ones of main tunnel without the slabs, which are 3.992×10^{-4}, 9.076×10^{-1}, 8.626×10^{-1}, respectively (see Figure 77). What also can be seen is that the maximum damages and stiffness degradation of the tunnel lining with and without the slabs occur in different positions: NODE 546385 and NODE PART-1-1.100673 (maximum displacement), NODE 543242 and NODE PART-1-1.100665 (maximum velocity), and NODE 543229 and NODE PART-1-1.99882 (maximum acceleration), respectively. These differences may be attributed to the stress concentration around the junction of the tunnel lining and the slabs, leading to the stress redistribution and stress amplification which cause more damage to the tunnel lining. Based on the observations above, it is concluded that the slabs have negligible influence on the motion of main tunnel lining under explosions, but more damage is likely to appear on the tunnel lining under strong explosions with the presence of the slabs.

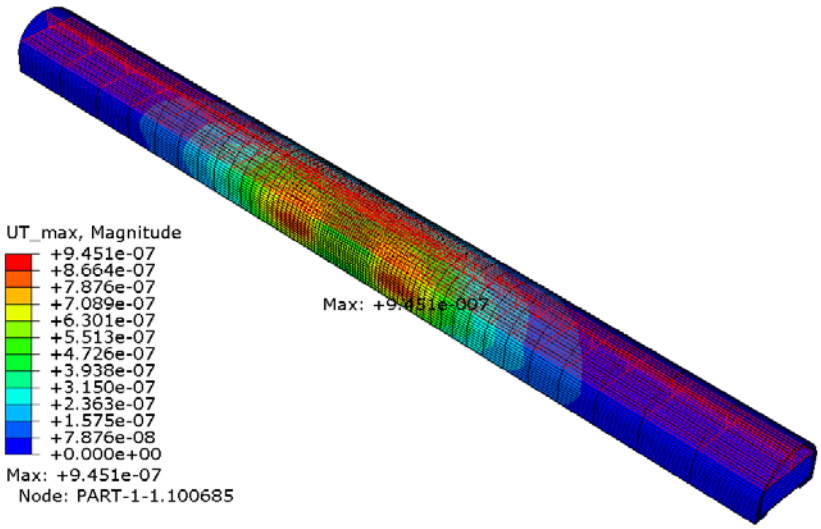

(a) The distribution of the maximum displacement

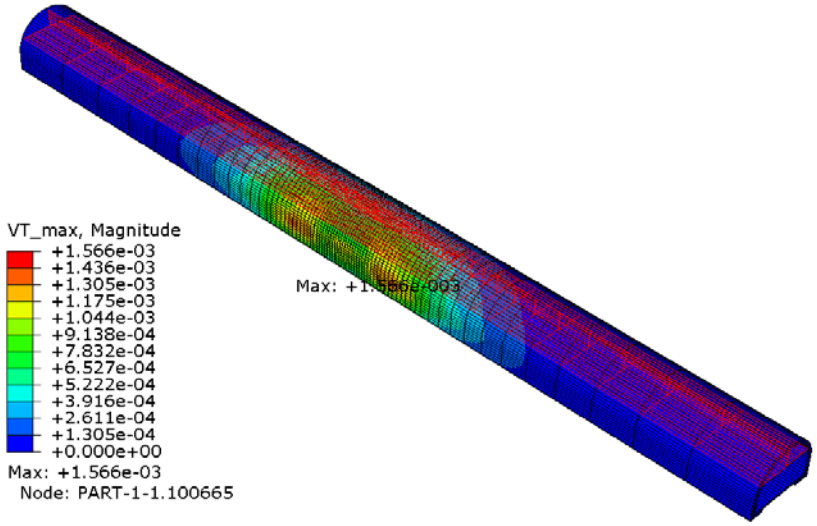

(b) The distribution of the maximum velocity

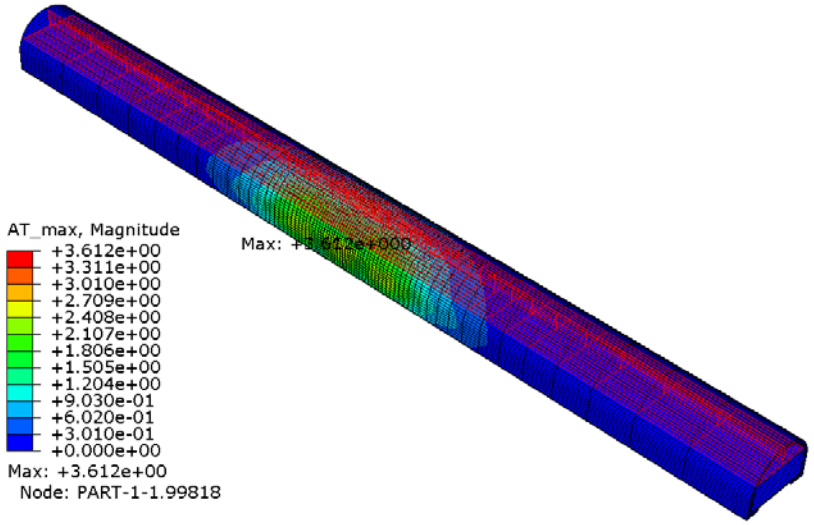

(c) The distribution of the maximum acceleration

Figure 84. The distribution of maximum motion of main tunnel lining (CDP model) under explosions (the highlight part in red represents the slabs, the blast pressure is $P_{equivalent}$).

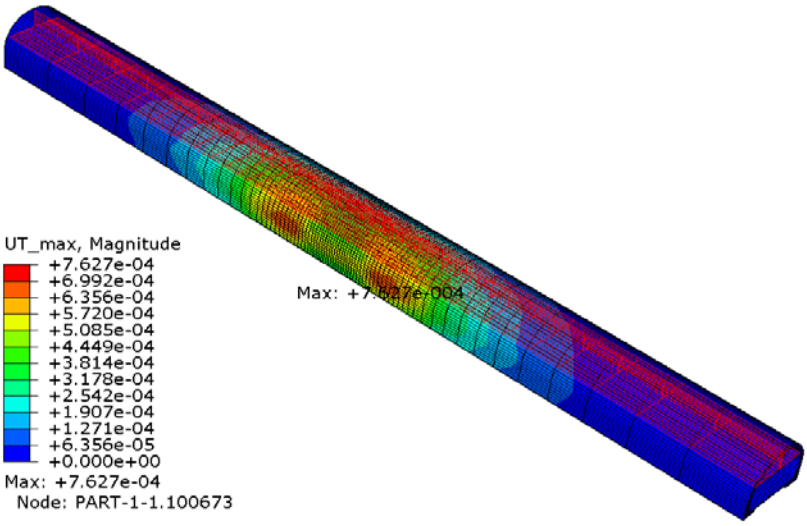

(a) The distribution of the maximum displacement

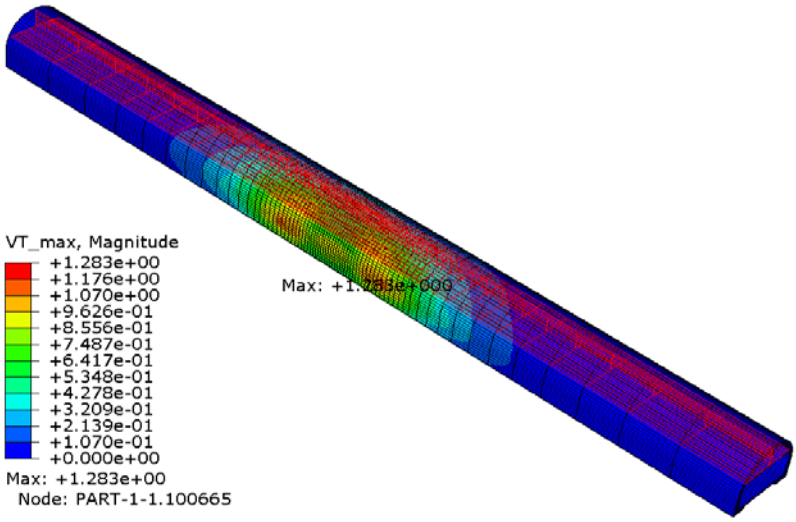

(b) The distribution of the maximum velocity

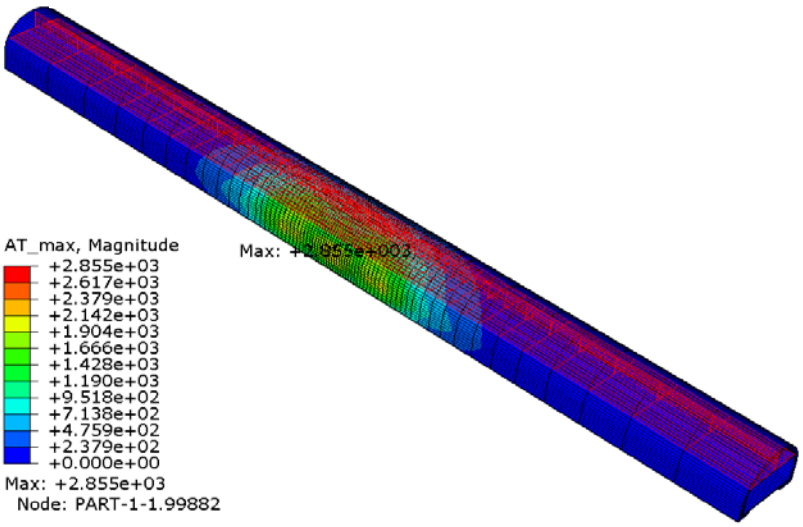

(c) The distribution of the maximum acceleration

Figure 85. The distribution of maximum motion of main tunnel lining (CDP model) under explosions (the highlight part in red represents the slabs, the blast pressure is $400P_{equivalent}$).

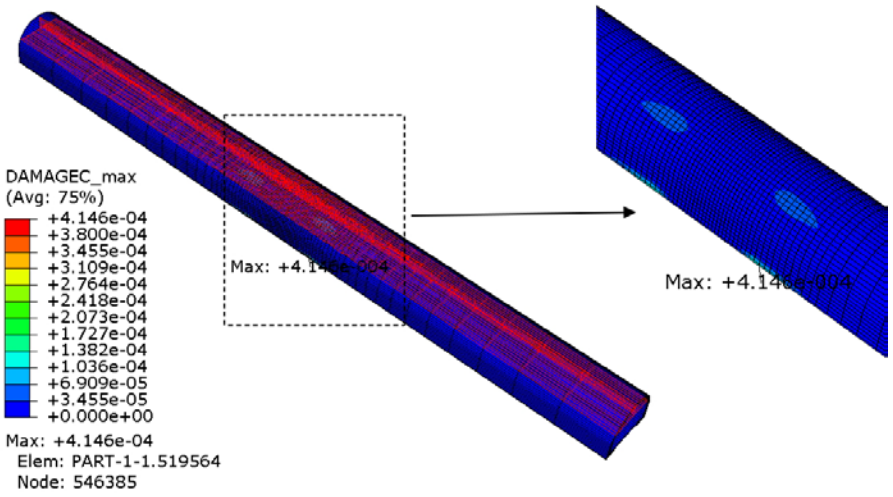

(a) The distribution of the maximum compression damage

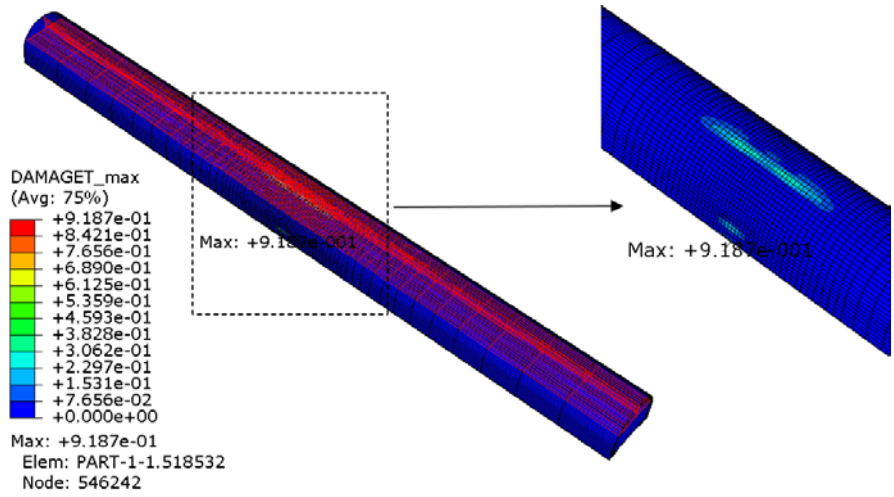

(b) The distribution of the maximum tension damage

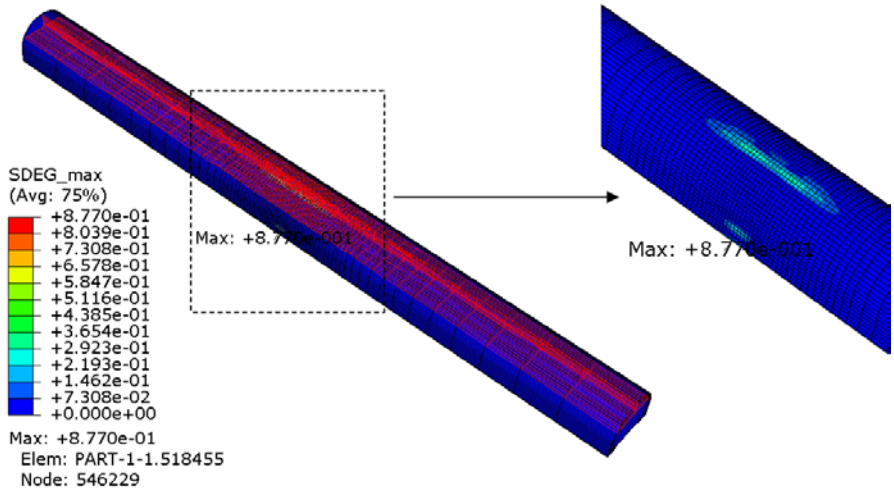

(c) The distribution of the maximum stiffness degradation

Figure 86. The distribution of maximum compression damage, tension damage and stiffness degradation of main tunnel lining (CDP model) under explosions (the highlight part in red represents the slabs, the blast pressure is $400P_{equivalent}$).

5.6.3 The responses of the slabs under explosions

In this Section, the responses of the slabs are firstly examined under weak explosions, and then strong explosions are adopted to investigate the maximum motion, the potential damage and the stiffness degradation of the slabs. A comparison study on the responses of the tunnel lining and the slabs are conducted as well.

5.6.3.1 The responses of the slabs under weak explosions

Figure 87 shows the distribution of maximum motion of slabs under weak explosions, where the blast pressure is assumed to be $P_{equivalent}$. It is seen that the maximum displacement, velocity and acceleration do not occur in the central section of the slabs, but some distances away from it. What also can be seen is that the distribution of maximum motion of slabs is similar to that of the main tunnel lining (see Figure 84). The reason may be attributed to the "tie" constraint which is used to connect the lining structure and the slabs, enforcing their motion, particularly the parts around their junctions to be compatible with each other. It should be mentioned, however, that although the distribution of the motion of the lining and the slabs is similar, the maximum motion of these two parts is different. Specifically, the maximum displacement, velocity and acceleration of the slabs, which are 8.722×10^{-7} m, 1.141×10^{-3} m/s and 2.419 m/s^2, respectively, are smaller than the corresponding ones of the tunnel lining, which are 9.456×10^{-7} m, 1.551×10^{-3} m/s and 3.604×10^{3} m/s^2, respectively. It seems that the tunnel lining partly plays a role in protecting the slabs from vibration. In addition, it is found that the maximum displacement, velocity and acceleration of the slabs appear in the horizontal slab (on the side near the explosions), as expected. Figure 88 represents the distribution of maximum compression damage, tension damage and stiffness degradation of the slabs under the blast pressure of $P_{equivalent}$. Since the blast pressure is so small that both of the tunnel lining and slabs keep elastic, there is no damage or stiffness degradation on the slabs.

5.6.3.2 The responses of slabs under strong explosions

Figure 89 shows the distribution of maximum motion of the slabs under strong explosions, where the blast pressure is assumed to be $400P_{equivalent}$. Like what is observed in Section 5.6.3.1, the maximum motion of slabs is smaller than that of the tunnel lining. On the other hand, it is seen that the maximum displacement, velocity and acceleration of the slabs, which are 7.376×10^{-4} m, 1.033 m/s and 2.175×10^{3} m/s^2, respectively, are respectively 845.68, 905.35 and 899.13 times as large as the corresponding ones of the slabs in the case of the blast pressure of $P_{equivalent}$ (see Figure 87). Since the blast pressure increases by only 400 times but the generated motion of the slabs increases by more than 800 times, it is inferred that large plastic deformation has appeared on the slabs. This can be confirmed by Figure 90, which represents the distribution

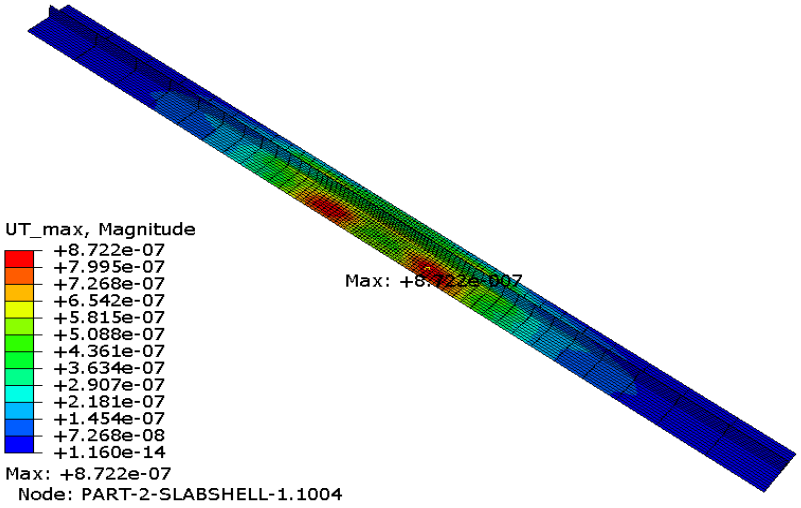

(a) The distribution of the maximum displacement

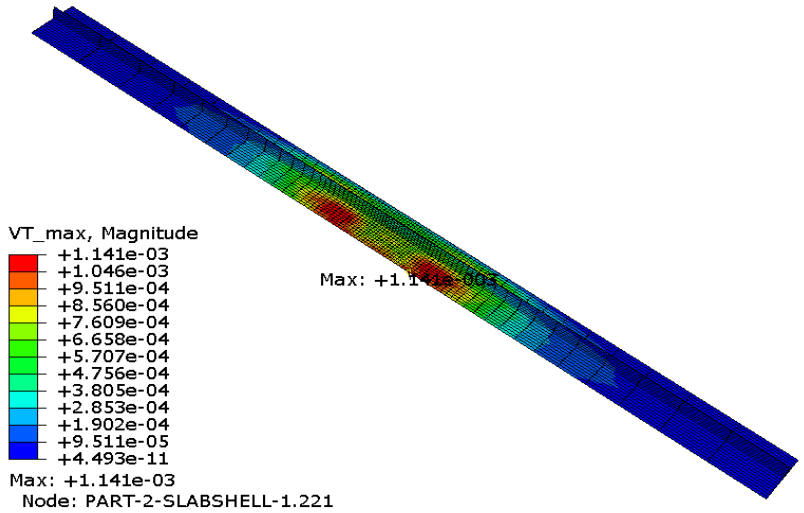

(b) The distribution of the maximum velocity

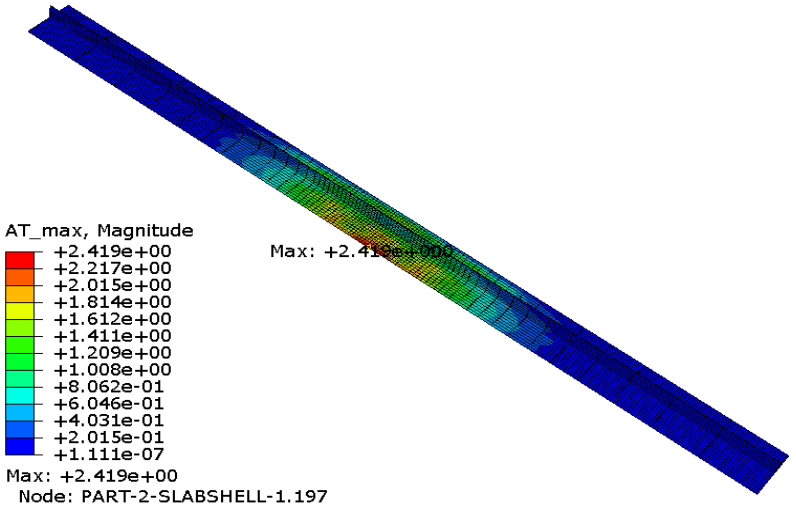

(c) The distribution of the maximum acceleration

Figure 87. The distribution of maximum motion of the slabs under weak explosions (the blast pressure is $P_{equivalent}$).

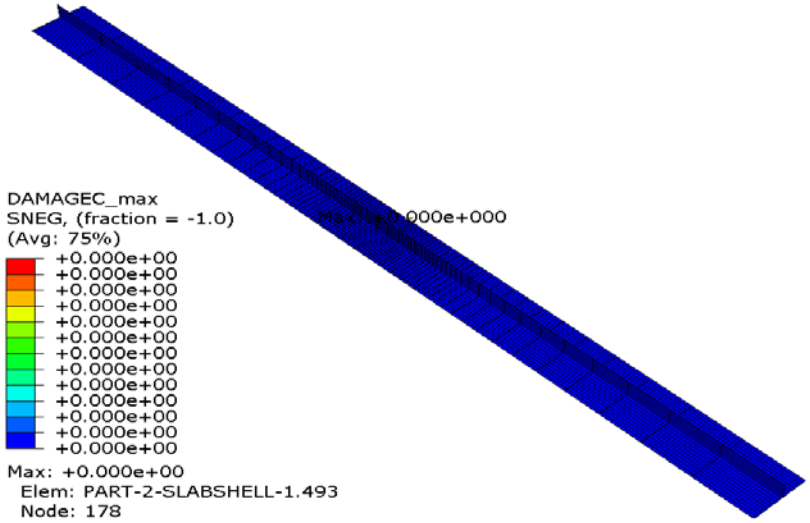

(a) The distribution of the maximum compression damage

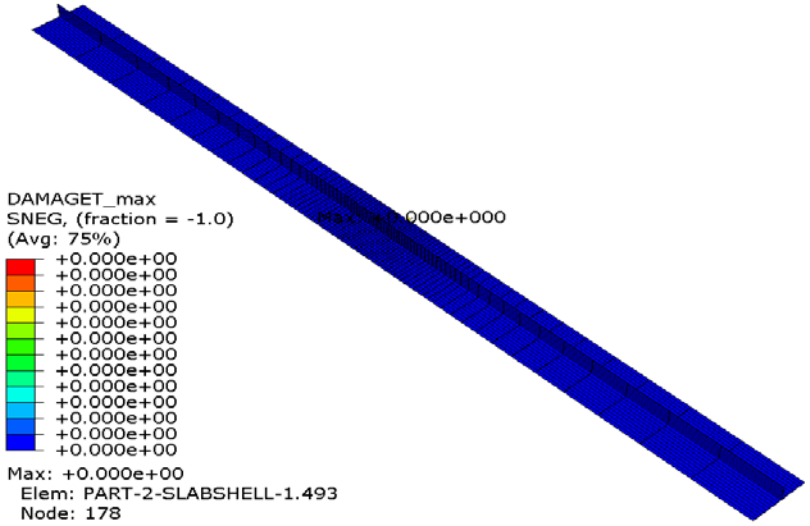

(b) The distribution of the maximum tension damage

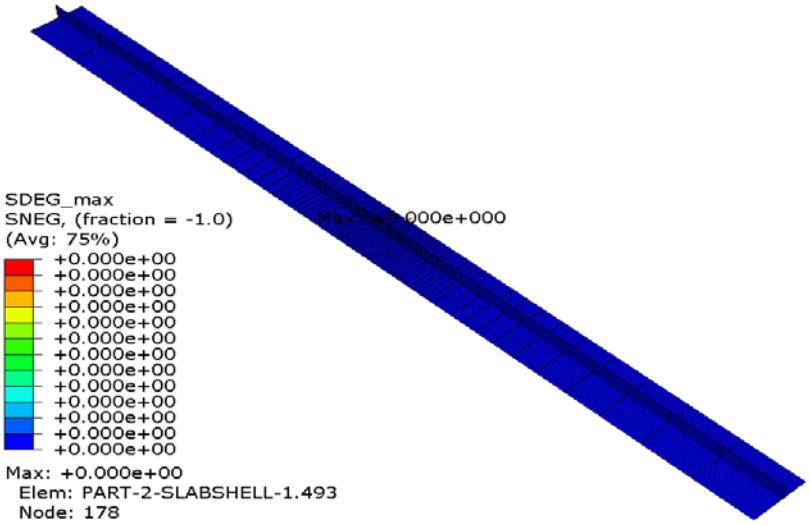

(c) The distribution of the maximum stiffness degradation

Figure 88. The distribution of maximum compression damage, tension damage and stiffness degradation of the slabs under weak explosions (the blast pressure is $P_{equivalent}$).

of maximum compression damage, tension damage and stiffness degradation of the slabs. Enlarged views of the central areas of the slabs are presented in order to provide a clear image of the most affected areas. It can be seen that both the damage and the stiffness degradation appear. Particularly, it is observed that the areas of the horizontal slab which are close to the junction of the lining and the slabs (on the side near the explosions) are the most vulnerable areas, where most of the damage and stiffness degradation occur. It is worth mentioning that there is tension damage and stiffness degradation but no compression damage in the vertical slab, and the horizontal slab which is far away from the explosions seems to be relatively safe, for almost no damage and stiffness degradation is observed on it. It is interesting to point out that, although the maximum motion of the slabs is smaller than that of the tunnel lining and therefore the tunnel lining seems to protect the slabs, the compression damage, tension damage and stiffness degradation of the slabs, which are 4.428×10^{-4}, 9.801×10^{-1} and 9.801×10^{-1}, respectively, are larger than the ones of the tunnel lining, which are 4.146×10^{-4}, 9.187×10^{-1}, 8.770×10^{-1}, respectively (see Figure 86). This may be because the slabs are so thin that they have little ability to resist the blast pressure and therefore more likely to suffer damage and stiffness degradation compared with the relatively thick tunnel lining with an arch shape.

From Figure 89, it is found that the Node: PART-2-SLABSHELL-1.1025 (Node 1025), Node: PART-2-SLABSHELL-1.221 (Node 221) and Node: PART-2-SLABSHELL-1.197 (Node 197) of the slabs respectively have the maximum displacement, velocity and acceleration in the case of the blast pressure of $400P_{equivalent}$. Here, in order to further investigate the vibration of the slabs under explosions, the evolution of the motion of these three nodes is plotted, as shown in Figure 91. It can be seen that the Node 197 and Node 221 begin to vibrate a little earlier than the Node 1025, this is because these two Nodes are closer to the explosions than the Node 1025, therefore, the waves arrive earlier in these two Nodes than in Node 1025. Also, it is seen that after the initial and major vibration, the motion of Node 197 and Node 221 become smaller and smaller. However, that is not the same case for Node 1025. Unlike experiencing an initial and major response and then decaying rapidly, the displacement of Node 1025 remains quite large as time goes by. This seems to be strange, because after the major response, there is no blast pressure at all; the vibrations of all the nodes in the slabs are expected to gradually become weaker and weaker. The possible explanation for that is the large plastic deformation of slabs caused by explosions. As mentioned earlier, remarkable damage and stiffness degradation of slabs have appeared during strong explosions. And the plastic deformation is so large that it can still generate tremendous displacement, even though the blast waves have already passed the slabs. Figure 92 demonstrates the evolution of the maximum motion of the slabs, the lining with slabs inside and the lining without slabs inside under blast pressures. This figure provides a good comparison study on the motion of the different parts of the whole main tunnel during explosions. It is

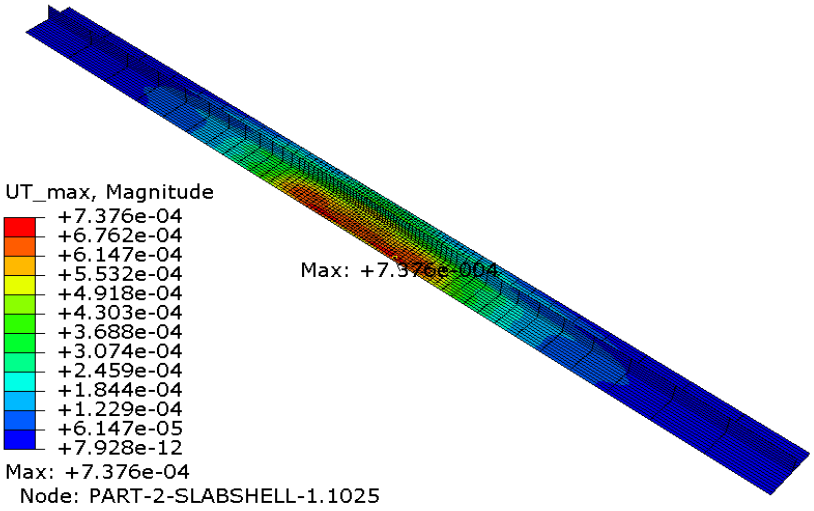

(a) The distribution of the maximum displacement

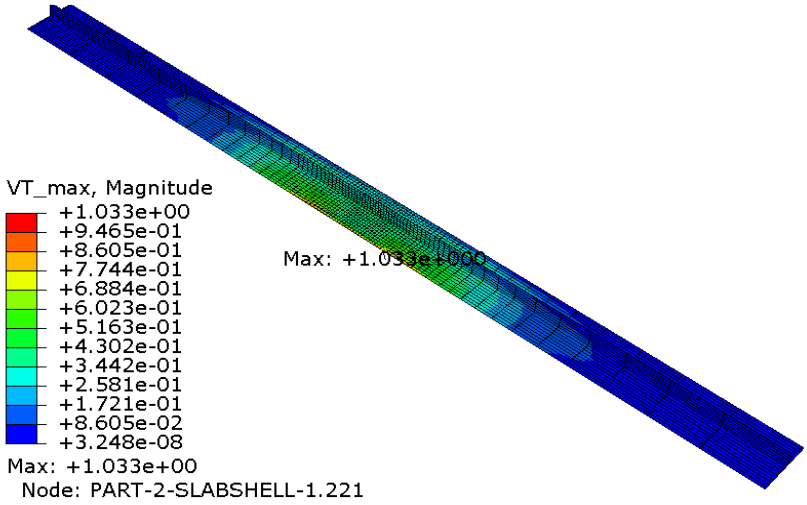

(b) The distribution of the maximum velocity

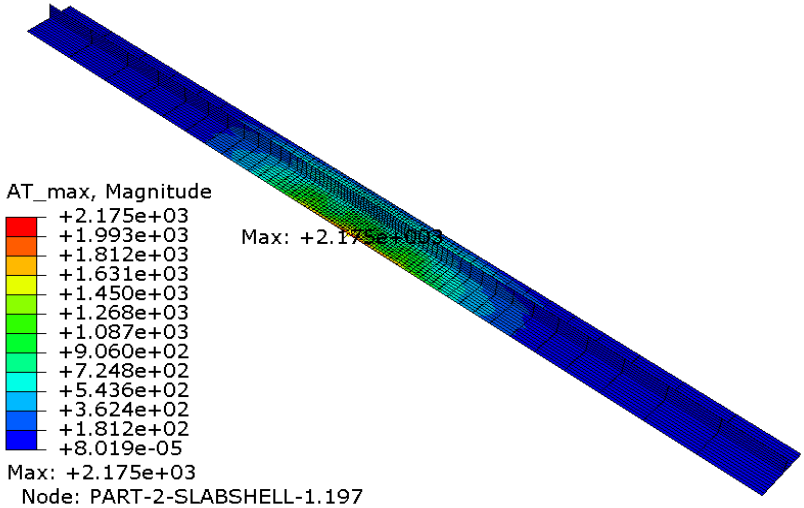

(c) The distribution of the maximum acceleration

Figure 89. The distribution of maximum motion of the slabs under strong explosions (the blast pressure is $400P_{equivalent}$).

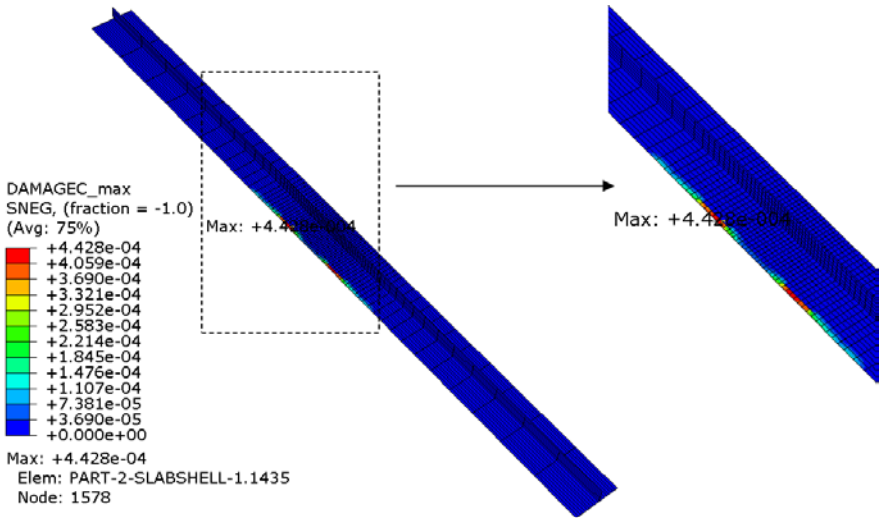

(a) The distribution of the maximum compression damage

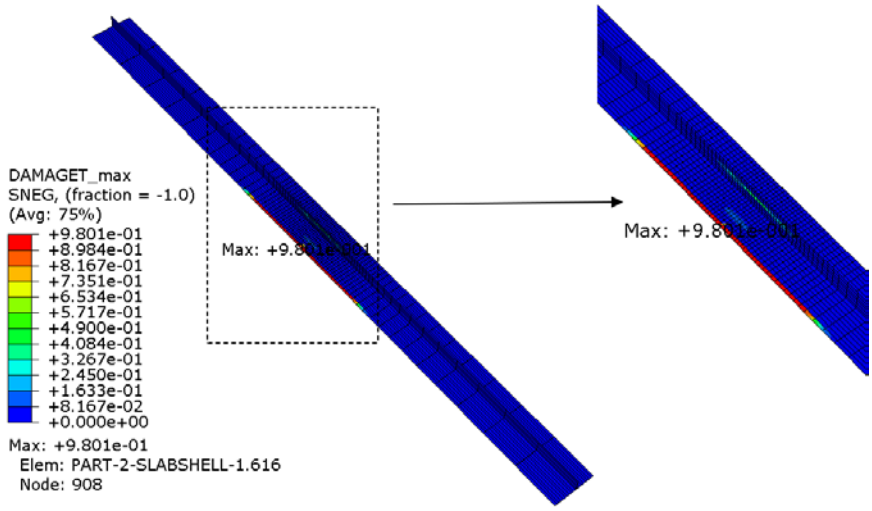

(b) The distribution of the maximum tension damage

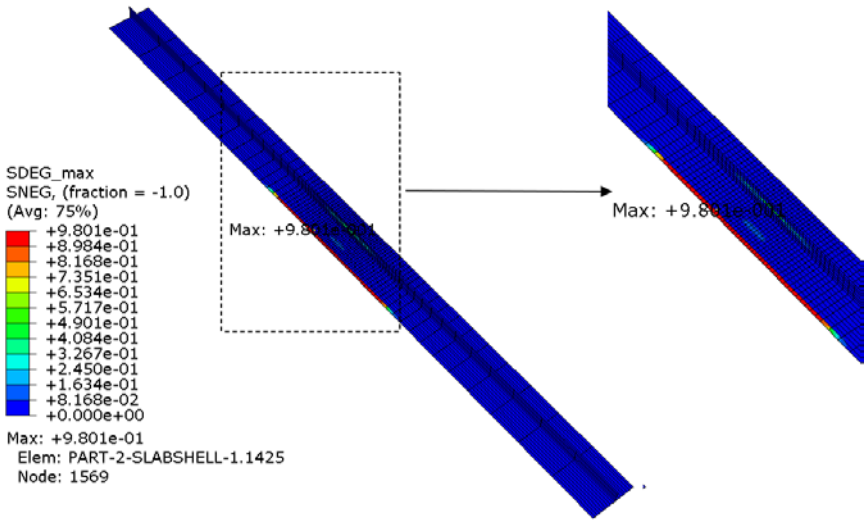

(c) The distribution of the maximum stiffness degradation

Figure 90. The distribution of maximum compression damage, tension damage and stiffness degradation of the slabs under strong explosions (the blast pressure is $400P_{equivalent}$).

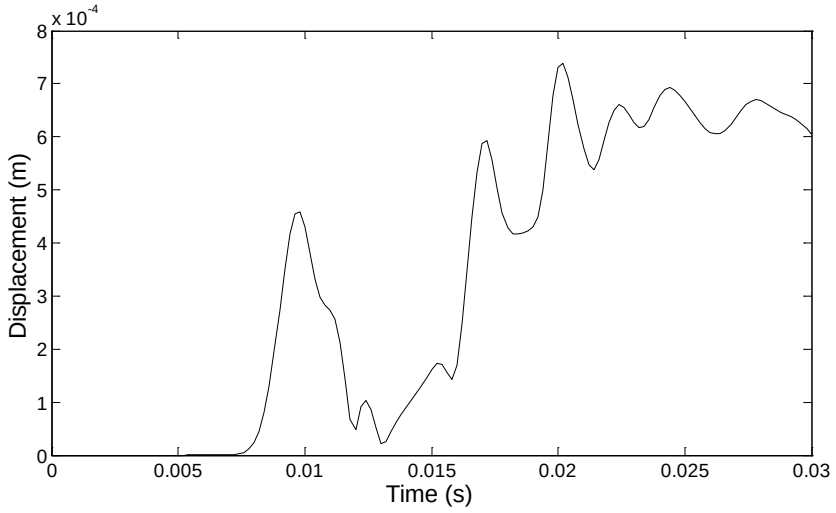

(a) The displacement of the Node: PART-2-SLABSHELL-1. 1025

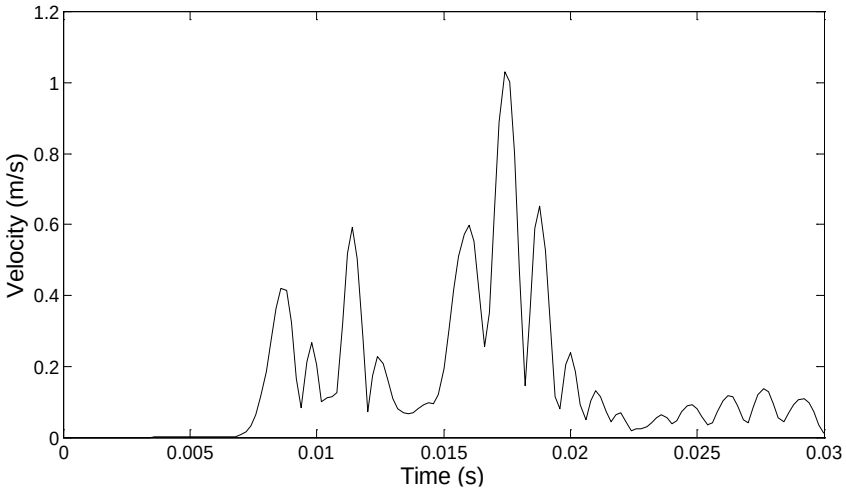

(b) The velocity of the Node: PART-2-SLABSHELL-1. 221

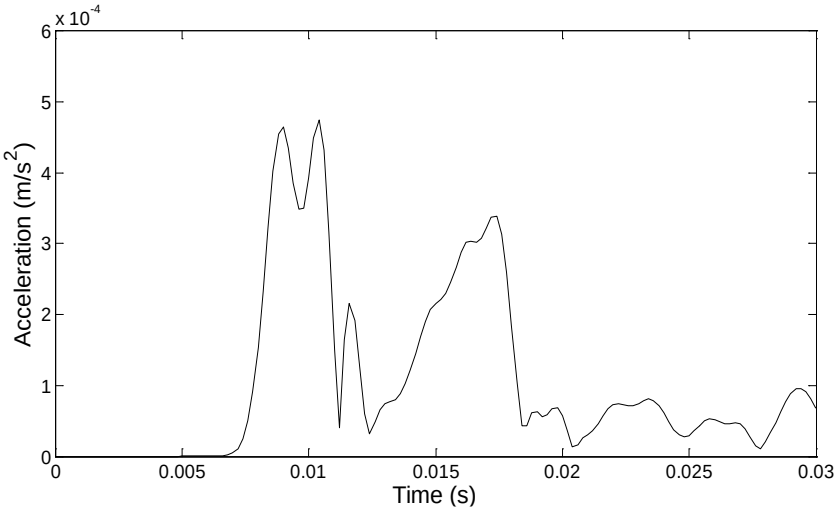

(c) The acceleration of the Node: PART-2-SLABSHELL-1. 197

Figure 91. The evolution of maximum motion of nodes on the slabs under strong explosions (the blast pressure is $400P_{equivalent}$).

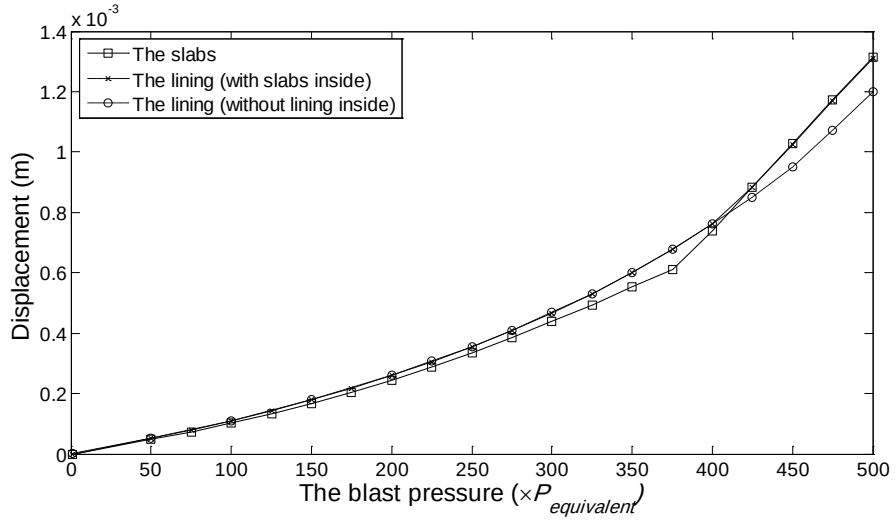

(a) The evolution of the maximum displacement

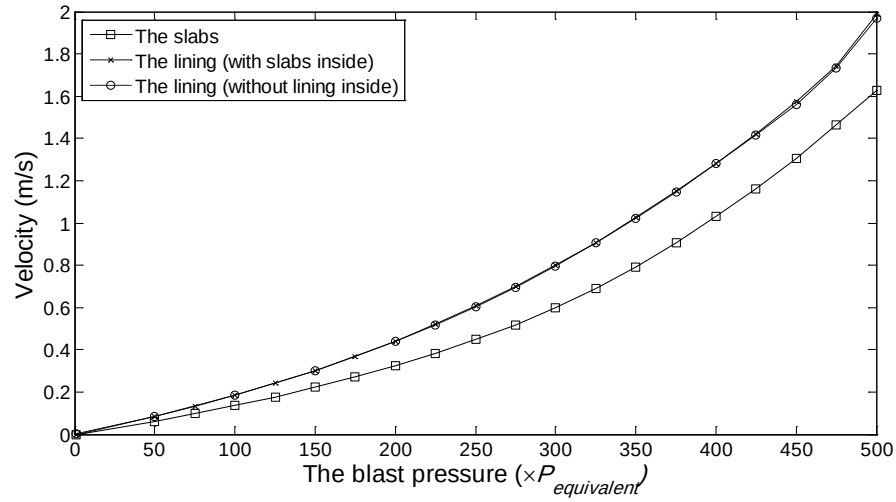

(b) The evolution of the maximum velocity

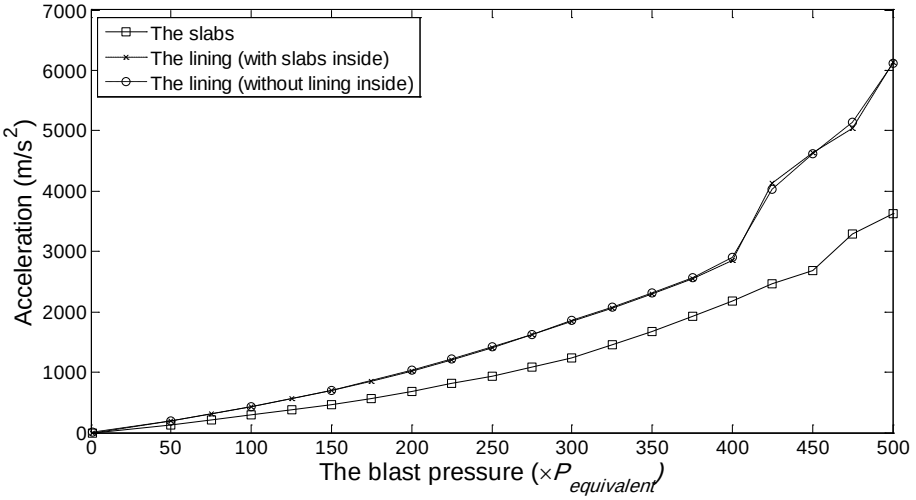

(c) The evolution of the maximum acceleration

Figure 92. The evolution of maximum motion of the slabs, the lining with slabs inside and the lining without slabs inside under blast pressures.

clear to see that the maximum velocity and acceleration of the slabs are smaller than those of the lining with or without slabs. This indicates that the vibration of the slabs is relatively minor than that of the tunnel lining. On the other hand, it is seen that the differences of the maximum displacement among three of them seem to be relatively small. This may be due to the fact that the actual displacement of the lining and the slabs as a whole should be generally "continuous", therefore, it is unlikely that there exist big differences between the maximum displacement of the lining and the slabs. Besides, it is worth mentioning that the motion of the lining appears to change little whether there are slabs inside or not. This indicates that the slabs have little impact on the motion of the tunnel lining under explosions.

5.6.3.3 Comparison study on the damage of main tunnel lining and the slabs

In the Section 5.5, the damage evaluation of main tunnel lining without the slabs has been conducted. In the Section 5.6.3.2, an investigation on the motion and the damage of the slabs under strong explosions has been presented as well. However, it is still unclear what the exact evolution of the damage and stiffness degradation of the slabs is with an increasing blast pressure. Moreover, it is necessary to carry out a comparison study on the damage of main tunnel lining and the slabs under the same explosions to find out the most vulnerable areas for the main tunnel as a whole, which is crucial for the security of the tunnel design. This Section will focus on the issues mentioned above. It is noted that only the central areas of the slabs and the tunnel lining are shown in order to provide a clear image of the most affected areas under explosions.

Figures 93 and 94 respectively present the compression damage and tension damage nephogram of the slabs and the lining (with slabs inside) under explosions. It can be seen that with an increasing blast pressure, more and more damages appear in slabs. Specifically, the compression damage seems to locate in the areas close to the junction of the lining and the horizontal slab (on the side near the explosions), and the larger the blast pressure becomes, the more severe compression damage will be generated. It should be mentioned, however, that the maximum compression damage of the slabs is quite small (1.508×10^{-3}) even though the blast pressure increases to be as large as $500P_{equivalent}$. This means that compression damage is so minor that it can almost be ignored; on the other hand, when the blast pressure is relatively small (= $250P_{equivalent}$), no tension damage is observed on the slabs. But after a slight increase of the blast pressure from 250 $P_{equivalent}$ to 300 $P_{equivalent}$, it is seen that the tension damage begins to appear in the similar areas where the compression damage occurs, more importantly, it develops very quickly, the maximum tension damage suddenly increases from 0 to 0.7585. As the explosions continue to become stronger, not only the maximum tension damage increases to its limiting value, but also the affected areas develop from the horizontal slab to the vertical slab. When the blast pressure is 450 $P_{equivalent}$, for example, it is seen that large tension damage areas appear in

both the horizontal and vertical slabs. In such case, it is very likely that the slabs will experience tension failure. Similar phenomenon can be observed from the evolution of the compression damage and tension damage of the lining. It is worth mentioning that the tension damage which is the dominate damage mechanism develops slower in the lining than in the slabs with an increasing blast pressure. This means that the tension failure of the slabs is expected to appear earlier than that of the lining. Therefore, proper reinforcement measures should be taken to strengthen the ability of the slabs to resist vibration. In addition, compared with the tension damage of the lining without the slabs under explosions (see Figures 81), it seems that the lining with the slabs inside experiences more serious damage. From this point of view, it is inferred that the slabs have a negative influence on the lining to resist the vibration-induced damage. The reason may still be the stress redistribution and stress amplification due to the stress concentration around the junction of the lining and the slabs. Figure 95 represents the stiffness degradation nephogram of the slabs and the lining under explosions. Like the phenomenon observed in Figure 82, the evolution of stiffness degradation for both the slabs and the lining firstly keeps coincident with that of compression damage when the blast pressure is relatively small (i.e. there is compression damage but no tension damage). As the blast pressure increases and the tension damage becomes the dominate damage mechanism, the evolution of the stiffness degradation turns to keep coincident with that of the tension damage. Once again, it is found that the slabs suffer larger stiffness degradation than the lining under the same blast pressure. This confirms the conclusion made in Section 5.6.3.2 that the slabs are more vulnerable than the lining during explosions. Figure 96 presents the evolution of compression damage, tension damage and stiff degradation of the slabs, the lining with slabs inside and the lining without slabs inside under blast pressures. It is clear to see that the compression damages for three of them are so small that they can be almost ignored. For the tension damage, the slabs are the earliest to experience tension failure, then the lining with the slabs inside, and finally the lining without the slabs inside. The corresponding blast pressures which result in tension failure for three of them are $325P_{equivalent}$, $425P_{equivalent}$, $450P_{equivalent}$, respectively. It is concluded that during the tunnel design, if there are slabs inside, they should be the first consideration in terms of tension failure. Proper measures like the installation of damping material (e.g. the rubber) inside the junction of the tunnel lining and the slabs can be taken to mitigate the slabs vibration. Besides, more tension damage of the tunnel lining seems to appear with the presence of the slabs, this problem can probably be relieved by mitigating the stress concentration around the junction of the slabs and the lining. Finally, since the tension damage is much more remarkable and serious than the compression damage, it is generally unnecessary to consider the compression damage problem during the tunnel protection design under explosions.

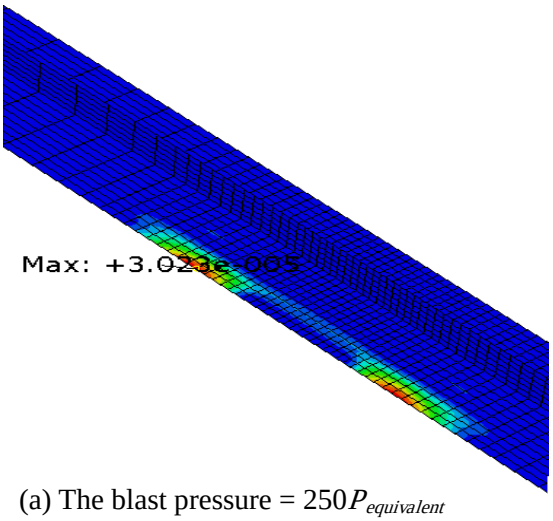

(a) The blast pressure = 250$P_{equivalent}$
(for the slabs)

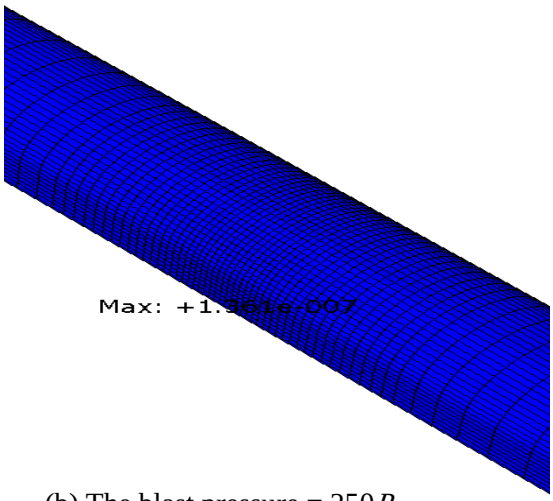

(b) The blast pressure = 250$P_{equivalent}$
(for the lining)

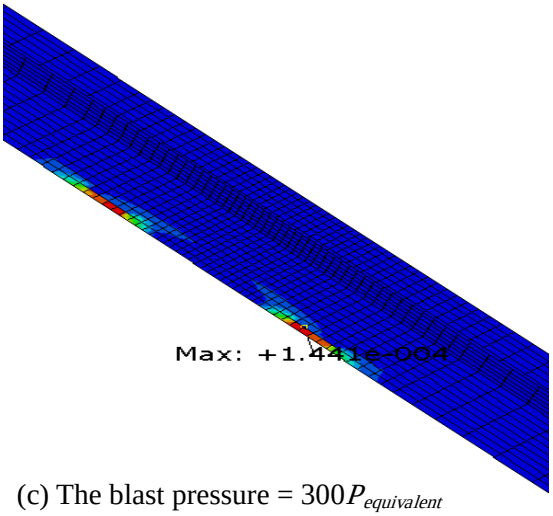

(c) The blast pressure = 300$P_{equivalent}$
(for the slabs)

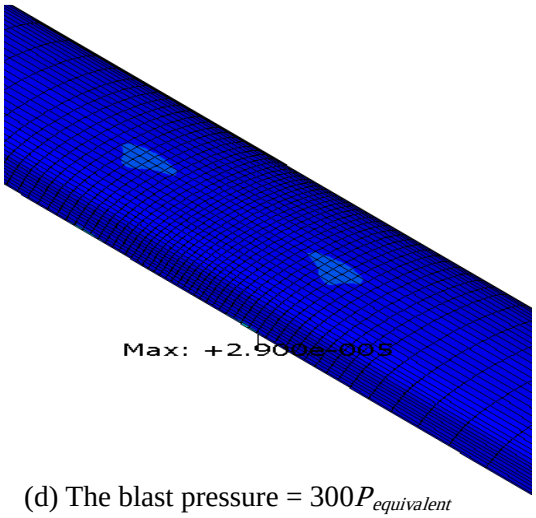

(d) The blast pressure = 300$P_{equivalent}$
(for the lining)

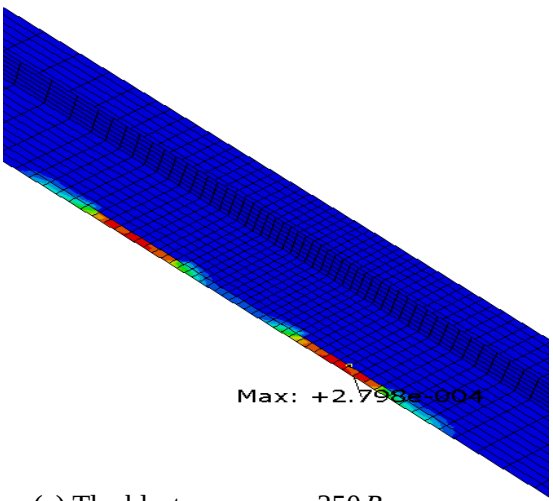

(e) The blast pressure = 350$P_{equivalent}$
(for the slabs)

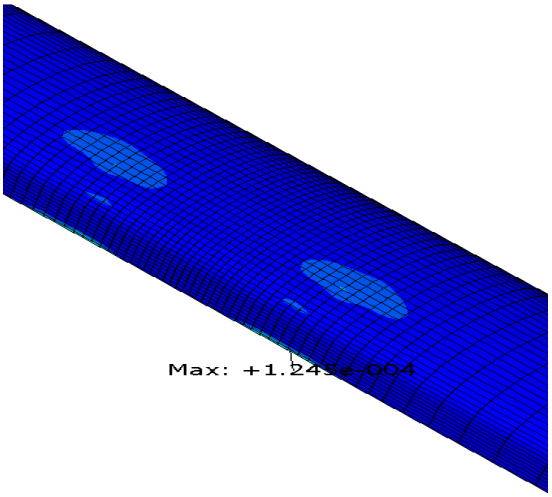

(f) The blast pressure = 350$P_{equivalent}$
(for the lining)

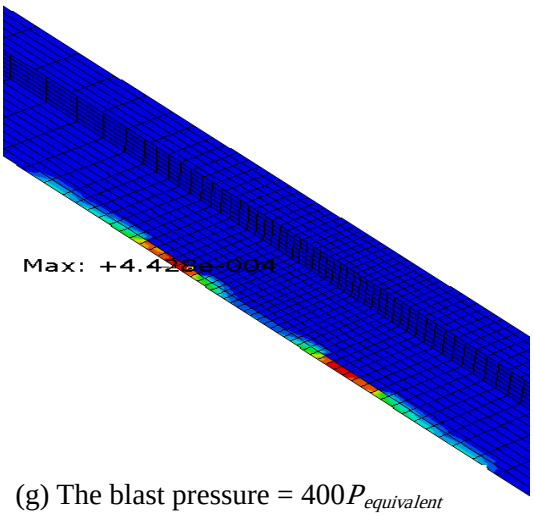

(g) The blast pressure = $400P_{equivalent}$ (for the slabs)

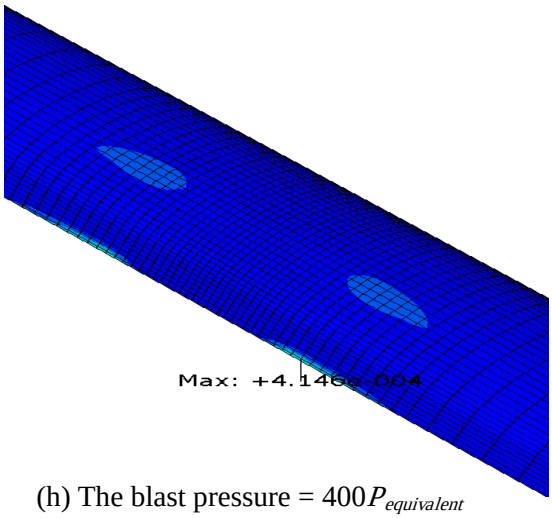

(h) The blast pressure = $400P_{equivalent}$ (for the lining)

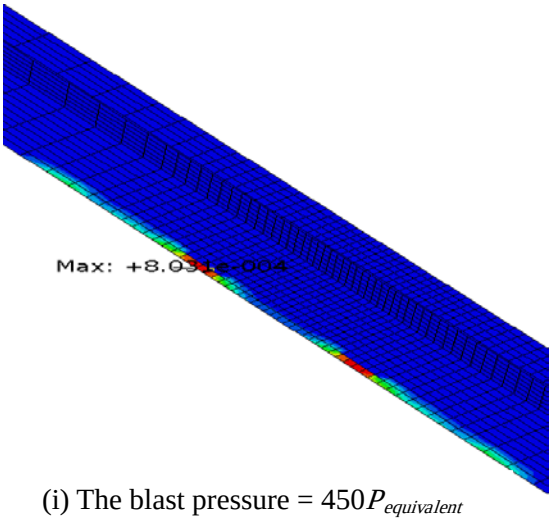

(i) The blast pressure = $450P_{equivalent}$ (for the slabs)

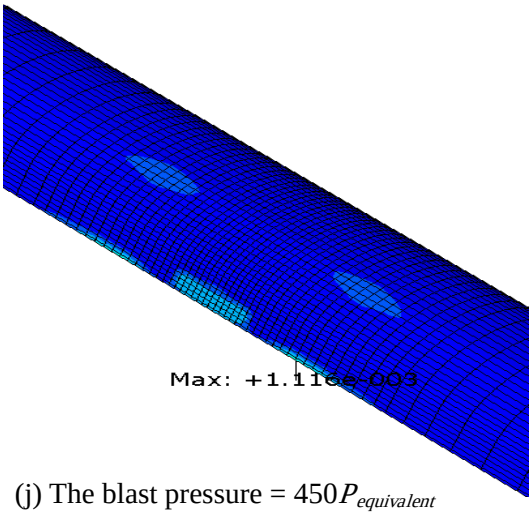

(j) The blast pressure = $450P_{equivalent}$ (for the lining)

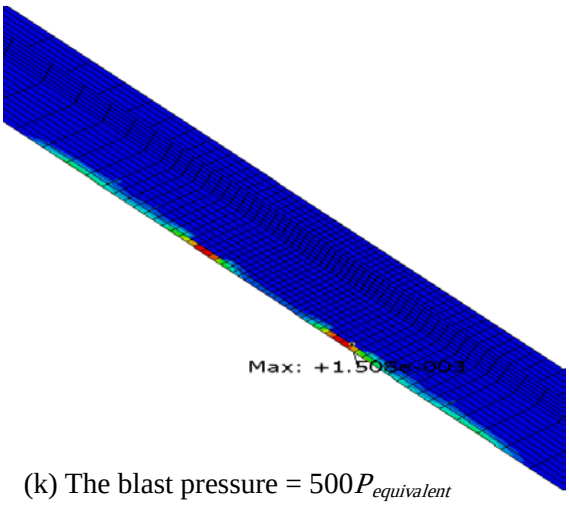

(k) The blast pressure = $500P_{equivalent}$ (for the slabs)

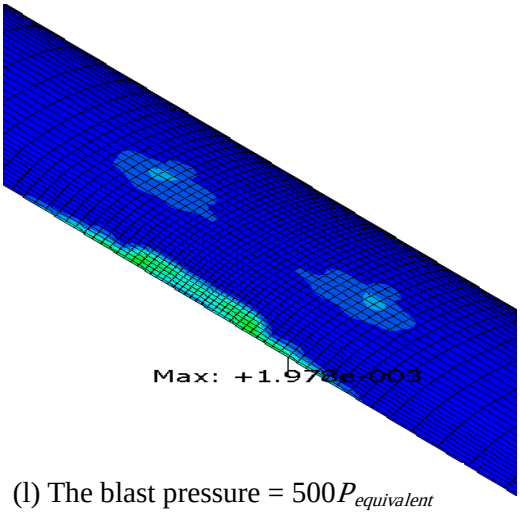

(l) The blast pressure = $500P_{equivalent}$ (for the lining)

Figure 93. Compression damage nephogram of the slabs and the lining (with slabs inside) under blast pressures.

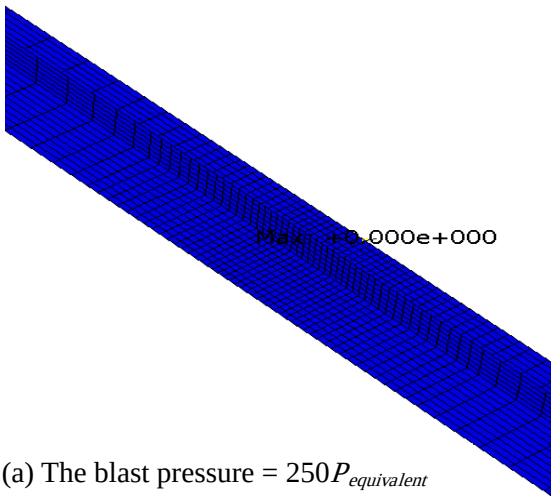

(a) The blast pressure = $250P_{equivalent}$ (for the slabs)

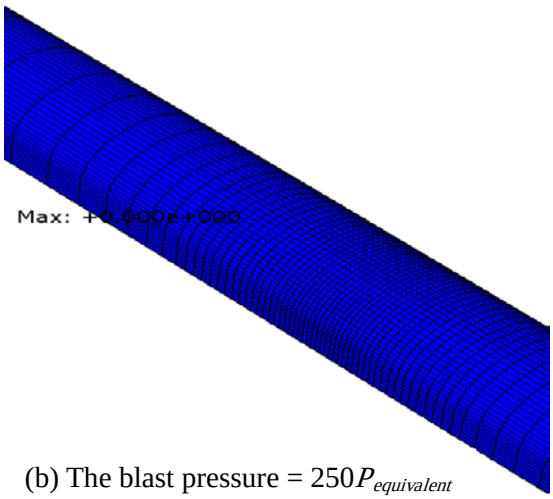

(b) The blast pressure = $250P_{equivalent}$ (for the lining)

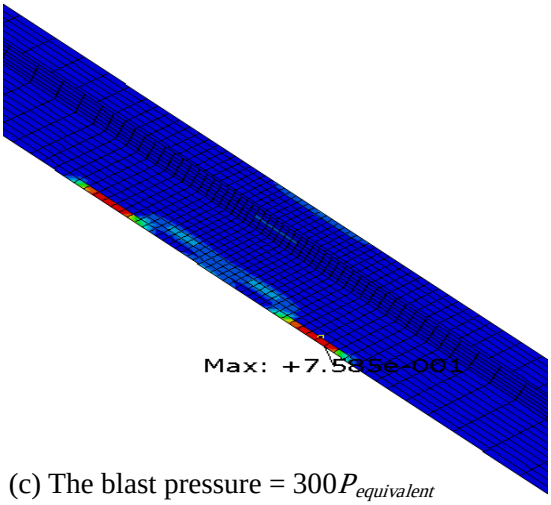

(c) The blast pressure = $300P_{equivalent}$ (for the slabs)

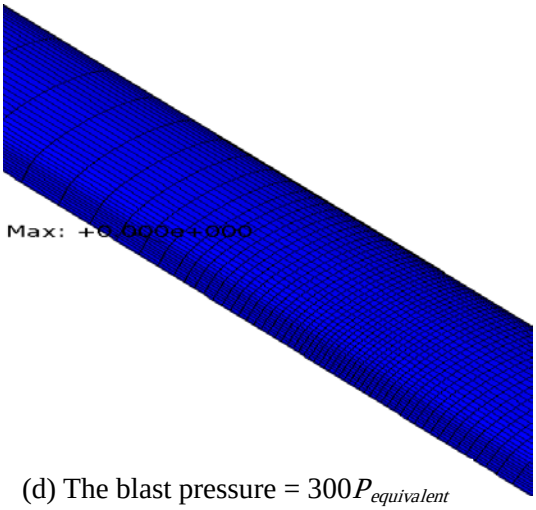

(d) The blast pressure = $300P_{equivalent}$ (for the lining)

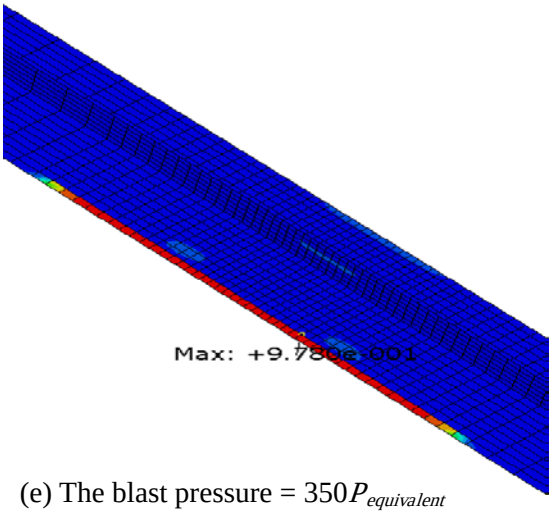

(e) The blast pressure = $350P_{equivalent}$ (for the slabs)

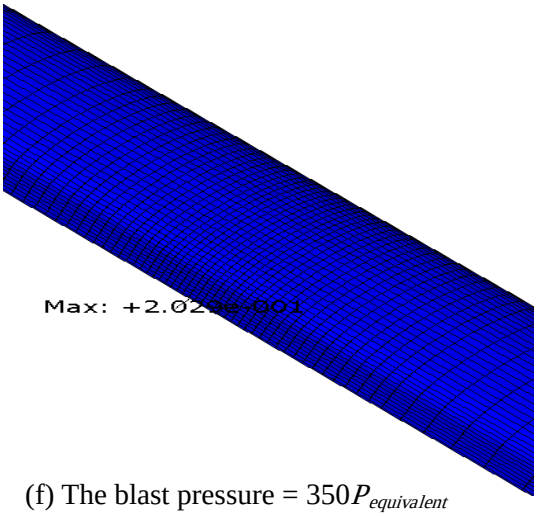

(f) The blast pressure = $350P_{equivalent}$ (for the lining)

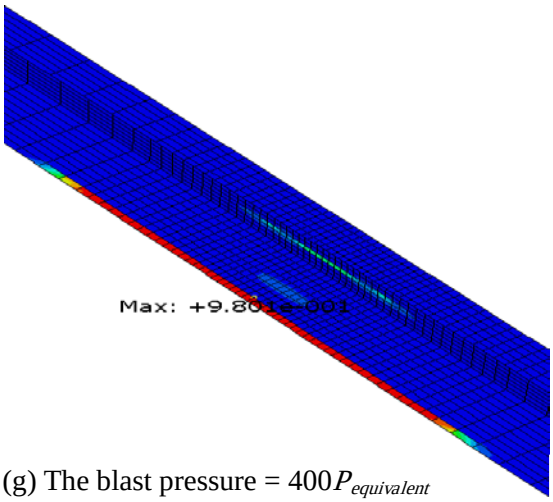

(g) The blast pressure = $400P_{equivalent}$ (for the slabs)

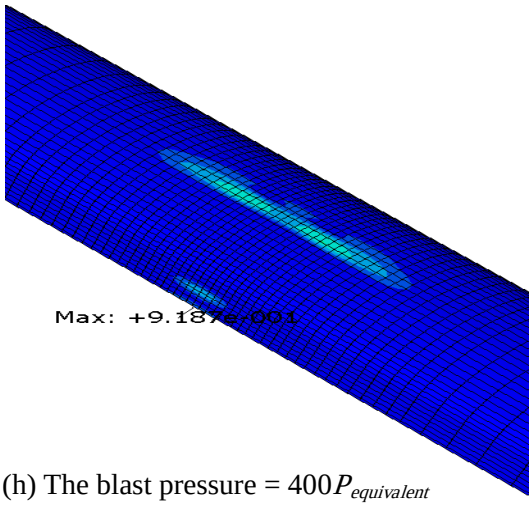

(h) The blast pressure = $400P_{equivalent}$ (for the lining)

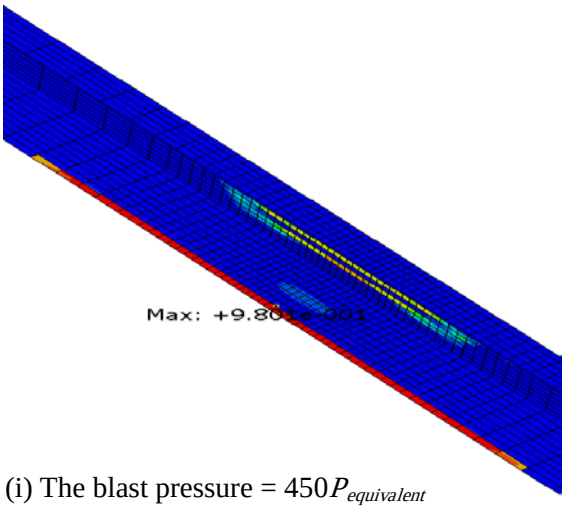

(i) The blast pressure = $450P_{equivalent}$ (for the slabs)

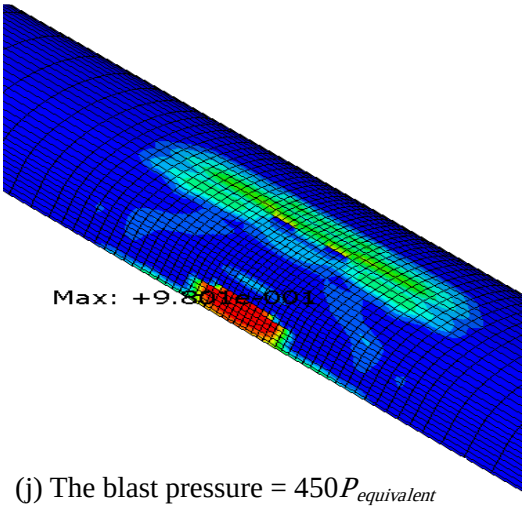

(j) The blast pressure = $450P_{equivalent}$ (for the lining)

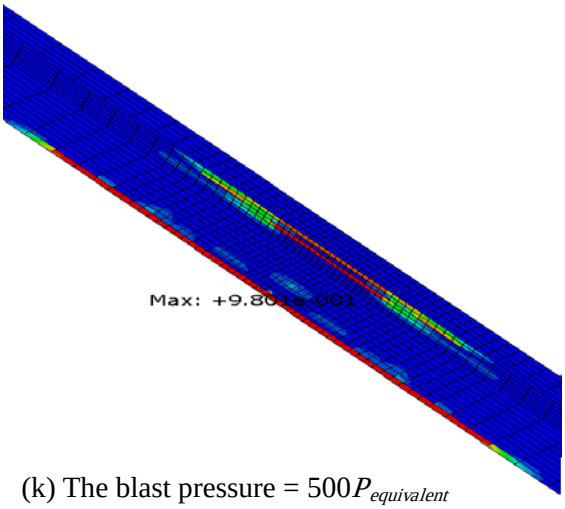

(k) The blast pressure = $500P_{equivalent}$ (for the slabs)

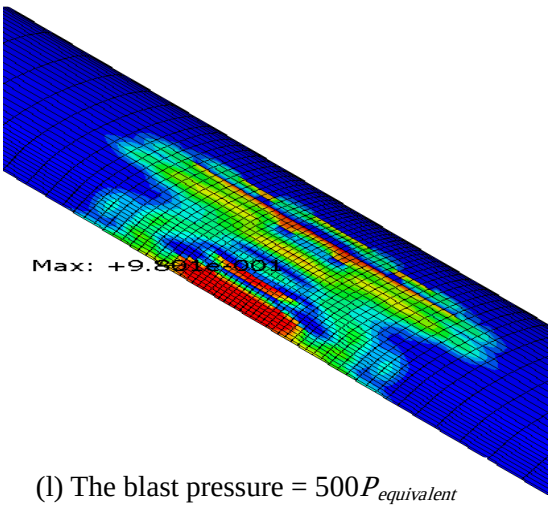

(l) The blast pressure = $500P_{equivalent}$ (for the lining)

Figure 94. Tension damage nephogram of the slabs and the lining (with slabs inside) under blast pressures.

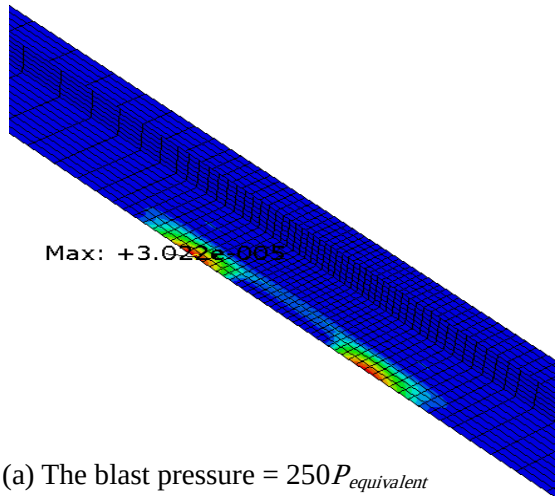

(a) The blast pressure = 250$P_{equivalent}$
(for the slabs)

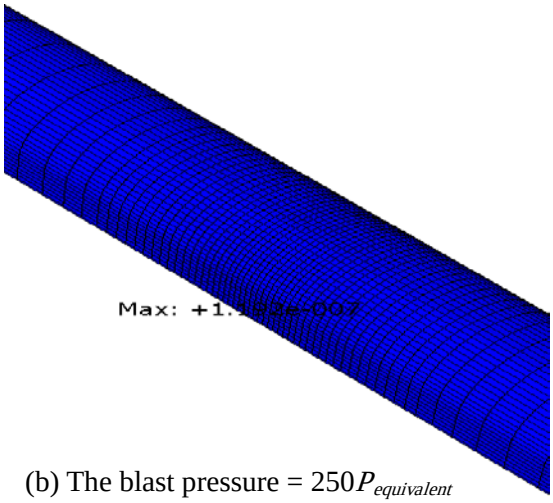

(b) The blast pressure = 250$P_{equivalent}$
(for the lining)

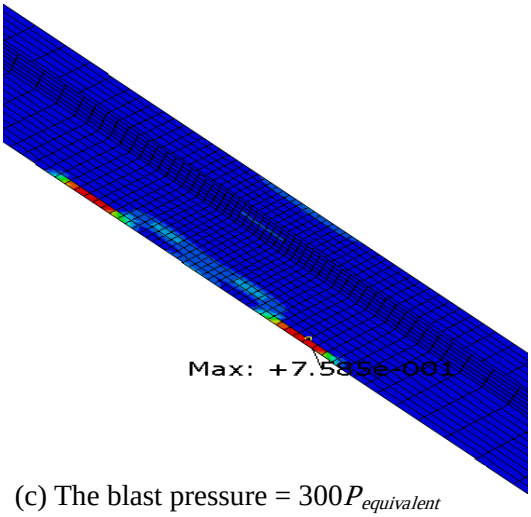

(c) The blast pressure = 300$P_{equivalent}$
(for the slabs)

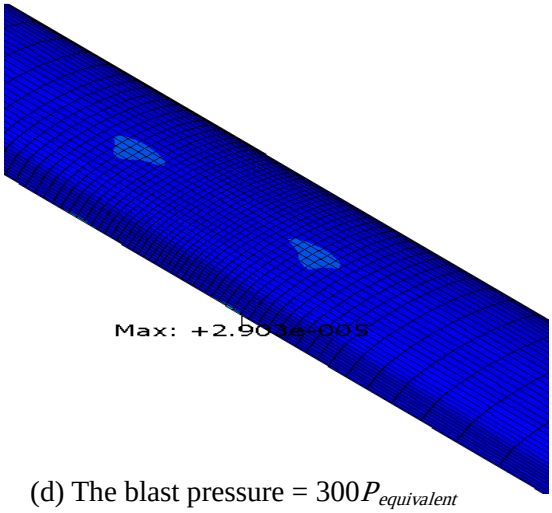

(d) The blast pressure = 300$P_{equivalent}$
(for the lining)

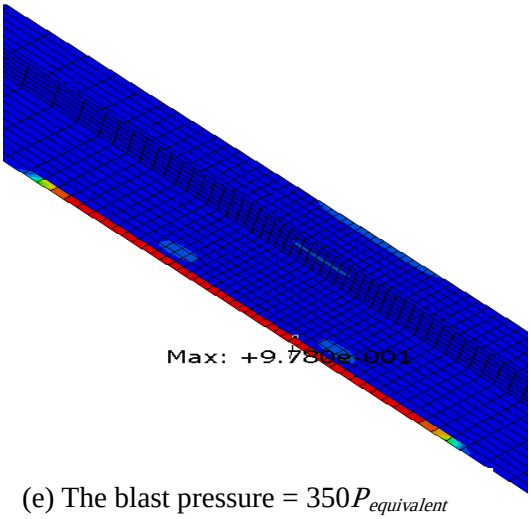

(e) The blast pressure = 350$P_{equivalent}$
(for the slabs)

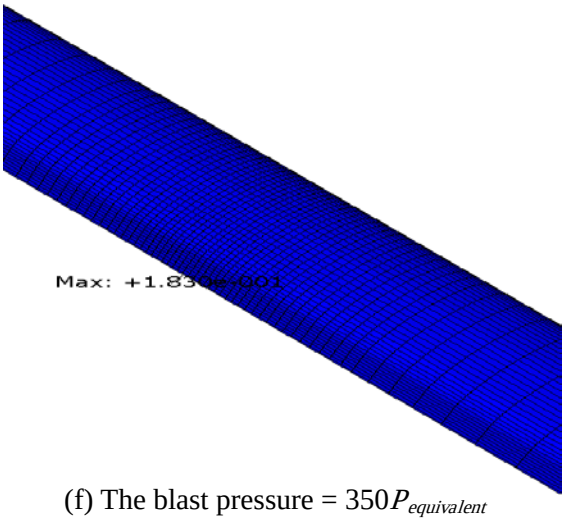

(f) The blast pressure = 350$P_{equivalent}$
(for the lining)

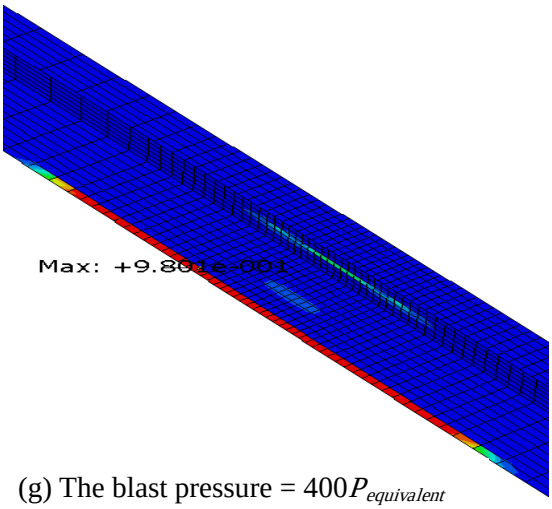

(g) The blast pressure = $400P_{equivalent}$ (for the slabs)

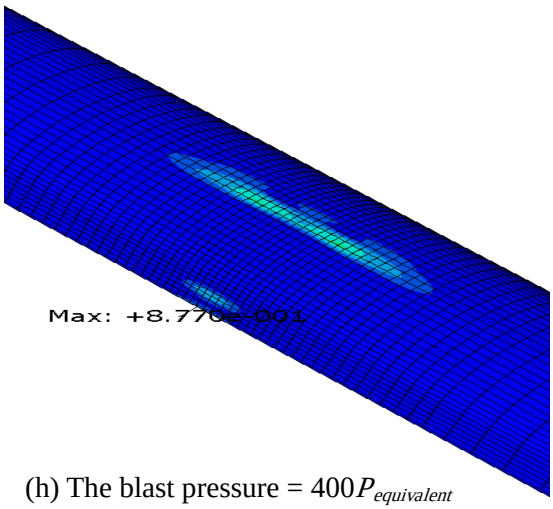

(h) The blast pressure = $400P_{equivalent}$ (for the lining)

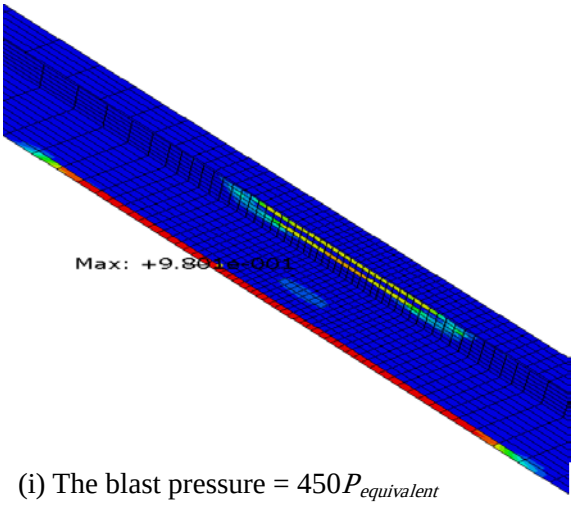

(i) The blast pressure = $450P_{equivalent}$ (for the slabs)

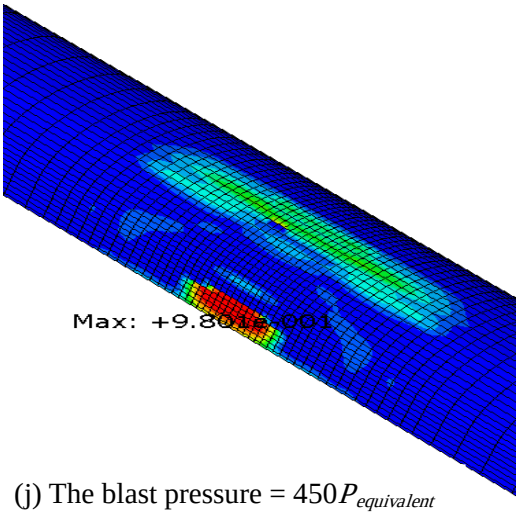

(j) The blast pressure = $450P_{equivalent}$ (for the lining)

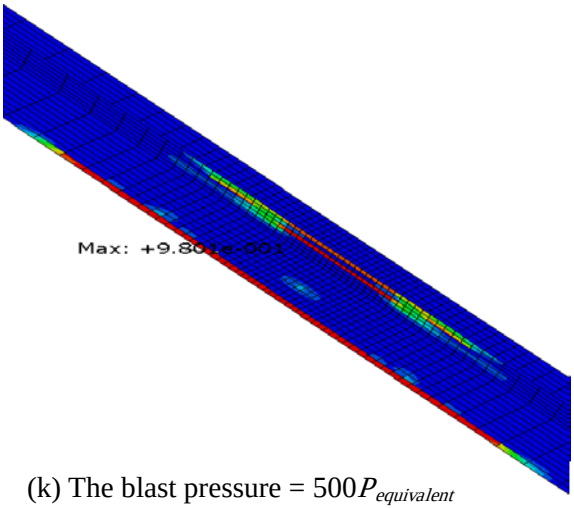

(k) The blast pressure = $500P_{equivalent}$ (for the slabs)

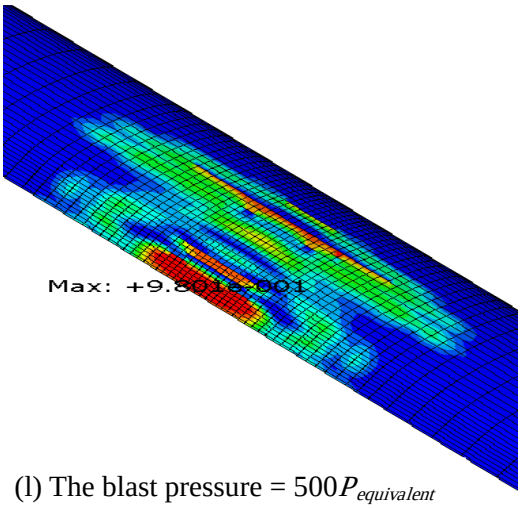

(l) The blast pressure = $500P_{equivalent}$ (for the lining)

Figure 95. Stiffness degradation nephogram of the slabs and the lining (with slabs inside) under blast pressures.

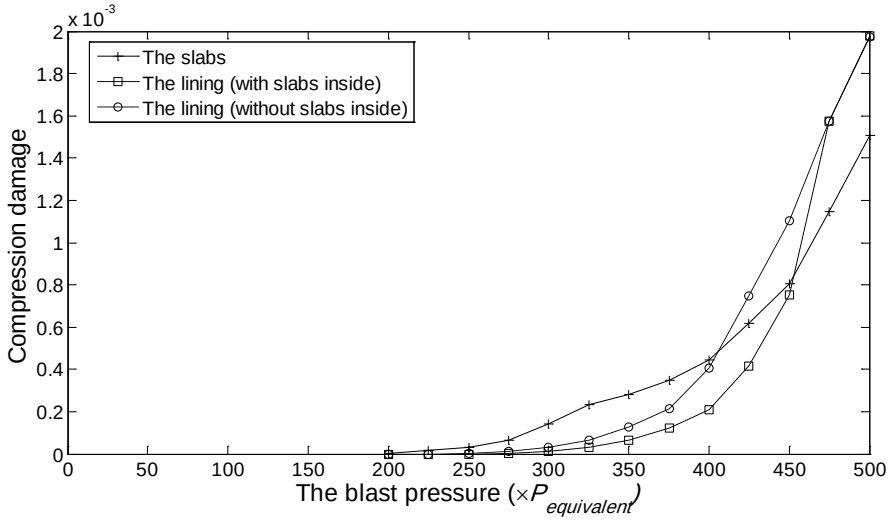

(a) The evolution of compression damage

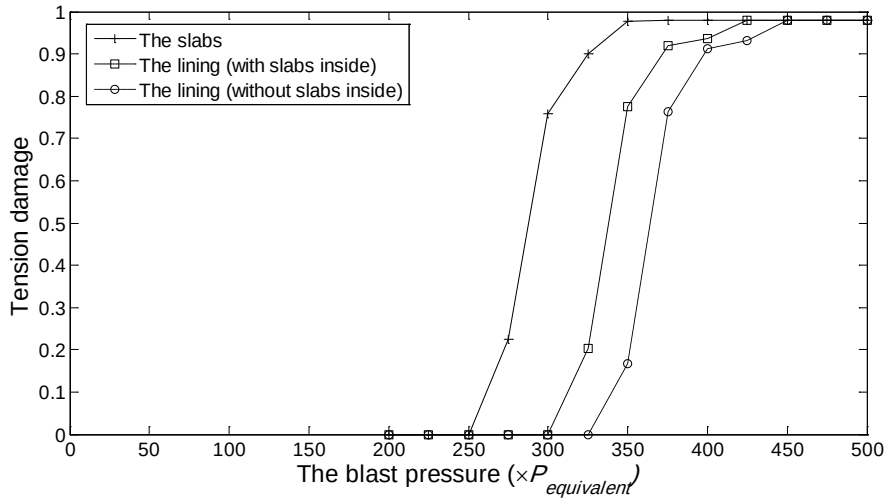

(b) The evolution of tension damage

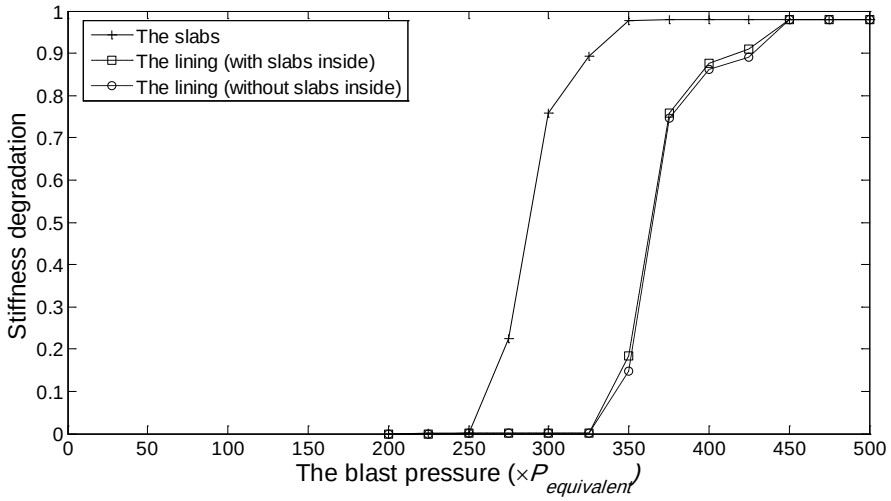

(c) The evolution of stiffness degradation

Figure 96. The evolution of compression damage, tension damage and stiff degradation of the slabs, the lining (with slabs inside) and the lining (without slabs inside) under blast pressures.

5.7 Conclusions

In this chapter, the dynamic behavior of main tunnel under nearby explosions is comprehensively studied. Firstly, the 2D and 3D numerical models of rock-tunnel system are respectively created. Comparison study shows that 3D analysis has to be used in order to produce accurate results. Then based on the 3D model, a parametric study which includes the lining stiffness, the lining thickness, the distance of explosions from main tunnel, the position of explosions along the section of cross passage, the buried depth of main tunnel and the magnitude of blast pressure, is performed to investigate their influences on the motion of main tunnel. It is found that the lining stiffness, the distance of explosions from main tunnel and the magnitude of the blast pressure are crucial parameters that significantly affect the vibration of tunnel under explosions. Then the concreted damaged plasticity (CDP) model is adopted for better simulating the dynamic behavior of main tunnel lining under strong explosions. Comparison study between the CDP model and elastic model shows that elastic model can be used to simulate the rock-tunnel system under weak explosions ($< 60P_{equivalent}$), while CDP model has to be adopted in the case of strong explosions ($\geq 60P_{equivalent}$). Numerical results also reveal that the compression damage, tension damage and stiffness degradation of main tunnel lining firstly appear on the top heading of the lining arch and then at the bottom of the sidewall (on the side near the explosions). Considering that there are slabs inside the main tunnel lining in reality, a 3D finite element model of the rock-tunnel system with the slabs inside is created. The responses of both the tunnel lining and the slabs are investigated. A comparison study on the behavior of the slabs, the lining with the slabs and the lining without the slabs is carried out as well. The results show that both the lining and the slabs are likely to experience tension damage rather than compression damage during strong explosions. And the slabs are more vulnerable to suffer tension damage than the lining, The lining without the slabs inside performs better in resisting potential vibration-induced damage than the lining with the slabs inside. In addition, the vibration of the slabs is generally smaller than the vibration of the tunnel lining, and the slabs seem to have little influence on the maximum motion of the tunnel lining.

6. Mitigation measures for reducing vibration of main tunnel

Since one of the major objectives of this research is to ensure the security of main tunnel under explosions, any mitigation measure that can reduce the tunnel vibration effectively and economically is encouraged. Considering the limitations in reality, it is generally difficult to prevent wave propagation in rock media, especially when tunnels are deeply built in mountains. Therefore, mitigation measures are more likely to be carried out around the vibratory source (i.e. the explosives) and the protected structure (i.e. the protected tunnel). In this study, two mitigation methods are examined: one is the installation of a protective layer along the main tunnel lining; the other is the usage of time-delayed explosions (rather than instantaneous explosions). In general, a protective layer can reflect and/or absorb the impinging waves back to the rock media; as a result, the protected tunnel vibration can be attenuated. On the other hand, by choosing explosions with appropriate delay times which can generate destructive wave interference during wave propagation in rock media, the ground vibration is expected to be reduced as well. In this chapter, investigation on the isolation performance of a protective layer is firstly presented, and then comparison study on the influence of time-delayed explosions and instantaneous explosions is carried out. It is noted that main tunnel without slabs inside is investigated, for considering the conclusion made in the last chapter that the tunnel lining has a stronger vibration than the slabs and the slabs have little impact on the motion of the tunnel lining. In addition, it generally takes much longer time to simulate the rock-tunnel system with slabs than the one without slabs, especially in the later optimization design, the calculation time of the numerical model with slabs may be too long to be acceptable.

6.1 Mitigation measure I: installation of a protective layer

In order to verify the necessity of installing a protective layer along the protected tunnel lining to reduce the tunnel vibration, the dynamic scenarios of blasting vibration propagation in rock is presented, as shown in Figure 97. The investigated time is 0.02 s. From Figure 97(c)-(e), it is very clear to see that waves are reflected when they propagate in the interface between the rock and the tunnel lining. Therefore, it is reasonable to estimate that an installation of a protective layer that lies outside the lining is able to reflect and/or absorb more waves to reduce the tunnel vibration. Figure 98 shows the sketch section of the main tunnel with a protective layer which lies along the lining structure. It is noted that this protected layer can be considered as “wave barrier” to prevent or block wave propagation into the tunnel lining. The following investigation

focuses on the isolation performance of the protective layer and the optimization design for the protective layer made of real materials, aiming to provide a better understanding of the protective layer screening efficiency. The numerical results are able to act as a reference for the tunnel protection design under nearby explosions.

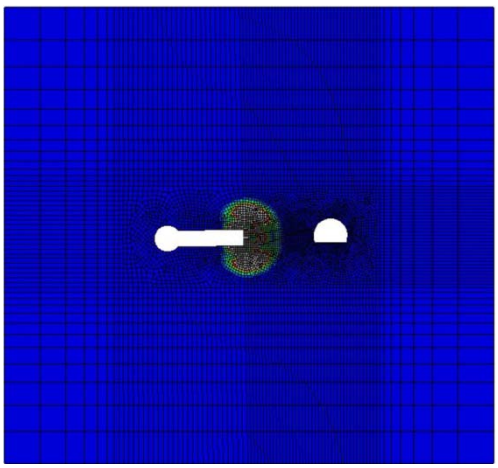

(a) Time = 4.42 ms

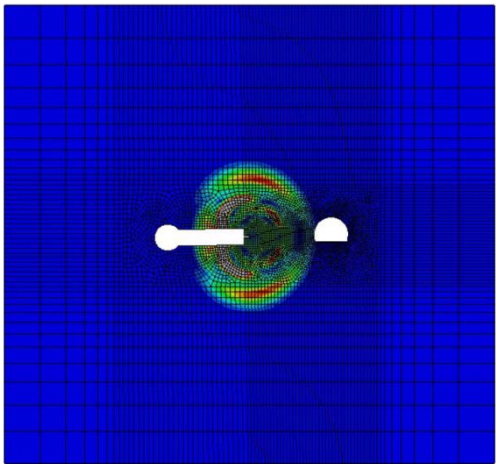

(b) Time = 8.44 ms

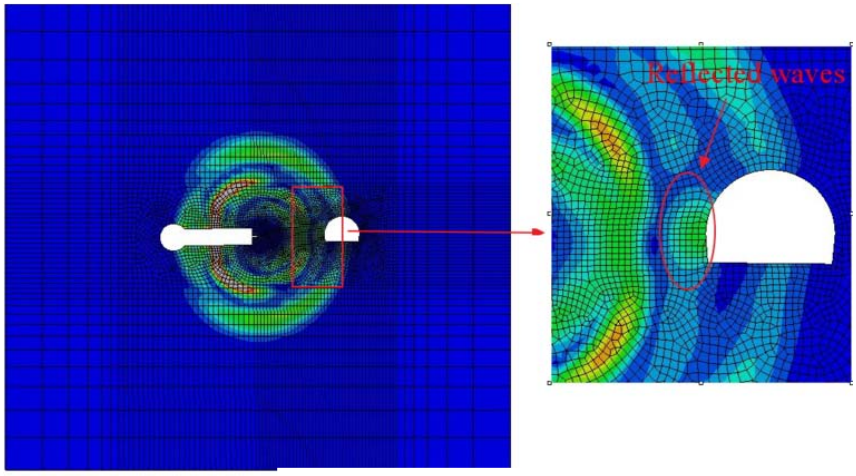

(c) Time = 11.61 ms

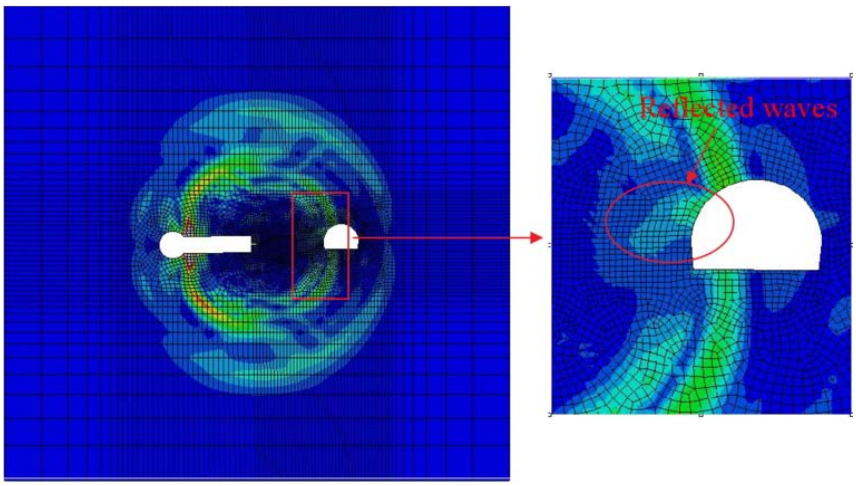

(d) Time = 17.41 ms

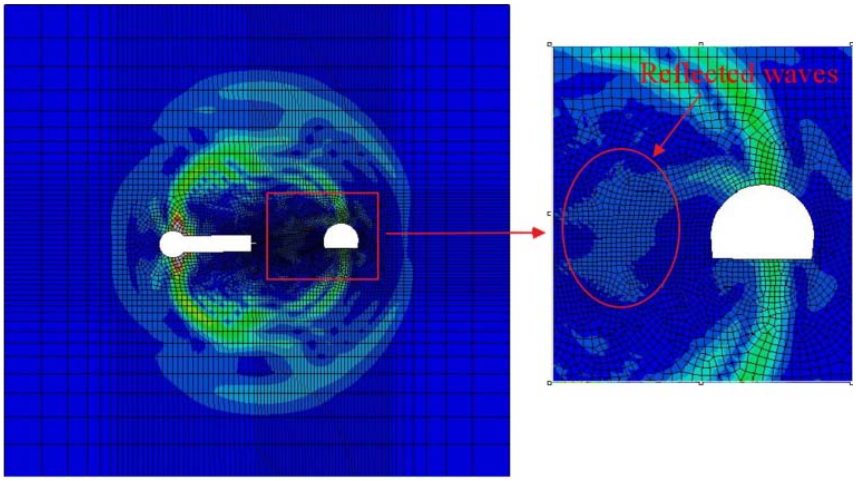

(e) Time = 20.00 ms

Figure 97. Displacement amplitude nephogram at different times during explosions.

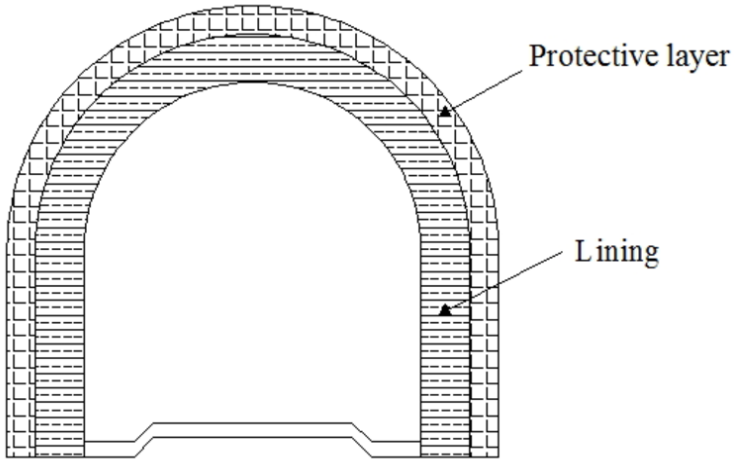

Figure 98. The sketch section of main tunnel with a protective layer.

For the protective layer design, there are generally two important considerations: one is the material properties; the other is the thickness. Different types of protective layer may have quite different vibration isolation effectiveness. And the protective layer thickness has to be carefully examined for the considerations on the construction cost and the construction requirements. In the present study, four typical types of material are examined: cement grout, wood, rubber and EPS, which are very common in civil engineering. The representative values of the four material properties are listed in Table 18. According to the Table 7, it is known that the investigated type of EPS is actually EPS46. It is noted that the damping ratio of all the materials is assumed to be 5%. Like the investigations presented in the last chapter, considering that the 3D analysis is able to produce more accurate results than the 2D analysis, the investigation on the isolation performance of the protective layer is based on 3D model as well.

Table 18. Material properties of the protective layer.

Material	Density (kg/m^3)	Poisson's ratio	Young's modulus (GPa)	Damping ratio
Cement grout	1900	0.20	20	5%
Wood	700	0.30	10	5%
Rubber	1150	0.49	0.05	5%
EPS	45.7	0.26	0.0128	5%

Figure 99 presents the 3D finite element mesh model of rock-tunnel system built in ABAQUS, where a protective layer (in red color) is included. Compared with the model shown in Figure 56, the only difference is that there is a protective layer which lies along the lining (in yellow color). And the protective layer is assumed to be homogeneous, isotropic and elastic, the interfaces are perfected bonded. In order to provide a quick look on the protective layer isolation effectiveness, once again, two points "a1" and "b1" (see Figure 55) are chosen. Figures 100 and 101 show the motion of these two points over time with and without a protective layer. The protective layer is assumed to be EPS with a thickness of 0.3 m. It is observed from Figure 100 that there is a time delay of the appearance of maximum motion of point "a1" with the presence of the protective layer. This may be due to the wave reflection by the protective layer, which postpones the arrival time of waves on the tunnel lining. What also can be seen is that the maximum displacement, velocity and acceleration of point "a1" are remarkably reduced, as the dash lines show. However, a very different phenomenon is observed from Figure 101, which reflects the motion of point "b1". Firstly, there is little difference of the arrival time of waves with and without the protective layer. More importantly, the maximum displacement, velocity and acceleration are unexpectedly amplified due to the installation of the protective layer. The possible explanation is as follows: point "b1", which is located far away from the explosions, seems to be unprotected by the protective layer, because the waves are more likely to propagate from point "b1" to the protective layer, rather than from the opposite direction. Therefore, the waves reflected by the protective layer during wave propagation from the protective layer to point "b1" may inversely amplify the motion of point "b1". It is worth mentioning that in the Section 5.3, it is found that the motion of left half part of main tunnel (i.e. the half part near the explosions) is much larger than that of the right half part (i.e. the half part far away from the explosions), so it is sufficient to just examine the vibration of the left half part of main tunnel under explosions. However, when a protective layer lies along the lining structure, it becomes unclear which part has a stronger motion, because the vibration on the left half part is reduced but is amplified on the right half part. In fact, the maximum displacement, velocity and acceleration of point "a1", which are 3.997×10^{-7} m, 4.621×10^{-4} m/s and 0.779 m/s^{-2} respectively, are only slightly larger than the corresponding ones of point "b1", which are 3.526×10^{-7} m, 2.772×10^{-4} m/s and 0.417 m/s^{-2}, respectively. Therefore, the motion of the whole main tunnel should be examined if a protective layer is installed along the outside the tunnel lining.

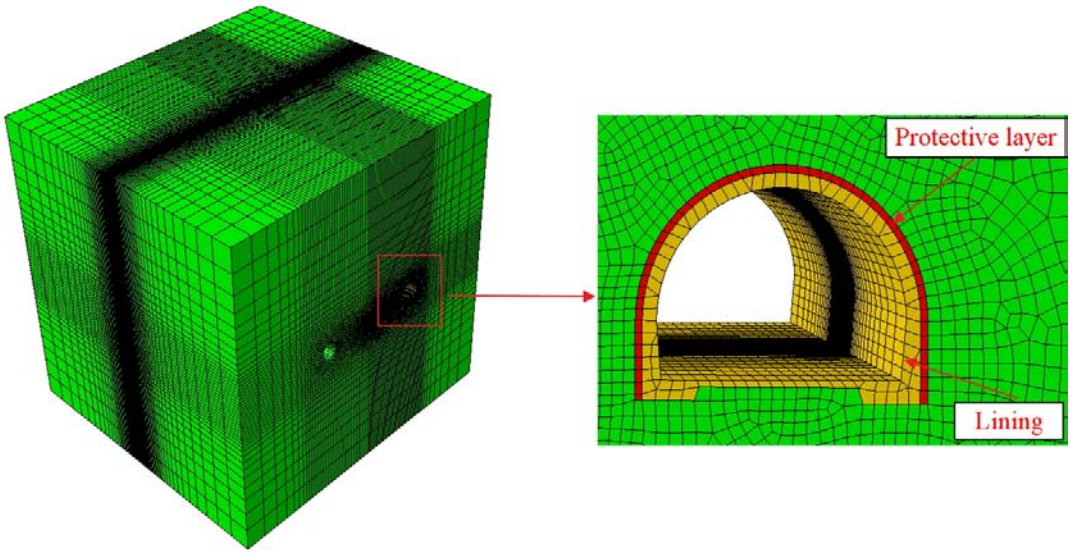

Figure 99. The 3D finite element mesh model with a protective layer.

To investigate the vibration reduction effectiveness of the protective layer quantitatively, at least one of the three quantities, tunnel displacement, velocity and acceleration has to be used. It is well known that Peak Particle Velocity (PPV) is one of the most widely used controlling indexes to assess the level of structure vibration [115]. And study [116] also indicates that the velocity of vibration is a better measure of structure damage than either the displacement or acceleration. Thus, in the present study, the reduction ratio of the maximum velocity v_r is used to evaluate the isolation effectiveness of the protective layer, and v_r is expressed as follows:

$$v_r = \frac{V_{with}}{V_{without}} \tag{30}$$

where V_{with} and $V_{without}$ are the maximum velocity of main tunnel with and without the protective layer under explosions. Since the PPV is measured in three mutually perpendicular directions (radial, vertical and transverse), the v_{rr}, v_{rv} and v_{rt} are respectively used to represent the maximum radial, vertical and transverse velocity reduction ratio. These three parameters can provide a quantitative evaluation of the vibration screening performance of the protective layer, for example, if v_{rr} = 0.6, v_{rv} = 0.7, v_{rt} = 0.8, it means that 40%, 30% and 20% maximum velocity reduction is achieved in the radial, vertical and transverse direction, respectively. Based on the parametric study in the Section 5.4, it is known that the distance of explosions from main tunnel, the blast pressure and the stiffness of main tunnel are the most important factors that affect the tunnel motion. Therefore, the investigation on the isolation performance of the protective layer will be carried out under different conditions of those parameters. In addition, considering that the thickness of the protective layer is often an important design parameter for construction cost and construction requirements in practice, its influence on the isolation effectiveness is examined as well.

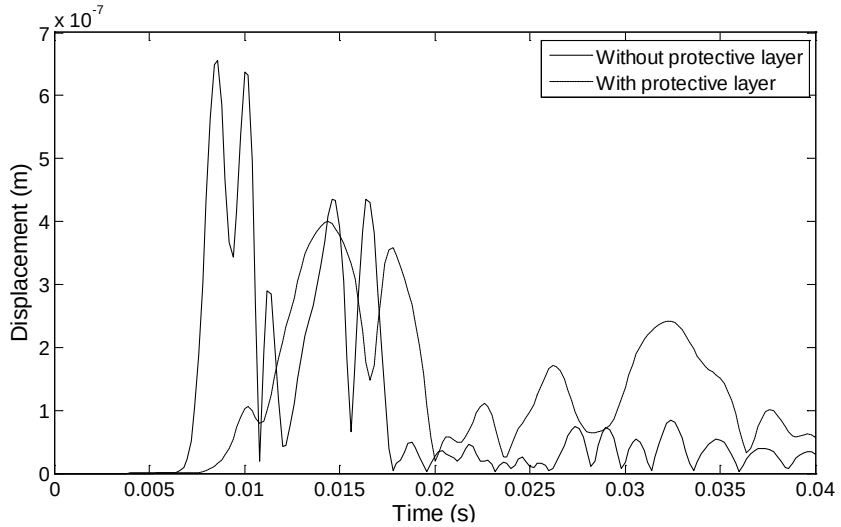

(a) The displacement of point “a1”

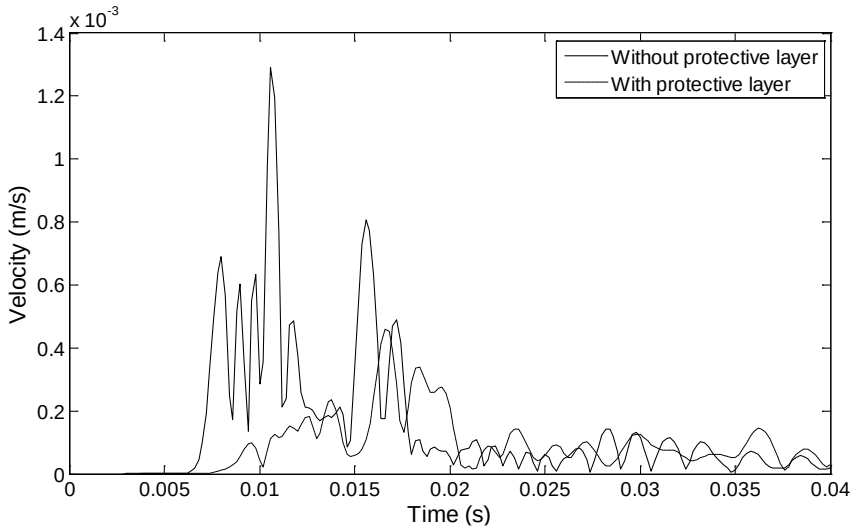

(b) The velocity of point “a1”

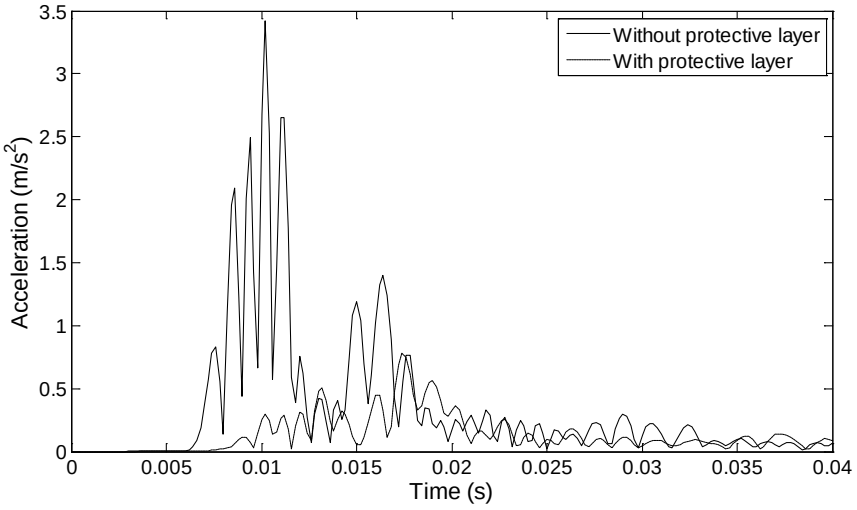

(c) The acceleration of point “a1”

Figure 100. The motion of main tunnel at point “a1” with and without the protective layer under explosions.

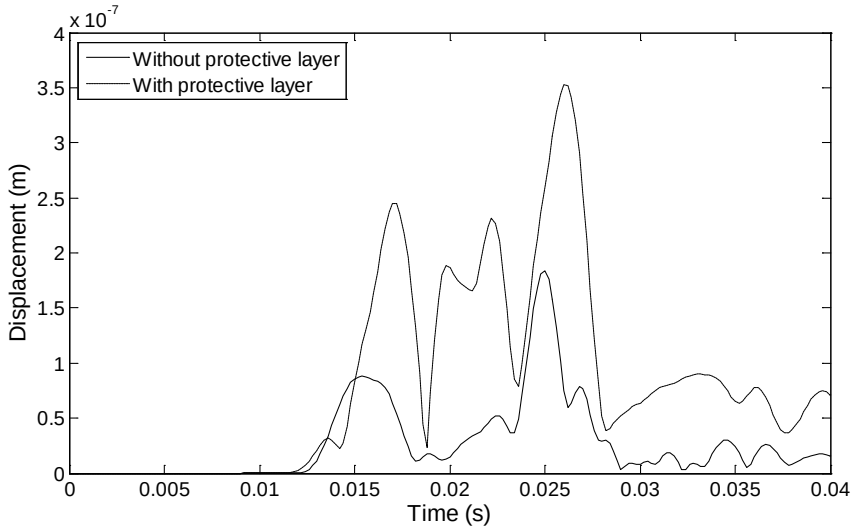

(a) The displacement of point “b1”

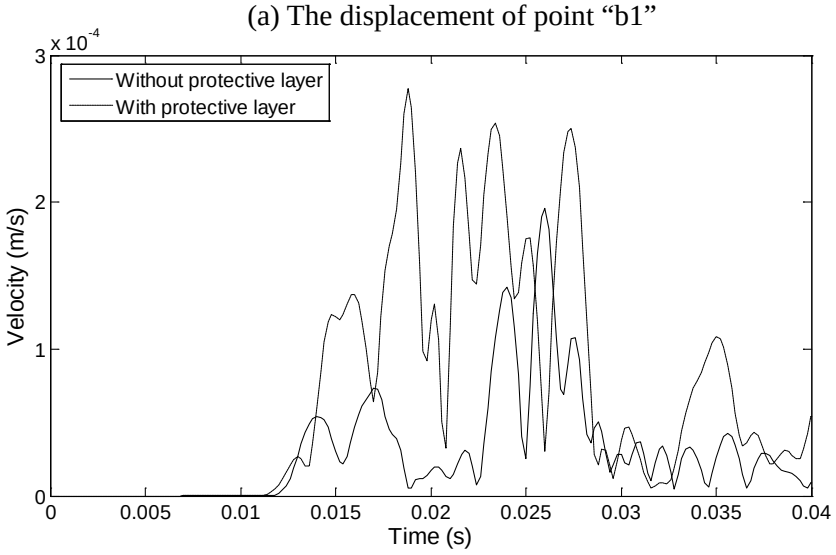

(b) The velocity of point “b1”

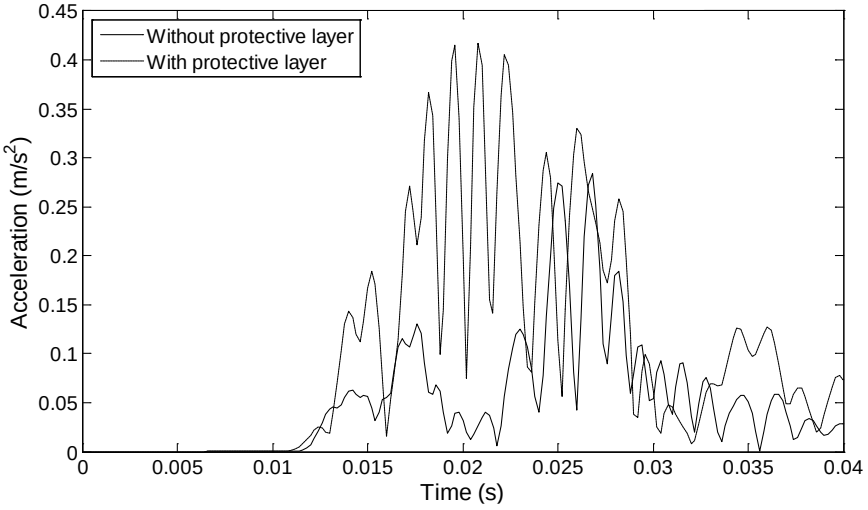

(c) The acceleration of point “b1”

Figure 101. The motion of main tunnel at point “b1” with and without the protective layer under explosions.

6.1.1 Parametric study

To examine the sensitivity of important parameters on the vibration isolation effectiveness of the protective layer, a parametric study is carried out. Four typical types of materials for the protective layer provided in Table 18 are investigated. The evaluated parameters include the thickness of the protective layer, the distance of explosions from main tunnel and the magnitude of blast pressure. The following part presents the analyses and results from the numerical investigation.

6.1.1.1 Effect of the thickness of the protective layer

Figure 102 shows the effect of the thickness of protective layer on the vibration isolation effectiveness. The examined thickness ranges from 0.1 m to 0.5 m. It is clear to see that the protective layer made of EPS performs much better than the ones made of other materials in all the radial, vertical and transverse directions. Specifically, the wood layer does not reduce the tunnel vibration at all, but slightly amplifies it. And the cement grout layer seems to be useless, for the values of v_{rr}, v_{rv} and v_{rt} are almost equal to 1. This may be due to the fact that the material properties of cement grout are the closest to the ones of plain concrete which is the material for the tunnel lining structure. The rubber layer with thickness larger than 0.35 m seems to perform better than the thinner ones. However, such velocity reductions are relatively small compared with the ones achieved by EPS protective layer, where the velocity reduction ratios in all the three directions reduce to be about 0.4. This means that the maximum velocity of tunnel decreases by 60% due to the installation of EPS protective layer. It should be pointed out, however, that the thickness of EPS layer appears to have little influence on the vibration isolation effectiveness, the values of v_{rr}, v_{rv} and v_{rt} change little with an increasing EPS layer thickness. Therefore, the thickness of the protective layer is not an important consideration during the vibration isolation design if the EPS protective layer is installed.

6.1.1.2 Effect of the distance of explosions from main tunnel

Figure 103 shows the effect of the distance of explosions from main tunnel on the vibration isolation effectiveness. It is assumed that the thickness of the protective layer is 0.3 m. Basically, it can be seen that the velocity reduction ratios in all the three directions change little when explosions move away from main tunnel in the case of protective layers made of cement grout, wood and EPS. In other words, these protective layers have stable isolation performance regardless of the blast location (EPS layer performs quite good, cement grout layer and wood layer are useless). On the other hand, it is observed that certain velocity reductions are achieved by rubber layer in some locations (e.g. the investigated distance is within 10 m for reducing the transverse component of velocity). However, there is no doubt that EPS layer still performs much better than the rubber layer. In addition, it is worth mentioning that although the blast

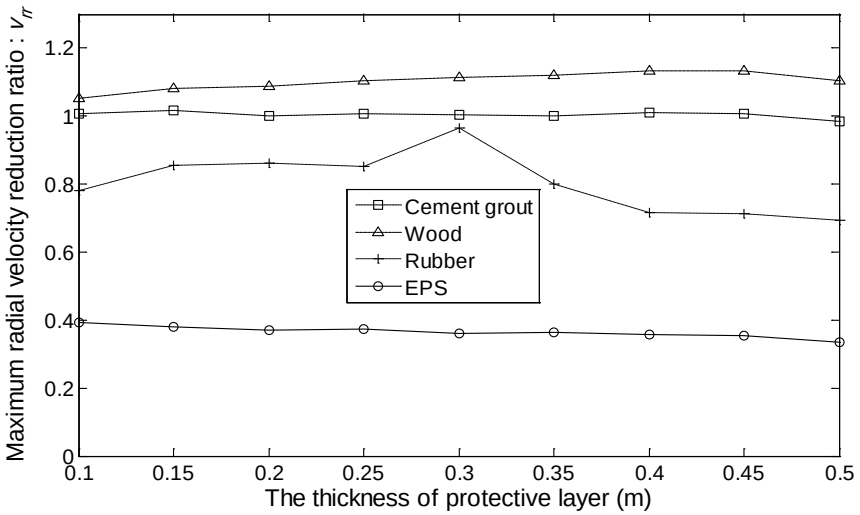

(a) The maximum radial velocity reduction ratio

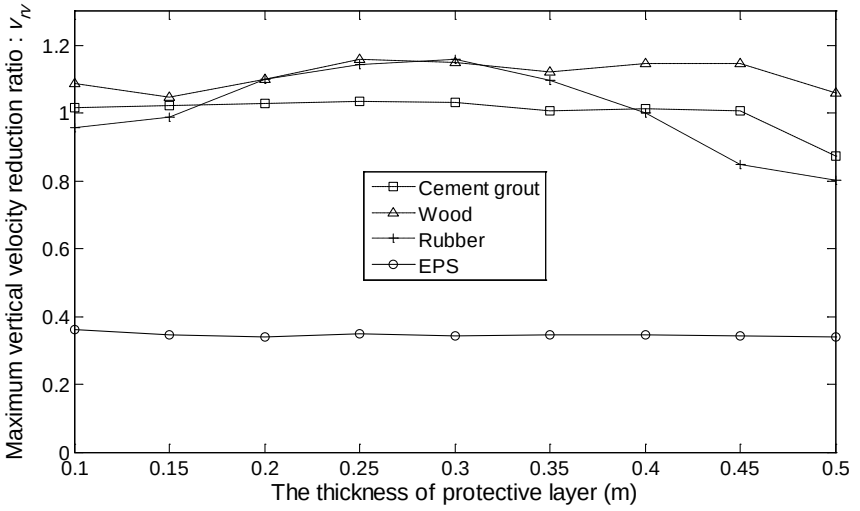

(b) The maximum vertical velocity reduction ratio

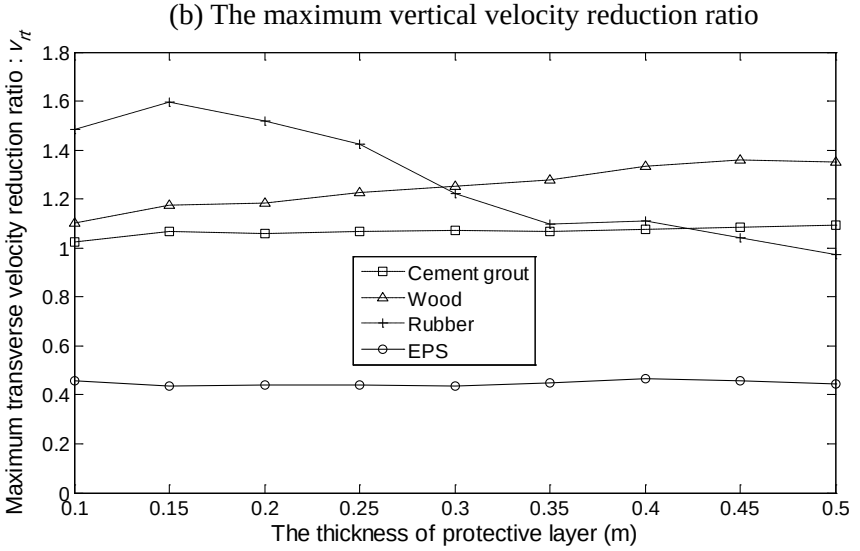

(c) The maximum transverse velocity reduction ratio

Figure 102. Effect of the thickness of protective layer on the vibration isolation effectiveness.

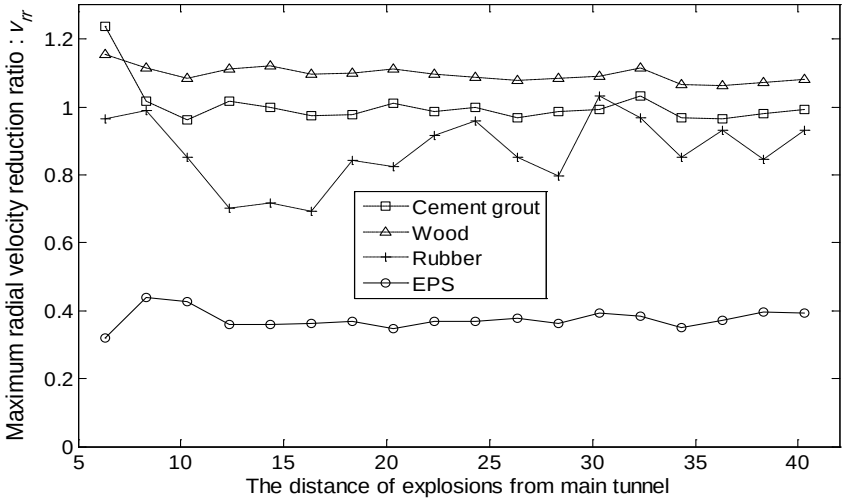

(a) The maximum radial velocity reduction ratio

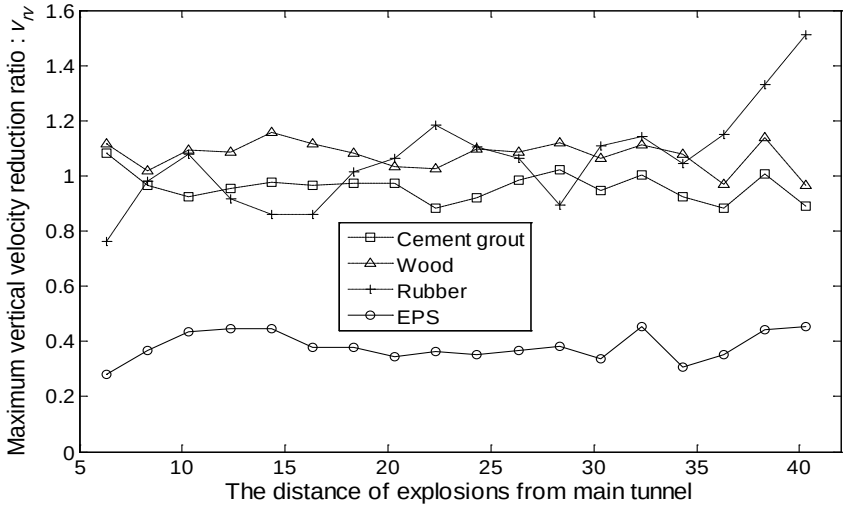

(b) The maximum vertical velocity reduction ratio

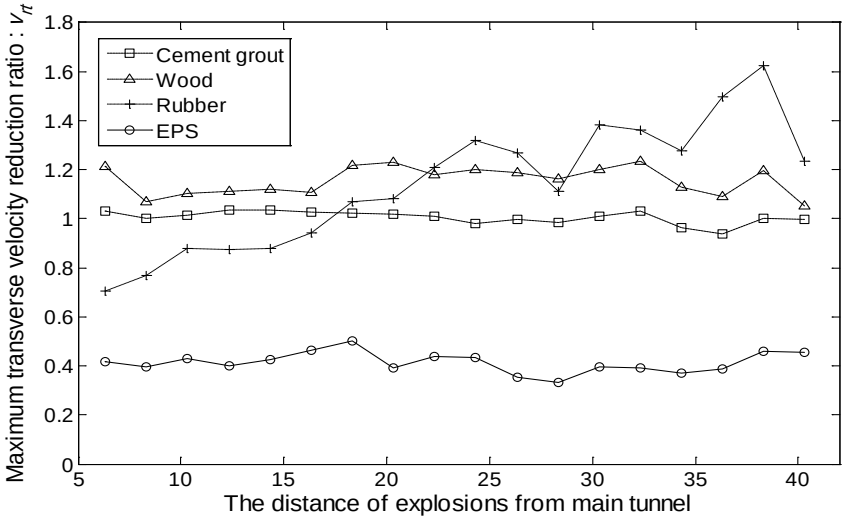

(c) The maximum transverse velocity reduction ratio

Figure 103. Effect of the distance of explosions from main tunnel on the vibration isolation effectiveness.

location generally has minor or negligible influence on the vibration isolation effectiveness of the protective layer, the absolute responses of main tunnel will undoubtedly become stronger as the explosions move closer to main tunnel, regardless of the presence of the protective layer.

6.1.1.3 Effect of blast pressure

Figure 104 shows the effect of blast pressure on the vibration isolation effectiveness. Since the whole model is homogeneous, isotropic and elastic, the velocity reduction ratios keep constant, as expected. It should be pointed out that such conclusion is based on elastic assumption. If the blast pressure is strong enough to generate plastic deformation or even damage of the protective layer and/or main tunnel lining, numerical models with elastic-plastic constitutive relations or more complicated models have to be introduced in order to produce reasonable and reliable simulations of the rock-tunnel system under explosions.

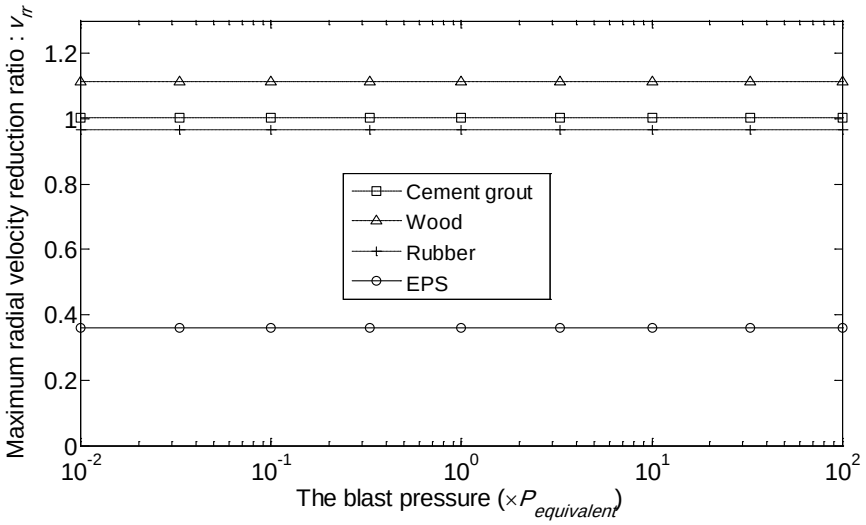

(a) The maximum radial velocity reduction ratio

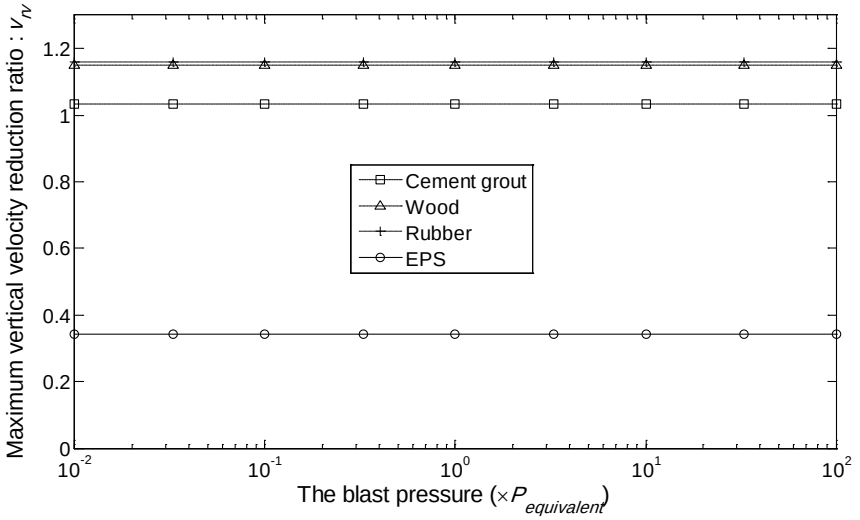

(b) The maximum vertical velocity reduction ratio

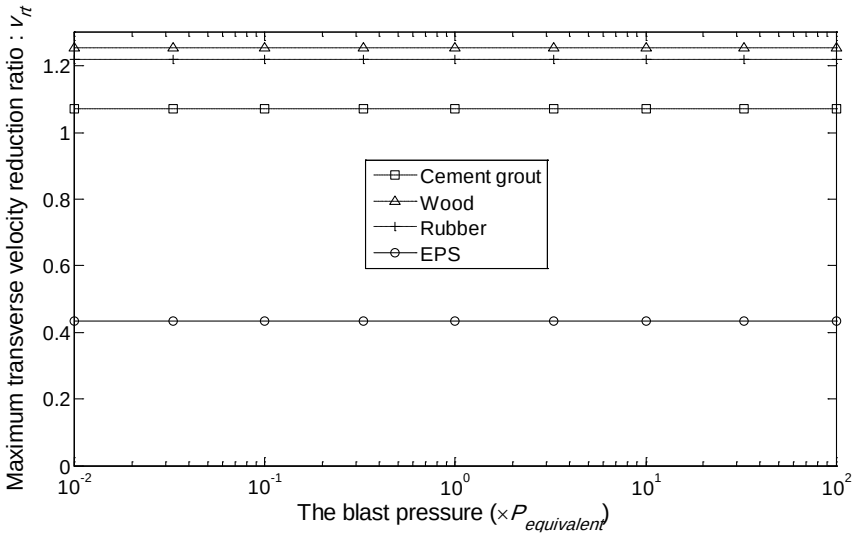

(c) The maximum transverse velocity reduction ratio

Figure 104. Effect of the blast pressure on the vibration isolation effectiveness.

6.1.2 Optimization design of the EPS protective layer

In this section, the optimization design of the protective layer made of EPS is carried out. Like the optimization design method presented in the Chapters 3 and 4, only key parameters are chosen in order to save the calculation time, and the distribution of key parameters to be optimized for EPS protective layer is listed in Table 19. It is mentioned that although the layer thickness is not an important factor, it is still included in the Python script during the optimization design, for considering its importance in other fields, such as construction cost and construction requirements. Again, a Python script is written and run in ABAQUS for the optimization design of EPS protective layer. The final results are shown in Tables 20, 21 and 22, which represents the maximum velocity reduction of main tunnel for parameter optimization of EPS protective layer in the radial, vertical and transverse direction, respectively. Only the best and the worst vibration isolation effectivenesses are shown due to the space constraint. It can be clearly seen that different types of EPS, different layer thicknesses and different blast locations produce quite different isolation effects. Those tables are able to provide a reference for the tunnel protection design under explosions in practice.

Table 19. The distribution of key parameters to be optimized for EPS protective layer

Parameters	Typical values
The thickness of EPS protective layer (m)	0.1, 0.2, 0.3, 0.4, 0.5
The distance of explosions from main tunnel (m)	7, 10, 13, 16, 19, 22, 25, 28, 31, 34, 37, 40
Types of EPS Geofoam	EPS12, EPS15, EPS19, EPS22, EPS29, EPS39, EPS46

Table 20. Final results of the maximum radial velocity reduction of main tunnel for parameter optimization of EPS protective layer

Sequence	Types of EPS	Thickness of protective layer (m)	Distance from main tunnel (m)	A_{rr}
1	EPS46	0.4	13	0.338672
2	EPS39	0.4	13	0.341002
3	EPS29	0.4	13	0.343942
4	EPS12	0.4	13	0.344245
5	EPS15	0.4	13	0.344927
6	EPS22	0.4	13	0.345285
7	EPS19	0.4	13	0.345368
8	EPS46	0.1	4	0.351627
9	EPS46	0.1	10	0.35746
10	EPS39	0.1	10	0.358247
11	EPS29	0.1	10	0.359247
12	EPS39	0.1	4	0.359328
13	EPS46	0.1	13	0.359577
14	EPS39	0.1	13	0.359848
15	EPS12	0.1	10	0.360106
16	EPS29	0.1	13	0.360904
17	EPS46	0.2	13	0.361145
18	EPS15	0.1	10	0.362019
19	EPS39	0.2	13	0.362385
20	EPS22	0.1	13	0.362619
…	…	…	…	…
400	EPS15	0.1	1	0.470214
401	EPS19	0.1	1	0.470302
402	EPS22	0.1	1	0.470365
403	EPS15	0.4	1	0.470377
404	EPS29	0.1	1	0.470533
405	EPS19	0.4	1	0.470684
406	EPS39	0.1	1	0.470764
407	EPS22	0.4	1	0.470846
408	EPS46	0.1	1	0.471014
409	EPS29	0.4	1	0.471116
410	EPS46	0.4	1	0.471475
411	EPS39	0.4	1	0.471753
412	EPS15	0.2	25	0.472347
413	EPS12	0.2	25	0.475332
414	EPS46	0.4	25	0.498222
415	EPS39	0.4	25	0.504864
416	EPS29	0.4	25	0.510881
417	EPS22	0.4	25	0.515292
418	EPS19	0.4	25	0.516892
419	EPS15	0.4	25	0.519177
420	EPS12	0.4	25	0.520601

Table 21. Final results of the maximum vertical velocity reduction of main tunnel for parameter optimization of EPS protective layer

Sequence	Types of EPS	Thickness of protective layer (m)	Distance from main tunnel (m)	A_{rv}
1	EPS46	0.2	10	0.279220
2	EPS39	0.2	10	0.279417
3	EPS29	0.2	10	0.280299
4	EPS22	0.2	10	0.281631
5	EPS19	0.2	10	0.282327
6	EPS29	0.1	10	0.290414
7	EPS39	0.1	10	0.290637
8	EPS46	0.1	13	0.307489
9	EPS46	0.4	10	0.317308
10	EPS39	0.1	16	0.325461
11	EPS46	0.1	10	0.325553
12	EPS46	0.1	16	0.326063
13	EPS22	0.1	10	0.332616
14	EPS12	0.5	22	0.334944
15	EPS15	0.5	22	0.335001
16	EPS19	0.5	22	0.335161
17	EPS22	0.5	22	0.335299
18	EPS29	0.5	22	0.335825
19	EPS39	0.5	22	0.336818
20	EPS19	0.1	10	0.337333
…	…	…	…	…
400	EPS46	0.4	31	0.492629
401	EPS39	0.4	31	0.493456
402	EPS29	0.4	31	0.494596
403	EPS22	0.4	31	0.495670
404	EPS19	0.4	31	0.496139
405	EPS15	0.4	31	0.496839
406	EPS12	0.4	31	0.497348
407	EPS46	0.1	31	0.498766
408	EPS39	0.1	31	0.500993
409	EPS46	0.2	31	0.503106
410	EPS29	0.1	31	0.503239
411	EPS39	0.2	31	0.503511
412	EPS29	0.2	31	0.504562
413	EPS22	0.1	31	0.505010
414	EPS19	0.1	31	0.505690
415	EPS22	0.2	31	0.505887
416	EPS19	0.2	31	0.506502
417	EPS15	0.1	31	0.506679
418	EPS12	0.1	31	0.507331
419	EPS15	0.2	31	0.507505
420	EPS12	0.2	31	0.508235

Table 22. Final results of the maximum transverse velocity reduction of main tunnel for parameter optimization of EPS protective layer

Sequence	Types of EPS	Thickness of protective layer (m)	Distance from main tunnel (m)	A_{rt}
1	EPS29	0.5	22	0.328660
2	EPS39	0.5	22	0.328664
3	EPS22	0.5	22	0.328670
4	EPS46	0.5	22	0.328674
5	EPS19	0.5	22	0.328675
6	EPS15	0.5	22	0.328687
7	EPS12	0.5	22	0.328695
8	EPS12	0.5	19	0.334304
9	EPS15	0.5	19	0.334310
10	EPS19	0.5	19	0.334324
11	EPS22	0.5	19	0.334331
12	EPS29	0.5	19	0.334362
13	EPS39	0.5	19	0.334409
14	EPS46	0.5	19	0.334481
15	EPS46	0.4	25	0.336727
16	EPS46	0.5	25	0.336948
17	EPS39	0.5	25	0.336973
18	EPS29	0.5	25	0.337031
19	EPS22	0.5	25	0.337080
20	EPS19	0.5	25	0.337104
…	…	…	…	…
400	EPS46	0.5	34	0.416721
401	EPS19	0.5	34	0.416729
402	EPS15	0.5	34	0.416781
403	EPS12	0.5	34	0.416809
404	EPS12	0.1	34	0.419715
405	EPS15	0.1	34	0.420038
406	EPS19	0.1	34	0.420521
407	EPS22	0.1	34	0.420839
408	EPS46	0.4	4	0.420892
409	EPS29	0.1	34	0.421643
410	EPS39	0.4	4	0.421843
411	EPS19	0.4	1	0.422308
412	EPS39	0.1	34	0.422587
413	EPS29	0.4	4	0.423210
414	EPS46	0.1	34	0.423513
415	EPS22	0.4	4	0.424404
416	EPS19	0.4	4	0.424902
417	EPS15	0.4	1	0.425318
418	EPS15	0.4	4	0.425666
419	EPS12	0.4	4	0.426202
420	EPS12	0.4	1	0.427304

6.2 Mitigation measure II: millisecond-delay explosions

In the preceding study, all the explosions are assumed to be a single hole blast, while multiple holes blast, which is very common in reality, has not yet been investigated. Since multiple holes blast is so widely used in practice, it is necessary to examine the influence of multiple holes blast on the responses of existing tunnel. Generally speaking, there are two kinds of multiple holes blast: one is the instantaneous explosions (all the explosives are fired at the same time), and the other is the time-delayed explosions (explosives are fired one by one). The latter is considered able to mitigate the existing tunnel vibrations by controlling the delay times among a series of explosions, which produces destructive wave interference during wave propagation in rock media. Figure 105 shows a simple example of two-hole blast along the section of cross passage between the safety tunnel and main tunnel. Two blastholes "h(0)"and "h(T)" detonate at 0 s and T s, respectively. Point "o" is the center of the cross passage section. The distance between the two blastholes is denoted as "S". Suppose that only the single hole blast in the rock-tunnel model (see Figure 56) is replaced by multiple hole blast, the rest of the model keeps constant, a similar numerical model of rock-tunnel system with multiple hole blast can be created in ABAQUS. Figure 106 shows an example of the finite element mesh model with two-hole blast. It is seen that two explosions exist in the cross passage. Again, in order to provide a quick look at the mitigating effect induced by multiple holes blast, two typical points of main tunnel: "a1" and "b1" (see Figure 55) are chosen for comparison study of the motion of main tunnel caused by instantaneous explosions and time-delayed explosions (millisecond-delay explosions). From the Figures 107 and 108, which respectively show the evolution of main tunnel motion at point "a1" and "b1", it can be seen that the maximum motion generated by millisecond-delay explosions (the delayed time "T" is assumed to be 5 ms) is smaller than the one caused by instantaneous explosions. Moreover, the appearance of peak motion at point "a1" seems to be postponed in the case of millisecond-delay explosions. On the other hand, the peak motion of point "b1" is also reduced in the case of millisecond-delay explosions, but there seems to be no delay of the appearance of its peak motion. Besides, it is clear to see that the maximum motion of point "a1" is much larger than the one of point "b1". Based on the observations above, it is inferred that the vibration of main tunnel can be mitigated by the millisecond-delay explosions, and still, the major concern of the main tunnel during the millisecond-delay explosions should be the vibration of the left half part of main tunnel (i.e. the half part of tunnel near the explosions). It is worth noting that the phenomenon presented above is somehow different from what is observed during the investigation of the responses of main tunnel with the installation of a protective layer, where the vibration of both the left and right half part of tunnel has to be examined.

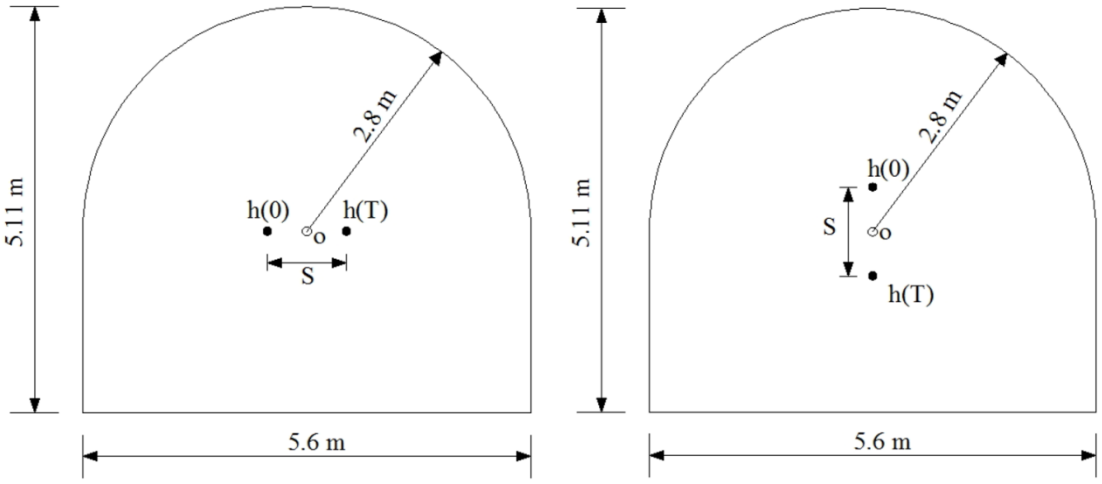

(a) Horizontal distribution (Pattern-H) (b) Vertical distribution (Pattern-V)

Figure 105. The plan of the two-hole blast along the section of cross passage.

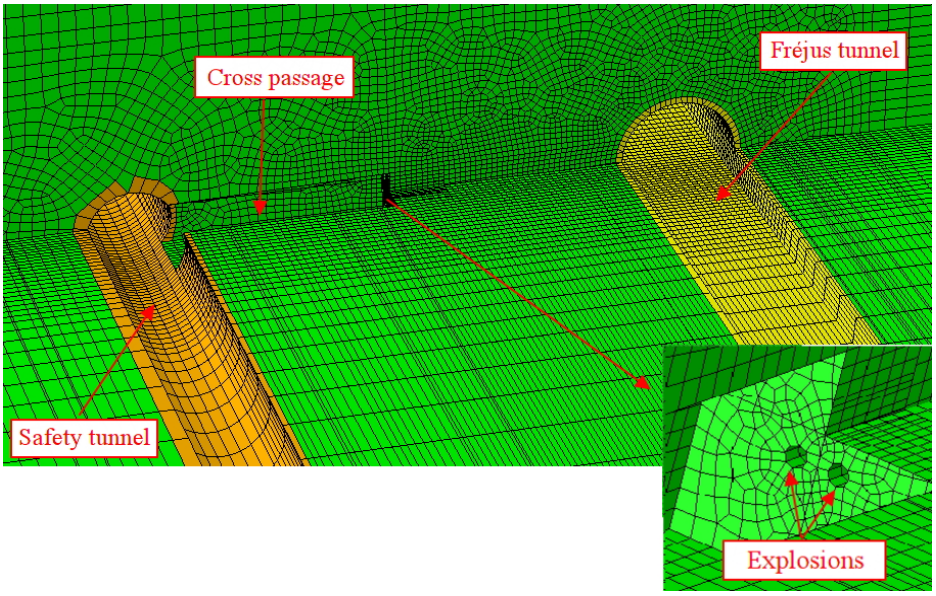

Figure 106. The 3D finite element mesh model with two-hole blast.

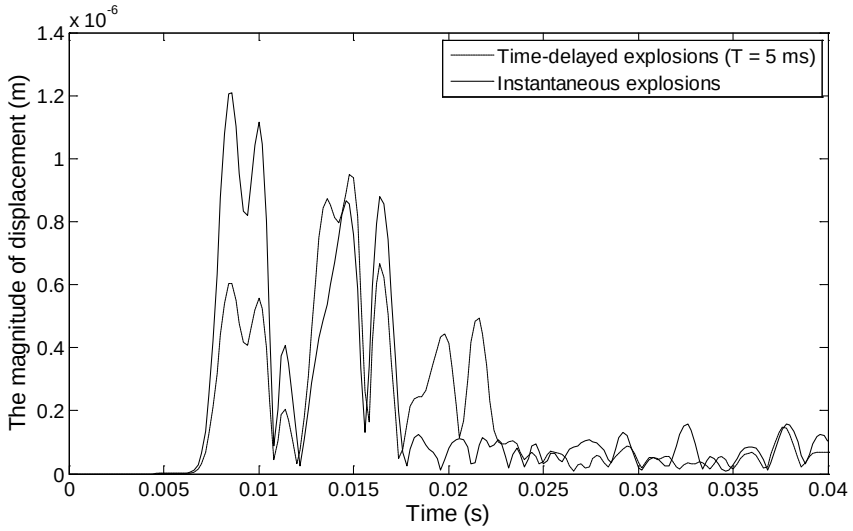

(a) The evolution of displacement

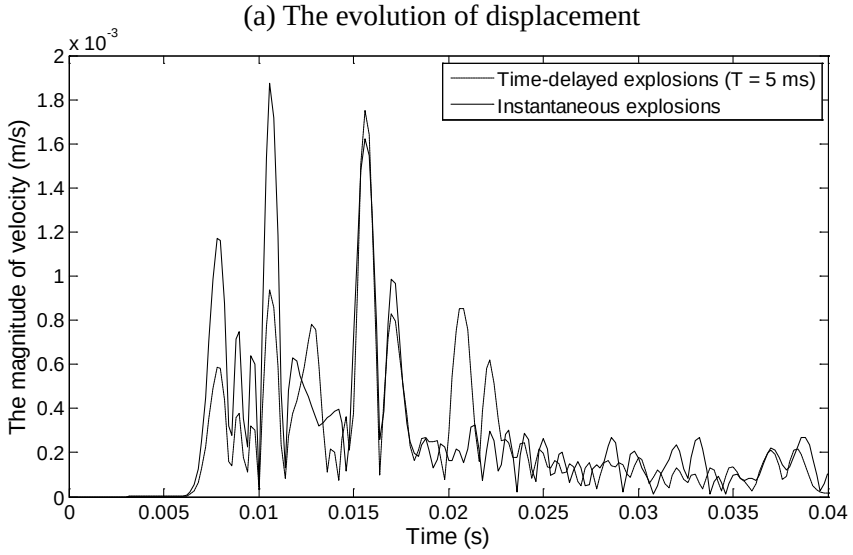

(b) The evolution of velocity

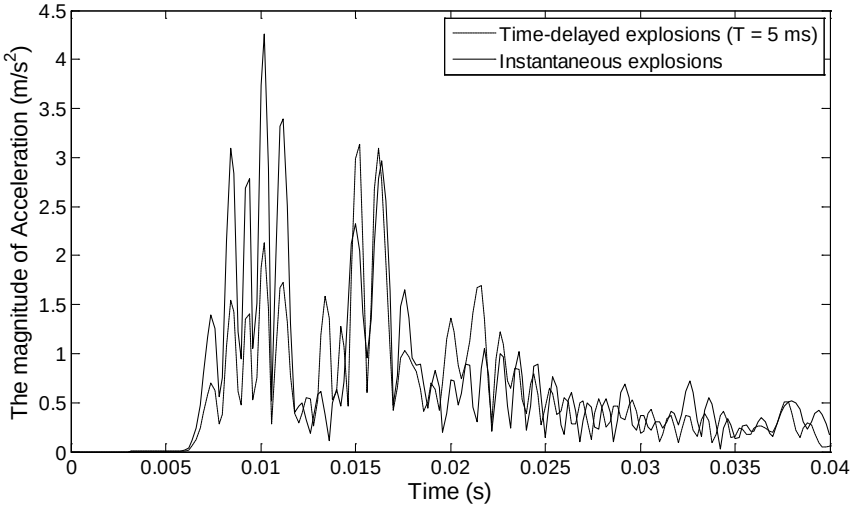

(c) The evolution of acceleration

Figure 107. The motion of point “a1” during the two-hole blast.

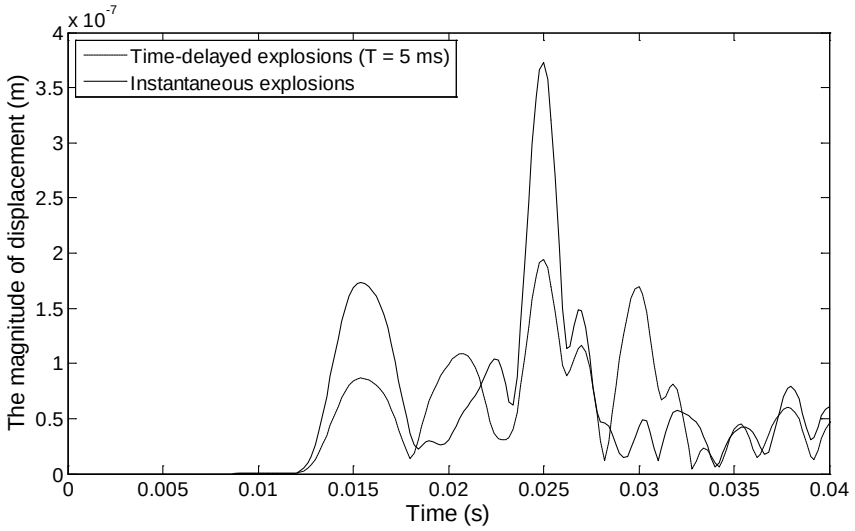

(a) The evolution of displacement

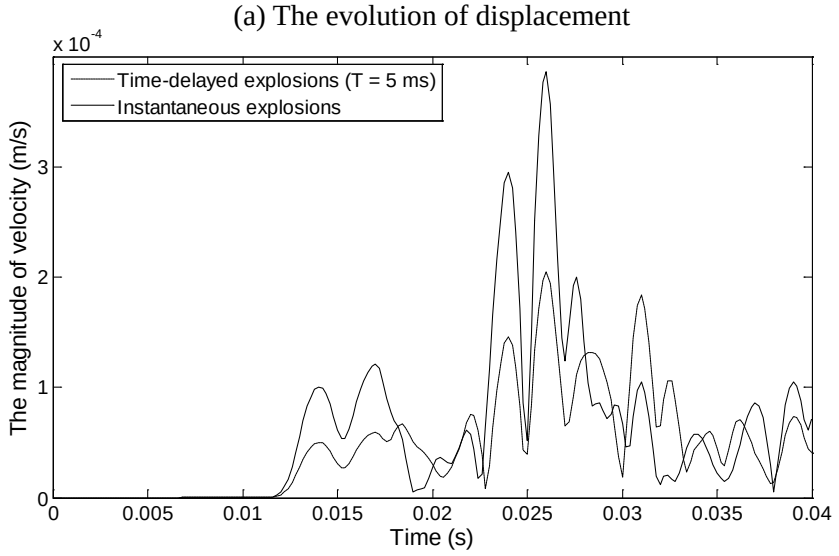

(b) The evolution of velocity

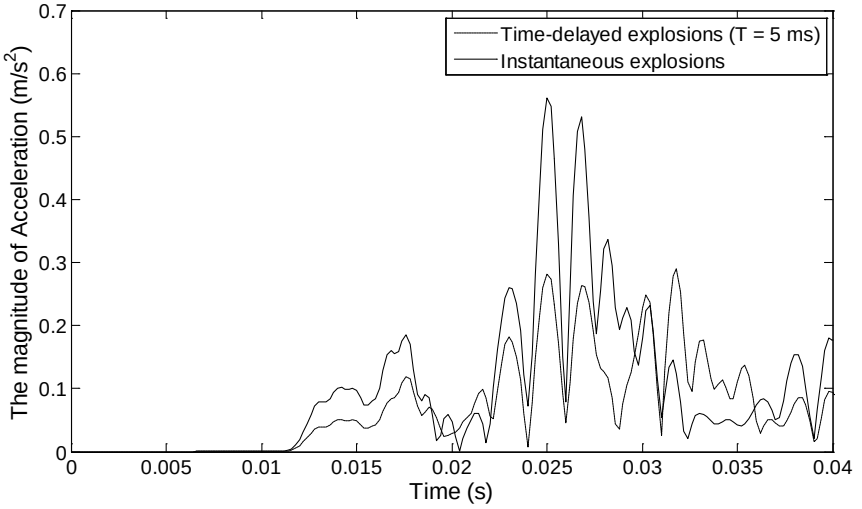

(c) The evolution of acceleration

Figure 108. The motion of point “b1” during the two-hole blast.

Figure 109 presents the dynamic scenarios of two-hole blast vibration propagation along the section of cross passage within 2 ms, the left and right figures show the evolution of displacement during instantaneous explosions and millisecond-delay explosions (the delayed time "T" is assumed to be 0.4 ms), respectively. It is clear to see two explosions from Figure 109(a) on the left side, while only one explosion is seen on the right side. As time goes by, the delayed explosive is fired, and two explosions are observed in Figure 109(b) on the right side, but the area affected by the delayed explosion is relatively small compared with the one affected by original explosion. In addition, it is observed that the distribution of wave propagation is symmetric in the case of instantaneous explosions, but not in the case of millisecond-delay explosions, as expected. It is noted that the Figure 109(a)-(g) provides a clear image on the wave propagation along the section of cross passage during both the instantaneous explosions and millisecond-delay explosions. The following paragraphs will further show an extensive investigation on the blast-induced vibration of main tunnel generated by instantaneous explosions and millisecond-delay explosions.

Before examining the vibration reduction effectiveness of millisecond-delay explosions, it is worth pointing out two important considerations during the multiple-hole explosions design: the first one is the pattern of blastholes. It is well known that there is a variety of blasthole patterns in practice. It is interesting to find out the possible responses of main tunnel in the case of different patterns of blastholes under explosions. In this study, some basic patterns of blastholes are discussed. The second consideration is the distance *"*S*"* between the blastholes, which has to be examined carefully. Explosions with too large *"*S*"* may not be strong enough to break rock, while too small *"*S*"* may cause excessive usage of explosives. In the present study, the value of *"*S*"* is assumed to be 1 m.

To evaluate the performance of millisecond-delay explosions in reducing the vibration of main tunnel, the maximum velocity reduction ratio v_r is adopted, and v_r is denoted as:

$$v_r = \frac{V_{delayed}}{V_{instantaneous}} \tag{31}$$

where $V_{delayed}$ and $V_{instantaneous}$ are the maximum velocity of main tunnel under millisecond-delay explosions and instantaneous explosions, respectively. Again, the v_{rr}, v_{rv} and v_{rt} are respectively used to represent the maximum radial, vertical and transverse velocity reduction ratio. These three parameters provide a quantitative evaluation of the tunnel vibration reduction in the case of millisecond-delay explosions, for example, if v_{rr} = 0.6, v_{rv} = 0.7, v_{rt} = 0.8, it means that 40%, 30% and 20% maximum tunnel velocity reduction is achieved in the radial, vertical and transverse direction, respectively.

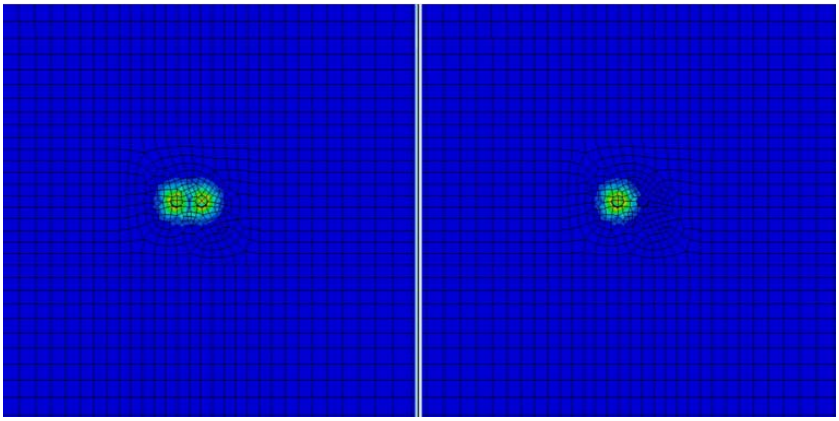

(a) Time = 0.4 ms

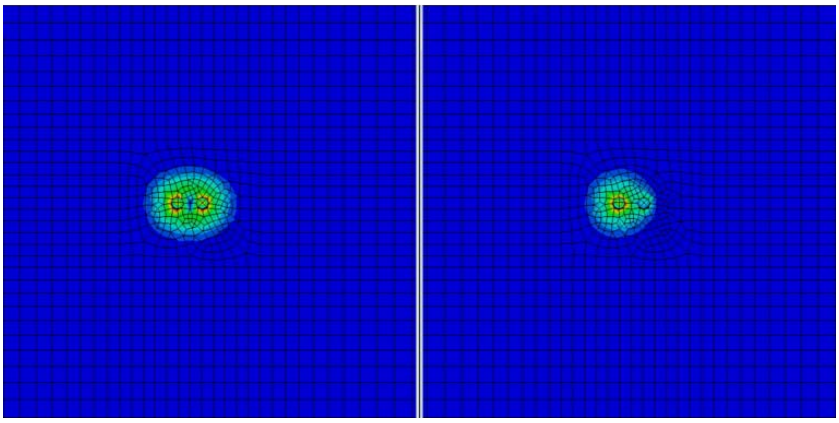

(b) Time = 0.6 ms

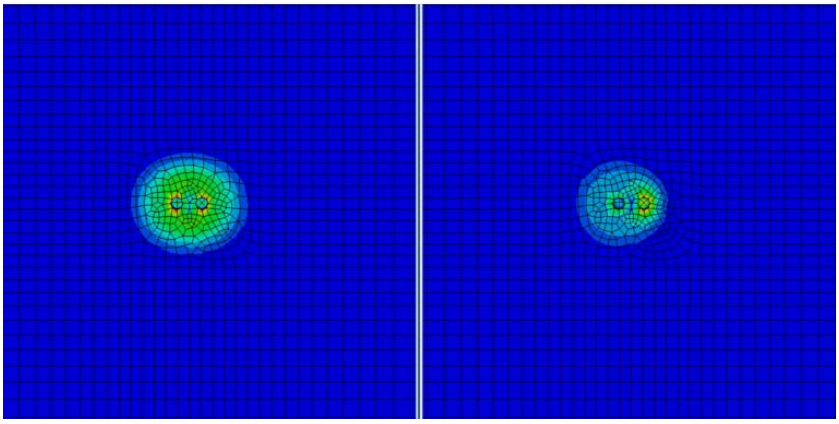

(c) Time = 0.8 ms

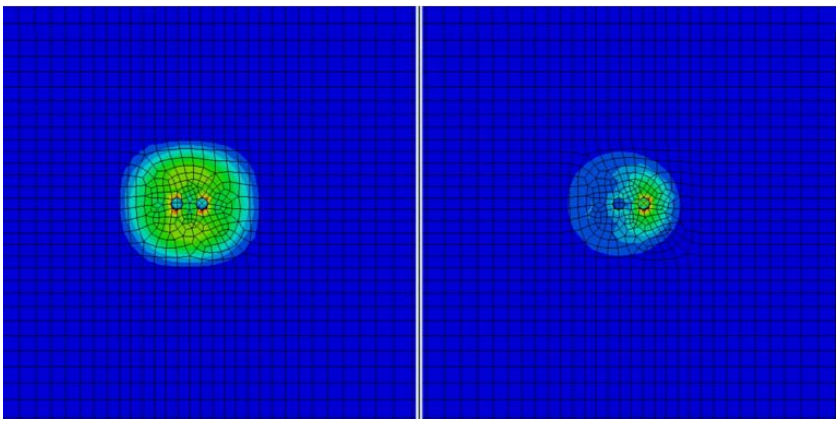

(d) Time = 1.0 ms

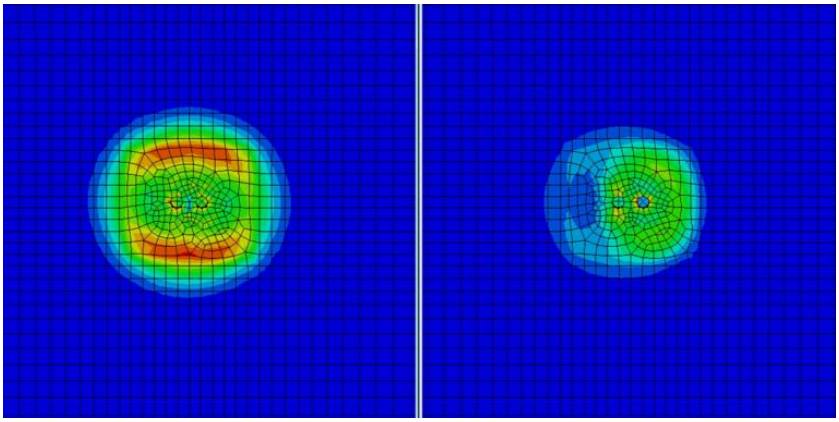

(e) Time = 1.4 ms

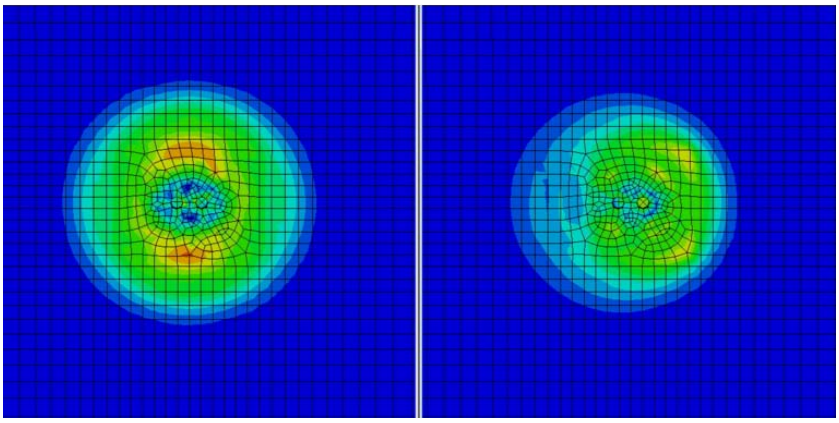

(f) Time = 1.8 ms

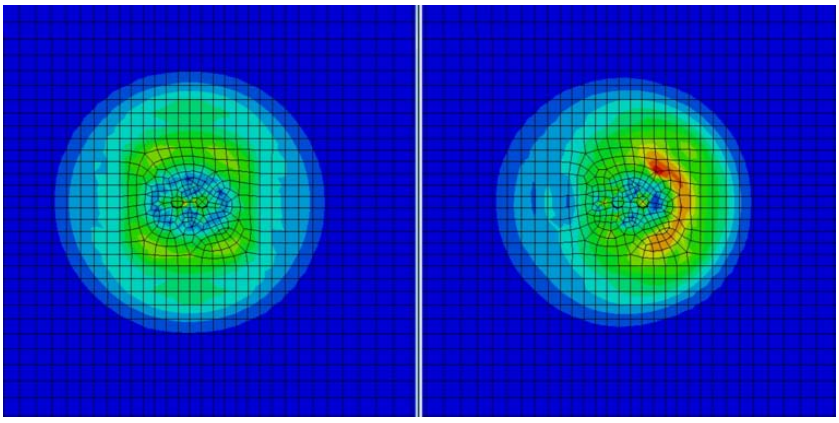

(g) Time = 2.0 ms

Figure 109. Displacement amplitude nephogram over times during two-hole blast (Instantaneous explosions on the left side and millisecond-delay explosions on the right side).

6.2.1 Two-hole blast

Figure 105 describes the plan of two-hole blast along the section of cross passage. Two basic patterns of blastholes are presented: one is the horizontal distribution (see Figure 105(a)), the other is vertical distribution (see Figure 105(b)), which are denoted as Pattern-H and Pattern-V, respectively. Figure 110 shows the maximum velocity reduction effectiveness of millisecond-delay explosions with two-hole blast. It is clearly seen that all the velocity reduction ratios in the three directions are smaller than 1.0. This means that the main tunnel vibrations generated by millisecond-delay explosions are smaller than the ones caused by instantaneous explosions. What can also be seen is that the motion of main tunnel basically becomes smaller with an increasing delayed time "T", but when "T" is larger than 20 ms, there seems to be little further velocity reduction. The possible explanation is that negligible interaction exists between the first and the delayed explosion if "T" is larger than 20 ms. Based on the observation above, it can be concluded that millisecond-delay explosions are effective in mitigating the responses of main tunnel. And explosions with different delayed times may produce quite different vibration reduction effectiveness. Moreover, explosions with delayed time larger than 20 ms can be considered as a series of separate explosion with little interaction among them. Thus, the following investigation will focus on the examination of vibration reduction effectiveness of millisecond-delay explosions with delayed time "T" smaller than 20 ms.

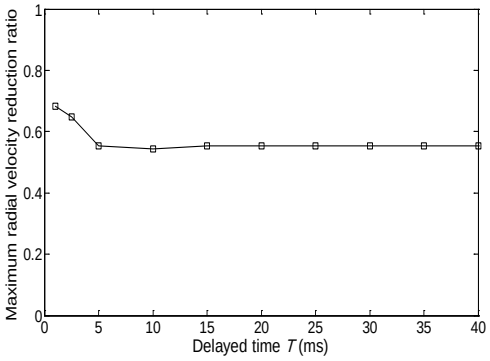

(a) The maximum radial velocity reduction ratio (Pattern-H)

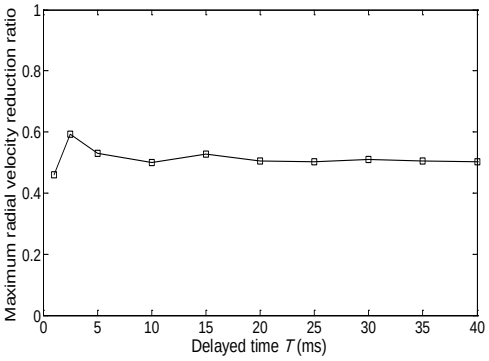

(b) The maximum radial velocity reduction ratio (Pattern-V)

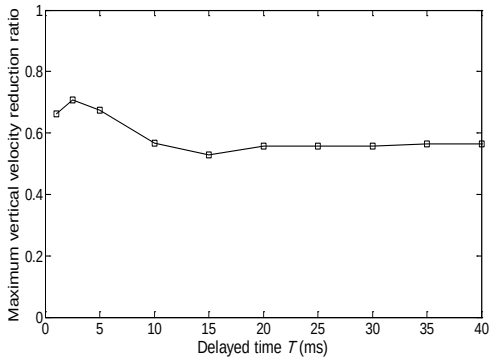

(c) The maximum vertical velocity reduction ratio (Pattern-H)

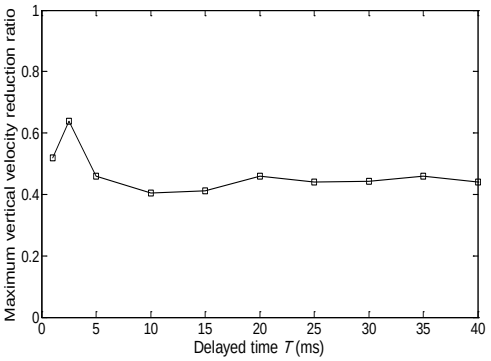

(d) The maximum vertical velocity reduction ratio (Pattern-V)

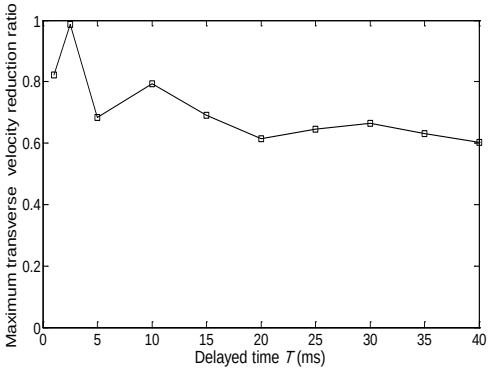

(e) The maximum transverse velocity reduction ratio (Pattern-H)

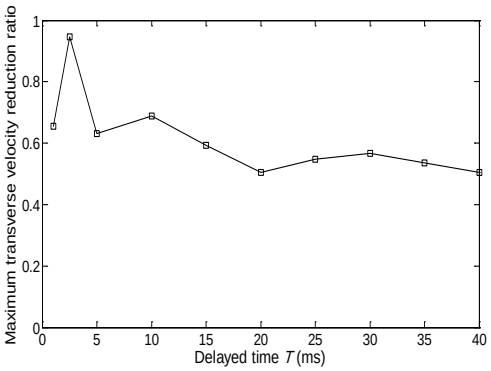

(f) The maximum transverse velocity reduction ratio (Pattern-V)

Figure 110. The maximum velocity reduction effectiveness of millisecond-delay explosions with two-hole blast (Pattern-H and Pattern-V are shown in Figure 105).

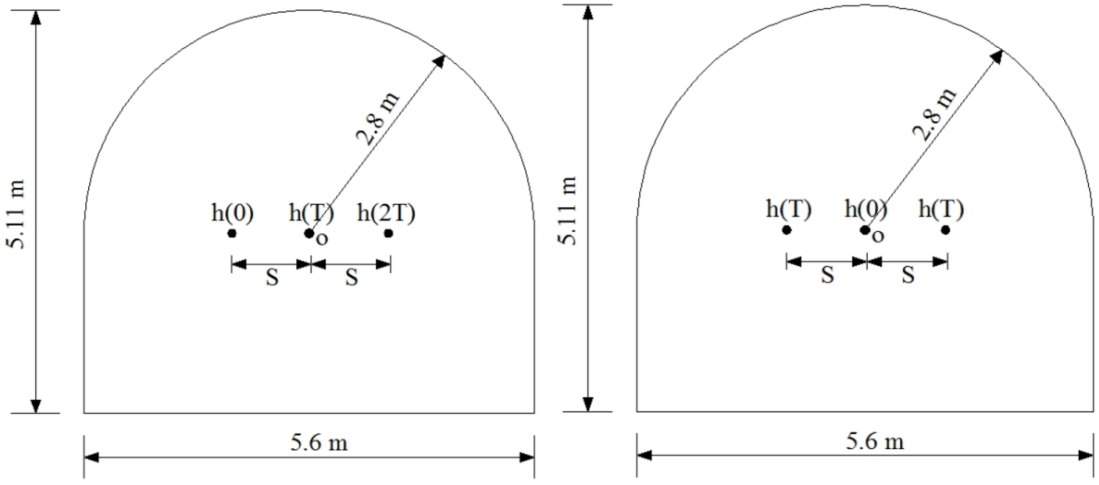

(a) Three-hole blast (Pattern-H1)

(b) Three-hole blast (Pattern-H2)

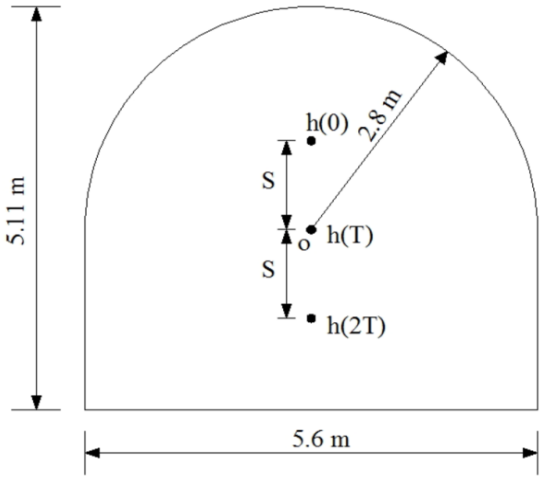

(c) Three-hole blast (Pattern-V1)

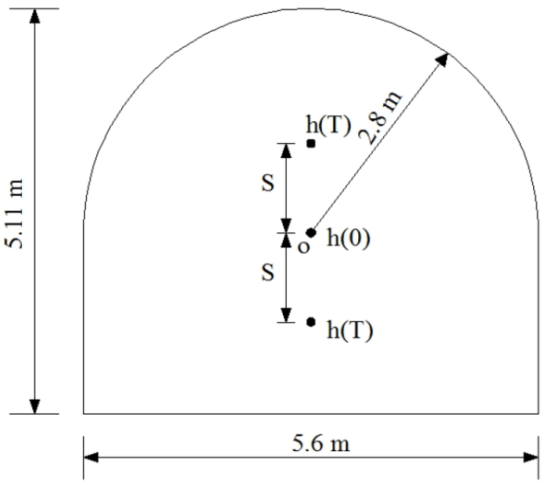

(d) Three-hole blast (Pattern-V2)

Figure 111. The plan of the three-hole blast along the section of cross passage.

6.2.2 Three-hole blast

Figure 111 shows the plan of three-hole blast along the section of cross passage. Four typical patterns of blastholes are presented: Pattern-H1, Pattern-H2, Pattern-V1 and Pattern-V2 (see Figure 111(a)-(d), respectively). The major difference between the three-hole blast and the two-hole blast is that there are typically two ways of firing explosives during the three-hole blast. One way is that explosives are fired from one side to another side, as shown in Figure 111(a) and (c); the other way is that explosives are firstly fired in the middle and then in the two sides, as shown in Figure 111(b) and (d). It is noted that the blasthole "h(2T)" detonates at 2T, and the definitions of other parameters are the same as those mentioned in the two-hole blast study. Since these four patterns of three-hole blast are so common in practice, it is necessary to examine all their velocity reduction effectivenesses. Figure 112(a), (c) and (e) show the maximum velocity reduction effectiveness of millisecond-delay explosions with three-hole blast in Pattern-H1 and Pattern-H2. It is seen that the motion of main tunnel is reduced to some extent. Specifically, more than half of the maximum velocity reduction is achieved in the radial and vertical directions, and about 40% maximum velocity reduction in the transverse direction in the case of the millisecond-delay explosions in Pattern-H1. By contrast, the millisecond-delay explosions in Pattern-H2 reduce the maximum velocity of main tunnel by only about 40%, 40% and 30% in the radial, vertical and transverse direction, respectively. Therefore, it is inferred that time-delayed explosions in Pattern-H1 are more efficient in reducing the tunnel vibration than the ones in Pattern-H2. Similar phenomenon can be observed in Figure 112(b), (d) and (f), which reflects the maximum velocity reduction effectiveness of millisecond-delay explosions with three-hole blast in Pattern-V1 and Pattern-V2, i.e. the millisecond-delayed explosions in Pattern-V1 are more efficient in reducing the tunnel vibration than the ones in Pattern-V2. Thus, it is strongly suggested to fire the explosives from one side to another side (rather than from the middle to its sides) in order to mitigate the vibration of the main tunnel.

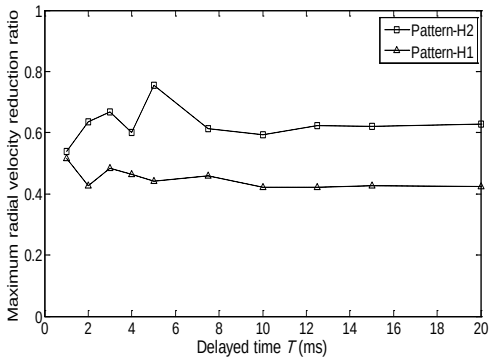

(a) The maximum radial velocity (Pattern-H1, H2)

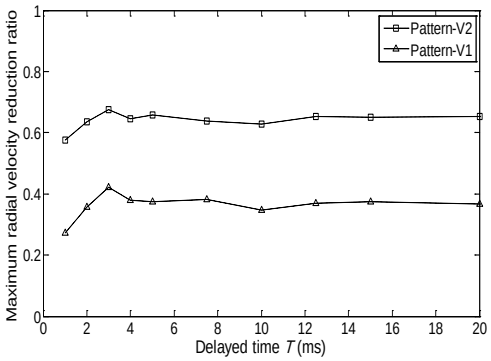

(b) The maximum radial velocity (Pattern-V1, V2)

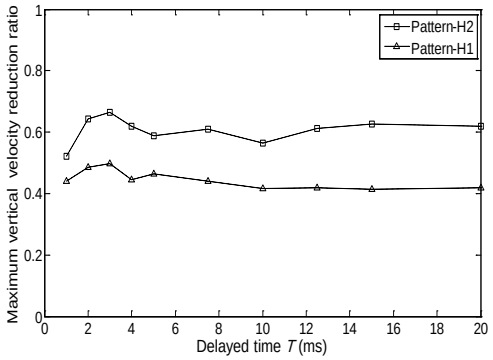

(c) The maximum vertical velocity (Pattern-H1, H2)

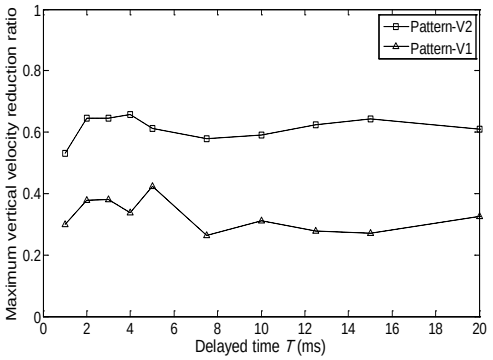

(d) The maximum vertical velocity (Pattern-V1, V2)

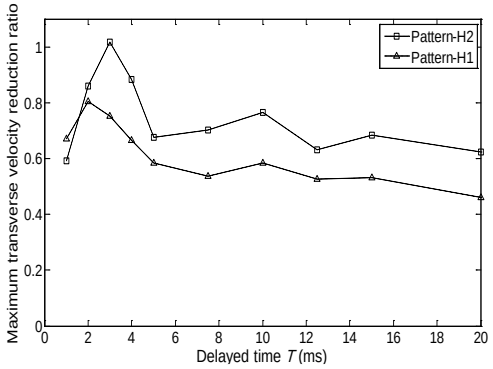

(e) The maximum transverse velocity (Pattern-H1, H2)

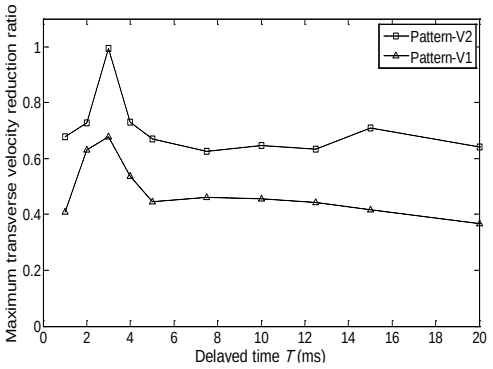

(f) The maximum transverse velocity (Pattern-V1, V2)

Figure 112. The maximum velocity reduction effectiveness of millisecond-delay explosions with three-hole blast (Pattern-H1, H2, V1 and V2 are shown in Figure 111).

6.2.3 Four-hole blast

Figure 113 shows the plan of four-hole blast along the section of the cross passage. Six typical pattern of four-hole blast are included: Pattern-H1, Pattern-V1, Pattern-H2, Pattern-V2, Pattern-H3 and Pattern-V3, which are shown in Figure 113(a)-(f), respectively. Investigation on the millisecond-delay explosions in these six patterns can provide not only an insight of the effect of delayed time "T", but also an examination on the influence of relative positions of the blastholes on the tunnel motion. It is assumed that the plan of four blastholes of instantaneous explosions is the same as the one in Pattern-H1 (see Figure 113(a)). Figure 114 shows the maximum velocity reduction effectiveness of millisecond-delay explosions with four-hole blast. It is seen that an average of 40% to 60% tunnel velocity reduction can be achieved in the radial and vertical directions. However, the efficiency of reducing transverse velocity is relatively low, especially when the delayed time "T" is smaller than 5 ms. It is interesting mentioning that the millisecond-delay explosions in Pattern-H1 and Pattern-H2 generally perform a little better than the ones in Pattern-H3 when "T" is larger than 8 ms, but inverse phenomenon seems to be observed for the millisecond-delay explosions in Pattern-V1, V2 and V3, i.e. the millisecond-delay

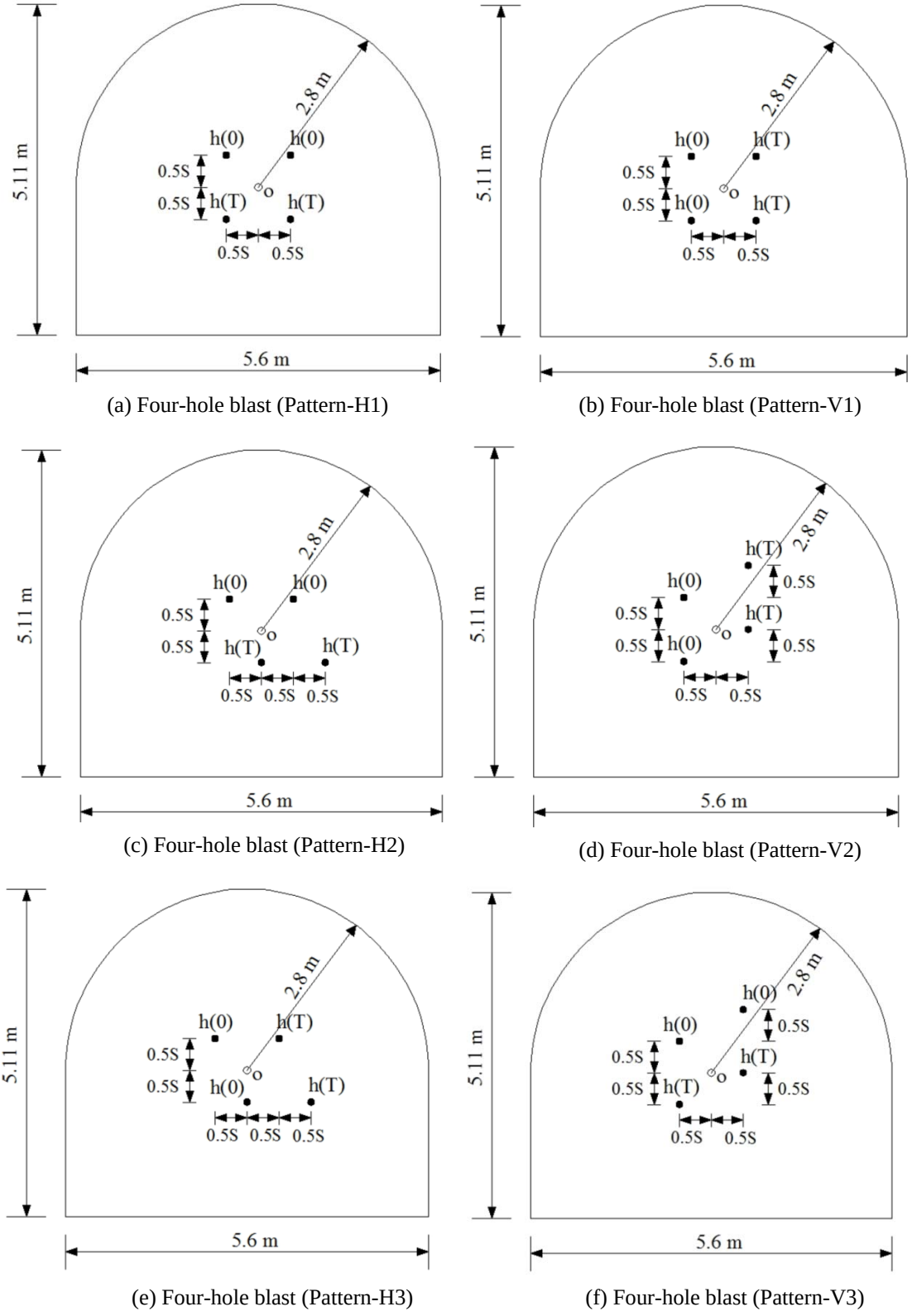

Figure 113. The plan of the four-hole blast along the section of cross passage.

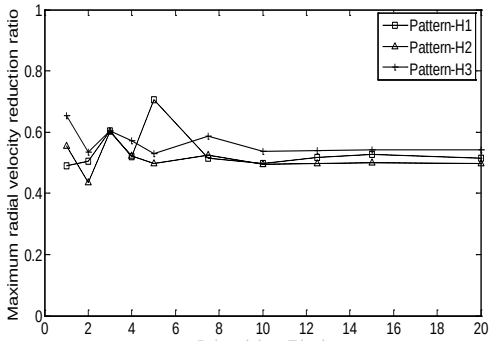

(a) The maximum radial velocity (Pattern-H1, H2, H3)

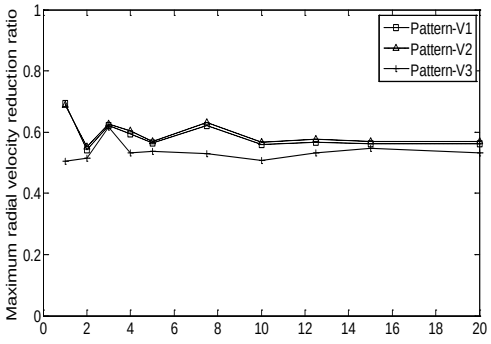

(b) The maximum radial velocity (Pattern-V1, V2, V3)

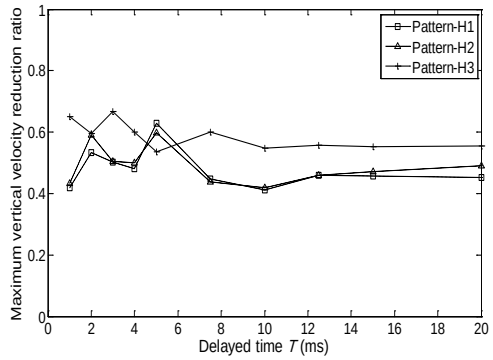

(c) The maximum vertical velocity (Pattern-H1, H2, H3)

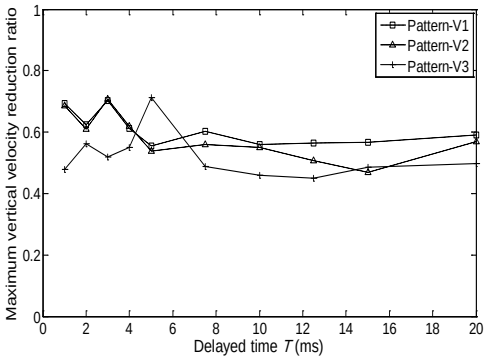

(d) The maximum vertical velocity (Pattern-V1, V2, V3)

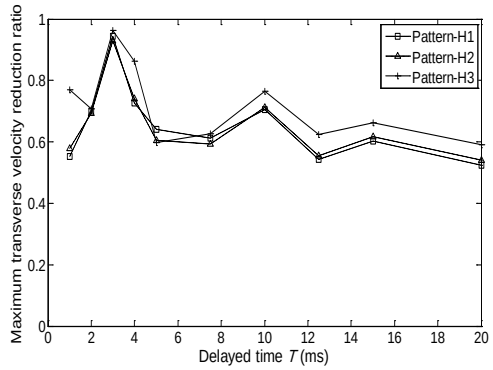

(e) The maximum transverse velocity (Pattern-H1, H2, H3)

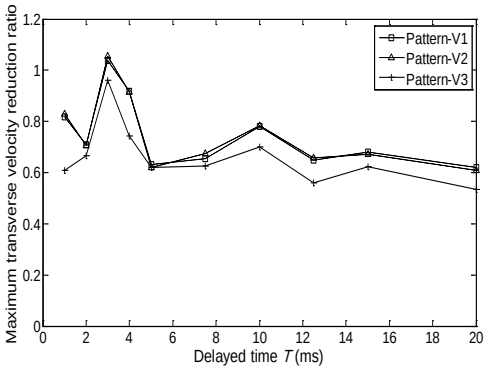

(f) The maximum transverse velocity (Pattern-V1, V2, V3)

Figure 114. The maximum velocity reduction effectiveness of millisecond-delay explosions with four-hole blast (Pattern-H1, H2, H3, V1, V2 and V3 are shown in Figure 113).

explosions in Pattern-V3 basically appear to perform a little better than the ones in Pattern-V1 and Pattern-V2. This may be due to the complicated wave interference caused by different patterns of blastholes and the relative positions between the main tunnel and the blastholes. Nevertheless, as long as the delayed time is long enough ("T" > 10 ms), the differences of the maximum velocity reduction effectiveness of millisecond-delay explosions with four-hole blast in different patterns are very small. Therefore, it is inferred that the patterns of blastholes have a limited impact on the vibration reduction of main tunnel under millisecond-delay explosions with a relatively long delayed times.

6.2.4 Nine-hole blast (in parallelogram shape)

Figure 115 shows the plan of nine-hole blast along the section of the cross passage. Twelve typical patterns of nine-hole blast, which are denoted as Pattern-H1, Pattern-H2, Pattern-H3, Pattern-H4, Pattern-H5, Pattern-H6, Pattern-V1, Pattern-V2, Pattern-V3, Pattern-V4, Pattern-V5 and Pattern-V6, are presented, as shown in Figure 115(a)-(m), respectively. Examination of time-delayed explosions in these twelve patterns can further provide a comprehensive understanding on the effect of the delayed time "T", the relative positions of the blastholes as well as the sequence of firing explosives. Figure 116 presents the maximum velocity reduction effectiveness of millisecond-delay explosions with nine-hole blast (in parallelogram shape). It can be observed that millisecond-delay explosions in Pattern-H2, H4 and H6 (Pattern-V2, V4 and V6) perform better than the ones in Pattern-H1, H3 and H5 (Pattern-V1, V3 and V5). This means that it is more efficient in mitigating the vibration of main tunnel when the explosives are fired from one side to the other side, rather than from the middle to the sides. This agrees with the conclusion made in Section 6.2.2 that millisecond-delay explosions with explosives fired from one side to another side should be used to minimize the tunnel motion. It is also seen that the differences of the velocity reduction ratios of millisecond-delay explosions in Pattern-H2, H4 and H6 ((Pattern-H1, H3, and H5), (Pattern-V2, V4 and V6), ((Pattern-V1, V3, and V5)) are relatively small. This means that the relative positions of blastholes have little impact on the vibration of main tunnel. It confirms the inference made in Section 6.2.3 that the positions of blastholes have limited influence on the vibration reduction effectiveness. Based on the analyses above, it is summarized that millisecond-delay explosions with explosives fired from one side to the other side is the effective way to reduce the blast-reduced vibration, and the distribution of blastholes along the section of cross passage is relatively unimportant for the vibration of tunnel.

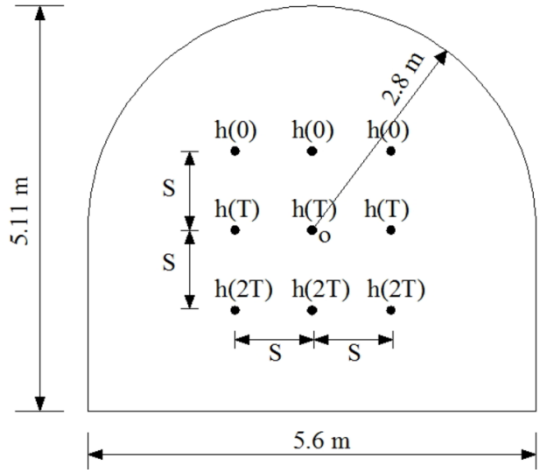

(a) Nine-hole blast (Pattern-H1)

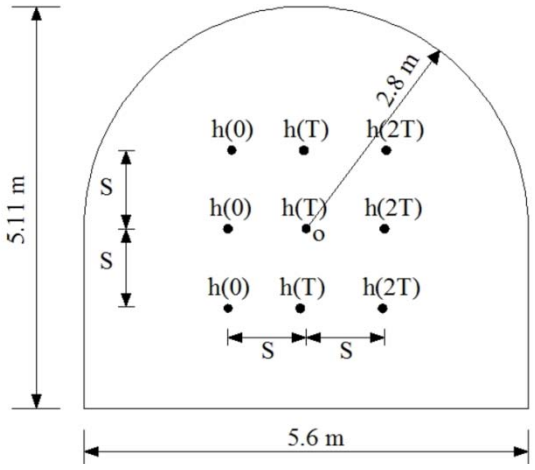

(b) Nine-hole blast (Pattern-V1)

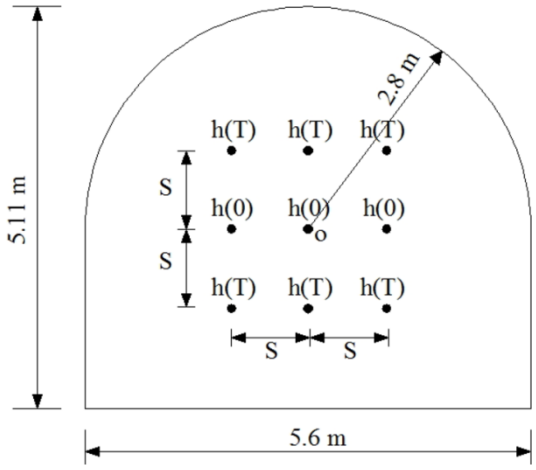

(c) Nine-hole blast (Pattern-H2)

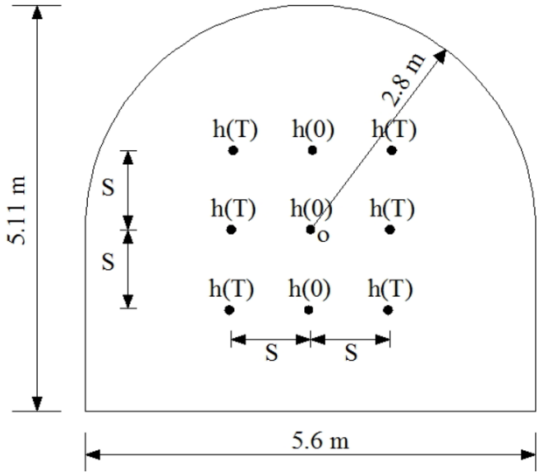

(d) Nine-hole blast (Pattern-V2)

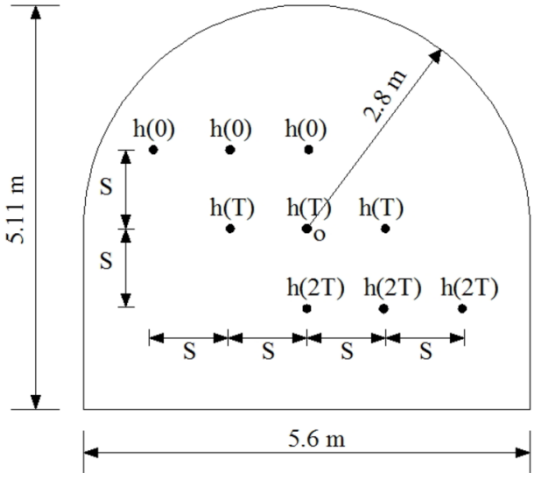

(e) Nine-hole blast (Pattern-H3)

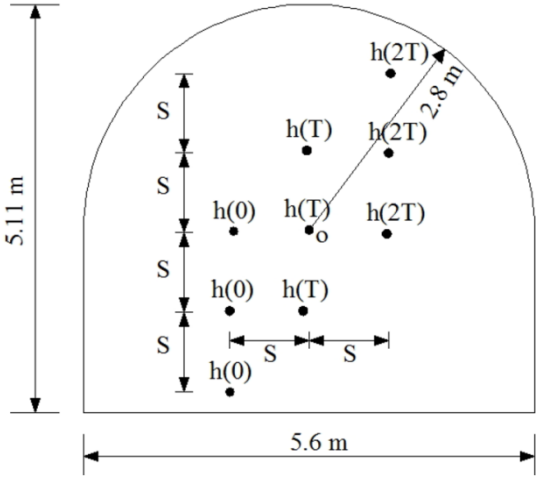

(f) Nine-hole blast (Pattern-V3)

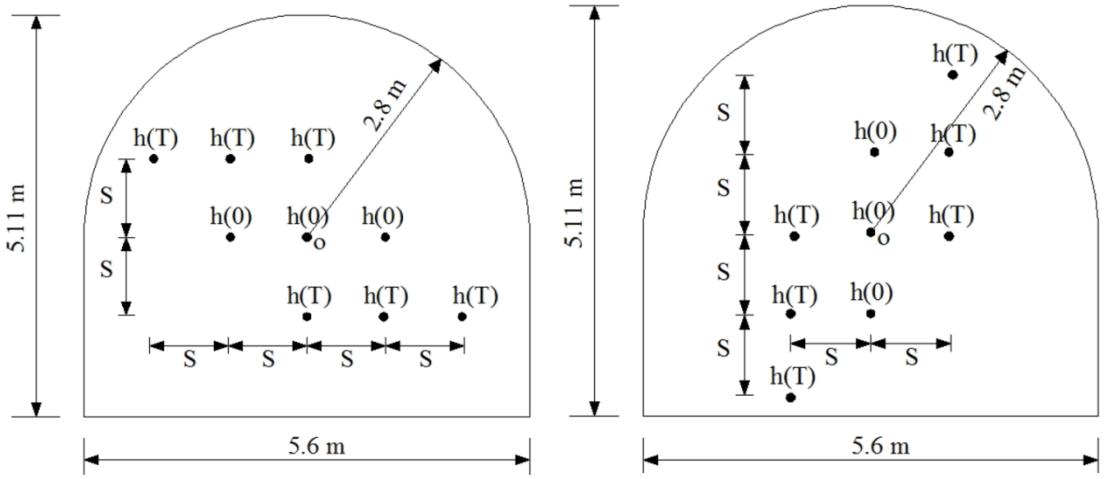

(g) Nine-hole blast (Pattern-H4)

(h) Nine-hole blast (Pattern-V4)

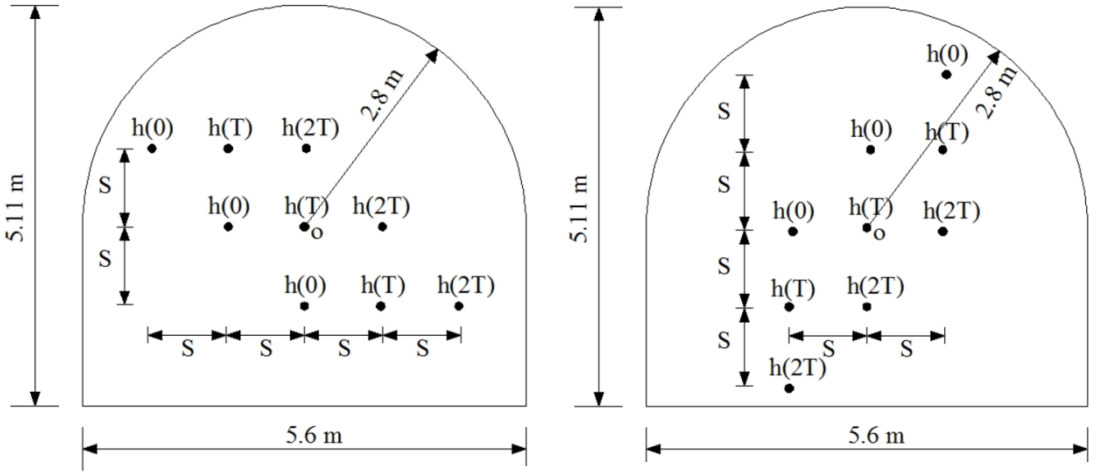

(i) Nine-hole blast (Pattern-H5)

(j) Nine-hole blast (Pattern-V5)

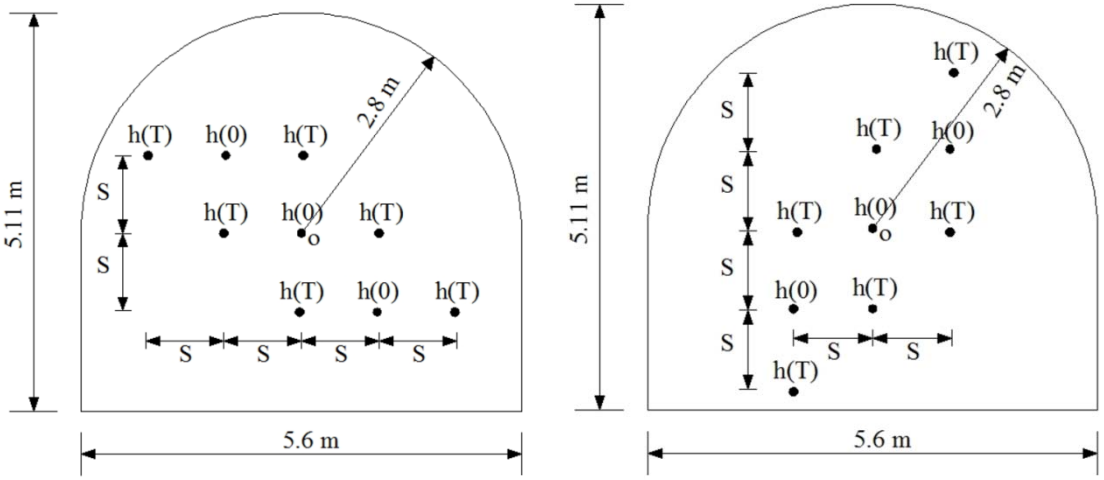

(k) Nine-hole blast (Pattern-H6)

(m) Nine-hole blast (Pattern-V6)

Figure 115. The plan of the nine-hole blast (in parallelogram shape) along the section of cross passage.

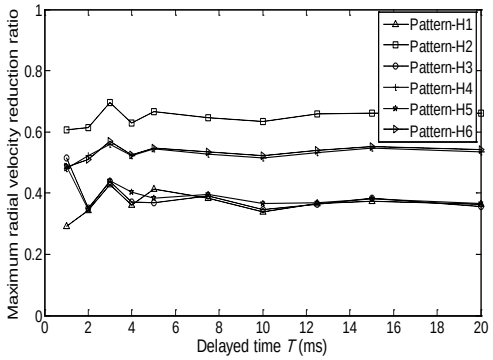

(a) The maximum radial velocity (Pattern-H1, H2, H3, H4, H5, H6)

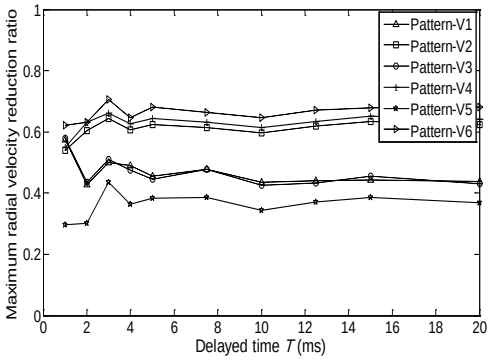

(b) The maximum radial velocity (Pattern-V1, V2, V3, V4, V5, V6)

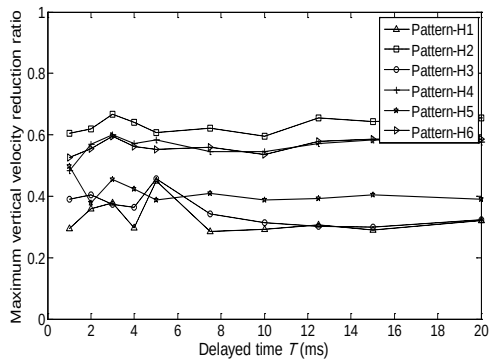

(c) The maximum vertical velocity (Pattern-H1, H2, H3, H4, H5, H6)

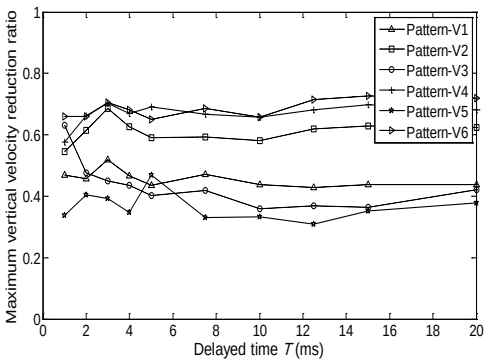

(d) The maximum vertical velocity (Pattern-V1, V2, V3, V4, V5, V6)

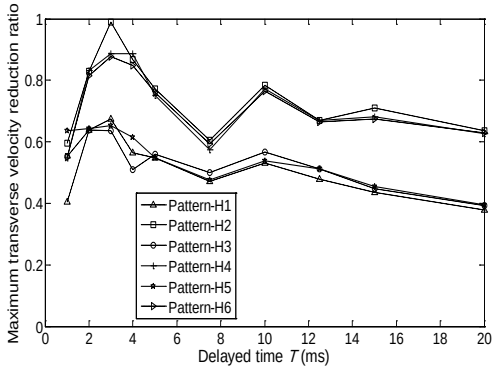

(e) The maximum transverse velocity (Pattern-H1, H2, H3, H4, H5, H6)

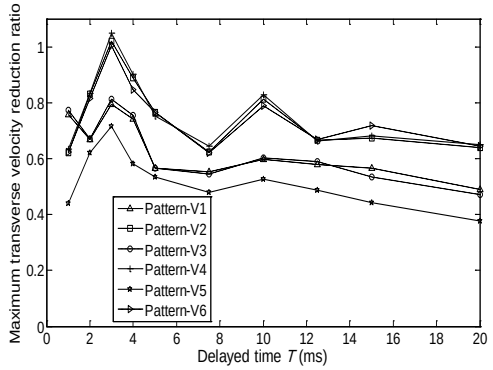

(f) The maximum transverse velocity (Pattern-V1, V2, V3, V4, V5, V6)

Figure 116. The maximum velocity reduction effectiveness of millisecond-delay explosions with nine-hole blast (in parallelogram shape, Pattern-H1, H2, H3, H4, H5, H6, V1, V2, V3, V4, V5 and V6 are shown in Figure 115).

6.2.5 Multiple-hole blast in triangle shape

To study the millisecond-delay explosions in a more practical way, a common plan of blastholes which is in triangle shape is presented, as shown in Figure 117. There are generally four patterns of blastholes: Pattern-1, Pattern-2, Pattern-3 and Pattern-4 (see Figure 117(a)-(d), respectively). For the Pattern-1 and Pattern-3, explosives are fired from the center to outside; While for the Pattern-2 and Pattern-4, explosives are firstly fired in the middle place and then toward the inside and outside. Observed from Figure 118, which shows the maximum velocity reduction effectiveness of millisecond-delay explosions with multiple-hole blast in triangle shape, it is found that the vibration of main tunnel generated by multiple-hole blast in Pattern-1 (Pattern-3) is smaller than the one in Pattern-2 (Pattern-4). This confirms again that it is better to fire explosives from one side (center) to another side (outside) rather than firing explosives from the middle place to its sides.

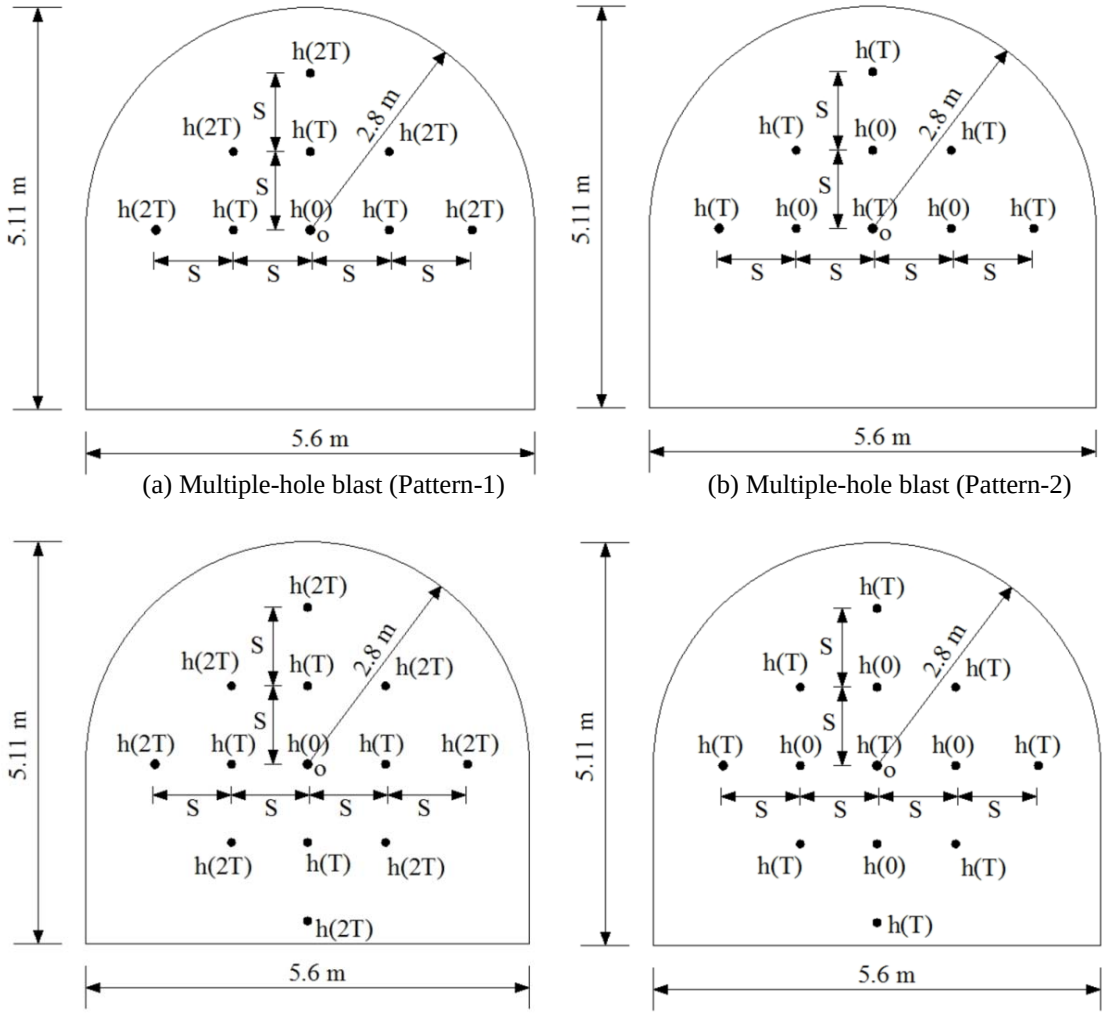

(a) Multiple-hole blast (Pattern-1)

(b) Multiple-hole blast (Pattern-2)

(c) Multiple-hole blast (Pattern-3)

(d) Multiple-hole blast (Pattern-4)

Figure 117. The plan of the multiple-hole blast (in triangle shape) along the section of cross passage.

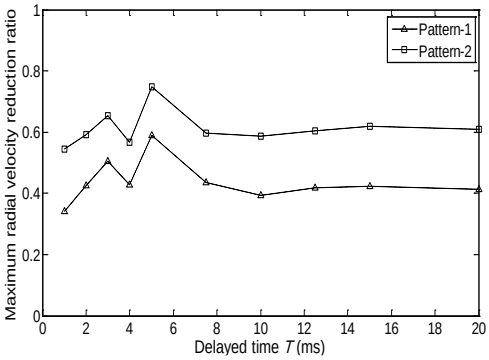

(a) The maximum radial velocity (Pattern-1, 2)

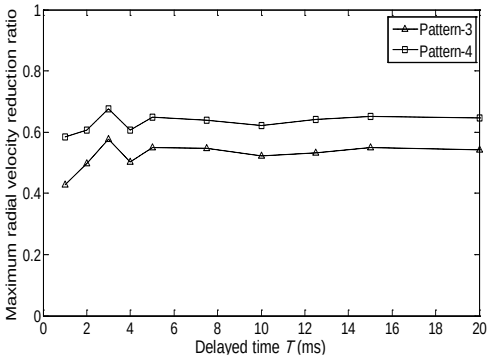

(b) The maximum radial velocity (Pattern-3, 4)

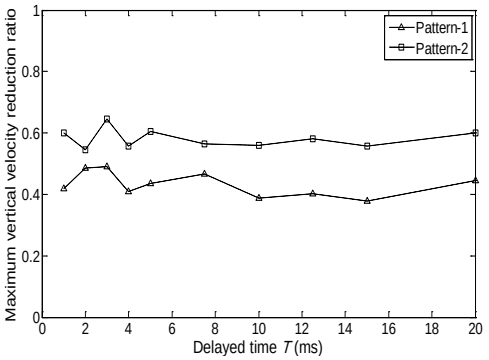

(c) The maximum vertical velocity (Pattern-1, 2)

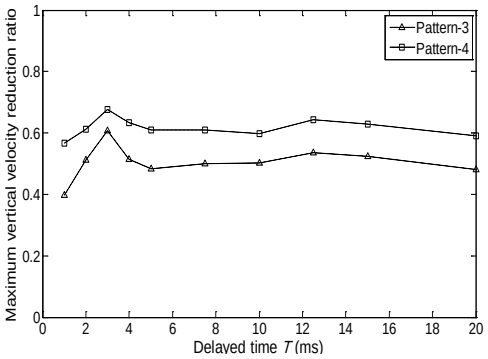

(d) The maximum vertical velocity (Pattern-3, 4)

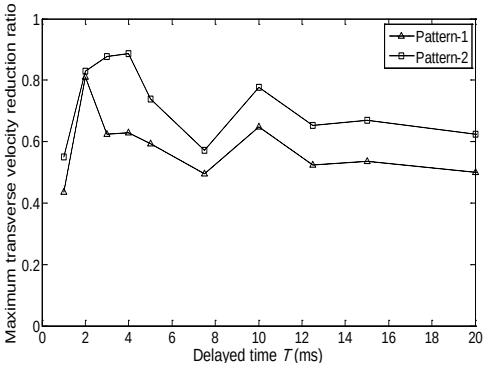

(e) The maximum transverse velocity (Pattern-1, 2)

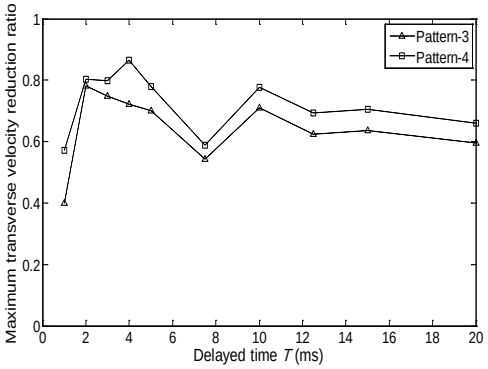

(f) The maximum transverse velocity (Pattern-3, 4)

Figure 118. The maximum velocity reduction effectiveness of millisecond-delay explosions with multiple-hole blast (in triangle shape, Pattern-1, 2, 3 and 4 are shown in Figure 117).

6.3 Conclusions

Two effective mitigation measures, which are the installation of a protective layer along the main tunnel lining and the millisecond-delay explosions, are investigated for the blast-induced vibration of main tunnel through 3D numerical simulation in ABAQUS. The mitigation effect of installing a protective layer is examined by a comprehensive parametric study and a developed optimization design method (EPS protective layer as an example), and the mitigation effect of millisecond-delay explosions is examined by choosing different delayed times, different patterns of blastholes and different sequences of firing explosives. Based on the analyses and discussions above, the following understandings and conclusions are made:

- The installation of a protective layer made of soft material is very effective in reducing the vibration of main tunnel under nearby explosions; for example, an estimated 50- 60% maximum velocity reduction can be achieved if the EPS protective layer is installed along the main tunnel lining. Protective layers made of hard materials (e.g. wood, cement grout) seem to have little or no contribution in reducing the tunnel motion.
- The thickness of the protective layer, the distance of explosions from main tunnel and the magnitude of blast pressure have quite limited influence on the vibration isolation effectiveness of the protective layer (however, it does not mean that the absolute motion of main tunnel change little with the variation of parameters mentioned above).
- Remarkable vibration reduction can be achieved if millisecond-delay explosions (rather than instantaneous explosions) are adopted. The delayed time larger than 20 ms is encouraged to minimize the motion of main tunnel.
- Millisecond-delay explosions with explosives fired from one side to another side is more effective in mitigating the motion of main tunnel than the ones where explosives are fired from the middle place to its sides. Therefore, the former detonation method is recommended in practice in order to mitigate the blast-induced vibration of existing tunnel.

7. Conclusions and future work

In this chapter, the main conclusions drawn in the previous chapters are summarized and the areas where future work may be achieved are pointed out.

7.1 Conclusions

Ground vibration generated by dynamic sources has attracted an increasing attention in recent years, due to its variety of adverse influences, like damaging nearby buildings, disturbing inhabitants, affecting the accuracy of sensitive equipments. To deal with it, many vibration reduction methods have been proposed and applied in practice, one of them is the installation of wave barrier between the dynamic source and the protected structures, which is considered a cost-effective way. Over the past decades, extensive efforts have been made to investigate the barrier vibration isolating effectiveness, and remarkable achievements have been made. However, to the best of the writer's knowledge, few researchers focus on the optimization design for wave barriers. On the other hand, with more and more second parallel tunnels being constructed by blasting and drilling method and a series of terrorist attacks in public subway systems, the dynamic behavior and the security of existing tunnels under nearby explosions has generated more and more attention. Up to now, little work has been done on the mitigation measures of reducing the blast-induced vibration of existing tunnel. To overcome these drawbacks, this dissertation investigates the isolation performance of wave barrier by conducting a comprehensive parametric study and developing an optimization design, aiming to provide an effective, reasonable and economic way for the wave barrier design in practice. Besides, the dynamic behavior of existing tunnel under nearby explosions is examined as well; two mitigation measures for reducing the vibration of main tunnel are presented with details, aiming to provide a reference for the tunnel protection design under explosions.

From the Chapters 3 and 4, it is found that the ground vibration generated by surface harmonic source and subsurface explosions can be significantly reduced if wave barrier with proper parameters is installed. Soft barriers with large depth are particularly effective in reducing the ground motion in protective sites. It is noted that the barrier width and inclination angle seem to have little influence on the isolation effectiveness in the case of subsurface explosions, but their influences cannot be ignored in the case of surface harmonic load. Specifically, under the surface harmonic load, a proper increase in the barrier width is beneficial, wave barrier with width slightly larger than its depth performs better than the one with other widths. Moreover, wave barrier with a small inclination angle away from vertical direction has a better screening effect

than vertical ones. If it is feasible to install inclined barriers, slightly oblique barriers are encouraged. Other parameters like the barrier Poisson's ratio, damping ratio, the barrier location, the magnitude of external load has negligible or no influence on the vibration isolation effectiveness under the surface harmonic source and subsurface explosions. Furthermore, by using Python scripts in ABAQUS, the optimization design method is developed for the wave barrier design in practice. Once all the possible available parameters are given, barriers ranging from performing the best to being the worst can be identified. With the suggested method, plus the experiences of engineers and the limitations in reality, the best choice of barriers is expected to become available.

Based on the results from Chapters 5 and 6, it is found that the main tunnel lining stiffness, the distance of explosions from main tunnel and the magnitude of the blast pressure significantly affect the motion of main tunnel under explosions. The influences of other parameters like the lining thickness, the position of explosions along the section of cross passage, and the buried depth of main tunnel are negligible. Numerical results show that elastic model can be used for simulating the dynamic behavior of main tunnel under weak explosions ($< 60P_{equivalent}$), but concrete damage plasticity (CDP) model has to be adopted to better reflect the real behavior of main tunnel under strong explosions ($\geq 60P_{equivalent}$), where plastic deformation or even possible damage and stiffness degradation appear. Numerical results also reveal that the compression damage, tension damage and stiffness degradation of main tunnel lining firstly occur on the top heading of the lining arch and then at the bottom of the sidewall (on the side near the explosions) with an increasing blast pressure. If there are slabs inside the main tunnel, the slabs are more vulnerable to experience tension damage than the lining; however, the vibration of the slabs is generally smaller than the vibration of the tunnel lining. In addition, the lining without slabs inside performs better in resisting potential vibration-induced damage than the lining with slabs inside, but the slabs seem to have little influence on the maximum motion of the tunnel lining. For the whole main tunnel, both the lining and the slabs are likely to experience tension failure rather than compression failure under strong explosions. In Chapter 6, two effective mitigation measures: the installation of a protective layer and the usage of time-delayed explosions are proposed in reducing the blast-induced vibration of main tunnel. It is found that significant velocity reduction can be achieved if soft protective layer is installed, for example, an estimated 50- 60% maximum velocity reduction is achieved in the presence of EPS protective layer. Remarkable vibration isolation effectiveness can also be observed when millisecond-delay explosions with delayed time larger than 20 ms are adopted. And millisecond-delay explosions with explosives fired from one side to another side is more efficient in reducing the tunnel vibration than the ones where explosives are fired from the middle place to the its sides. Therefore,

the former detonation method is suggested in practice in order to maximally reduce the vibration of existing tunnel.

7.2 Recommendations for future work

Although some work has been done to better understand the isolation performance of wave barrier and the mitigation measures for protecting existing tunnel under explosions, there are still much work to do. The following paragraphs show the recommendations for future work.

The wave barrier investigation is based on the assumptions that the whole model is homogeneous, isotropic and elastic, and the interface between the soil (or rock) and wave barrier is perfected contacted. Apparently, such assumptions can hardly reflect the real conditions. Heterogeneous and anisotropic soil media widely exists in reality and exhibits complicated constitutive relation under external load, especially under strong dynamic sources. Nonlinear behaviors of the interface between the soil and wave barrier like the slippage, separation and rebound are also common. To take these effects into account, more practical models which are able to reflect the real behavior of the soil-barrier system ought to be developed. It is noted that although some researchers have developed more practical models and some progresses have been achieved, it should be pointed out, however, that it generally takes (much) longer time to finish the calculation of the numerical simulation of soil-barrier system with (much) more complicated constitutive relations. Given the huge combination number of parameters during the optimization design for wave barrier, the total calculation time may be too long to be acceptable if (too) complicated constitutive relations of the soil-barrier system are adopted. Therefore, how to deal with the contradiction between more accurate model and longer calculation time may also be an important research field. In addition, the protected site in this dissertation is just a point, if a relatively large zone is required to be protected in practice, it is perhaps more straightforward to investigate the isolation performance of wave barrier for protecting a zone, although a zone can be generally decomposed into a series of connected points. For the study on the dynamic behavior of existing tunnel under nearby explosions, there are similar problems in this dissertation, i.e. the homogeneous, isotropic and elastic model of rock-tunnel system is too simple to represent the real conditions when the main tunnel is subjected to nearby explosions. Although it is reasonable to assume that the rock media keeps elastic when it is far away from the explosions and the concrete damaged plasticity constitutive relation is proposed for the main tunnel lining and the slabs under strong explosions, the assumption that the interfaces among the rock, the lining and the slabs are perfected contacted is undoubtedly not realistic. Besides, the detonation of explosive charges often produces a wide variation of pressure-time histories, even when identical charges are used [132]. Therefore, it may be unreliable to define the blast pressure that simply comes from previous empirical equations. Such simplified treatment may be

acceptable if the explosive is far away from the existing tunnels [91], but if the explosions occur near the existing tunnels, in-field measurements should be committed to obtain the accurate values of blast pressure. In addition, dynamic material properties of both the rock media and the tunnel should be adopted during the numerical investigation, for static material properties often cause conservative results, especially when the rock is relatively soft and the explosions are very strong. It is noted that a protective layer is proposed to be installed along the outside of main tunnel lining, however, since the lining structure generally has several different layers, it may be necessary to examine the isolation performance of the protective layer which lies between different layers of tunnel lining or inside the tunnel lining. It is also interesting to examine the isolation efficiency of two or even more protective layers installed with different material properties, positions, thicknesses, etc. Although millisecond-delay explosions with some basic patterns of blastholes have been investigated, there is no doubt that the influence of more practical patterns of blastholes needs to be examined. The last point that is worth mentioning is that the research in this dissertation is purely numerical investigation, experimental study is strongly recommended to be carried out to verify the numerical results.

References

[1] Assessing Vibration: a technical guideline. *Department of Environment and Conservation (NSW)*. Feb 2006.

[2] B. Yousef, V.V. Bertero. Earthquake Engineering: From Engineering Seismology to Performance-Based Engineering. *CRC Press*. 2004.

[3] Earthquake Engineering Research. *Committee on Earthquake Engineering, Research Commission on Engineering and Technical Systems*, National Research Council, National Academy Press, Washington, D.C. 1982.

[4] M.H. El-Naggar, K. J. Bentley. Dynamic analysis for laterally loaded piles and dynamic p-y curves. *Canadian Geotechnical Journal*, 37(6):1166–1183, 2000.

[5] M.R.M. Javan, A. Noorzad, M.L. Namin. Three-dimensional nonlinear finite element analysis of pile groups in saturated porous media using a new transmitting boundary. *International Journal for Numerical and Analytical Methods in Geomechanics*, 32(6): 681–699, 2008.

[6] F. Lopez-Caballero, A. Modaressi, F. Razavi, H. Modaressi. Nonlinear numerical method for earthquake site response analysis I - elastoplastic cyclic model and parameter identification strategy. *Bulletin of Earthquake Engineering*, 5(3):303–323, 2007.

[7] R. Gilbert. Towards sustainable transportation. *Conference proceedings, Organization for Economic Cooperation and Development*, British Columbia, 1996.

[8] H.E.M. Hunt. Measurement and modeling of traffic-induced ground vibration. *PhD dissertation, University of Cambridge*, 1998.

[9] G.R. Watts. The generation and propagation of vibration in various soils produced by the dynamic loading of load pavements. *Journal of Sound and Vibration*, 156(2):191-206, 1992.

[10] French Train Hits 357 mph Breaking World Speed Record. Foxnews.com. 4 April 2007. Retrieved 11 Feb 2010.

[11] Y.B. Yang, H.H. Hung. Wave propagation for train-induced vibrations: a finite/infinite element approach. *World Scientific*, 2009.

[12] K.A. Kuo. Vibration from underground railways: considering piled foundations and twin tunnels. *PhD dissertation. University of Cambridge*, 2010.

[13] D.M. Hiller, V.S. Hope. Ground-borne vibration generated by mechanized construction activities. *Proceedings of the Institution of Civil Engineers-Geotechnical Engineering*, 131(4):223-232, 1998.

[14] L.W. Braile. Seismic waves and the slinky: a guide for teachers. *Department of Earth and Atmospheric Sciences Purdue University West Lafayette*, IN 47907-2051.

[15] F.E. Richart, J.R. Hall, R.D. Woods. Vibrations of soils and foundations. *Prentice-Hall, Inc., Englewwood Cliffs, New jersey*, 1970.

[16] R.E. Sheriff, L.P. Geldart. Exploration seismology. *Cambridge University Press*, 1995.

[17] R.D. Woods. Screening of surface waves in soils. *Journal of the Soil Mechanics and Foundations Division. Proceeding, ASCE*, 94(4):951-979, 1968.

[18] R.D. Woods, F.E. Richart. Screening of elastic surface waves by trenches. *International Symposium on Wave Propagation and Dynamic Properties of Earth Materials*, Albuquerque, New Mexico, August 1967.

[19] W.M. Ewing, W.S. Jardetzky, F. Press. Elastic waves in layered media. *McGraw-Hill Book Co.* New York. 1957.

[20] G.F. Miller, H. Pursey. On the partition of energy between elastic waves in a semi-infinite solid. *Proceedings of the Royal Society*, London, A 233:55-69, 1995.

[21] S. Fidell, D. Barber, T. Schultz. Updating a dosage-effect relationship for the prevalence of annoyance due to general transportation noise. *Journal of the Acoustical Society America*, 89:221-233, 1991.

[22] J.M. Fields, J.G. Walker. The response to railway noise in residential areas in Great Britain. *Journal of Sound and Vibration*, 85(2):177-255, 1982.

[23] K. Kryter. Community annoyance from aircraft and ground vehicle noise. *Journal of the Acoustical Society of America*, 72:1212-1242, 1982.

[24] H. Miedema, H. Vos. Exposure-response relationships for transportation noise. *Journal of the Acoustical Society of America*, 104(6):3432-3445, 1998.

[25] T. Schultz. Synthesis of social surveys on noise annoyance. *Journal of the Acoustical Society of America*, 64:377-405, 1978.

[26] D. Dinges, F. Pack, K. Williams, K. Gillen, J. Powell, G. Ott, C. Aptowicz, A. Pack. Cumulative sleepiness, mood disturbance and psychomotor vigilance performance decrements during a week of sleep restricted to 4-5 hours per night. *Sleep*, 20(4):267-277, 1997.

[27] M. Ferrara, L.D. Gennaro. How much sleep do we need? *Sleep Medicine Reviews*, 5(2): 155-179, 2001.

[28] A.J. Brammer. Human response to vibration and mechanical shock. *Canadian Acoustics*. 30(3):112-113, 2002.

[29] M. Kutz. Standard Handbook for Biomedical Engineering & Design, *McGraw Hill*, New York, 2002.

[30] A. Mayers. Vibration acceptance criteria. *Australian Bulk Handing Review*. pp 54-55, 2009.

[31] J. Andrew, E. Wong, H.Y. Xi. China reports student toll for quake. *New York Times*. May 7, 2009.

[32] More than 4.8 million homeless in Sichuan quake: official. *Relief Web. Agence France-Presse*. May 16, 2008.

[33] DUAP. Assessment of noise, vibration and blasting impacts. *EIS manual. Department of Urban Affairs and Planning*, Sydney. 1997.

[34] C.J.C. Jones, J.R. Block. Prediction of ground vibration from freight trains. *Journal of Sound and Vibration*, 193(1):205-213, 1996.

[35] M. Petyt, C.J.C. Jones. Modeling of ground-borne vibration from railways. *In: Fryba, Naprstek, editors. Structural dynamics-EURODYN'99*, vol. I. Rotterdam: Balkema; pp: 79-87, 1999.

[36] A.T. Peplow, C.J.C. Jones, M. Petyt. Surface vibration propagation over a layered elastic half-space with an inclusion. *Applied Acoustics*, 56:283-296, 1999.

[37] D.D. Barkan. Dynamics of based and foundations. *MacGraw-Hill Book Company Inc*. pp: 374-406, 1962.

[38] H. Kolsky. Stress waves in solids. *Dover Publications. Inc.* New York, 1963.

[39] L. Rayleigh. On waves propagated along the plane surface of an elastic solid. *London Mathematical Society Proceeding,* 17:4-44, 1885.

[40] H. Lamb. On the propagation of tremors over the surface of an elastic solid. *Philosophical Transactions of the Royal Society.* London, Ser. A. 203:1-42, 1903.

[41] R.M. White. Elastic Wave Scattering at a Cylindrical Discontinuity in a Solid. *Journal of the Acoustical Society of America.* 30 (8):771-785, 1958.

[42] L. Knopoff. Scattering of compression waves by spherical obstacles. *Geophysics* 24:30-39, 1959.

[43] L. Knopoff. Scattering of shear waves by spherical obstacles. *Geophysics* 24:209-219, 1959.

[44] S.A. Thau, Y.H. Pao. Diffractions of horizontal shear waves by a parabolic. *Journal of Applied Mechanics* 33:785-792, 1966.

[45] V.R. Thiruvenkatachar, K. Viswanathan. Dynamic response of an elastic half-space with cylindrical cavity to time-dependant surface traction over the boundary of the cavity. *Journal of Applied Mathematics and Mechanics*, 14:541-572, 1965.

[46] K. Viswanathan, V.R. Thiruvenkatachar. Dynamic response of an elastic half-space with cylindrical cavity to time-dependent surface tractions over boundary of the cavity. II. *Proceedings of the Royal Society, A*, 300:159-186, 1967.

[47] M.D. Trifunac. Scattering of plane SH waves by a semi-cylindrical canyon. *Earthquake Engineering & Structural Dynamics.* 1(3):267-281, 1972.

[48] C.C. Mei, M.A. Foda. An analytical theory of resonant scattering of SH waves by thin overground structures. *Earthquake Engineering & Structural Dynamics*, 7(4):335-353, 1979.

[49] F. Höllinger, F. Ziegler. Scattering of pulsed Rayleigh surface waves by a cylindrical cavity. *Wave Motion*, 1(3):225-238, 1979.

[50] A. Boström, G. Kristensson. Elastic wave scattering by a three-dimensional inhomogeneity in an elastic half space. *Wave Motion*, 2(4):335-353, 1980.

[51] A. Boström, G. Kristensson. Scattering of a pulsed Rayleigh wave by a spherical cavity in an elastic half space. *Wave Motion*, 5(2):137-143, 1983.

[52] V.W. Lee. A Note on the Scattering of Elastic Plane Waves by a Hemispherical Canyon. *Earthquake Engineering & Structural Dynamics*, 66:109-123.

[53] K.R. Massarsch. Vibration isolation using Gas-filled cushions. *Soil Dynamics Symposium in Honor of Professor Richard D. Woods. Proceedings of the Sessions of the Geo-Frontiers*.Austin, Texas, January 24-26, 2005.

[54] C. Murillo, L. Thorel, B. Caicedo. Ground vibration isolation with geofoam barriers: Centrifuge modeling. *Geotextiles and Geomembranes* 27: 423-434, 2009.

[55] A. Alzawi, M.H. EI-Naggar. Full scale experimental study on vibration scattering using open and in-filled(geofoam) wave barriers. *Soil Dynamics and Earthquake Engineering* 31: 306-317, 2011.

[56] M.O. Al-Hunaidi, J.H. Rainer. Remedial measures for traffic-induced vibrations at a residential site. I. Field tests. *Journal of the Canadian Acoustical Association*, 19(1):3-13, 1991.

[57] J. Aboudi. Elastic waves in half-space with thin barrier. *Journal of the Engineering Mechanics Division (ASCE)*, 99(1):69-83, 1973.

[58] T.M. Al-Hussaini, S. Ahmad. Design of wave barriers for reduction of horizontal ground vibration. *Journal of Geotechnical and Geoenvironmental Engineering (ASCE)*, 117(4): 616-636, 1991.

[59] T.M. Al-Hussaini, M. Ahmad. Simplified design for vibration screening by open and in-filled trenches. *Journal of Geotechnical and Geoenvironmental Engineering (ASCE)*, 117 (1):67-88, 1991.

[60] R. Motamed, K. Itoh, K. Hirose, A. Takahashi, O. Kusakabe. Evaluation of wave barriers on ground vibration reduction through numerical modeling in ABAQUS. *SIMULIA Customer Conference*, 2009.

[61] G. Segol, C.Y. Lee, J.F. Abel. Amplitude reduction of surface waves by trenches. *Journal of the Engineering Mechanics Division*, 104(3):621-641, 1978.

[62] M. Fuyuki, Y. Matsumoto. Finite difference analysis of Rayleigh wave scattering at a trench. *Bulletin of the Seismological Society of America*, 70(6):2051–2069, 1980.

[63] K. Emad, G.D. Manolis. Shallow Trenches and Propagation of Surface Waves. *Journal of Engineering Mechanics*, 111(2):279-282, 1985.

[64] D. Beskos, G. Dasgupta, I. Vardoulakis. Vibration isolation using open or filled trenches, Part 1: 2-D homogeneous soil. *Computational Mechanics*, 1:43–63, 1986.

[65] K. Leung, D. Beskos, I. Vardoulakis. Vibration isolation using open or filled trenches, Part 3: 2-D nonhomogeneous soil. *Computational Mechanics*, 7:137–48, 1990.

[66] Y.B. Yang, H.H. Hung. A parametric study of wave barriers for reduction of train-induced vibrations. *International Journal for Numerical Methods in Engineering*, 40:3729–3747, 1997.

[67] M.O. Al-Hunaidi, J.H. Rainer. Remedial measures for traffic-induced vibrations at a residential site. Π. FEM simulations. *Journal of the Canadian Acoustical Association*, 19(2): 11-20, 1991.

[68] M. Adam, O.V. Estorff. Reduction of train-induced building vibrations by using open and filled trenches. *Computer and Structures*, 83:11-24, 2005.

[69] O.V. Estorff, M.J. Prabucki. Dynamic response in the time domain by coupled boundary and finite elements. *Computational Mechanics*, 6(1):35-46, 1990.

[70] K. Itoh, M. Koda, K. Lee, O. Murata, O. Kusakabe. Centrifugal simulation of wave propagation using a multiple ball dropping system. *International Journal of Physical modeling in Geotechnics*, 2(2):33-51, 2002.

[71] K. Itoh, X. Zeng, M. Koda, O. Murata, O. Kusakabe. Centrifuge simulation of wave propagation due to vertical vibration on shallow foundations and vibration attenuation countermeasures. *Journal of Vibration and Control*, 11:781–800, 2005.

[72] S. Liao, D.A. Sangrey. Use of piles as isolation barriers. *Journal of the Geotechincal Engineering Division*, 104(9):1139-1152, 1978.

[73] G. Wass. Linear two-dimensional analysis of soil dynamics problems in semi-infinite layered media. *Ph. D. thesis, University of California*, Berkeley, California, 1972.

[74] H.J. Dolling. Schwingungsisolierung von Bauwerken durch tiefe auf geeignete Weise stabilisierte Schiltze. *VDI-Berichte* 88, S.3741, 1965. (in German).

[75] H. Neumeuer. Untersuchungen uber die Abschirmung eines bestehenden Gebaudes gegen Erschutterungen beim Bau und Betrieb einer U-Bahnstrecke, Baumaschine and Bautechnik-10. *Jahrgang, Heft* 1:23-29, 1963. (in German).

[76] R.L. McNeill, B. E. Margason, F.M. Babcock. The role of soil dynamics in the design of stable test pads. *Proceedings Guidance and Control Conference*, 366-375, 1965.

[77] D.E. Beskos, G. Dasgupta, I.G. Vardoulakis. Vibration isolation of machine foundations. Vibration problems in geotechnical engineering, *G. Gazetas and E. T. Selig, eds., ASCE*, New York, N.Y., 138-151, 1985.

[78] K. Emad, G.D. Manolis. Shallow trenches and propagation of surface waves. *Journal of Engineering Mechanics (ASCE)*, 111(2):279-282, 1985.

[79] M.C.R. Davies. Dynamic Soil Structure Interaction Resulting from Blast Loading. *Leung, Lee and Tan(Eds.), Centrifuge 94*, Balkema, Rotterdam, 319-324, 1994.

[80] J.G. Wang, W. Sun, S. Anand. Numerical investigation on active isolation of ground shock by soft porous layers, *Journal of Sound and Vibration*, 321: 492–509, 2008.

[81] J. Avilés, F.J. Sánchez-Sesma. Foundation isolation from vibrations using piles as barriers. *Journal of Engineering Mechanics ASCE*, 114(11):1854-1870, 1988.

[82] M.H. El-Naggar, A.G. Chehab. Vibration Barriers for Shock-Producing Equipment, *Canadian Geotechnical Journal*, 42: 297-306, 2005.

[83] G. Pflanz, K. Hashimoto, N. Chouw. Reduction of structural vibrations induced by a moving load*. Journal of Applied Mechanics*, 5:555-563, 2002.

[84] J. Lysmer, G. Waas. Shear waves in plane infinite structures. *Journal of the Engineering Mechanics Division ASCE*, 98(1):85-105, 1978.

[85] S.E. Kattis, D. Polyzos, D.E. Beskos. Vibration isolation by a row of piles using a 3-D frequency domain BEM. *Numerical Methods in Engineering*, 46(5):713-728, 1999.

[86] P.H. Tsai, Z.Y. Feng, T.I. Jen. Three-dimensional analysis of the screening effectiveness of hollow pile barriers for foundation-induced vertical vibration. *Computers and Geotechnics*, 35(3):489-499, 2008.

[87] A. Dix. Terrorism – the new challenge for old tools. *Tunn and Tunn Int*, 36(10):41-43, 2004.

[88] B.M. Jenkins. Protecting public surface transportation against terrorism and serious crime: an executive overview. *The Mineta Transportation Institute, College of Business, San José State University*, 2001.

[89] Blue Ribbon Panel on Bridge and Tunnel Security. Recommendations for bridge and tunnel security, 2003.

[90] S. Choi, J. Wang, G. Munfakh, E. Dwyre. 3D Nonlinear blast model analysis for underground structures. *In: Proceedings of geocongress*, pp: 206, 2006.

[91] Y. Lu, Z. Wang, K. Chong. A comparative study of buried structure in soil subjected to blast load using 2D and 3D numerical simulations. *Soil Dynamics and Earthquake Engineering*, 25:275–288, 2005.

[92] M.W. Gui, M.C. Chien. Blast-resistant analysis for a tunnel passing beneath Taipei Shongsan airport—a parametric study. *Geotechnical and Geological Engineering*, 24: 227–248, 2006.

[93] H.B. Liu. Dynamic analysis of subway structures under blast loading. *Geotechnical and Geological Engineering*, 27:699-711, 2009.

[94] K. Bian, D. Liu, J. Jia. Investigation and analysis of effect of engineering blasting on railway tunnel failure. *In: Feng S (ed) Colloquium on engineering blasting*. Metallurgical Industry Press, Beijing, pp:199–205, 1988. (in Chinese)

[95] G. Berta. Blasting-induced vibration in tunneling. *Tunnel and Underground Space Technology*, 9:175–187, 1994.

[96] Q.G. Liang, J. Li, D.W. Li, E.F. Ou. Effect of blast-induced vibration from new railway tunnel on existing adjacent railway tunnel in Xinjiang, China. *Rock Mechanics and Rock Engineering*, 46(1):19-39, 2012.

[97] J.Cl. Debremaecker. Transmission and reflection of Rayleigh waves at corners. *Geophysics*, 23(2):253-266, 1958.

[98] W.A. Haupt. Isolation of vibration by concrete core walls. *Proceedings of 9th International Conference of Soil Mechanics and Foundation Engineering, 2, Japanese Society of Soil Mechanics and Foundation Engineering*, pp:251-256, 1977.

[99] W.A. Haupt. Surface waves in nonhomogeneous half-space. *Dynamical methods in soil and rock mechanics*, B. Prange, ed., A. A. Balkema, Rotterdam, The Netherlands, pp:335-367, 1978.

[100] J.C. Li, H.B. Li, G.W. Ma, Y.X. Zhou. Assessment of underground tunnel stability to adjacent tunnel explosion. *Tunnelling and Underground Space Technology*, 35:227-234, 2013.

[101] N. Juang, C.B. Zhou. Blasting vibration safety criterion for a tunnel liner structure. *Tunnelling and Underground Space Technology*, 32:52-57, 2012.

[102] Y.B. Yang, X.Y. Xie, R.L. Wang. Numerical simulation of dynamic response of operating metro tunnel induced by ground explosion. *Journal of Rock Mechanics and Geotechnical Engineering*, 2(4):373-384, 2010.

[103] G.D. Hatzigeorgiou, D.E. Beskos. Soil–structure interaction effects on seismic in elastic analysis of 3-Dtunnels. *Soil Dynamics and Earthquake Engineering*, 30:851-861, 2010.

[104] D.L. Wang. Seismic isolation effect of a tunnel covered with expanded polystrene geofoam. *Advanced Materials Research*, 194-196:1943-1946, 2011.

[105] H. Shahnazari, M. Esmaeili, H.H. Ranjbar. Simulating the effects of projectile explosion on a jointed rock mass using 2D DEM: a case study of ardebil-mianeh railway tunnel. *International Journal of Civil Engineering*, 8(2):125-133, 2010.

[106] S. Huang, W.Z. Chen, J.P. Yang, X.H. Guo, C.J. Qiao. Research on earthquake-induced dynamic responses and aseismic measures for underground engineering. *Chinese Journal of Rock Mechanics and Engineering*, 28:483–490, 2009. (in Chinese)

[107] S. Shimamura, H. Kasai, M. Haruumi. Seismic isolation effect for a tunnel with a soft isolation layer. *Structural Engineering and Earthquake Engineering, JSCE*, 16(3):143-154, 1999.

[108] *http://blogs.detroitnews.com/history/1998/09/16/horror-in-a-port-huron-water-intake-tunnel/* Michigan History - The Detroit News (accessed October 2013)

[109] *http://www.hugchina.com/china/stories/chinese-society/explosion-inside-an-under-construction-expressway-tunnel-killed-20-2012-05-19.html* Chinese Society (accessed October 2013)

[110] J.W. Kopp, D.E. Siskind. Effects of millisecond-delay intervals on vibration and airblast from surface coal mine blasting. *Report of Investigation 9026, Bureau of Mines*, United States Department of the Interior, 1986.

[111] X.Z. Shi, SH.R. Chen. Delay time optimization in blasting operations for mitigation the vibration-effects on final pit walls' stability. *Soil Dynamics and Earthquake Engineering*, 31:1154-1158, 2011.

[112] Z. Ester, M. Dobrilović, D. Vrkljan. Dynamic influence caused by close blasting on primary and secondary support system in tunnel "SV. ROK". *Rudarsko-Geološko-Naftni Zbornik* 15, 2003.

[113] L.D. Leet. Vibrations from delay blasting. *Bulletin of the Seismological Society of America*, 39:9-20, 1949.

[114] S.L. Kramer. Geotechnical earthquake engineering. *Upper Saddle River, NJ:Prentice-Hall Inc*, 1996.

[115] M. Ataei, M. Kamali. Prediction of blast-induced vibration by adaptive neuro-fuzzy inference system in Karoun 3 power plant and dam. *Journal of Vibration and Control* 22(2):1-9, 2012.

[116] W.I. Duvall, D.E. Fogelson. Review of Criteria for Estimating Damage to Residences From Blasting Vibrations. *Bureau of Mines Rept. of Investigations*, pp:19, 1962.

[117] G. Gazetas, E.T. Selig. Vibration Problems in Geotechnical Engineering. *Proceedings of a symposium sponsored by the Geotechnical Engineering Division in conjunction with the ASCE Convention in Detroit*, Michigan, October 22, 1985.

[118] ASTM D6817 Standard specification for rigid cellular polystyrene geofoam, 2011.

[119] J.S. Horvath. Expanded polystyrene (EPS) geofoam: an introduction to material behavior. *Geotextitles and Geomembranes* 13(4):263-280, 1994.

[120] A.M. Starfield, J.M. Pugliese. Compression waves generated in rock by cylindrical explosive charges: a comparison between a computer model and field measurements. *International Journal of Rock Mechanics and Mining Sciences & Geomechanics* 5:65-77, 1968.

[121] M.A.E. Farsangi, S.K.S. Durucan. The effects of velocity of detonation of explosives on ground vibration in time and frequency domains. *In: Proceedings of the 6th. International. symposium on Rock Fragmentation by Blasting, August 1999*. Johannesburg, South Africa, 1999.

[122] D. Park, B. Jeon, S. Deon. A numerical study on the screening of blast-induced waves for reducing ground vibration. *Rock Mechanics* and *Rock Engineering*, 42:449-473, 2009.

[123] ABAQUS 6.11 Analysis User's Manual

[124] T. Jankowiak, T. Odygowski. Identification of parameters of concrete damage plasticity constitutive model. *Foundation of Civil and Environment Engineering*, 6:53-69, 2005.

[125] *http://en.wikipedia.org/wiki/Fr%C3%A9jus_Road_Tunnel* (accessed October 2013)

[126] Tunnel routier du Fréjus galerie de securite. *Société française du tunnel routier du Fréjus & Società Italiana Traforo Autostradale Fréjus, Project 2006, N.Rif :6145.3-R-32*. 2006. (in French)

[127] J.F. Hubert. Études prealables dámenagement de la galerie de securite du tunnel Du Fréjus. *Rapport dóption, Sol et Sous-sol, Ref:OJHUB091217, Mines ParisTech*, 2009. (in French)

[128] G. Exel, C. Jolivet. Safety tunnel for the Fréjus road tunnel. Site Visit, *Tunnels et Espace Souterrain*, n°224, pp:167-168, 2011.

[129] *http://www.razel-bec.com/page.php?accueil_id=169&search_text=Fréjus* (accessed October 2013)

[130] *http://abaqusscript.blogspot.fr/* (accessed October 2013)

[131] Wu, G.H. Finite element study of vibration isolation using an underground trench. *PhD theis, Texas Tech University*, 1997.

[132] J.L. O'Daniel, T. Krauthammer. Assessment of numerical simulation capabilities for medium-structure interaction systems under explosive loads. *Computers & Structures*, 63(5): 875-887, 1997.